DOCTORAL THESIS

CONCRETE SUBJECTED TO FIRE LOADING – FROM EXPERIMENTAL INVESTIGATION OF SPALLING AND MASS-TRANSPORT PROPERTIES TO STRUCTURAL SAFETY ASSESSMENT OF TUNNEL LININGS UNDER FIRE

DISSERTATION

BETON UNTER BRANDBELASTUNG – VON DER EXPERIMENTELLEN UNTERSUCHUNG DES ABPLATZVERHALTENS UND DER TRANSPORT-EIGENSCHAFTEN ZUR STRUKTURANALYSE VON TUNNELSCHALEN UNTER FEUERLAST

ausgeführt zum Zweck der Erlangung des akademischen
Grades eines Doktors der technischen Wissenschaften

eingereicht an der Technischen Universität Wien
Fakultät für Bauingenieurwesen

von

Dipl.-Ing. Matthias Zeiml

Matrikelnummer: 97 25 702

Helene-Potetz-Weg 7/1.08, 1120 Wien, Österreich

Referent: Univ.-Prof. Dipl.-Ing. Dr. techn. Roman Lackner
Fachgebiet Computational Mechanics, Technische Universität München,
Arcisstraße 21, 80333 München, Deutschland

Koreferent: Prof. Dr. Bernhard A. Schrefler
Dept. of Structural and Transportation Engineering, University of Padua,
Via F. Marzolo 9, 35131 Padua, Italien

Wien, im Juli 2008   . . . .

Eine Investition in Wissen bringt noch immer die besten Zinsen.
Benjamin Franklin

Danksagung

Zum Abschluss meiner Dissertation möchte ich die Gelegenheit ergreifen all jenen zu danken, die einen Beitrag zum Entstehen und Gelingen dieser Arbeit geleistet haben.

Mein Dank gebührt all meinen derzeitigen und ehemaligen KollegInnen des Instituts für Mechanik der Werkstoffe und Strukturen (IMWS) der Technischen Universität (TU) Wien, allen voran Univ.-Prof. Dipl.-Ing. Dr.techn. Roman Lackner für seinen über die meiste Zeit uneingeschränkten Einsatz und sein Engagement bei der Betreuung dieser Dissertation. Roman Lackner sowie O.Univ.-Prof. Dipl.-Ing. Dr.techn. Dr.h.c.mult. Herbert Mang, Ph.D. und Univ.-Prof. Dipl.-Ing. Dr.techn. Josef Eberhardsteiner ermöglichten durch meine Anstellung mein Doktoratsstudium. Wolfgang Dörner, Ing. Christian Schmid und Dr.phil. Roland Reihsner unterstützten mich tatkräftig in experimentellen Fragestellungen und bei der Versuchsdurchführung. Mag.(FH) Martina Pöll, Dipl.-Ing. Elisabeth Aigner, Dipl.-Ing. Dr.techn. Klaus Meinhard, Dipl.-Ing. Dr.techn. Christian Pichler, Dipl.-Ing. Josef Füssl, Dipl.-Ing. Dr.techn. Andreas Jäger und alle weiteren KollegInnen trugen wesentlich zum angenehmen und produktiven Arbeitsklima am Institut bei.

Durch meine Beteiligung am Straßenforschungsprojekt "Brandbeständigkeit von Faser-, Stahl- und Spannbeton" ergab sich mein Weg ans IMWS und zum Doktoratsstudium. Ich möchte daher allen Projektpartnern, insbesondere Prof. Dipl.-Ing. Dr.techn. Wolfgang Kusterle (Hochschule Regensburg, Deutschland) und Dipl.-Ing. Dr.techn. Wolfgang Lindlbauer, herzlich für die Möglichkeit der Mitarbeit danken.

In Zusammenhang mit der Durchführung der in dieser Arbeit vorgestellten Experimente bin ich einer Vielzahl von Personen zu Dank verpflichtet. Mein Studienkollege Dipl.-Ing. David Leithner sowie Dipl.-Ing. Georg Ferner unterstützten mich bei den in dieser Arbeit präsentierten Permeabilitätsversuchen. Ing. Alfred Leithner von der Donau Chemie AG (Pischelsdorf) hat wesentlichen Anteil an der Entwicklung des Messaufbaus. O.Univ.Prof. Dipl.-Ing. Dr.techn. Dr.h.c. Ulrich Schneider ermöglichte die Nutzung der Infrastruktur des Zentrums für Baustoffforschung, Werkstofftechnik und Brandschutz (IBBB) der TU Wien. Dipl.-Ing. Dr.techn. Johannes Horvath und Dipl.-Ing. Hadubrand Harand gebührt mein Dank für die Hilfestellung bei der Nutzung dieser Infrastruktur. Mit Ass.Prof. Dipl.-Ing. Dr.techn. Heinrich Bruckner und Dipl.-Ing. Johannes Kirnbauer ergab sich eine fruchtbare Kooperation im Rahmen der präsentierten, am IBBB durchgeführten Brandversuche. Dipl.-Ing. Günter Sinkovits und Dipl.-Ing. Christian Baierl sei für die reibungslose Zusammenarbeit bei diesen Brandversuchen gedankt. Ing. Christian Zaruba vom Institut für Materialwissenschaften und Werkstofftechnologie der TU Wien erzeugte SEM-Aufnahmen (Scanning Electron Microscopy) der verwendeten Polypropylen-Fasern, Ann N. Lambrechts[1], MScE von NV Bekaert SA (Zwevegem, Belgien) stellte Informationen bezüglich dieser PP-Fasern zur Verfügung. Beim Gedankenaustausch mit

---

[1] Ann N. Lambrechts from NV Bekaert SA (Zwevegem, Belgium) supplied me with information on the polypropylene fibers used within the presented experimental program.

Ass.Prof. Dr. Roberto Felicetti[2] vom Department of Structural Engineering der Technischen Universität Mailand (Italien) erhielt ich wertvolle Hinweise zur Bestimmung der Bruchenergie von Beton.

Ebenso wie bei der Druchführung der Experimente gilt es auch im Zusammenhang mit der Modellbildung und der numerischen Simulation einer Reihe von Personen zu danken. Mit Ao.Univ.Prof. Dipl.-Ing. Dr.techn. Karl Ponweiser und Ao.Univ.Prof. Dipl.-Ing. Dr.techn. Andreas Werner vom Institut für Thermodynamik und Energiewandlung der TU Wien führte ich fruchtbare und wertvolle Diskussionen bezüglich der Abplatzphänomene. Prof. Dr. Bernhard A. Schrefler[3] vom Department of Structural and Transportation Engineering der Universität Padua (Italien) ermöglichte mir im Rahmen eines Forschungsaufenthalts das Studium des in Padua entwickelten Analysetools "HITECO", wodurch eine fruchtbare Kooperation und ein wesentlicher Teil dieser Arbeit entstand. Für die dabei erhaltene Hilfestellung in zahlreichen Diskussionen die komplexen Transportprozesse im brandbelasteten Beton betreffend möchte ich Dr. Francesco Pesavento (Universität Padua) und Ass.Prof. Dr. Dariusz Gawin vom Department of Building Physics and Building Materials der Technischen Universität Łódź (Polen) herzlich danken. Wertvolle Informationen bezüglich des Lainzer Tunnels von Dipl.-(HTL)Ing. Johann Lemmerer und Dipl.-Ing. Oliver Wagner von der ÖBB-Infrastruktur Bau AG sowie von Dipl.-Ing. Jessica Krastanov von iC consulenten GesmbH (Wien) ermöglichten die Strukturanalyse eines konkreten Ausführungsprojektes.

Weiters sei die finanzielle Unterstützung durch den Fonds zur Förderung der wissenschaftlichen Forschung (FWF) via Projekt P16517-N07 "Transportprozesse im Beton bei hohen Temperaturen" sowie durch das Bundesministerium für Verkehr, Innovation und Technologie (bm.vit) via KIRAS-Projekt (Österreichisches Förderungsprogramm für Sicherheitsforschung) 813794 "Sicherheit von Hohlraumbauten unter Feuerlast" dankend erwähnt.

Während meines gesamten Studiums konnte ich auf die uneingeschränkte Unterstützung und den Rückhalt meiner Familie zählen. Meine Eltern Anna und Alfred Zeiml und mein Bruder Christoph begleiteten mich durch alle Höhen und Tiefen im "Projekt Dissertation", sowohl beruflich als auch privat.

Meine Patenfamilie Barbara und Paul Chmelar hat ebenfalls großen Anteil an meiner beruflichen und persönlichen Entwicklung, sie gaben mir in wichtigen Phasen meines Lebens die richtigen Impulse.

Zu guter Letzt danke ich all meinen Freunden, mit denen ich besonders in den arbeitsintensiven Phasen der Ausarbeitung dieser Dissertation den nötigen Ausgleich fand.

Kurzfassung

Tunnelbrände haben in der Vergangenheit gezeigt, welch erheblichen Schaden eine daraus resultierende Brandbelastung an der Betoninnenschale verursachen kann. Während eines Brandes wird die Tragfähigkeit der Struktur durch die temperaturbedingte Verminderung von Steifigkeit und Festigkeit des Betons und des Bewehrungsstahls sowie das Abplatzen oberflächennaher Betonschichten reduziert, was im äußersten Fall zum Versagen der Tragstruktur führen kann. In dieser Arbeit wird die Wirkung der Brandbelastung auf Tunnelinnenschalenbeton mittels experimenteller Untersuchungen und numerischer Simulationen studiert. Folgende Fragestellungen werden behandelt:

1. *Welche Prozesse sind für das Abplatzen des Betons hauptverantwortlich und welchen Einfluss haben sie?*
   Ausgehend von der experimentellen Untersuchung der Abplatzungen von Beton ermöglichen Aufnahmen einer Hochgeschwindigkeitskamera die Bestimmung von Größe, Form und Geschwindigkeit der abgeplatzten Betonfragmente. Darauf aufbauend kann die während des Abplatzens freiwerdende Energie abgeschätzt und mit numerischen Ergebnissen verglichen werden. Letztere legen Abplatzungen aufgrund des im Beton entstehenden Dampfdrucks sowie der behinderten thermischen Ausdehnung zugrunde. Dieser Vergleich gibt Aufschluss über den Einfluss verschiedener mechanischer, thermischer und hygrischer Prozesse und lässt auf die Haupteinflussfaktoren für Abplatzungen schließen. Aufgrund des daraus abgeleiteten, großen Einflusses der Permeabilität des Betons auf das Abplatzverhalten (übereinstimmend mit Ergebnissen früherer Untersuchungen) werden Permeabilitätsexperimente unter abfallendem oder konstantem Luftdruck an der druckbeaufschlagten Seite des Probekörpers vorgestellt. Es wurden sowohl unter Baustellenbedingungen (*in-situ*) gefertigte Probekörper als auch Laborprobekörper, mit bzw. ohne Zugabe von Polypropylen-Fasern (PP-Fasern), bei Raumtemperatur getestet, nachdem sie unterschiedlichen Temperaturregimen unterzogen wurden. Die Ergebnisse werden mit der Porenstruktur von thermisch geschädigtem Beton, welche mit Hilfe von Quecksilberporosimetriemessungen untersucht wurde, in Beziehung gesetzt. Dadurch kann der Einfluss der PP-Fasern sowie von Zusatzmitteln und des Fertigungsprozesses (*in-situ* vs. *Labor*) auf die Transporteigenschaften und dadurch auf das Brandverhalten von Beton bestimmt werden.

2. *Die Berücksichtigung welcher Phänomene ist für eine realistische Abschätzung der Temperaturverteilung im brandbelasteten Beton erforderlich?*
   Um den Einfluss der Permeabilität von Beton mit bzw. ohne PP-Fasern auf das Abplatzverhalten zu untersuchen, werden Finite-Elemente-Analysen (FE-Analysen) präsentiert, wobei die wesentlichen Kopplungen zwischen Wärme- und Massetransport berücksichtigt werden. Im Vergleich zu Ergebnissen aus einer rein thermischen

Berechnung stimmen die Temperaturverteilungen aus der gekoppelten Analyse besser mit den experimentellen Werten überein. Zusätzlich geben die erhaltenen Gasdruckverteilungen im Beton Aufschluss über das Abplatzrisiko von Beton mit unterschiedlichem Fasergehalt, die erhaltenen Trends stimmen mit experimentellen Beobachtungen überein. Die numerische Untersuchung unterschiedlicher Abplatzgeschichten zeigt den Einfluss von Abplatzungen auf die Temperatur- und Gasdruckverteilung im Querschnitt.

3. *Wie wird das Tragverhalten von Tunnelinnenschalen aus Beton durch die Temperaturbelastung während eines Brandes beeinflusst?*
   Der Einfluss von Abplatzungen und der Temperaturbelastung auf das Tragverhalten von Tunnelinnenschalen wird mit Hilfe eines Strukturprogramms untersucht, das sowohl Abplatzungen von Betonschichten als auch die Abnahme der Festigkeit des Betons aufgrund von Temperatur- und Gasdruckbelastung berücksichtigt. Die zuvor bestimmten, numerischen Ergebnisse für Temperatur- und Gasdruckverteilung dienen hierbei als Eingabewerte. Im Zuge der Strukturanalyse wird ein Querschnitt des Lainzertunnels (Österreich) mit geringer Überdeckung (oberflächennaher Tunnel) untersucht.

Abstract

Tunnel fires of the past have demonstrated the severe impact of temperature loading on concrete tunnel shells. During fire loading, the load-bearing capacity of the supporting structure is reduced by temperature-induced degradation of stiffness and strength of concrete and reinforcing steel as well as by spalling of near-surface concrete layers, eventually causing collapse of the tunnel. In this work, the effect of fire on concrete used for tunnel linings is studied by means of experimental investigations and numerical simulations, addressing the following questions:

1. *What are the main processes responsible for spalling and what is their individual influence?*
   Starting with experimental investigation of spalling, high-speed camera images allow determination of the size, shape, and velocity of the spalled-off pieces. With this information at hand, the released energy associated with spalling is computed and compared to the energies associated with pore-pressure and thermal-stress spalling. This comparison provides new insight into the impact of various thermal, mechanical, and hydral processes as well as the main influencing parameters controlling explosive spalling of concrete. Having identified the permeability of concrete as one of the main parameters influencing spalling (which is in agreement with earlier-reported experimental findings), permeability experiments are presented, considering two different experimental procedures, characterized by either a constant or a decreasing pressure history at the pressurized side of the specimen. Specimens made of *in-situ* as well as *laboratory-cast* concrete with or without additional polypropylene (PP) fibers after cooling from high temperature were tested. The obtained permeability values are related to the pore structure, accessible via mercury-intrusion-porosimetry (MIP) tests, highlighting the effect of the PP-fibers as well as of additives and the production process on transport properties and, thus, on the performance of concrete under fire attack.

2. *Which phenomena shall be considered for realistic predictions of temperature distributions within heated concrete?*
   In order to illustrate the effect of the permeability of concrete with and without PP-fibers on spalling, finite-element (FE) analyses, taking the coupling between heat and mass transport into account, are presented. In contrast to consideration of heat transport only, the results from the coupled thermo-hydro-chemical analysis show better agreement with experimental values. In addition, the obtained gas-pressure distributions within the tunnel lining provide insight into the risk of spalling of concrete for varying amount of PP-fibers, agreeing well with experimental observations. Consideration of different spalling histories reveals the effect of spalling on the temperature and gas-pressure distributions within the tunnel lining.

3. *How is the structural behavior of concrete tunnel linings affected by fire loading?*
   The effect of spalling and temperature loading on the structural performance of tunnel linings is investigated by a structural analysis tool, considering spalling of near-surface concrete layers as well as the effect of temperature and gas pressure on the mechanical properties of the heated lining concrete. Hereby, the temperature and gas-pressure distributions obtained from the coupled FE-analysis serve as input for the structural model. Within this structural safety assessment, a cross-section of the Lainzer tunnel (Austria) characterized by low overburden (shallow tunnel) is analyzed.

Contents

List of symbols

a_p	[m/s^2]	acceleration of spalled-off piece
A	[m^2]	cross-sectional area
A'	[m^2]	cross-sectional area of spalled-off piece
$\langle A \rangle_p$	[–]	localization tensor
b	[Pa]	slip-flow constant
c_p	[kJ/(kg K)]	specific heat capacity of concrete
c_p^g, c_p^w	[kJ/(kg K)]	specific heat capacity of gas and water
d	[m]	thickness of tunnel lining or spalled-off piece
d_s, d_s^∞	[m]	actual and final spalling depth
$\mathbf{D}_{eff}$	[m^2/s]	effective diffusivity of concrete
E	[MPa]	Young's modulus
E_F	[J]	fracture energy
E_{kin}	[J]	kinetic energy of motion
$E_{kin}^{th}, E_{kin}^{tm}$	[J]	E_{kin} associated with thermo-hydral and thermo-mechanical processes
f_b	[MPa]	biaxial compressive strength of concrete
f_c	[MPa]	compressive strength of concrete
f_t	[MPa]	tensile strength of concrete
f_y	[MPa]	yield stress of reinforcement steel
f_r	[–]	volume fraction of different phases in concrete (with $r \in \{m \dots$ cement matrix, $a \dots$ aggregates, $l \dots$ liquid phase, $g \dots$ gas phase$\}$)
G_F	[J/m^2]	specific fracture energy
h	[kJ/kg]	specific enthalpy of vaporization
H	[m]	height of permeability specimen
$\bar{K}$	[N/m]	stiffness of soil spring-element
k_r	[MPa]	bulk modulus of different phases in concrete (with $r \in \{m \dots$ cement matrix, $a \dots$ aggregates, $l \dots$ liquid phase, $g \dots$ gas phase$\}$)
k_{int}	[m^2]	intrinsic permeability of concrete
$\mathbf{k}, k$	[m^2]	absolute permeability of concrete
k^{rg}, k^{rw}	[–]	relative permeability of concrete to gas and water
l	[m]	size (length) of spalled-off piece
l_ξ^w	[kJ/kg]	specific enthalpy of dehydration
L	[%]	level of loading
L_{equ}	[m]	length representing pressurized volume used in finite-element model for simulation of permeability experiments

m	[kg]	mass of spalled-off piece
$\dot{m}_{dehydr}$	[kg/(m³ s)]	water source term associated with dehydration
$\dot{m}_{vap}$	[kg/(m³ s)]	water source term associated with vaporization
M_a, M_w, M_g	[kg/mol]	molar mass of air, water, and gas
n	[–]	porosity of concrete or polytropic exponent
n	[mol]	moles of gas
n_e	[–]	number of finite elements
p^{atm}	[Pa]	atmospheric pressure
p^c, p^g	[Pa]	capillary and gas pressure
p_0^c, p_0^g	[Pa]	initial capillary and gas pressure
$\overline{p}^c, \overline{p}^g$	[Pa]	prescribed capillary and gas pressure
		at inner surface of lining
p_b^c	[Pa]	bubbling pressure
p^{ga}, p^{gw}	[Pa]	pressure of dry air and water vapor
p_∞^{gw}	[Pa]	prescribed vapor pressure of the surroundings
p^{gws}	[Pa]	saturation vapor pressure
p^w	[Pa]	water pressure
p	[MPa]	overpressure acting on porous network (concrete)
p_t, p_b	[Pa]	gas pressure at top and bottom of permeability specimen
$\overline{p}_t, \overline{p}_b$	[Pa]	temporal average of gas pressure at top and bottom
		of permeability specimen
p_p	[Pa]	pressure in pressure piston
q^{ga}, q^{gw}	[kg/(m² s)]	prescribed mass flux of dry air and water vapor
q_c^{gw}	[kg/(m² s)]	convective mass flux of water vapor
q^w	[kg/(m² s)]	prescribed mass flux of water
q^T	[kJ/(h m²)]	prescribed heat flux
q_c^T, q_r^T	[kJ/(h m²)]	convective and radiative heat flux
Q, Q_t	[m³/s]	gas flux and experimentally-obtained gas flux
		at top of permeability specimen
r	[m]	pore radius
R	[m]	radius of tunnel cross-section
RH	[–]	relative humidity of concrete
S	[–]	Eshelby tensor
S_w	[–]	degree of saturation
S_{w0}	[–]	initial degree of saturation
S_w^r, S_w^{cr}	[–]	residual and critical degree of saturation
t	[s]	time
T	[°C]	temperature
T_0	[°C]	initial temperature
$\overline{T}$	[°C]	prescribed temperature at inner surface of lining
T_{crit}	[°C]	critical temperature
$T_m, \Delta T$	[°C], [°C/m]	equivalent temperature load

$\mathbf{u}, u$	[m]	displacement of tunnel lining
u_p	[m]	movement of pressure piston in permeability experiments
U	[J]	elastic strain energy
v	[m]	vertical displacement at top of tunnel cross-section
v_0	[m]	vertical displacement at top of tunnel cross-section at beginning of fire loading
v_f, v_p	[m/s]	velocity of spalling front and spalled-off piece
v_p^{exp}	[m/s]	experimentally-obtained velocity of spalled-off piece
v_p^{th}, v_p^{tm}	[m/s]	v_p associated with thermo-hydral and thermo-mechanical processes
V	[m^3]	volume
V_0	[m^3]	pressurized pore volume
V_p	[m^3]	pore volume of concrete
x	[m]	horizontal coordinate
x_k, x_{k0}	[m]	actual and original coordinate of k-th node
y	[m]	vertical coordinate
$\varnothing$	[m]	diameter of permeability specimen
α	[–]	reduction factor for strength of concrete
α_T	[°C^{-1}]	thermal expansion coefficient
β_s	[°C^{-1}]	cubic thermal expansion coefficient of concrete
β_c	[m/s]	convective mass-transfer coefficient
$\varepsilon^{th}, \varepsilon^{lits}$	[–]	thermal and load-induced thermal strain
Θ	[K]	absolute temperature
η^g, η	[Pa s]	dynamic viscosity of gas
η^w, η^{gw}	[Pa s]	dynamic viscosity of water and water vapor
λ	[kJ/(h m K)]	thermal conductivity of concrete
λ_{eff}	[kJ/(h m K)]	effective thermal conductivity of concrete
ν	[–]	Poisson's ratio
ξ	[–]	degree of hydration
ξ_{dehydr}	[–]	degree of dehydration
ρ, ρ_c	[kg/m^3]	apparent density of concrete
ρ^s	[kg/m^3]	solid-phase density
ρ^g	[kg/m^3]	gas density
ρ^{ga}, ρ^{gw}	[kg/m^3]	density of dry air and water vapor
ρ^w	[kg/m^3]	water density
$(\rho c_p)_{eff}$	[kJ/(m^3 K)]	effective thermal capacity of concrete
σ	[MPa]	stress
Σ	[MPa]	macroscopic stress
τ_{dec}, τ_{adv}	[s]	characteristic times associated with pressure decrease and pressure-driven flow

Chapter 1

Introduction

1.1 Motivation

In case of fire loading, concrete structures are affected by various physical (transport processes, cracking, spalling etc.) and chemical (dehydration etc.) processes, leading to degradation of the material parameters of concrete and spalling of near-surface concrete layers. Especially in case of tunnel fires, with the thermal load characterized by a steep temperature increase during the first minutes of the fire and a maximum temperature exceeding 1200 °C, spalling can be significant (see Figure 1.1). The resulting loss of parts of the cross-sectional area of the tunnel lining considerably reduces the load-carrying capacity and may lead to collapse of the structure.
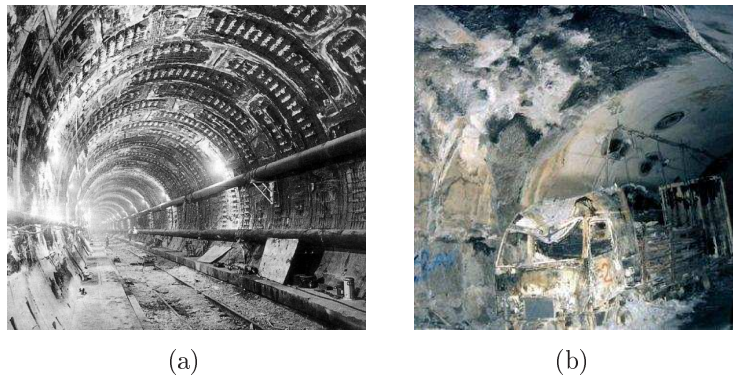

<div align="center">(a)   (b)</div>

Figure 1.1: Damage of tunnel lining showing severe spalling: (a) Channel Tunnel (1996) [18] and (b) Mont-Blanc Tunnel (1999) [51]

In the literature, different types of concrete spalling due to fire loading are defined [53, 59, 60, 110]. Depending on its location of occurrence, spalling can be divided into

1. aggregate spalling (splitting of aggregates),

2. corner spalling (i.e., corners of columns or beams fall off), and

3. surface spalling (surface layers of concrete fall off or burst out of the structural element).

Moreover, depending on its origin, spalling can be divided into

1. progressive spalling (or sloughing-off, where concrete pieces fall out of the structural element) and

2. explosive spalling (violent burst-out of concrete pieces characterized by sudden release of energy).

Two phenomena are considered to be the main causes for spalling (see Figures 1.2 and 1.3). On the one hand, the build-up of pore pressure in consequence of vaporization of water (*thermo-hydral processes*) results in tensile loading of the microstructure of concrete [4, 26, 53, 59, 78, 110], which can be referred to as pore-pressure spalling [60, 61]. On the other hand, restrained thermal dilation results in biaxial compressive stresses parallel to the heated surface which lead to tensile stresses in the perpendicular direction [10, 123]. This type of spalling in consequence of *thermo-mechanical processes* can be referred to as thermal-stress spalling [60, 61].

Recent fire experiments performed within a research project sponsored by the Austrian Federal Ministry of Transport, Innovation, and Technology (bm.vit) and the ÖBB-Infrastruktur Bau AG (formerly HL-AG, Austria) revealed that the spalling depth of concrete subjected to fire decreases with increasing amount of polypropylene (PP) fibers considered in the mix design (see Figure 1.4 and [67, 74]). According to the open literature (see, e.g., [58, 68, 110]), this can be explained by (i) the increased permeability in consequence of melting (at $T \approx$ 170 °C) and, finally, vaporization (at $T \approx 340$ °C) of the PP-fibers and (ii) the introduction of additional interfacial transition zones (ITZ) between the fibers and the cement paste. In contrast to the amount of PP-fibers, the mode of reinforcement and the type of mechanical loading, also varied within the aforementioned research project, showed marginal influence on the spalling depth. On basis of these observations, the permeability of concrete can be considered as one of the main parameters influencing spalling.

For the investigation of the structural performance of support structures under fire loading, the temperature distribution within the reinforced-concrete member is determined by means of numerical simulation tools. In case an uncoupled thermal analysis is performed,
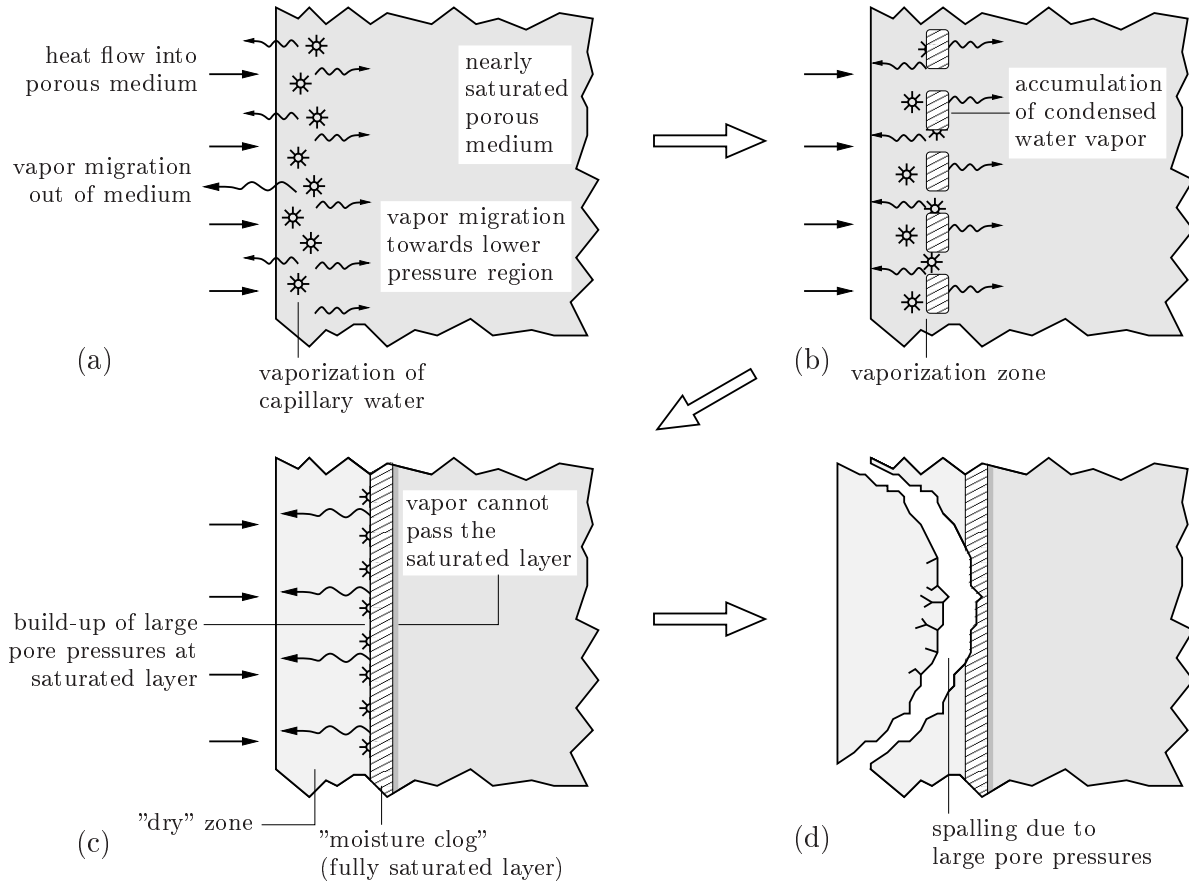
Figure 1.2: Illustration of spalling caused by thermo-hydral processes [4, 26]

taking no mass transport into account, the temperature increase within the structure is significantly overestimated, which can be illustrated when comparing numerical with experimental results (see Chapter 3 and, e.g., [132]). This trend is explained by the neglect of (i) heat sinks associated with physical and chemical processes and (ii) the cooling effect in consequence of mass transport. The discrepancy between experimental data and numerical results obtained from uncoupled thermal analyses led to the development of more realistic models, considering heat and mass transport in a coupled manner [1, 2, 10, 13, 14, 25, 26, 41, 43, 72, 73, 111, 112, 118, 134]. In engineering practice, the highly non-linear temperature distributions in concrete members resulting from fire loading are commonly converted into (and replaced by) linear temperature distributions (see, e.g., [98, 126], given by the temperature T_m [°C] in the middle plane of the lining and a constant temperature gradient ΔT [°C/m] over the lining thickness). In contrast to the non-linear temperature distribution, T_m and ΔT can be easily considered in standard software tools developed for the (linear) analysis of beams and frames (see, e.g., [98, 126]). The drawback of such simplified structural analyses is twofold. First, the stress state within the tunnel lining resulting from mechanical loading prior to temperature loading (i.e., self weight of the lining and load of the surrounding soil) is not
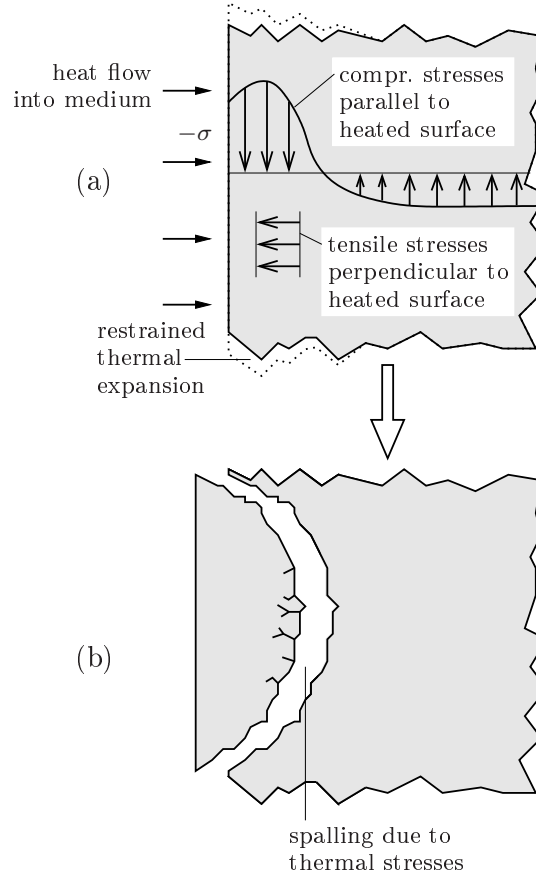
Figure 1.3: Illustration of spalling caused by thermo-mechanical processes [10, 123]
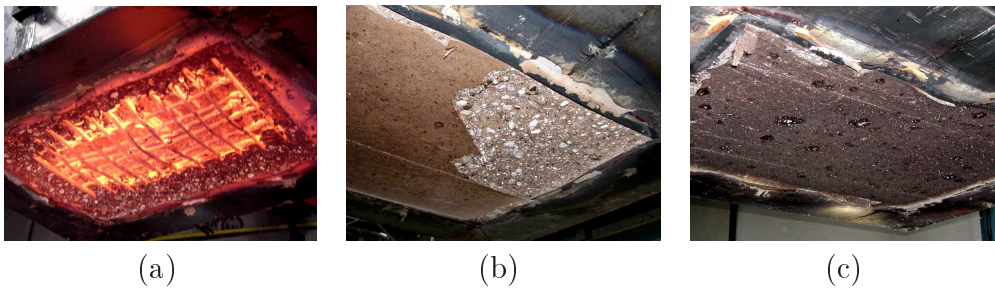
Figure 1.4: Spalling depth for concrete with (a) 0, (b) 1.5, and (c) 3.0 kg/m^3 PP-fibers [67] (heated surface after 120 min of fire loading)

considered within the determination of T_m and ΔT. Second, a linear-elastic analysis of the tunnel structure considering T_m and ΔT disregards stress redistribution due to the development of plastic regions within the structure. In order to avoid these questionable simplifications, analysis tools taking the non-linear temperature distributions as well as plastic deformations of the lining material into account have been developed (see, e.g., [3, 33, 93, 101, 113]).

1.2 Outline

In this work, the topic of concrete subjected to high temperature is treated in a hybrid manner, encompassing experimental investigations and numerical simulations of the underlying physical and chemical processes. The following questions are addressed:

1. *What are the main processes responsible for spalling and what is their individual contribution?*
   Based on fire experiments, where spalling of concrete was recorded visually by means of a high-speed camera, the velocity of the spalled-off pieces is determined in Subsection 2.1. This gives access to the released energy for every spalled-off piece. The obtained results are compared with results from respective models describing the underlying physical phenomena. The obtained results confirm the earlier-reported identification of the permeability as one of the main parameters influencing spalling. In Subsection 2.2, permeability experiments on *in-situ* as well as *laboratory-cast* concrete specimens with or without polypropylene (PP) fibers subjected to different pre-heating temperatures are presented. For conducting the experiments, a setup applicable to a wide range of permeability (as found in case of concrete with and without PP-fibers subjected to high temperatures) is presented. In addition, the pore space of pre-heated concrete with and without PP-fibers is investigated by means of mercury-intrusion porosimetry (MIP) experiments (see Subsection 2.3) in order to relate changes of the pore structure to changes of the permeability.

2. *Which phenomena shall be considered for realistic predictions of temperature distributions within heated concrete?*
   Heat and mass transport within concrete subjected to temperature loading can be simulated with different levels of complexity: (i) analyzing heat transport only (uncoupled analysis) or (ii) taking thermo-hydro-chemical couplings into account (coupled analysis). In addition, spalling of concrete layers influences the temperature distribution within the remaining cross section. In Chapter 3, numerical results from both uncoupled as well as coupled analyses are compared to experimentally-obtained temperature histories. Moreover, the influence of an increased permeability in consequence of addition of PP-fibers (observed during the permeability experiments presented in Subsection 2.2) on the distributions of temperature and gas pressure is investigated. Finally, different spalling histories are considered within the numerical analyses, giving insight into the influence of spalling on the temperature and gas-pressure distribution within the concrete lining.

3. *How is the structural behavior of concrete tunnel linings affected by fire loading?*
   Implementation of realistic material models as well as consideration of the governing processes is crucial for a realistic prediction of the response of support structures

subjected to fire loading. In Chapter 4, a "beam-spring" model is used for the structural safety assessment, employing layered finite elements which allow (i) implementation of spalling of concrete layers and (ii) layer-wise consideration of temperature-dependent material parameters. The numerically-obtained temperature and gas-pressure distributions (see Chapter 3) serve as input into the numerical model. With the presented analysis tool, the structural performance of a cross-section of the Lainzer tunnel (Austria) characterized by low overburden is investigated.

Chapter 2

Concrete at high temperature – experimental investigation of selected phenomena

Departing from qualitative investigation of spalling of concrete employing fire experiments on large-scale concrete blocks [67], selected phenomena taking place in heated concrete are investigated in order to obtain deeper insight into the main governing processes. In the following subsection, spalling experiments and the analysis of the governing processes responsible for spalling are presented.

2.1 Experimental investigation of spalling

2.1.1 Spalling experiments

Within the performed fire experiments, reinforced concrete slabs with the dimensions 0.60 m × 0.50 m × 0.12 m made of concrete C30/37 and C60/75 according to [86] (water/cement-ratios of $w/c = 0.55$ and 0.35, respectively; limestone aggregates) were subjected to fire loading. In selected batches, air-entraining agents and/or polypropylene (PP) fibers were added to the mix design. The PP-fibers (18 μm in diameter and 3 or 6 mm long, respectively) were introduced in order to investigate the earlier-reported beneficial effect (see, e.g., [4, 53, 60, 110]) of PP-fibers, reducing the amount of spalling. Two slabs were subjected simultaneously to a pre-specified temperature history, i.e., either the ISO fire curve [96] or the HCI (hydrocarbon increased fire, $T_{max} = 1300$ °C). In total,

60 slabs were tested. Figure 2.1 shows the experimental setup as well as a representative screen shot of the camera view. In order to improve visibility of the spalled-off pieces, the oven walls were covered by steel plates. During the fire experiments, the temperature history was recorded in the oven and at selected depths from the heated surface. For selected fire experiments (for 7 experiments, i.e., for 14 slabs, most of them made of concrete without PP-fibers), spalling was recorded visually by (i) a video camera, producing real-time movies, and (ii) a high-speed camera, recording selected spalling events at a rate of 250 frames per second.
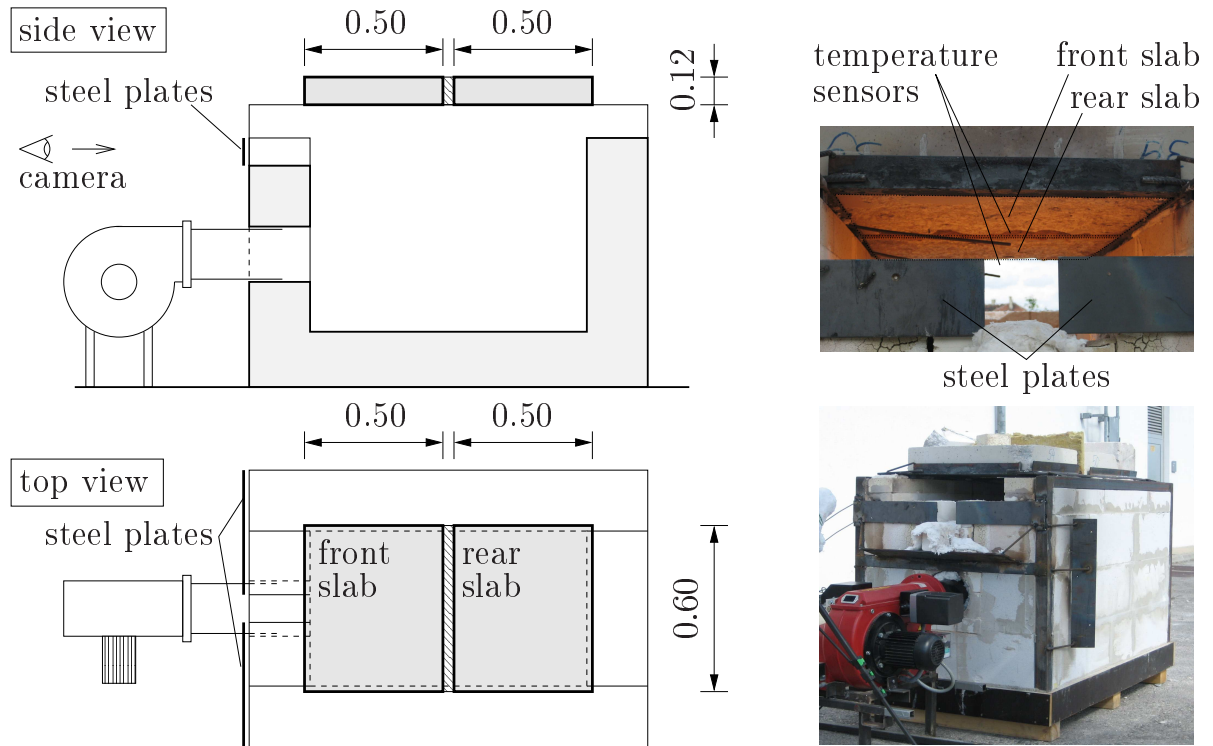
Figure 2.1: Experimental setup for performed spalling experiments [6, 116]

2.1.2 Results

Within the experiments, the earlier-reported beneficial effect of PP-fibers on the spalling behavior was observed [6, 116]. Moreover, concrete C60/75 proofed to be more prone to spalling than concrete C30/37. During visual observation of selected fire experiments, all previously mentioned types of spalling were observed. Whereas the most violent type of spalling (explosive spalling) was observed mostly as surface spalling, corner spalling was of explosive as well as progressive nature (with low velocity). The size (i.e., the volume and, hence, the mass, with the thickness ranging from 5 mm to 20 mm) was found to be inversely-proportional to the velocity of distinct pieces, with smaller velocities for bigger pieces. Moreover, the size of some pieces associated with corner spalling was considerably

bigger than the size of the pieces from surface spalling. Aggregate spalling was observed to be of explosive as well as progressive type. In every event, a so-called spalling front could be identified, which had the highest velocity within the respective spalling event. This spalling front mainly consisted of dust and small concrete chips. In some spalling events, only this cloud of concrete chips and no distinct spalled-off piece was visible. Moreover, in a few other events, a cloud of vapor was visible shortly before or during the spalling event, indicating a blow out of water vapor.

Figure 2.2 shows three screen shots of a selected spalling event (surface spalling). The

$t = 0$

$t = 8$ ms

$t = 16$ ms
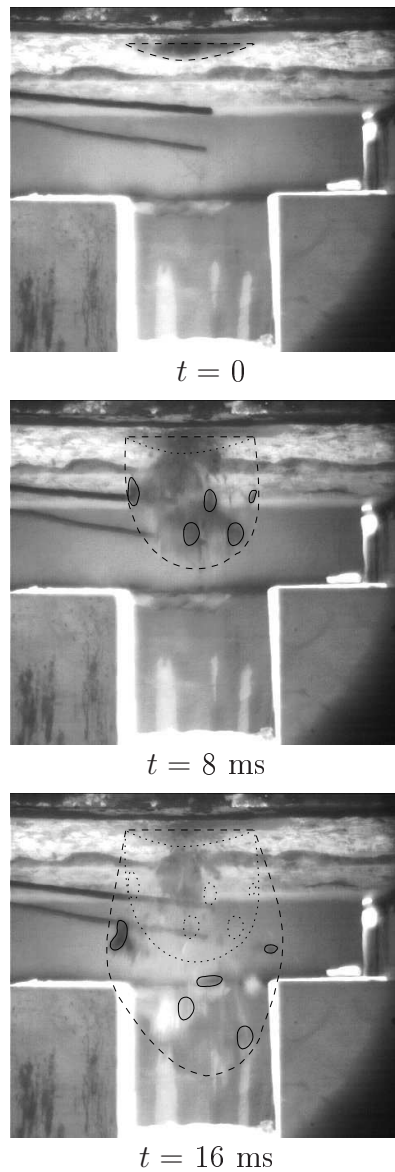
Figure 2.2: High-speed camera images from spalling experiment (C60/75, no PP-fibers): spalling front (dashed line) and spalled-off pieces (solid line) characterized by different velocities
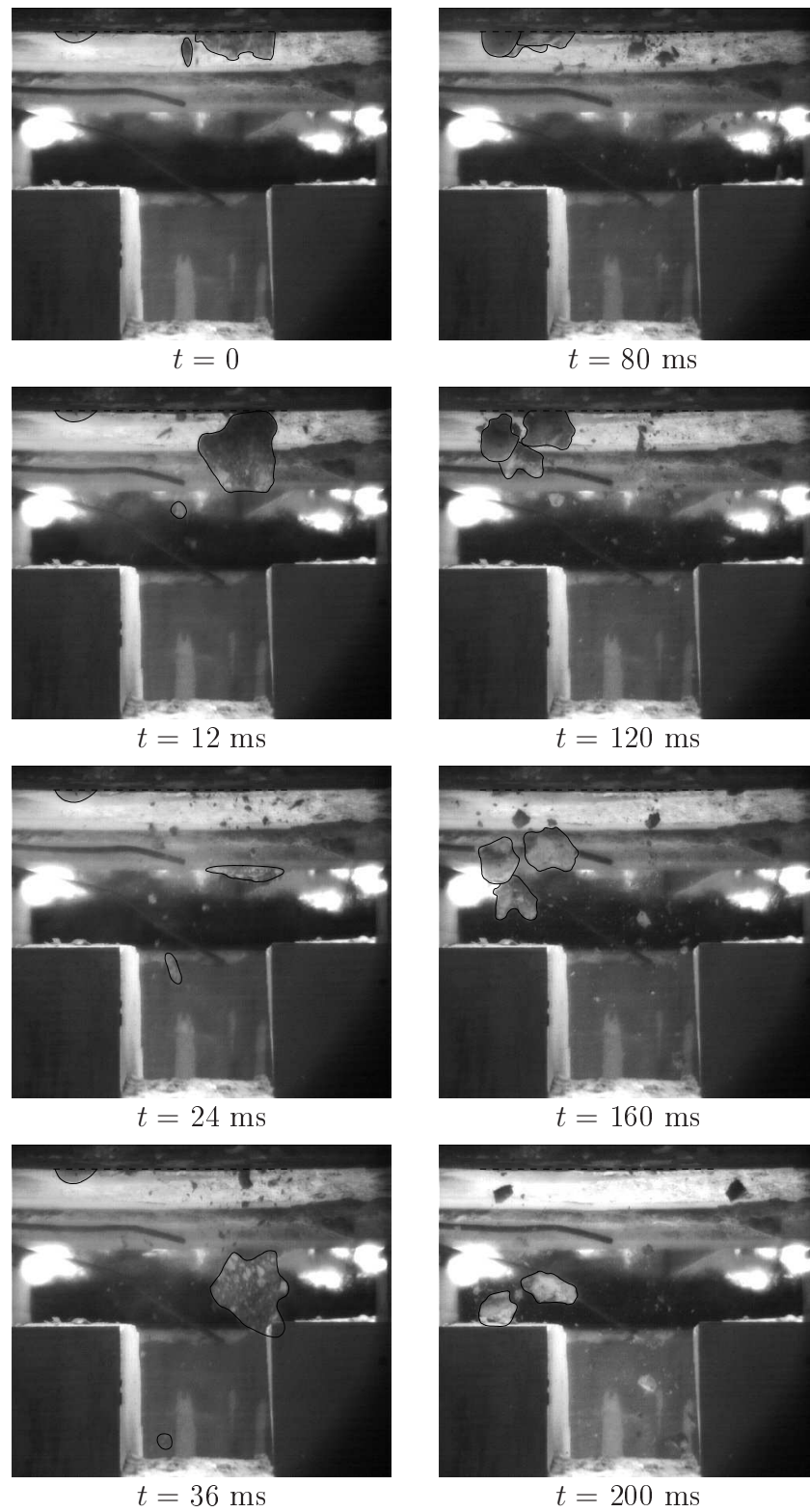
Figure 2.3: High-speed camera images from spalling experiment (C30/37, no PP-fibers): concrete pieces characterized by different size and velocity ($0 \leq t \leq 36$ ms) and concrete pieces in free fall ($80 \leq t \leq 200$ ms)

dashed lines mark the location of the aforementioned spalling front at selected time in-stants, whereas the solid lines mark distinct spalled-off pieces. It can be seen that, as already mentioned, the spalling front moves faster than the distinct spalled-off pieces. As regards the latter, different pieces exhibit different velocities. For the spalling event shown in Figure 2.2, the velocity of the spalling front was calculated as $v_f = 12$ m/s, whereas the velocity of the five distinct pieces ranged from $v_p = 5.6$ m/s to $v_p = 12$ m/s.

Figure 2.3 shows a spalling event associated with corner spalling. In the four screen shots corresponding to $0 \leq t \leq 36$ ms, the big plate-like piece is apparently much slower than the small piece, with the respective velocities calculated as 2.8 and 6 m/s, respectively. The marked concrete pieces in the four screen shots corresponding to $80 \leq t \leq 200$ ms move with an even lower velocity. Calculations showed that this velocity can be explained exclusively by gravity acceleration[1], meaning the pieces were simply detaching from the specimen and fell downwards.

From visual evaluation of the slow-motion sequences, the spalling-front velocity v_f [m/s] as well as the velocities of distinct pieces, v_p [m/s], were determined for each spalling event (see Figure 2.4). Pieces with a velocity $v_p \leq 1.5$ m/s were considered as being accelerated only by gravity forces, denoted as free-fall pieces. This event-wise evaluation led to frequency plots for v_f as well as the minimum and maximum piece velocity, $\min[v_p]$ and $\max[v_p]$, respectively (see Figure 2.5). The bulk of values for v_f is encountered within the range of $7.5 \leq v_f \leq 15$ m/s. The peaks for $\min[v_p]$ and $\max[v_p]$ are found in the range of $3 \leq \min[v_p] \leq 4.5$ m/s and $6 \leq \max[v_p] \leq 7.5$ m/s, respectively. As previously indicated, the velocity of the spalling front is in general greater than the piece velocity.

2.1.3   Discussion

The origin of spalling is still a topic of ongoing discussion (see, e.g., [4, 10, 26, 53, 59, 60, 61, 78, 110, 123]). As already indicated in Section 1, two phenomena are considered to cause spalling, namely *thermo-hydral processes* and *thermo-mechanical processes*.

In the past, different models were presented, investigating the governing processes and their influence on spalling:

---

[1]The four screen shots in Figure 2.3 corresponding to $80 \leq t \leq 200$ ms show three pieces in free fall. The visible path in the slow-motion sequence is $L = 13$ cm. Assuming zero velocity after detaching from the bottom surface of the specimen, the time span for a piece to move 13 cm in consequence of gravity acceleration ($g = 9.81$ m/s^2) is given by

$$t = \sqrt{\frac{2L}{g}} = \sqrt{\frac{2 \cdot 0.13}{9.81}} = 0.16 \text{ s} . \tag{2.1}$$

The time span between the first and the last of the respective screen shots in Figure 2.3 is 0.12 s which – considering that the pieces are already in the downward motion at $t = 80$ ms – corresponds well to the situation of free fall.

- In [45], spalling was investigated by determining the released energy at the time instant when spalling takes place. This released energy was considered to be transformed into kinetic energy of motion, accelerating the spalled-off piece. Hence, piece
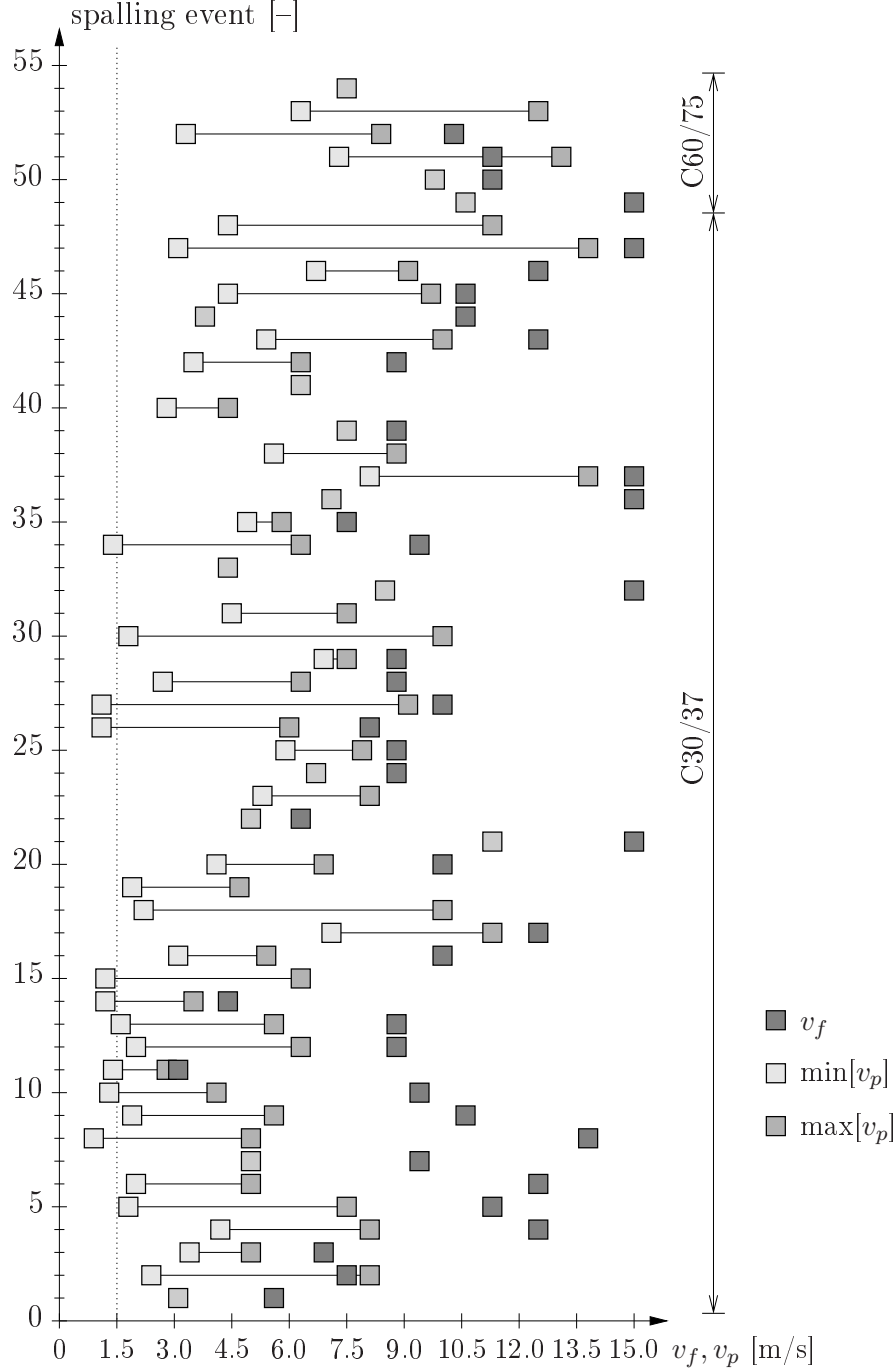
Figure 2.4: Spalling-front velocity v_f and minimum and maximum velocity of distinct spalled-off pieces ($\min[v_p]$, $\max[v_p]$) determined for every recorded spalling event (in case only one piece was visible within a spalling event, minimum and maximum piece velocities are equal)
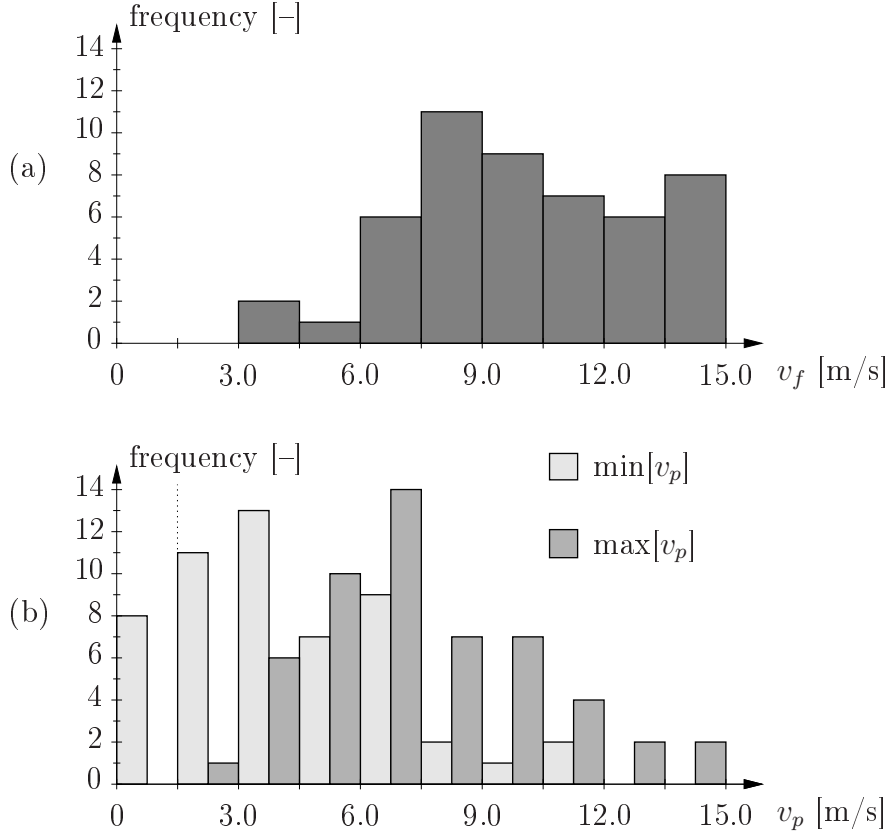
Figure 2.5: Frequency distribution of (a) velocity of spalling front and (b) minimum/maximum velocity of distinct spalled-off pieces within recorded spalling events

velocity v_p [m/s] was linked to the respective kinetic energy E_{kin} [J] by

$$E_{kin} = \frac{mv_p^2}{2} , \qquad (2.2)$$

with m [kg] as the mass of the spalled-off piece. In case of thermo-hydral processes, E_{kin} was related to the work associated with the expansion of water vapor[2] when the concrete piece is detaching. In case of thermo-mechanical processes, on the other hand, E_{kin} was set equal to the elastic strain energy stored in the piece prior to spalling reduced by the fracture energy consumed during detaching of the spalled-off piece. The numerical results presented in [45] showed that both the released elastic energy and the performed work during vapor expansion can result in a piece velocity in the range of $4 \leq v_p \leq 5$ m/s. When a combination of the two described processes was considered, the resulting velocity became 7 m/s. Both thermo-mechanical and thermo-hydral processes were considered to influence the stress state within the

---

[2]The previously built-up vapor pressure in consequence of vaporization of water was considered to be released abruptly when the spalled-off piece is detaching. Hereby, a certain initial volume, related to an initial crack width prior to dislocation of the spalled-off piece, was assigned to this vapor pressure.

concrete member, whereas the former (thermo-mechanical processes) were regarded to initiate cracking and, hence, trigger spalling. Thermo-hydral processes, on the other hand, were considered to substantially contribute to the acceleration of the spalled-off piece, depending on the magnitude of the water-vapor pressure within the concrete member. The ratio between kinetic energies resulting from thermo-hydral and thermo-mechanical processes was found within the range of $1 \leq E_{kin}^{th}/E_{kin}^{tm} \leq 6$.

- In [11], thermo-hydral processes were not regarded as being the major source for explosive spalling. They, nevertheless, were considered to contribute to the triggering of fracture and crack opening. Furthermore, after cracking and during crack opening, the pore pressure in the crack was considered to drop to zero almost instantly which was attributed to the increase of the available volume of the opening crack by several orders of magnitude. Therefore, thermo-mechanical processes were regarded as the major source for explosive spalling.

It is agreed upon the fact that in case of heating of concrete during fire loading, a combination of thermo-hydral and thermo-mechanical processes causes spalling (see, e.g., [11, 45, 61]). Whether the former or the latter is the main driving process has not been clarified yet. In any case, the effect of these two processes depends on numerous factors, such as concrete strength, moisture content, heating rate, etc.

In the following, the effect of the two mentioned processes involved in spalling of heated concrete is investigated. For this purpose, the kinetic energies as well as the velocities associated with thermo-hydral and thermo-mechanical processes (i.e., E_{kin}^{th}, v_p^{th}, E_{kin}^{tm}, and v_p^{tm}, respectively) are determined [45], giving access to the resulting kinetic energy E_{kin} and the corresponding piece velocity v_p:

$$E_{kin} = E_{kin}^{th} + E_{kin}^{tm} - E_F \quad \text{and} \quad v_p = \sqrt{\frac{2E_{kin}}{m}} \, . \tag{2.3}$$

In Equation (2.3), E_F [J] is the fracture energy which is consumed during dislocation of the spalled-off piece, reading

$$E_F = G_F A \, , \tag{2.4}$$

with G_F [J/m^2] as the specific fracture energy of concrete and A [m^2] as the fracture surface.

2.1.3.1   Determination of E_{kin}^{th}

In case of thermo-hydral processes, the effect of vapor expansion is considered by the equilibrium condition formulated for the spalled-off piece (see Figure 2.6), reading for time instant t:

$$F(t) = [p(t) - p_{atm}] \, A' = m \, a_p(t) \, , \tag{2.5}$$
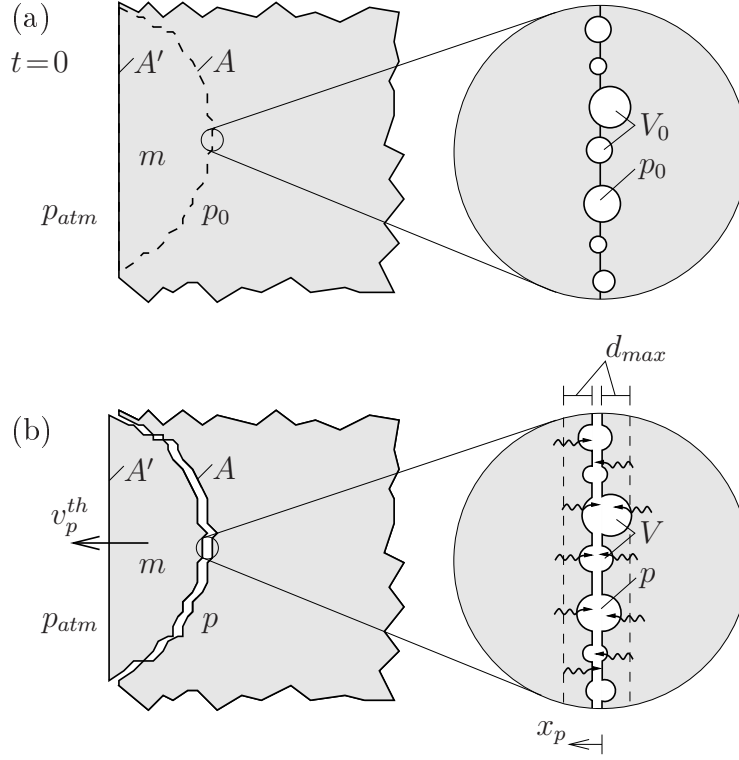
Figure 2.6: Modeling spalling in consequence of thermo-hydral processes (a)
before and (b) after dislocation of spalled-off piece

where p [Pa] and p_{atm} [Pa] are the pressure within the concrete member and the atmospheric pressure, respectively, and A' [m^2] is the cross-sectional area of the spalled-off piece. In Equation (2.5), m [kg] and a_p [m/s^2] are mass and acceleration, respectively, of the concrete piece. By application of the ideal-gas law, the pressure in the pore system can be linked to the corresponding volume V [m^3] by

$$p(t) = p_0 \left(\frac{V_0}{V(t)} \right)^n , \tag{2.6}$$

with p_0 [Pa] and V_0 [m^3] as pressure and available volume right before spalling (see Figure 2.6(a) and Appendix A) and n [–] as the polytropic exponent (see, e.g. [19]; $n = 1$ refers to isothermal expansion; $n = k = c_p/c_v$ refers to adiabatic expansion, with c_p [kJ/(kg K)] and c_v [kJ/(kg K)] as the isobaric and isochoric heat capacity, respectively, of the expanding medium). In Equation (2.6), the pore volume $V(t)$ increases during crack opening as (see Figure 2.6(b))

$$V[x_p(t)] = V_0 + A' \, x_p(t) , \tag{2.7}$$

with x_p [m] as the actual location of the spalled-off piece. Inserting Equations (2.6) and (2.7) into Equation (2.5) yields

$$\left[p_0 \left(\frac{V_0}{V_0 + A' \, x_p(t)} \right)^n - p_{atm} \right] A' = m \, a_p[x_p(t)] , \tag{2.8}$$
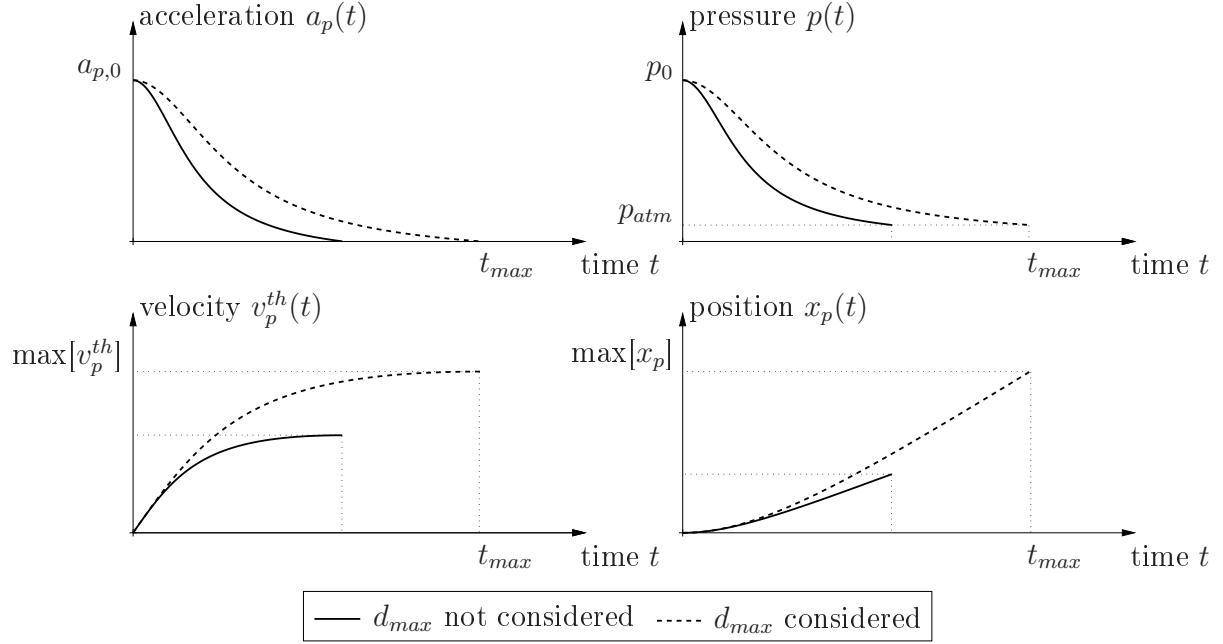
Figure 2.7: Acceleration process during spalling caused by thermo-hydral processes (input parameters: $p_0 = 12$ bar, $p_{atm} = 1$ bar, $A' = 4.9 \times 10^{-4}$ m², $m = 5.7 \times 10^{-3}$ kg, $V_0 = 4.9 \times 10^{-5}$ m³, $n = 0.165$)
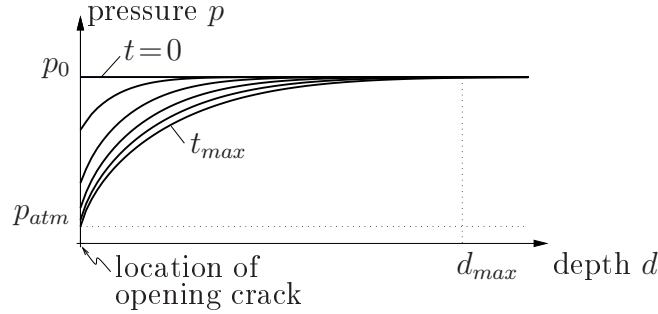
Figure 2.8: Numerical analysis of vapor transport for $0 \leq t \leq t_{max}$ with pressure drop at $d = 0$ serving as prescribed boundary condition (for employed input parameters, see Chapter 3 and [131])

which gives access to the acceleration and, finally, the velocity $v_p^{th}(t)$ [m/s] and the location $x_p(t)$ [m] of the spalled-off piece (see Figure 2.7).

In addition to the water vapor in the pore volume directly connected to the opening crack, V_0, the vapor located close to this opening gap also contributes to acceleration of the spalled-off piece (see Figure 2.6(b)). In order to quantify this contribution, a numerical simulation of water-vapor transport is performed (see Figure 2.8 and Chapter 3). Hereby, the previously-determined pressure history in the opening gap, $p(t)$ [Pa] (see Figure 2.7), serves as boundary condition. The performed simulation gives access to d_{max} [m], i.e., the size of the domain around the crack contributing to the inflow of water vapor into

the opening crack and, thus, to acceleration of the spalled-off piece. Finally, the increase of the pore volume contributing to acceleration of the spalled-off piece is obtained by[3] $2 A' d_{max} n$, where n [–] is the temperature-dependent porosity of concrete. The influence of d_{max} and, hence, the increased initial pore volume is also contained in Figure 2.7, showing an increase of $\max[v_p^{th}]$ and[4] t_{max}. Based on $\max[v_p^{th}]$, the kinetic energy associated with thermo-hydral processes, E_{kin}^{th} [J], is determined from Equation (2.2).

2.1.3.2 Determination of E_{kin}^{tm}

In case of thermo-mechanical processes, the kinetic energy E_{kin}^{tm} [J] is given by

$$E_{kin}^{tm} = U = \int_V \left(\frac{1}{2} \boldsymbol{\sigma} : \boldsymbol{\varepsilon}^e \right) dV , \tag{2.9}$$

where U [J] is the elastic strain energy, V [m^3] is the volume of the spalled-off piece and $\boldsymbol{\sigma}$ [MPa] and $\boldsymbol{\varepsilon}^e$ [-] are stress and elastic strain tensor, respectively, resulting from restrained thermal dilation. Assuming plane-stress conditions and fully-restrained boundary conditions, the absolute values of the in-plane normal-stress components $\sigma_1 = \sigma_2 = \sigma(T)$ – which are limited by the (temperature-dependent) biaxial compressive strength, $f_b(T)$ [MPa] – are determined by

$$| \sigma(T) | \;\; = \;\; \min \left\{ \frac{E(T)}{1-\nu} \left\{ \varepsilon^{th}(T) + \varepsilon^{lits}[T, \sigma(T)] \right\} , f_b(T) \right\} , \tag{2.10}$$

where $E(T)$ [MPa] is the temperature-dependent Young's modulus of concrete (see, e.g., [22]) and ν [–] is Poisson's ratio. In Equation (2.10), the free thermal strain $\varepsilon^{th}(T)$ [–] is determined according to [87] (see Figure 2.9) and the so-called load-induced thermal strain $\varepsilon^{lits}[T, \sigma(T)]$ [–] (see Figure 2.10 and, e.g., [5, 62, 63, 106, 107]) is obtained from the empirical relation presented in [107]. Finally, using

$$E_{kin}^{tm} = \frac{1}{2} \int_V \left(\frac{1-\nu}{E(T)} \sigma^2(T) \right) dV , \tag{2.11}$$

the velocity of the spalled-off piece in consequence of thermo-mechanical processes, v_p^{tm} [m/s], can be determined from Equation (2.2).

2.1.3.3 Parameter studies

In order to identify the main parameters influencing spalling of heated concrete and to determine their individual contribution to the kinetic energy, parameter studies were

---

[3]d_{max} is set to the location where $(p_0 - p)/p_0 < tol$ at $t = t_{max}$ (see Figure 2.8), with t_{max} [s] as the time instant at which $p = p_{atm}$ and $a_p = 0$.

[4]Since the considered increase of the initial pore volume causes an increase of t_{max}, $\max[v_p^{th}]$ is determined in an iterative manner.
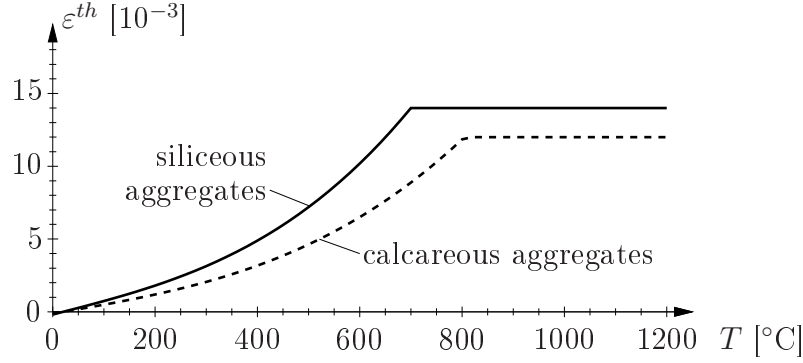
Figure 2.9: Free thermal strain $\varepsilon^{th}(T)$ according to [87]
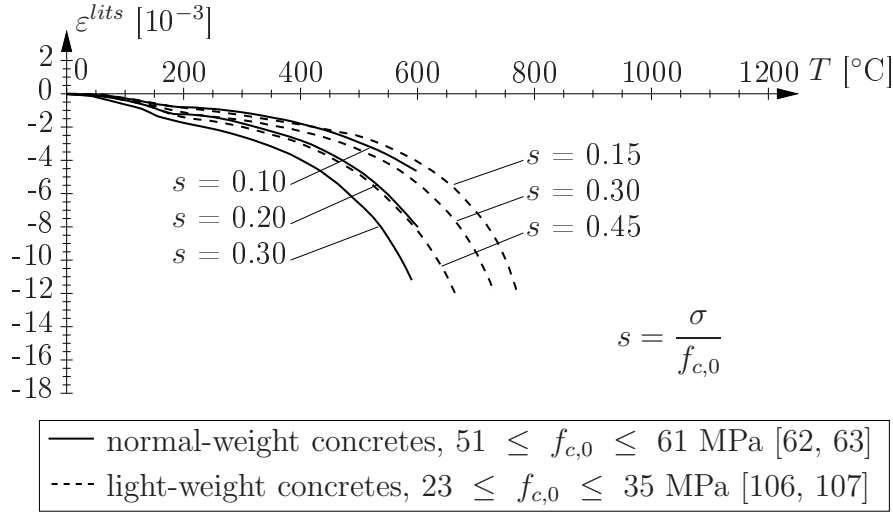
Figure 2.10: Load-induced thermal strain $\varepsilon^{lits}(T, s)$ extracted from experiments
outlined in [5, 62, 63, 106, 107] (s: degree of loading; $f_{c,0}$: 28-day cube
compressive strength)

performed. Hereby, isothermal expansion[5] of vapor was considered in case of thermo-hydral processes, thus $n = 1$. In case of thermo-mechanical processes, the elastic strain energy was determined from Equation (2.11) by assuming constant temperature and a uniform stress state within the spalled-off piece, yielding $E_{kin}^{tm} = 1/2 \left(\sigma_1 \, \varepsilon_1^e + \sigma_2 \, \varepsilon_2^e \right) V = \left[(1 - \nu)/E \right] \sigma^2 V$. The geometric properties of the spalled-off piece were approximated by an oblate spheroid, with (see Figure 2.11)

$$V = \frac{l^2 d}{6}\pi \quad \text{and} \quad A \approx A' = \frac{l^2}{4}\pi \quad \text{for} \quad \frac{d}{l} \ll 1 \,. \tag{2.12}$$

---

[5]Adiabatic and isothermal conditions represent the two limiting cases regarding expansion of vapor. Parameter studies showed that the assumption of adiabatic expansion results in a considerable temperature drop, resulting in very low and even negative temperatures. Therefore, isothermal conditions were assumed.
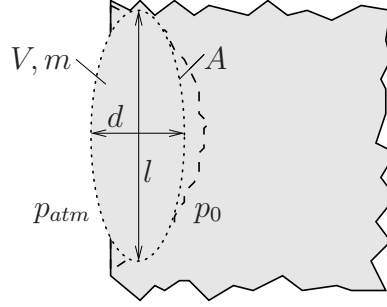
Figure 2.11: Approximation of geometric properties of spalled-off piece by oblate spheroid

Based on the results from the performed parameter studies, the following conclusions were drawn:

- The kinetic energy associated with thermo-hydral processes, E_{kin}^{th}, is almost independent of the thickness d [m] of the spalled-off piece[6] and shows an increasing behavior for increasing vapor pressure right before spalling, p_0 [Pa] (see Figure 2.12). The corresponding piece velocity, $\max[v_p^{th}]$, decreases with increasing thickness (see Figure 2.13), since the kinetic energy remains almost constant for different values of d and the mass to be accelerated increases linearly with the thickness. In addition, the velocity increases for increasing p_0 and for increasing temperature, whereas the latter is caused by an increase of the influencing region d_{max} via an increase of the permeability of concrete and, therefore, an increase of the vapor volume available for acceleration of the spalled-off piece.

- The kinetic energy associated with thermo-mechanical processes, E_{kin}^{tm}, increases linearly for increasing thickness d (see Figure 2.14). With respect to temperature T, E_{kin}^{tm} shows an increasing behavior for increasing temperatures up to $T \approx 550\,°\text{C}$ and decreases for higher temperatures, whereas the latter is explained by the restrained thermal stresses approaching the temperature-dependent compressive strength of concrete. The corresponding piece velocity v_p^{tm} is independent of thickness d (see Figure 2.15), which is explained by d canceling out in

$$v_p^{tm} = \sqrt{\frac{2E_{kin}^{tm}[V(l^2,d)]}{m[V(l^2,d)]}}\,. \tag{2.13}$$

- The size l of the spalled-off piece (see Figure 2.11) influences neither $\max[v_p^{th}]$ nor v_p^{tm}, canceling out in Equations (2.8) and (2.13).

---

[6]Obviously, the energy released during expansion of vapor is independent of the thickness of the spalled-off piece. The rather moderate dependence of E_{kin}^{th} is caused by the influencing region d_{max} increasing for larger values of d.
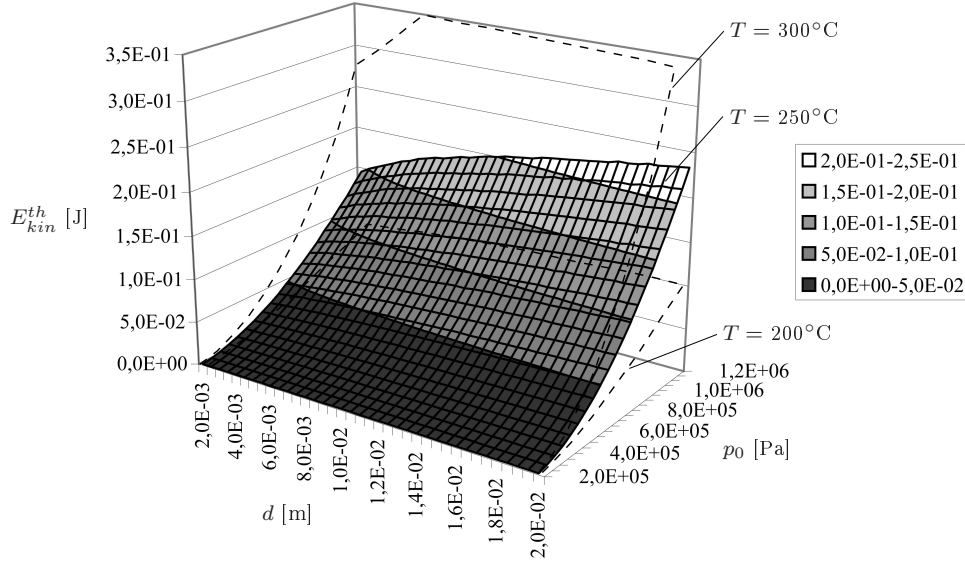
Figure 2.12: Kinetic energy associated with thermo-hydral processes (obtained
from Equations (2.8) and (2.2)) as a function of thickness d of spalled-
off piece and vapor pressure right before spalling, p_0, for three different
concrete temperatures T
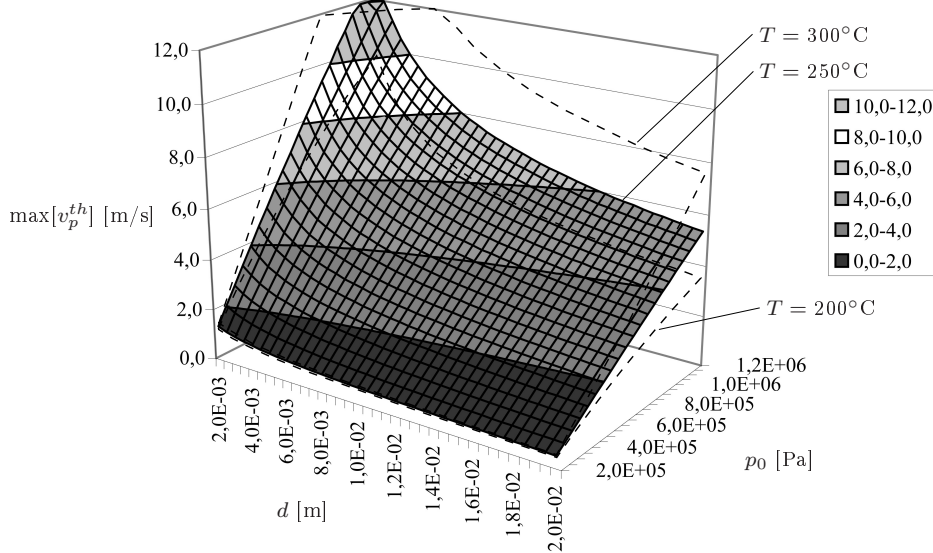
Figure 2.13: Velocity associated with thermo-hydral processes (obtained from
Equation (2.8)) as a function of thickness d of spalled-off piece and vapor
pressure right before spalling, p_0, for three different concrete tempera-
tures T
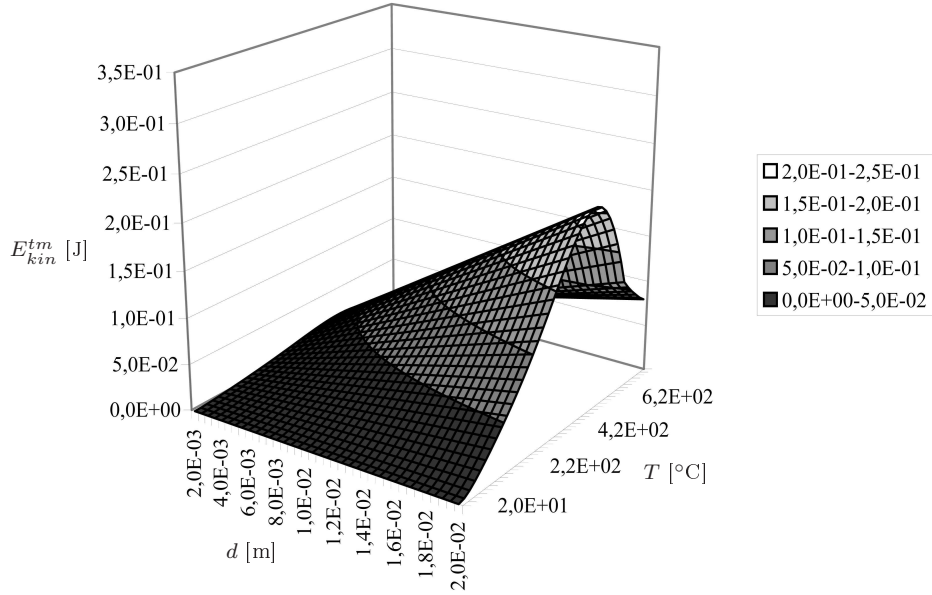
Figure 2.14: Kinetic energy associated with thermo-mechanical processes (obtained from Equation (2.11)) as a function of thickness d of spalled-off piece and concrete temperature T
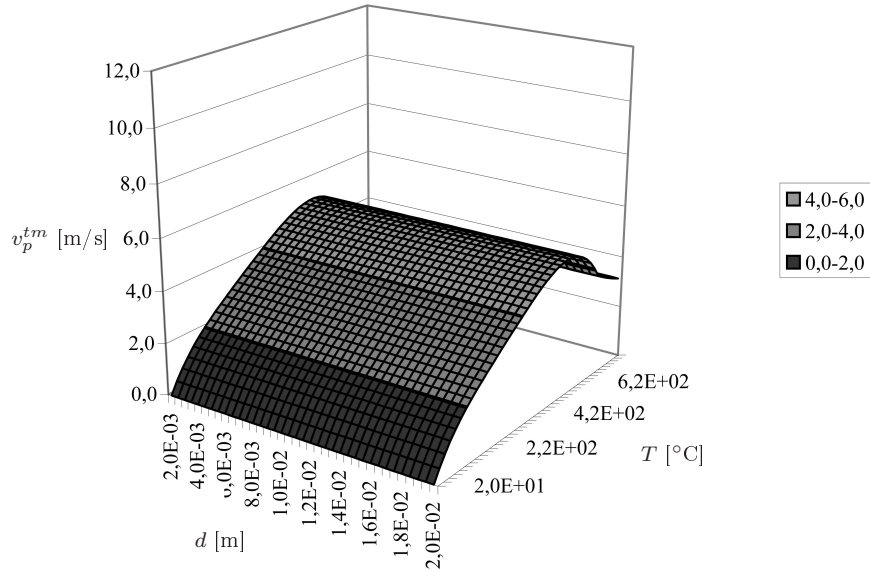
Figure 2.15: Velocity associated with thermo-mechanical processes (obtained from Equations (2.11) and (2.2)) as a function of thickness d of spalled-off piece and concrete temperature T

From the results of the performed parameter studies, the resulting piece velocities v_p were determined from E_{kin} (see Equation (2.3)), with the latter obtained as the sum of E_{kin}^{th} (see Equations (2.8) and (2.2)) and E_{kin}^{tm} (see Equation (2.11)) reduced by $E_F = G_F\,A$ (see Equation (2.4), with the specific fracture energy obtained as $G_F = 90$ J/m^2, see Appendix B). As depicted in Figure 2.16, zero velocity (i.e., no spalling) is indicated for small thickness and small pressure because of $E_F \geq E_{kin}^{th} + E_{kin}^{tm}$.

The described evaluation was performed for typical dimensions of the spalled-off piece as observed during the fire experiments (see Figures 2.2 and 2.3). Hereby, the vapor pressure right before spalling, p_0, was determined for three selected temperatures from comparison of the numerical results for v_p (see Figure 2.16) with the measured piece velocity, v_p^{exp} (see Table 2.1). The solution corresponding to typical values of p_0 and T observed during experiments (see, e.g., [26, 59]) and numerical studies (see, e.g., [10, 26, 45, 131]) – see bold values for p_0 in Table 2.1 – was then chosen for determination of the energies associated with the respective spalling event (see Table 2.1). Hereby, the ratio $E_{kin}^{th}/E_{kin}^{tm}$ (kinetic energy associated with thermo-hydral processes over kinetic energy associated with thermo-mechanical processes) decreased for increasing thickness of the spalled-off piece and increased for increasing piece velocities (see Figure 2.17). Moreover, this ratio increased for increasing gas pressure as well as for increasing temperature.

Table 2.1: Kinetic energies for selected concrete pieces (see Figure 2.3) computed from Equations (2.2), (2.3), (2.4), (2.8), and (2.11)

Piece no.	1	2	3	4	5	6	7
l [m]	0.015	0.025	0.055	0.030	0.050	0.060	0.105
d [m]	0.005	0.007	0.010	0.011	0.017	0.020	0.020
v_p^{exp} [m/s]	4.1	6.0	3.1	4.9	3.8	2.7	2.6
p_0 [bar] at$^+$							
$T = 200$ °C	10	–	**9**	–	12	**8**	**7.5**
$T = 250$ °C	**7**	10	6	**9**	**7.5**	5	4.5
$T = 300$ °C	5.5	**7.5**	4.5	6.5	5	2	2
E_{kin}^{th} [J]	0.020	0.117	0.282	0.162	0.328	0.296	0.811
E_{kin}^{tm} [J]	0.007	0.035	0.133	0.061	0.260	0.316	0.968
$E_{kin}^{th} + E_{kin}^{tm}$ [J]	0.027	0.152	0.415	0.223	0.588	0.612	1.779
E_F [J]	0.016	0.044	0.214	0.064	0.177	0.254	0.779
E_{kin} [J] *	0.011	0.108	0.201	0.159	0.411	0.358	1.000
$E_{kin}^{th}/E_{kin}^{tm}$ [–]	2.9	3.3	2.1	2.7	1.3	0.9	0.8

$^+$ Values for p_0 for different T giving $v_p = v_p^{exp}$;
   bold values are used for determination of energies;
   no value for p_0 corresponds to $v_p < v_p^{exp}$ even for $p_0 = p^{gws}$,
   with p^{gws} as the saturation vapor pressure
$^*E_{kin} = E_{kin}^{th} + E_{kin}^{tm} - E_F$
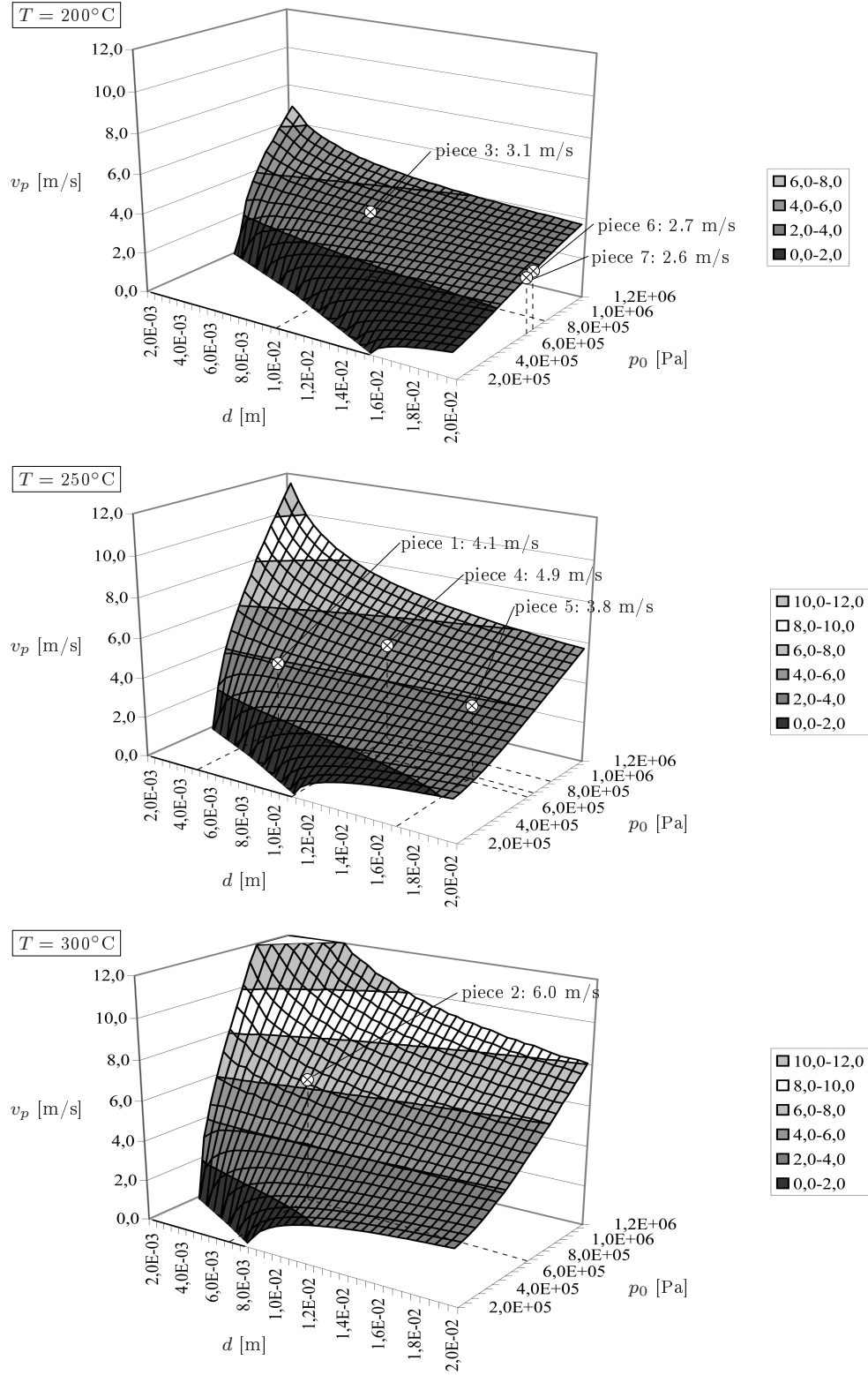
Figure 2.16: Resulting piece velocities as a function of thickness d of spalled-off piece and vapor pressure right before spalling, p_0, for three different concrete temperatures T
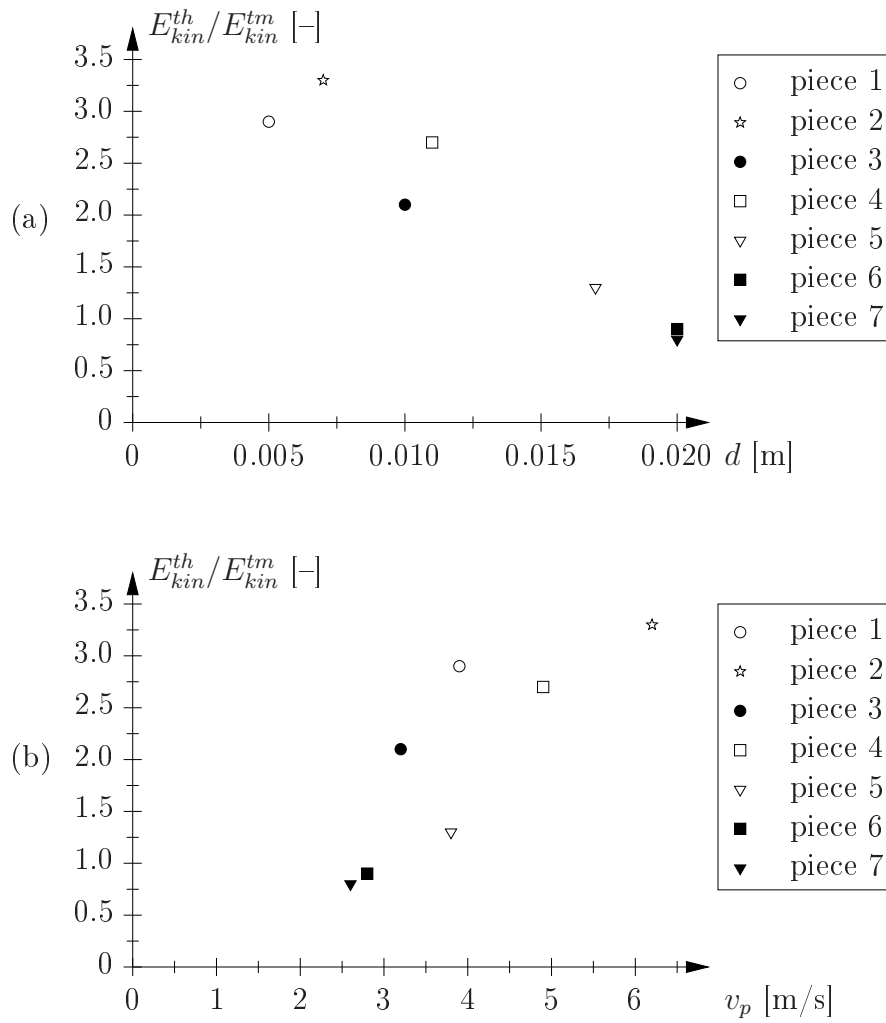
Figure 2.17: $E_{kin}^{th}/E_{kin}^{tm}$ as a function of (a) thickness d and (b) velocity v_p of spalled-off piece

2.2   Permeability of pre-heated *in-situ* and *laboratory-cast* concrete

Based on identification of the permeability as one of the main parameters influencing spalling of concrete subjected to fire loading, results from permeability experiments performed on *in-situ* as well as *laboratory-cast* concrete are presented.

2.2.1   Literature review

The permeability of cement-based materials (cement mortar or concrete) can be determined by using incompressible (liquids) and/or compressible media (gases). A wide range of experimental techniques, employed either on site (*in-situ* tests) or in the laboratory (*laboratory* tests) were proposed in the literature:

1. Using liquids as measurement medium:

   - *in-situ* tests, such as the Initial Surface Absorption Test (ISAT) [24, 37] or the Covercrete Absorption Test (CAT) [28];

   - *laboratory* tests, such as constant-head or falling-head experiments [7, 76], the beam-bending method [103, 125], or tests employing dynamic pressurization [48, 104].

2. Using gases as measurement medium:

   - *in-situ* tests, such as the Figg's test [21, 37] or the Air Permeability of Near Surface (APNS) test [24, 27];

   - *laboratory* tests, such as the CEM-Bureau method [58, 65, 79], the Hassler method [39, 58], or tests under changing thermal conditions [109].

So far, the application of these test methods for determination of the influence of temperature loading on the permeability of cement-based materials was restricted to laboratory-cast specimens. E.g., the influence of the amount of polypropylene fibers (PP-fibers) on the intrinsic permeability[7] k_{int} [m^2] for certain pre-heating temperatures was investigated in [58] (see Figure 2.18). Whereas k_{int} of concrete without fibers varied two orders of magnitude (caused by dehydration of the cement paste, microcracking due to temperature-induced stresses, etc.), a variation of k_{int} of four orders of magnitude was observed for concrete with fibers within a temperature range from 80 to 400 °C. In [58], the more pronounced increase of the intrinsic permeability for concrete with PP-fibers was explained

---

[7]k_{int} is an intrinsic parameter, describing the pore space of the material. It is independent of the medium flowing through the material. For compressible media (e.g., air or water vapor), the intrinsic permeability is defined as the permeability at infinite pressure, with $1/p = 0$ [57, 64].
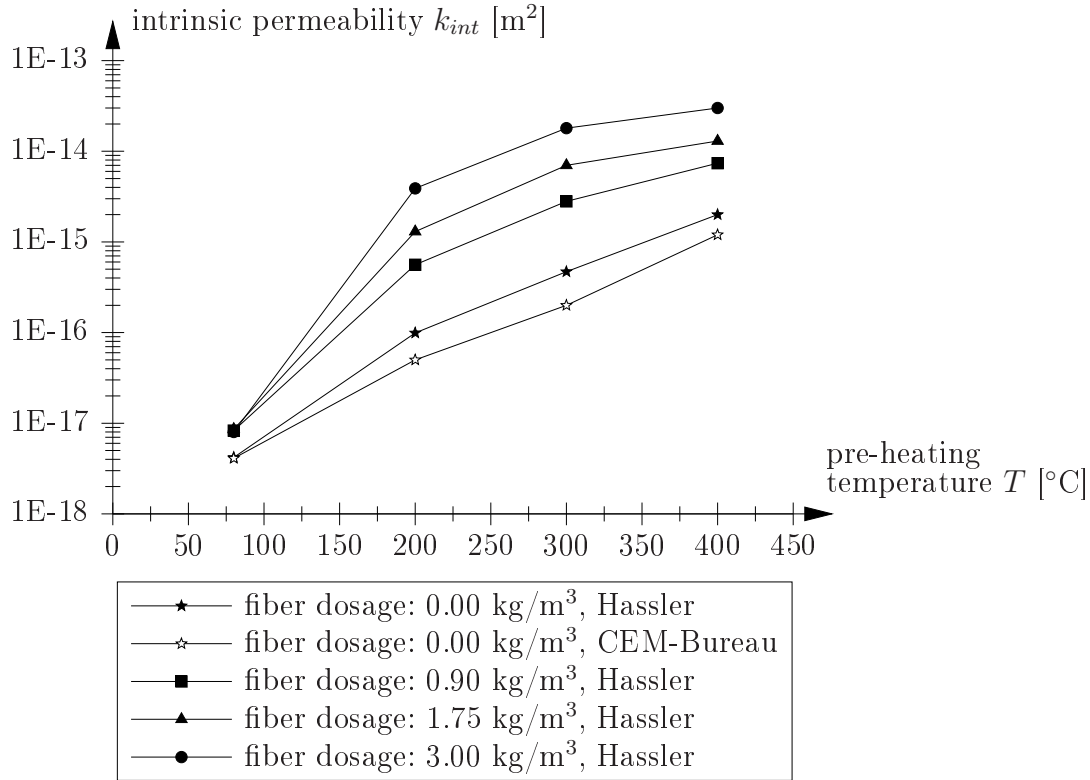
Figure 2.18: Intrinsic permeability of high-performance concrete as a function
of pre-heating temperature [58]

by melting of the fibers. Whereas the experiments presented in [58] were performed on
pre-heated concrete specimens which were cooled down and tested at room temperature,
the permeability experiments presented in [109] were conducted under changing thermal
conditions (see Figure 2.19). Hereby, the temperature was increased to the target temper-
ature and the permeability test was conducted at that temperature after the temperature
was kept constant for 10 hours. Subsequently, the temperature was increased to the next
temperature level and the procedure was repeated. The results exhibit a dent between
temperatures of 100 and 200 °C. When the time span the temperature was kept constant
at every temperature level was increased to 50 hours, the observed dent vanished (see
Figure 2.19). This indicates that the increased holding time is sufficient to assure that
vapor transport, which was considered to cause the aforementioned dent [109], does not
disturb the permeability experiments. In [39, 57], the influence of the degree of saturation
on the effective permeability k_{eff} (defined as k_{int} for partially-saturated concrete) of ce-
ment paste and concrete was studied using the Hassler [39] and CEM-Bureau method [57].
Hereby, k_{eff} decreased by two orders of magnitude for an increase of the degree of sat-
uration from 0 to 80% (see Figure 2.20). The same effect was reported in [77], where
the permeability was related to the mass loss of capillary water during air drying. As
reported in [57], the permeability of concrete is higher than the permeability of cement
mortar. Moreover, the permeability increases with increasing water/cement-ratio, which
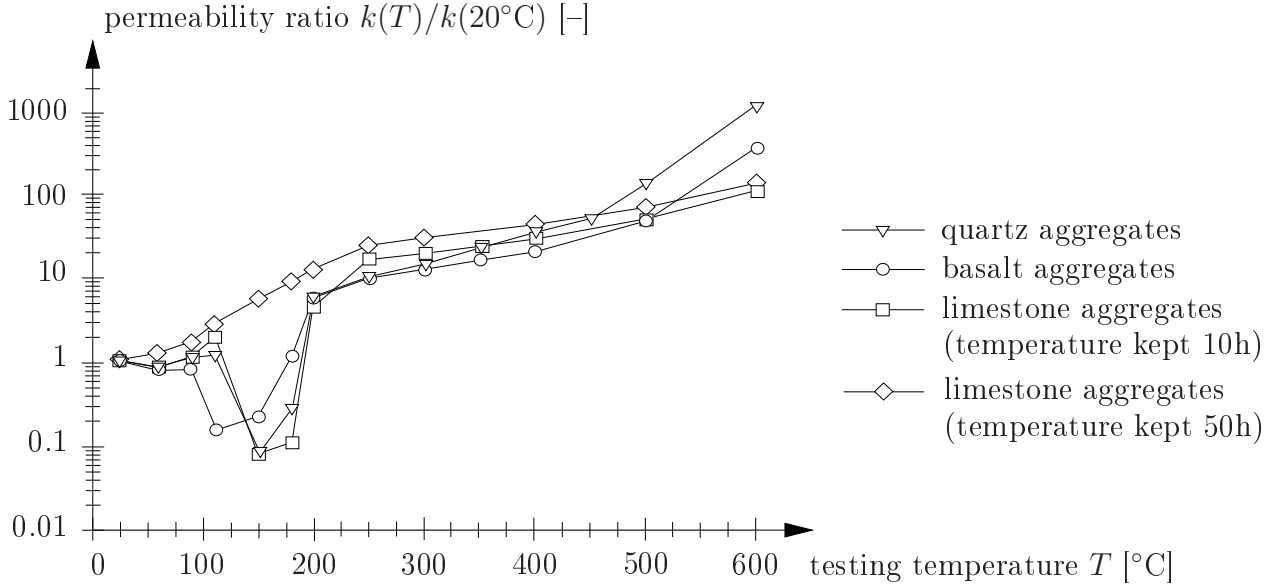
Figure 2.19: Permeability of concrete (water/cement-ratio: 0.5) tested at elevated temperatures [109]
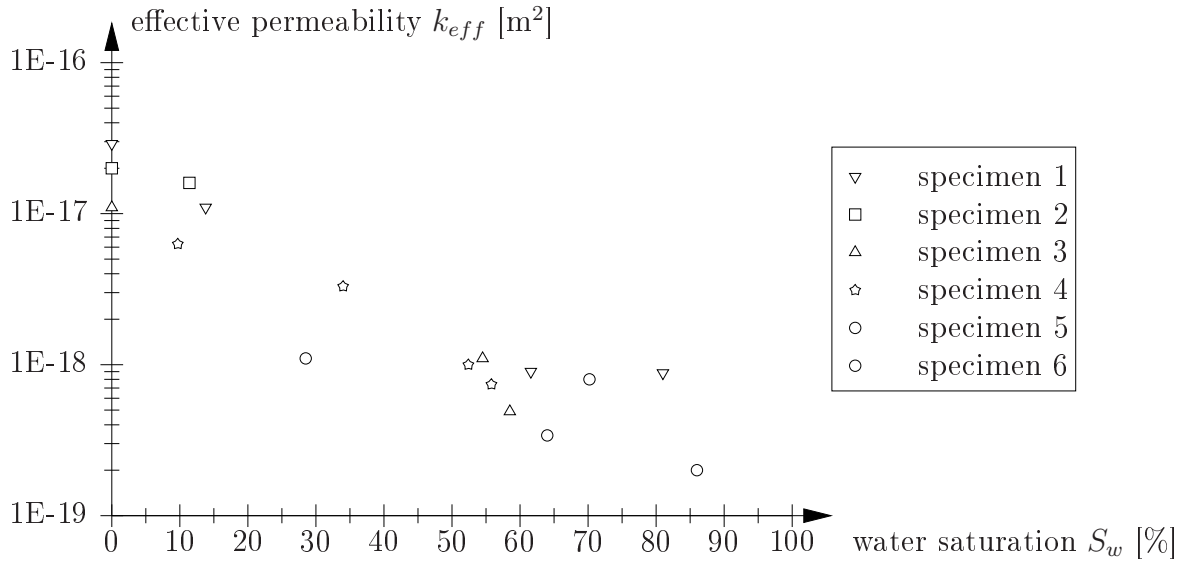
Figure 2.20: Effective permeability of two-year-old normal-weight concrete (water/cement-ratio: 0.45) as a function of the water saturation [57]

is explained by the increased pore space that develops during curing [57].

2.2.2   Experimental setup

The experimental device used for identification of the gas-transport properties of concrete is shown in Figures 2.21 and 2.22. Hereby, the pressure is applied via two pressure pistons with given volume. As the displacement of the pressure pistons is monitored, the amount
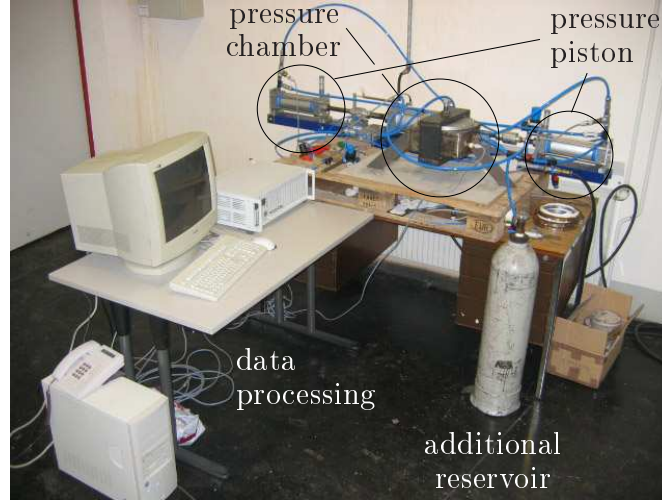
Figure 2.21: Experimental setup used for permeability tests

of pressurized air provided is known. In order to cover the wide range of the permeability of concrete subjected to temperature loading, an additional air reservoir was employed, which was added to the pressurized volume in case of concrete specimens characterized by a high permeability.

With the experimental setup shown in Figures 2.21 and 2.22, two different types of experiment may be conducted:

1. *Decreasing-pressure experiment (DPE):* Hereby, the pressure pistons are used to increase the pressure in the system. Then, the pumping speed of the pressure pistons (controlled by $u(t)$, see Figure 2.22) is adjusted in order to provide stationary air flow through the specimen at the target pressure of 8 bar (= 0.8 MPa). As stationary flow is established, the air supply is closed and the decrease of pressure by air flow through the specimen is recorded as a function of time, $p_t(t)$.

2. *Constant-pressure experiment (CPE):* Hereby, the pressure pistons (see Figure 2.22) are used to maintain an almost-constant pressure at certain target pressures (ranging from 5 to 8 bar). The air flow through the specimen is determined on basis of the monitored displacement history of the pressure pistons, $u(t)$.

2.2.3   Evaluation methods

Pressure-driven flow (i.e, advection) through porous media is described by Darcy's law, giving the flux Q [m³/s] for the one-dimensional case as

$$Q = -k\frac{A}{\eta}\frac{dp}{dx}\,,\tag{2.14}$$
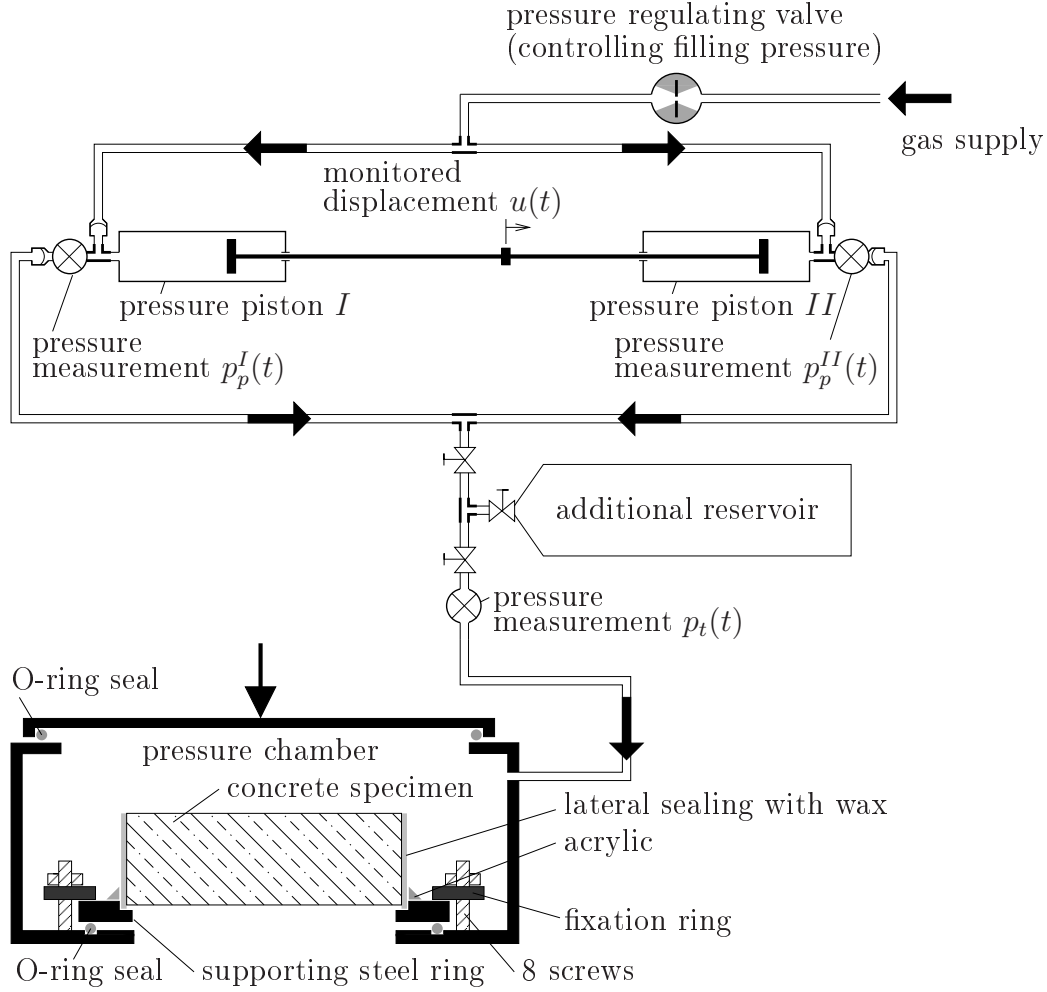
Figure 2.22: Schematic illustration of experimental device used for permeability tests

where k [m^2] is the permeability of the porous medium, A [m^2] is the cross-sectional area, η [Pa s] is the dynamic viscosity of the transported fluid, and dp/dx [Pa/m] is the pressure gradient. In case an incompressible fluid is advected through the porous structure, the permeability k in Equation (2.14) is equal to the intrinsic permeability, with $k = k_{int}$. In case of advection of compressible fluids, the so-called slip-flow phenomenon [64] (see Appendix C for details) is considered by

$$Q = -k\frac{A}{\eta}\frac{dp}{dx} = -k_{int}\left(1+\frac{b}{p}\right)\frac{A}{\eta}\frac{dp}{dx}\,, \qquad (2.15)$$

where the pressure-dependent permeability k is given by

$$k = k_{int}\left(1+\frac{b}{p}\right)\,, \qquad (2.16)$$

with b [Pa] as the so-called slip-flow constant.

2.2.3.1   Determination of permeability parameters k_{int} and b by means of stationary analysis

For the case of one-dimensional flow as given in the experimental setup, Equation (2.15) is multiplied by pressure p and, thereafter, integrated over the specimen height H. Accounting for $Qp = \text{constant}$[8] in case of stationary conditions yields

$$Qp \int_0^H dx = -k_{int}\frac{A}{\eta} \int_{p_t}^{p_b} (p + b)dp \; , \tag{2.18}$$

and (after evaluation of the integrals)

$$QpH = -k_{int}\frac{A}{\eta} \left[\frac{p_b^2 - p_t^2}{2} + b(p_b - p_t) \right] \; , \tag{2.19}$$

where $p_b = p_0 \approx 1$ bar (atmospheric pressure) represents the pressure at the bottom of the specimen. During the experiments, Q and p at the top of the specimen (denoted as Q_t and p_t), which are accessible through the monitored pressure history $p_t(t)$ and the history of the piston displacement $u(t)$, are determined for selected time intervals $t_1 \leq t \leq t_2$. Within each time interval, an averaged pressure at the top of the specimen is introduced as $\overline{p}_t = [p_t(t_1) + p_t(t_2)]/2$. Considering the given values for Qp at the top surface of the specimen and considering $k = k_{int}(1 + b/p)$ in Equation (2.19), where p is set equal to $(\overline{p}_t + p_0)/2$, one gets

$$k = \frac{2H\eta}{A(\overline{p}_t^2 - p_0^2)}Q_t\overline{p}_t \; , \tag{2.20}$$

where p_t is replaced by $\overline{p}_t$. Equation (2.20) is solved for different time intervals $t_1 \leq t \leq t_2$ and the obtained values for the permeability k are plotted as a function of $1/p$, where p is again set equal to $(\overline{p}_t + p_0)/2$. The permeability parameters k_{int} and b are obtained from linear regression as illustrated in Figure 2.23. The parameters used for determination of k from the experimental data are summarized in Table 2.2 (additionally, $\eta = 18 \cdot 10^{-6}$ Pa s). In the following, the determination of $Q_t\overline{p}_t$ required in Equation (2.20) will be described for both DPE and CPE.

Determination of $Q_t\overline{p}_t$ for DPE

During a DPE, the pressure at the top of the specimen continuously decreases in consequence of air flow through the specimen (see Figure 2.24). Considering a time interval

---

[8]In contrast to the volumetric flux Q [m³/s], which is not constant along the direction of flow in case of compressible (stationary) flow through porous media, the molar flux dn/dt [mol/s] is constant. Hence, under isothermal conditions ($\Theta = \text{constant}$), Clapeyron's law for ideal gases yields

$$nR\Theta = Vp \quad \rightarrow \quad \frac{dn}{dt}R\Theta = \frac{dV}{dt}p = Qp = \text{ constant} \,. \tag{2.17}$$
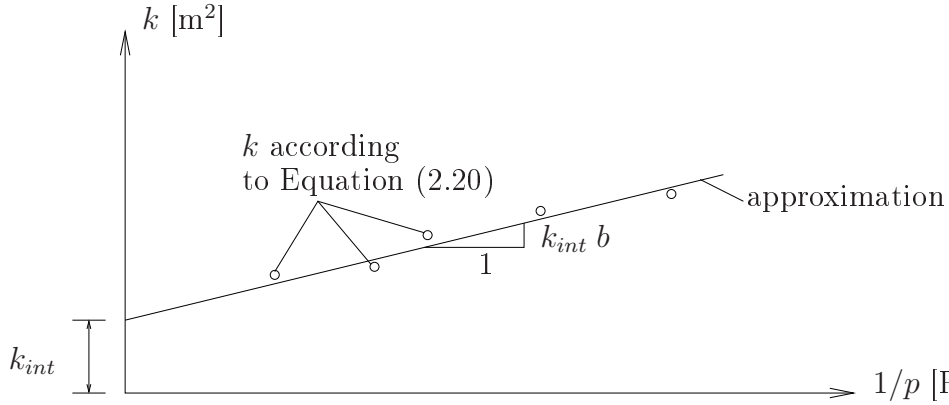
Figure 2.23: Illustration of identification of permeability parameters k_{int} and b from regression analysis (p was set equal to $(\overline{p}_t + p_0)/2$ of the respective time interval)
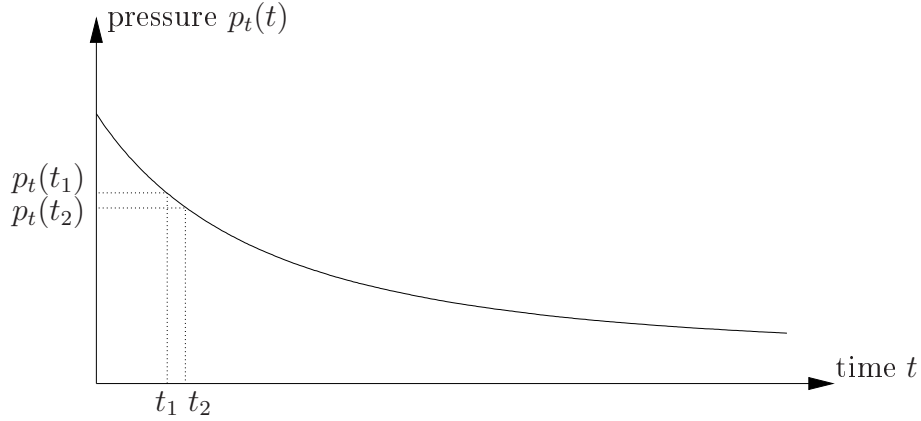
Figure 2.24: Decrease of pressure p_t at top of specimen recorded during DPE

$t_1 \leq t \leq t_2$, the amount of moles present within the pressurized volume at time t_i is

$$n(t_i) = \frac{p_t(t_i)V(t_i)}{R\Theta(t_i)} \,, \tag{2.21}$$

where $V(t_i) = V$ [m^3] is the constant pressurized volume (see Figure 2.25 and Tables 2.2 and 2.3) and $\Theta(t_i) = \Theta$ [K] is the constant temperature (considering isothermal conditions). The amount of moles that pass through the specimen within time interval $t_1 \leq t \leq t_2$, given by $n(t_1) - n(t_2)$, yields the molar flux within the considered time interval as

$$n(t_1) - n(t_2) = \frac{[p_t(t_1) - p_t(t_2)]\,V}{R\Theta} \quad \rightarrow \quad \frac{\Delta n}{\Delta t} = \frac{\Delta p_t V}{\Delta t R\Theta} \,, \tag{2.22}$$

where $\Delta n = n(t_1) - n(t_2)$, $\Delta t = t_2 - t_1$, and $\Delta p_t = p_t(t_1) - p_t(t_2)$. Rewriting Clapeyron's law for ideal gases (Equation (2.17)) for the time interval $t_1 \leq t \leq t_2$ and replacing Q by Q_t and p by $\overline{p}_t$, one gets

$$\frac{\Delta n}{\Delta t} \approx Q_t \overline{p}_t \frac{1}{R\Theta} \,. \tag{2.23}$$
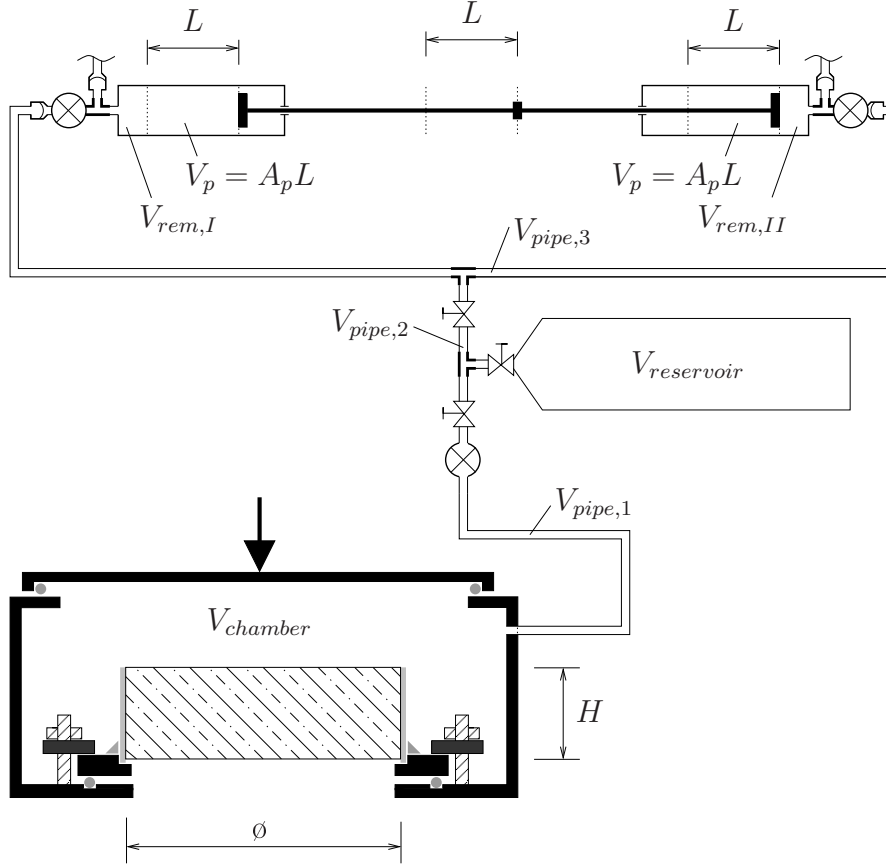
Figure 2.25: Pressurized volume in experimental setup

Table 2.2: Specimen dimensions and pressurized volume in experimental setup

Parameter	In-situ concrete	Laboratory-cast concrete
Specimen diameter ø [m]	0.143	0.150
Specimen area A [m^2]	$1.606 \cdot 10^{-2}$	$1.767 \cdot 10^{-2}$
Specimen height H [m]	0.05	0.05
L [m]	$-$	0.132
A_p [m^2]	$5.027 \cdot 10^{-3}$	$5.027 \cdot 10^{-3}$
$V_{chamber}$ [l]	4.953	4.942
$V_{pipe,1}$ [l]	0.0176	0.0176
$V_{pipe,2}$ [l]	0.0251	0.0144
$V_{reservoir}$ [l]	20.8	20.8
$V_{pipe,3}$ [l]	0.2637	0.2637
$V_{rem,I}$ [l]	0.1392	0.1392
$V_{rem,II}$ [l]	0.1078	0.1078

Obviously, the quality of approximation (2.23) depends on the difference between $p_t(t_1)$ and $p_t(t_2)$ and improves for smaller differences, i.e., for small time intervals $t_1 \leq t \leq t_2$.

Table 2.3: Pressurized volume V during permeability experiments

Experiment type	Pressurized volume V [l]	
DPE – in-situ – no reservoir	4.97	$(V = V_{chamber} + V_{pipe,1})$
DPE – in-situ – incl. reservoir	25.80	$(V = V_{chamber} + V_{pipe,1} + V_{pipe,2} + V_{reservoir})$
DPE – lab-cast – incl. reservoir	25.77	$(V = V_{chamber} + V_{pipe,1} + V_{pipe,2} + V_{reservoir})$
CPE – lab-cast – incl. reservoir	26.04	$(V = V_{chamber} + V_{pipe,1} + V_{pipe,2} + V_{reservoir}$ $+ V_{pipe,3})$

Combining Equations (2.22) and (2.23) gives access to $Q_t \overline{p}_t$ for the considered time interval:

$$Q_t \overline{p}_t = \frac{\Delta p_t V}{\Delta t} \; . \tag{2.24}$$

Determination of $Q_t \overline{p}_t$ for CPE

Within a CPE, the pumping mechanism (consisting of two pressure pistons and one driving piston) supplies air to the pressurized system (with the corresponding volume V given in Table 2.3) in an alternate manner (see Figure 2.26). One cycle of a piston consists of three phases:

1. Phase I (backwards movement): Air flows from the gas supply to the considered pressure piston whereas the other piston supplies air to the pressurized system.

2. Phase II (first part of piston stroke): The shift mechanism changes the pumping direction and the considered pressure piston becomes active. Since the filling pressure is chosen to be lower than the pressure in the pressurized system, the air must be compressed in Phase II before the one-way valve opens and the piston supplies air to the pressurized system.

3. Phase III (second part of piston stroke): The pressure in the piston exceeds the pressure in the pressurized system (the pressure difference needs to overcome the resistance of the one-way valve) and the piston supplies air to the pressurized system.

To determine the molar and, hence, the volumetric flux through the specimen, a mass balance is conducted over the piston stroke (Phases II and III). At the beginning of Phase II (corresponding to time instant t_1 in Figure 2.26), the piston is filled with air at filling pressure $p_p(t_1)$ and the pressurized volume V is at pressure $p_t(t_1)$, with $p_t(t_1) > p_p(t_1)$. Hence, the total amount of moles within the system (see Figure 2.25 and Table 2.3) at beginning of Phase II can be determined as

$$t = t_1 : \quad n(t_1) = \frac{1}{R\Theta} \left[p_p(t_1)(V_p + V_{rem}) + p_t(t_1)V \right] \; , \tag{2.25}$$
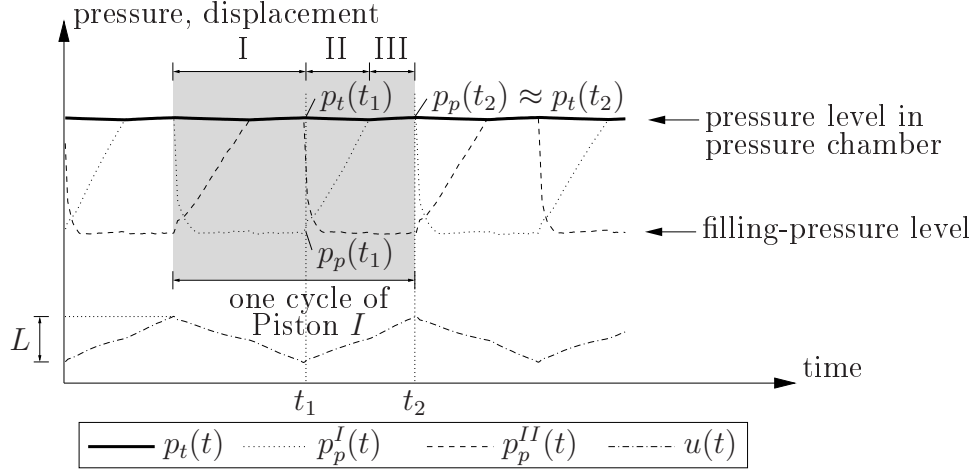
Figure 2.26: Representative plot of pressure and displacement history during CPE (p_t: pressure at top of specimen; p_p^I and p_p^{II}: pressure in Piston I and II, respectively; u: monitored piston displacement)

where $V_p = A_p L$, with A_p [m^2] as the cross-sectional area of the piston and L [m] as the length that the piston moves within one stroke (see Figure 2.26). In Equation (2.25), V_{rem} [l] is the volume of the part of the piston that remains filled with air at the end of Phase III. Thus, V_{rem} is not provided to the pressurized system. In Equation (2.25), V [l] corresponds to the pressurized volume given in Table 2.3 (see Figure 2.25). At the end of Phase III, when the pumping direction is reversed (corresponding to time instant t_2 in Figure 2.26), the pressures in the piston and the pressurized volume are almost equal, with $p_p(t_2) \approx p_t(t_2)$. Therefore, the amount of moles within the system at the end of the piston stroke is

$$t = t_2: \quad n(t_2) = \frac{1}{R\Theta} \left[p_p(t_2)V_{rem} + p_t(t_2)V \right] . \tag{2.26}$$

Equations (2.25) and (2.26) yield the molar flux provided to the pressurized system within $t_1 \leq t \leq t_2$ as

$$\frac{\Delta n}{\Delta t} = \frac{n(t_1) - n(t_2)}{\Delta t} = \frac{1}{R\Theta} \frac{p_p(t_1)V_p + \Delta p_p V_{rem} + \Delta p_t V}{\Delta t} , \tag{2.27}$$

where $\Delta p_t = p_t(t_1) - p_t(t_2) \neq 0$ even in case of CPE, caused by slight variations of the pressure in the pressurized volume. In Equation (2.27), $\Delta p_p = p_p(t_1) - p_p(t_2)$ and $\Delta t = t_2 - t_1$. Considering again Clapeyron's law for ideal gases (Equation (2.17)) gives $Q_t \overline{p}_t$ for the considered time interval $t_1 \leq t \leq t_2$ as

$$Q_t \overline{p}_t = \frac{p_p(t_1)V_p + \Delta p_p V_{rem} + \Delta p_t V}{\Delta t} , \tag{2.28}$$

with $\overline{p}_t = [p_t(t_1) + p_t(t_2)] / 2$.

2.2.3.2 Determination of permeability parameters k_{int} and b from DPE by means of transient analysis

Within the identification procedure presented in the previous subsection, stationary conditions were assumed within the considered time interval $t_1 \leq t \leq t_2$. During the DPE, the pressure in the pressurized volume decreases, approaching the atmospheric pressure as asymptotic limit. The characteristic time associated with this pressure decrease, τ_{dec} [s], is defined by (see Figure 2.27(a))

$$\tau_{dec}(t) := \frac{p_0 - p_t(t)}{dp_t/dt} , \tag{2.29}$$

where dp_t/dt [Pa/s] is determined from the experimentally-obtained history of pressure p_t.

The characteristic time associated with pressure-driven flow (advection) through the specimen, on the other hand, is given by (see, e.g., [75])

$$\tau_{adv}(t) = \frac{l}{v} = \frac{H}{-\dfrac{k}{\eta}\dfrac{dp}{dx}} , \tag{2.30}$$

with $l = H$ [m] as the characteristic length of advection (which is set equal to the specimen height in case of one-dimensional flow in the permeability experiments) and $v = -k/\eta \cdot dp/dx$ [m/s] as the velocity of Darcian flow (compare to Equation (2.14)). Since the permeability k and the pressure gradient dp/dx vary over the specimen height, τ_{adv} is determined (considering a stationary pressure distribution as approximation of the real transient pressure distribution) at the upper and lower surface of the specimen (with $x = 0$ and $x = H$, respectively, see Figure 2.27(b)), giving the upper and lower bound of τ_{adv} for a certain time instant.

Figure 2.28 illustrates the evolution of the characteristic times τ_{dec} and τ_{adv} for a selected DPE. For the calculation of τ_{adv}, the permeability k was determined from Equation (2.16) using intrinsic permeability k_{int} and slip-flow constant b determined from the stationary
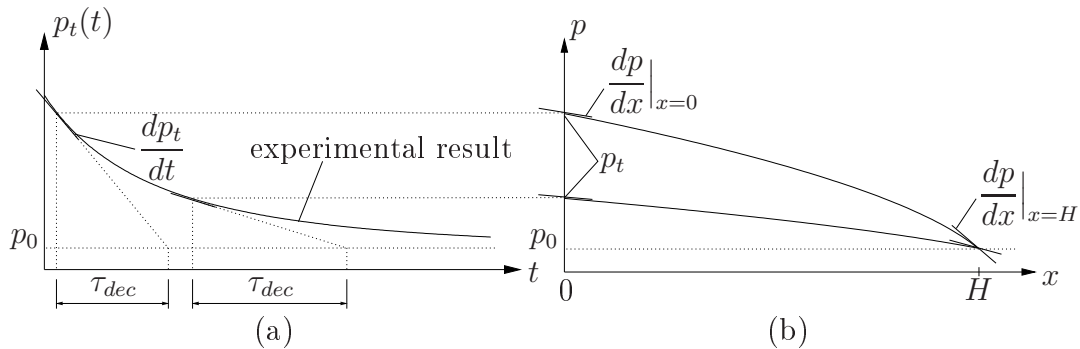
Figure 2.27: (a) τ_{dec} from history of pressure p_t and (b) (stationary) pressure distribution for two time instants characterized by different values of p_t
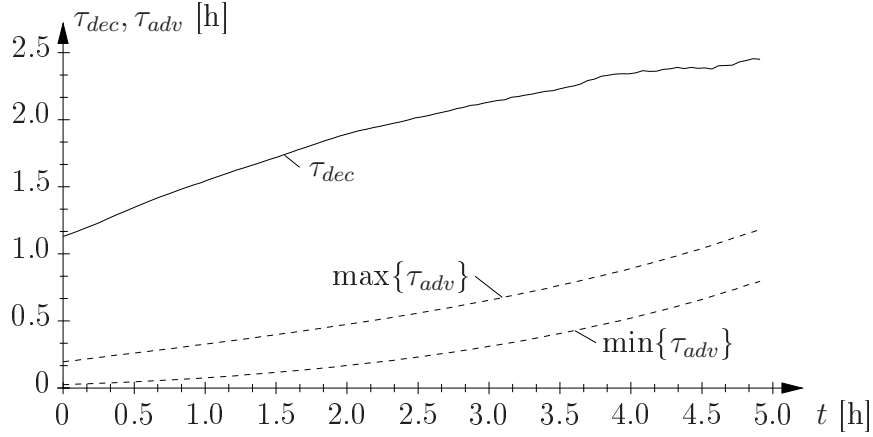
Figure 2.28: Characteristic times τ_{dec} and τ_{adv} for a selected DPE (parameters used: $H = 0.0495$ m; $k_{int} = 1.22 \cdot 10^{-16}$ m^2; $b = 1.34$ bar; $\eta = 18 \cdot 10^{-6}$ Pa s)

analysis presented in Subsection 2.2.3.1. As the pressure in the pressurized system decreases in the course of the DPE (see Figure 2.27(a)), both τ_{dec} and τ_{adv} increase. The ratio of the two time scales, τ_{dec}/τ_{adv}, obtained for experiments on specimens heated to different temperatures is given in Figure 2.29, ranging from 1 to 5 in case the additional reservoir is not included in the pressurized volume. When the additional reservoir is included in the experiment, the time scale of pressure decrease at the pressurized side of the specimen, τ_{dec}, increases by one order of magnitude, resulting in an increase of the ratio τ_{dec}/τ_{adv} (see Figure 2.29). Based on the obtained results, τ_{dec}/τ_{adv} was found to mainly depend on the amount of pressurized gas rather than the permeability of the tested material (controlled by temperature loading of the investigated concrete).

For $\tau_{dec}/\tau_{adv} \gg 1$, the transport through the specimen is significantly faster than the pressure decrease in the pressurized volume. Thus, for any pressure in the pressurized vol-
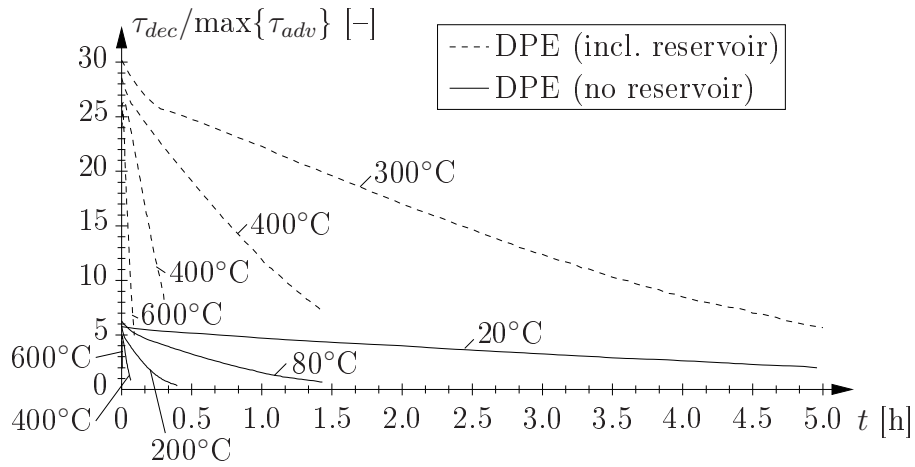
Figure 2.29: τ_{dec}/τ_{adv} obtained from testing of concrete heated to different temperature levels

Table 2.4: Initial and boundary conditions used within transient analysis

	Location	Value
Initial conditions:	$x = x_1$	$p = p_t(t = 0)$
	$x = x_{n_e+1}$	$p = p_0$
Boundary conditions:	$x = x_1$	$Q = 0$
	$x = x_{n_e+1}$	$p = p_0$

ume, a stationary pressure distribution is present within the specimen. For $\tau_{dec}/\tau_{adv} \ggg 1$, on the other hand, the pressure decrease in the pressurized volume affects the pressure distribution over the specimen height, thus, making a transient analysis necessary. For this analysis, the one-dimensional mass-balance equation (see Appendix E.3), reading

$$n\frac{\partial p}{\partial t} - \frac{k_{int}}{\eta}\frac{\partial}{\partial x}\left[(p + b)\frac{\partial p}{\partial x}\right] = 0 \qquad (2.31)$$

is solved numerically for the unknown pressure $p(x, t)$. In Equation (2.31), n [–] represents the porosity of concrete. In the analysis, the pressurized volume is included in the numerical model (see Figure 2.30), with the permeability of this part of the model as $k = 1 \cdot 10^{-3}$ m^2. The initial pressure distribution at $t = 0$ is set equal to the stationary solution, with $p = p_t(t = 0)$ at $x = x_1$ and $p = p_0$ at $x = x_{n_e+1}$ (see Table 2.4). For a given set of permeability parameters k_{int} and b, the transient analysis gives access to the history of the pressure decrease at the top surface of the specimen, $p_t^{num}(t)$. This numerically-obtained history is compared with the experimental history of p_t (i.e. $p_t^{exp}(t)$) for various pairs of k_{int} and b. The pair of k_{int} and b that minimizes the error between the numerically and experimentally-obtained pressure history represents the set of parameters identified from the transient analysis.
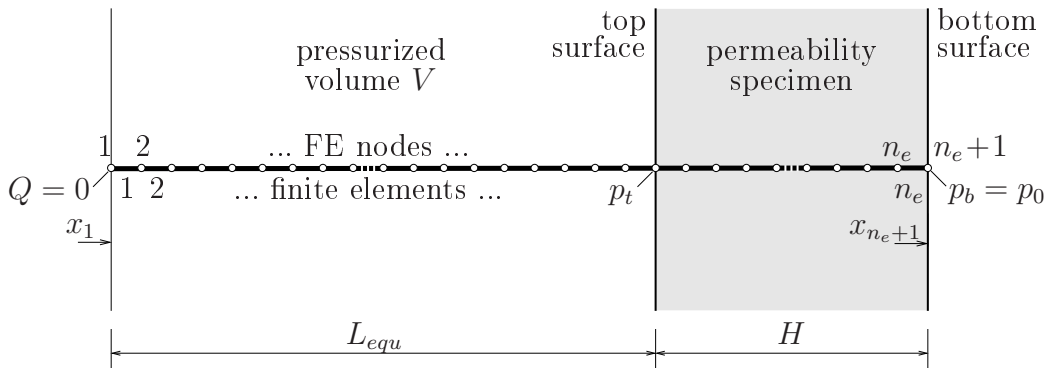
Figure 2.30:   Finite element (FE) model used within transient analysis (L_{equ}: length of part of model representing pressurized volume; n_e: number of finite elements)

2.2.4   Materials and specimen preparation

Specimens made of concrete C25/30 (which is commonly used for tunnel linings in Austria) with/without addition of 1.5 kg/m^3 PP-fibers were subjected to the presented permeability tests. Large-scale concrete blocks of the same concrete were tested within the fire experiments described in [67]. The mix design consists of cement CEM I 42.5 R (C$_3$A-free) and fly ash as binder, various other additives, and siliceous aggregates (see Table 2.5).

Table 2.5: Mix design of concrete B30/300(56)/SA/WU/LST/FB/PB/WDI*
[equivalent to C25/30(56)/WDI] [67, 132]

Cement CEM I 42.5 R (C$_3$A-free) [kg/m^3]	260
Additive (fly ash) [kg/m^3]	60
Liquefier P1 [kg/m^3]	3.10
Superplasticizer SP [kg/m^3]	3.49
Air-entrainer Readyair [kg/m^3]	0.90
Aggregates** [kg/m^3]	1909
Aggregate fraction 0–4 mm [mass-%]	45
Aggregate fraction 4–16 mm [mass-%]	36
Aggregate fraction 16–32 mm [mass-%]	19
Aggregate mineralogy:	
Quartz [mass-%]	90
Feldspar [mass-%]	5
Carbonate [mass-%]	5

* Definitions according to [85]:

SA ...   Sichtbeton, außen [exposed concrete, exterior]
WU ...   wasserundurchlässig [water-proof]
LST ...   stark lösender Angriff [severe leaching attack]
FB ...   frostbeständig [frost resistant]
PB ...   Pumpbeton [pumpable concrete]
WDI ...   wasserdichte Innenschale [water-proof tunnel lining]

** Aggregate content of concrete without PP-fibers,
   see Table 2.6 for details on concrete with PP-fibers.

In order to assure workability, the water/binder-ratio was varied during preparation of the laboratory-cast concrete (see Table 2.6). In case of in-situ concrete, the same water/binder-ratio was used for concrete with and without PP-fibers, resulting in a reduction of the slump by 2 cm. The air content of in-situ concrete with 1.5 kg/m^3 PP-fibers was back-calculated from the measurements of in-situ concrete without PP-fibers (see Table 2.6 and Appendix D).

The used PP-fibers were monofilament fibers with a diameter of approximately 18 μm and 6 mm length (see Figure 2.31). Monofilament PP-fibers are extruded from the molten

Table 2.6: Parameters at mixing and 28-day strength of in-situ and laboratory-cast concrete with/without PP-fibers

	In-situ concrete [67]		Laboratory-cast concrete	
PP-fiber content [kg/m^3]	0	1.5	0	1.5
Aggregates [kg/m^3]	1909	1874$^+$	1909	1776
Water [kg/m^3]	157	157*	152.1	165.7
Water/cement-ratio [–]	0.60	0.60	0.59	0.64
Water/binder-ratio [–]	0.49	0.49	0.48	0.52
Air content [%]	3.5	4.6**	4.0	6.5
Slump [cm]	45.0	43.0	44.8	45.5
Initial density [kg/m^3]	2386	2352	2381	2263
28d-concrete density ρ_c [kg/m^3]	2362		2355.6	2243.8
28d-cube compressive strength [MPa]	52.2		42.0	30.0
28d-bending strength [MPa]	6.41	6.25		

$^+$ Back-calculated from initial density (see Equation (D.3) in Appendix D).

* Presumably same water content for both in-situ concretes.

** Calculated value (see Equation (D.4) in Appendix D).

(a)   (b)
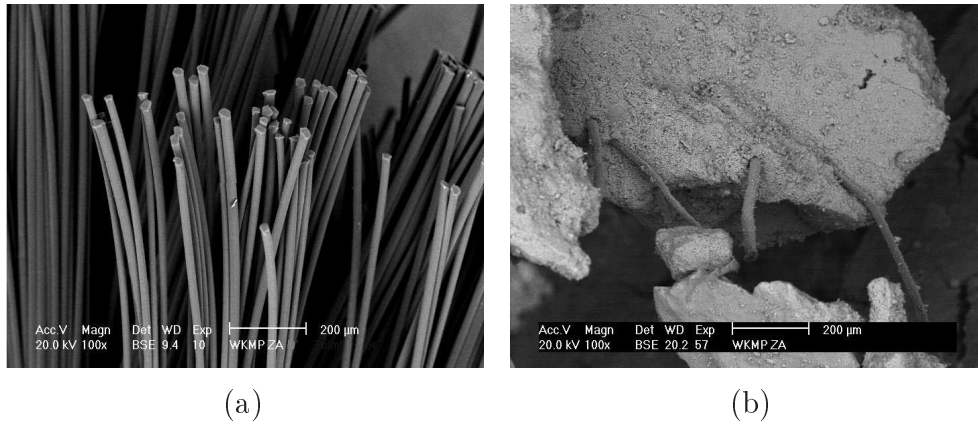
Figure 2.31: Scanning-electron-microscope image showing PP-fibers (a) before casting and (b) in broken-off piece of mature concrete

mass and drawn/elongated to reach the final diameter. Subsequently, they are cut to their final length [89]. The parameters of the fibers are listed in Table 2.7. The density of 100%-crystalline polypropylene is $\rho_c = 950$ kg/m^3, whereas 100%-amorphous polypropylene has a density of $\rho_a = 850$ kg/m^3 [89]. Considering the density of the used PP-fibers as $\rho = 910$ kg/m^3 yields a crystallinity of 60%.

The in-situ specimens were obtained from the large-scale concrete blocks (1.80 m × 1.40 m × 0.50 m) used within the fire experiments described in [67], which were cast under on-site conditions (see Figure 2.32). After casting, the large-scale specimens were dried at 50 °C

Table 2.7: Parameters of PP-fibers used within the concrete mix [70]

Parameter	Value
Diameter [m]	$18 \cdot 10^{-6}$
Length [m]	$6 \cdot 10^{-3}$
Density (solid) [kg/m^3]	910
Density (liquid) [kg/m^3]	850
Crystallinity [%]	60
Melting temperature [°C]	165
Vaporization temperature [°C]	350
Tensile strength [MPa]	400
Young's modulus [MPa]	3500 - 3900
Poisson's ratio [–]	0.40

using a heating mat placed at the center of the concrete block. Due to the rather short storage time of 15 weeks, however, the moisture content still ranged from 4.3 to 7.0 mass-% with an average value of 5.5 mass-%. After the fire experiments (see Figure 2.33(a)), cores 143 mm in diameter were taken from parts of the concrete blocks not affected by the fire load (see Figure 2.33(b)). Thereafter, the cores were cut into discs of 50 mm height, giving the in-situ permeability specimens (see Figure 2.33(c)).

The laboratory-cast specimens were produced in a similar manner. Hereby, concrete blocks with the dimensions 0.75 m × 0.30 m × 0.30 m were cast and stored under water for four weeks, together with cubes used to determine the compressive strength. The moisture content after storage ranged between 5.6 mass-% for concrete without PP-fibers and 6.4 mass-% for concrete with fibers. After curing, cores 150 mm in diameter were taken from the concrete blocks, which were then cut into 50 mm thick discs.

Figure 2.32: Casting of large-scale specimens for fire experiments under on-site conditions [67]

(a)   (b)   (c)
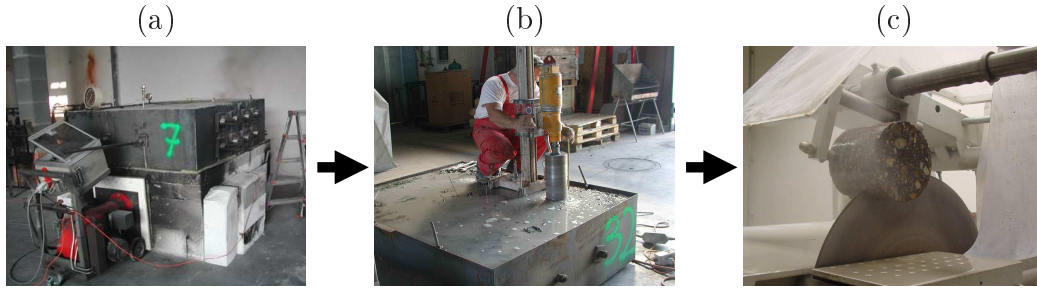
Figure 2.33: Extraction of specimens for permeability testing from large-scale
concrete blocks: (a) fire experiments [67]; (b) extraction of cores [67];
(c) cutting of cores into discs of 50 mm height

In-situ as well as laboratory-cast specimens were stored at similar pre-heating tempera-
tures. In case of in-situ concrete, each specimen was subjected to two permeability tests:
one without heat treatment (referred to as $T = 20$ °C in the following) or after heating
to 80 °C and another test after heating to 105, 140, 200, 300, 400, or 600 °C. In case
of laboratory-cast specimens, up to three experiments were performed on one specimen:
one after heating to 80 °C and one or two more after heating to 105, 169, 224, 329, or
423 °C. The target temperature was reached with a heating rate of 1 °C/min. The rather
slow temperature increase was chosen to avoid large temperature gradients in the speci-
men and, hence, severe microcracking, which would have altered the experimental results.
In order to ensure that the pre-heating temperature was reached everywhere within the
specimen, the samples were stored at the respective target temperature for time spans up
to 90 h. Thereafter, the temperature was reduced with a cooling rate of 1 °C/min.

(a)   (b)   (c)

(d)   (e)

specimen

wax

acrylic

steel ring
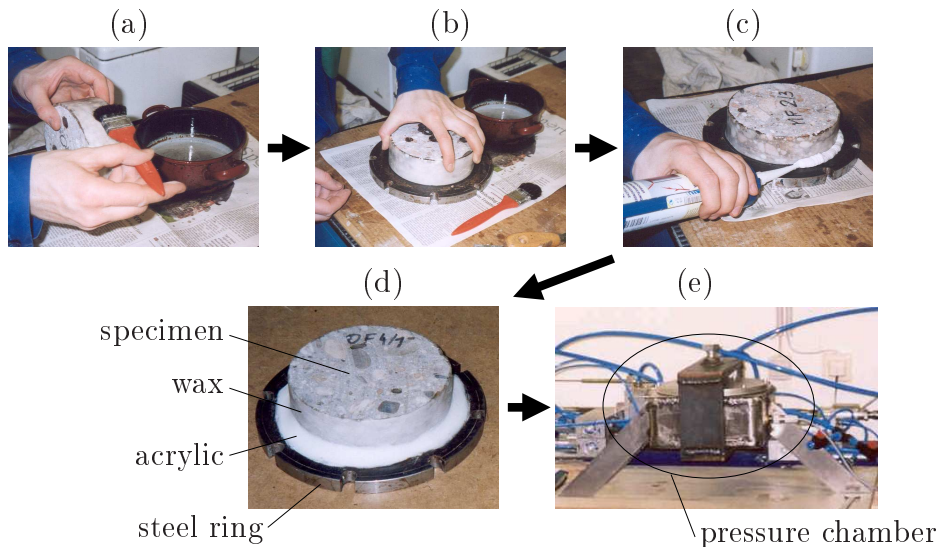
pressure chamber

Figure 2.34: Specimen preparation: (a) sealing of lateral surface, (b) placement
of specimen in steel ring, (c) sealing of gap, (d) specimen plus steel ring
before placement in pressure chamber, (e) pressure chamber containing
permeability specimen

After heat treatment, the lateral surfaces of the cylindrical specimen were sealed with wax in order to assure one-dimensional air flow through the specimen (see Figure 2.34(a)). Then the specimen was placed in a steel ring (Figure 2.34(b)) and the gap between specimen and ring was sealed with acrylic (see Figure 2.34(c)). The specimen together with the steel ring (Figure 2.34(d)) was fixed in the pressure chamber (see Figures 2.21 and 2.34(e)) and the permeability experiment was conducted at room temperature.

2.2.5   Results

2.2.5.1 k_{int} and b for in-situ concrete

Figures 2.35 and 2.36 show the permeability parameters k_{int} and b as a function of temperature for in-situ concrete with 0 and 1.5 kg/m^3 PP-fibers, respectively. The trend for the intrinsic permeability is the same for concrete with and without PP-fibers, namely an increase of k_{int} for increasing temperature. The slip-flow constant b, on the other hand, decreases until temperatures of 200 – 300 °C, and increases thereafter. In case of concrete without fibers, the results for pre-heating temperatures of 20 and 80 °C show large variations irrespective of the chosen evaluation method, which could be explained by evaporable water still present at these temperatures. This trend is also observed in case of concrete with PP-fibers, although the scatter is significantly smaller and the permeability values are higher. The obtained permeability parameters for both types of concrete show larger scatter in case the parameters were identified assuming stationary conditions.
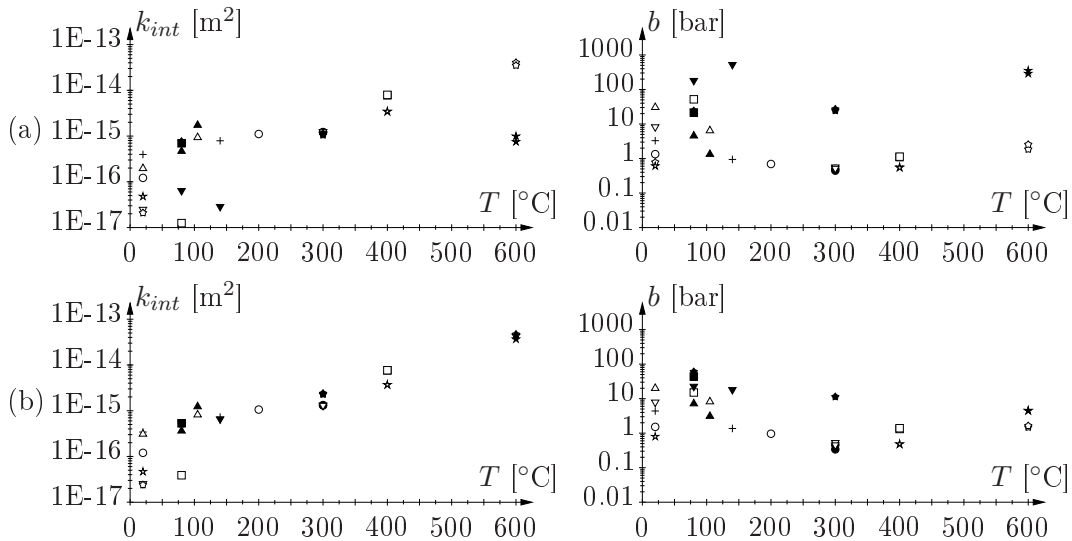
Figure 2.35: k_{int} and b obtained from DPE as a function of temperature for in-situ concrete with 0 kg/m^3 PP-fibers and different modes of parameter identification: (a) stationary and (b) transient analysis (each symbol refers to one specimen which was tested at different temperatures)
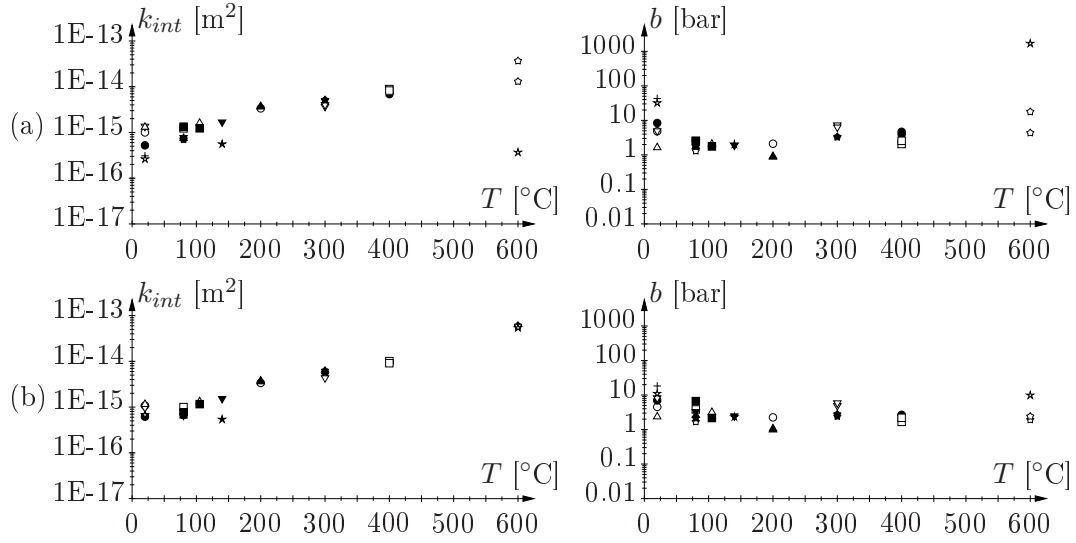
Figure 2.36: k_{int} and b obtained from DPE as a function of temperature for in-situ concrete with 1.5 kg/m^3 PP-fibers and different modes of parameter identification: (a) stationary and (b) transient analysis (each symbol refers to one specimen which was tested at different temperatures)

2.2.5.2 k_{int} and b for laboratory-cast concrete

Figures 2.37 to 2.40 show the permeability parameters k_{int} and b as a function of temperature for laboratory-cast concrete with 0 and 1.5 kg/m^3 PP-fibers. Hereby, parameters identified from DPE and CPE are depicted separately. The same general trend as found
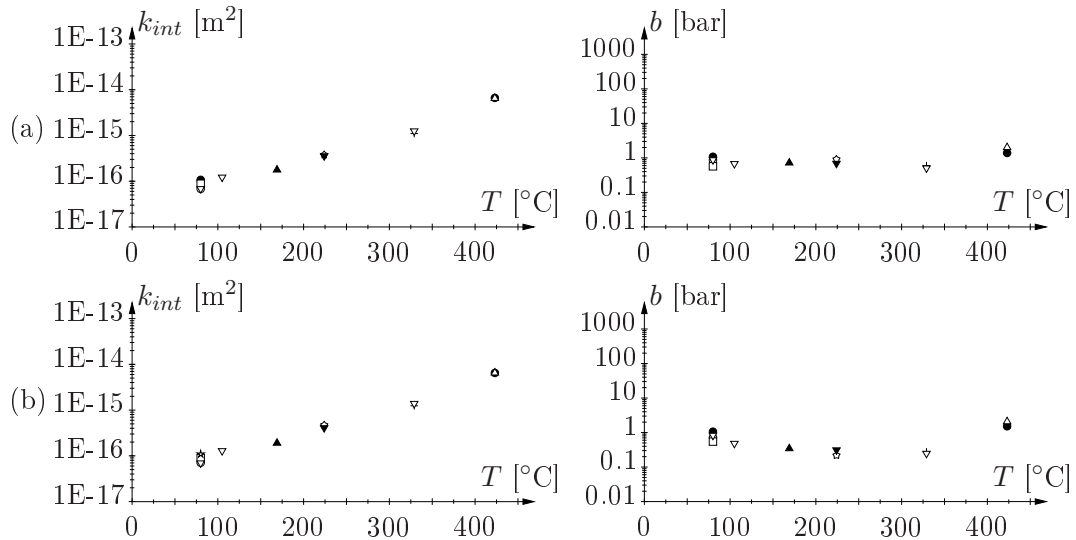
Figure 2.37: k_{int} and b obtained from DPE as a function of temperature for laboratory-cast concrete with 0 kg/m^3 PP-fibers and different modes of parameter identification: (a) stationary and (b) transient analysis (each symbol refers to one specimen which was tested at different temperatures)
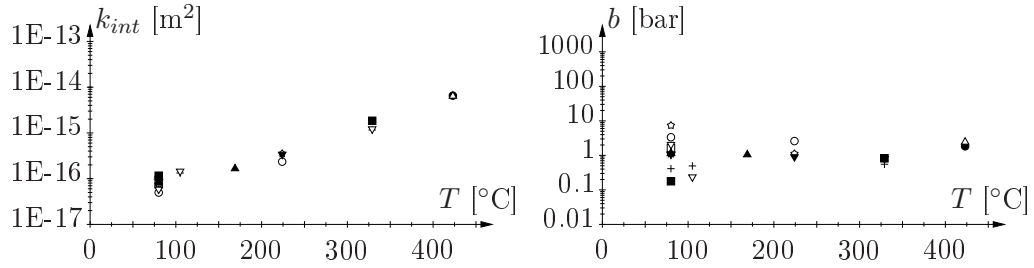
Figure 2.38: k_{int} and b obtained from CPE as a function of temperature for laboratory-cast concrete with $0\,\mathrm{kg/m^3}$ PP-fibers (stationary analysis, each symbol refers to one specimen which was tested at different temperatures)
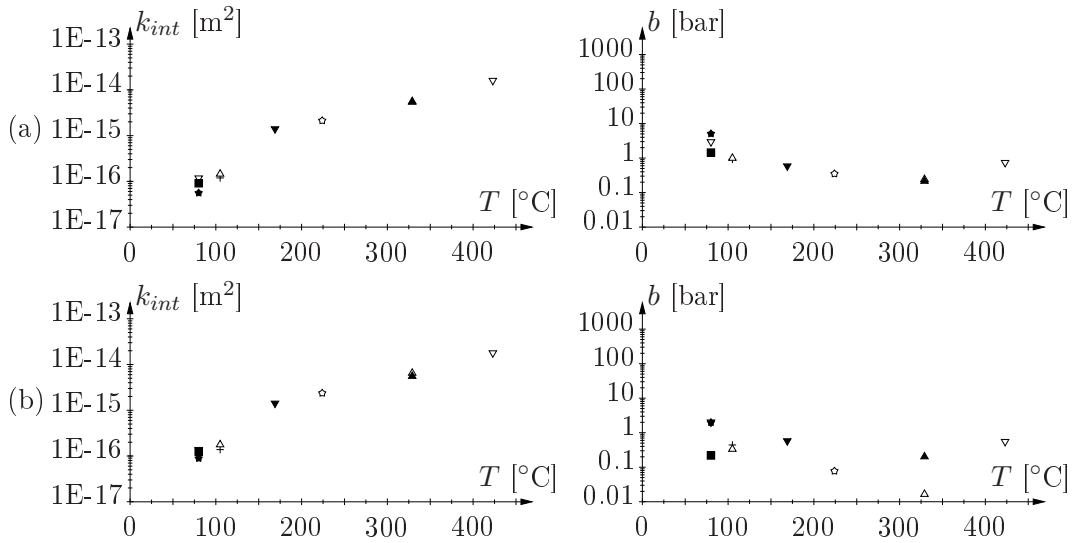
Figure 2.39: k_{int} and b obtained from DPE as a function of temperature for laboratory-cast concrete with $1.5\,\mathrm{kg/m^3}$ PP-fibers and different modes of parameter identification: (a) stationary and (b) transient analysis (each symbol refers to one specimen which was tested at different temperatures)

for in-situ concrete, namely an increasing intrinsic permeability k_{int} with increasing temperature, is observed for laboratory-cast concrete. As regards the slip-flow constant b, again a similar trend as for in-situ concrete is observed. Up to temperatures of 200 – 300 °C, b decreases for increasing pre-heating temperature. Thereafter it shows an increasing behavior. Comparing the different modes of parameter identification using results from DPE, the earlier (for in-situ concrete) observed deviation introduced by the assumption of stationary conditions is less pronounced. For this test series, the scatter of the identified parameters is larger when using experimental data from CPE (see Figures 2.38 and 2.40), which is explained by the larger number of CPE performed.
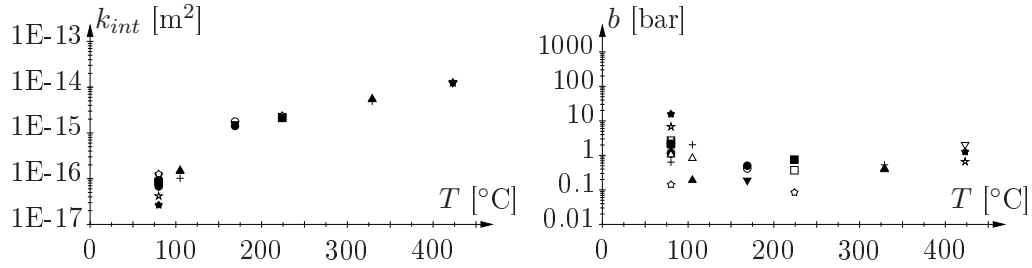
Figure 2.40: k_{int} and b obtained from CPE as a function of temperature for laboratory-cast concrete with 1.5 kg/m^3 PP-fibers (stationary analysis, each symbol refers to one specimen which was tested at different temperatures)

2.2.6   Discussion

2.2.6.1   Stationary versus transient analysis for parameter identification

The stationary analysis provides several permeability values k for different time intervals of the pressure history, giving access to k_{int} and b by linear approximation of the obtained permeability values and extrapolation towards $1/p = 0$ (see Figure 2.41). Since both DPE and CPE are conducted at pressures $p < 10$ bar, the variation of the permeability values k gives different possibilities for k_{int} and b, as illustrated in Figure 2.41. Therefore, the parameters identified from stationary analysis provide the correct permeability k (with $k = k_{int}(1 + b/p)$) in the pressure range considered in the experiment. Nevertheless, the identified values for k_{int} and b might show considerable scatter, especially in case of DPE (see, e.g., Figures 2.35(a) and 2.36(a)). The scatter of the experimental results may be reduced by increasing the pressure range considered in the experiments, which would result in k-values closer to $1/p = 0$. In this case, however, the pressurized volume must be increased in order to avoid transient effects at higher pressures as indicated in Figure 2.41. On the other hand, the increase of the pressurized volume results in an increased scatter at low pressures when the pressure decrease approaches the accuracy range of the pressure gauge. Figures 2.38 and 2.40 show that the scatter of the identified parameters from the stationary analysis is considerably smaller for CPE compared to the parameters obtained from the DPE (compare to Figures 2.35 and 2.36). This is explained by the almost constant pressure in the pressurized volume (see Figure 2.26). Thus, no pressure deviations alter the experimental results of the CPE and stationary conditions are guaranteed.

Compared to the stationary analysis, the transient analysis leads to less scatter for the permeability parameters identified from DPE (see, e.g., Figures 2.35(b) and 2.36(b)), which is explained by capturing transient effects when solving the one-dimensional mass-balance equation for the gas phase (see Equation (2.31)). Figure 2.42(a) shows the error between the numerically and experimentally-obtained pressure decrease for different values of k_{int} and b. Whereas the parameter identified from stationary analysis is located in
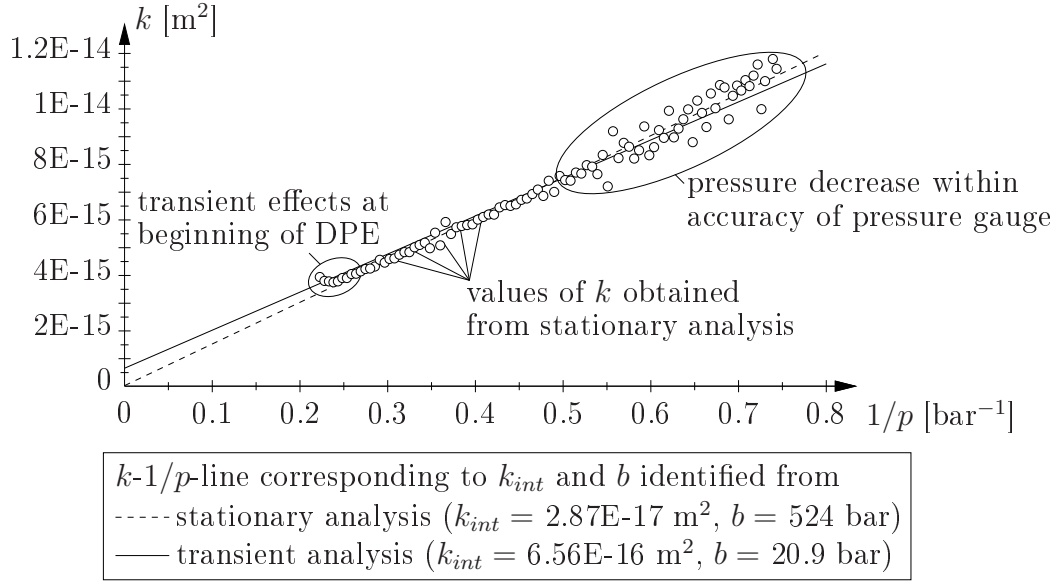
Figure 2.41: Parameter identification for selected DPE using stationary analysis (comparison with result from respective transient analysis)

the "valley" characterized by a lower error, the result of the transient analysis coincides with the global minimum of R (see Figure 2.42). The error between the numerically and experimentally-obtained pressure history is illustrated in Figure 2.43, showing $p_t(t)$ obtained from the transient analysis (i.e., $p_t^{num}(t)$) related to the respective experimental pressure history (i.e., $p_t^{exp}(t)$). As already indicated in Figure 2.42, the permeability parameters from the transient analysis give better agreement between the computed and measured pressure history obtained during DPE.

2.2.6.2 Are both k_{int} and b required to define gas-transport properties of concrete?

Figures 2.41 and 2.42 highlight the fact that different (k_{int}, b)-pairs give similar permeability values k measured during both DPE and CPE. In case of the stationary analysis, the same range of permeability values may be obtained in the pressure range the permeability experiment was performed using significantly different values for the intrinsic permeability k_{int} and the slip-flow constant b (see Figure 2.41). As indicated in Figure 2.42, k_{int} might vary over several orders of magnitude. Hereby, an increase of k_{int} is accompanied by a decrease of b until a certain value of k_{int} is reached. Thereafter, the "valley" observed in Figure 2.42 turns and k_{int} becomes independent of b, indicating pressure-independence for the permeability. As a consequence, the identification of k_{int} from gas-permeability tests is not unique. In fact, an infinite number of (k_{int}, b)-pairs would give proper permeability values in the pressure range considered in the experiment. Thus, both k_{int} *and* b must be provided in order to properly define the gas-transport properties of concrete. Among the different possibilities, the (k_{int}, b)-pair representing the measured k-values best corre-

sponds to the global minimum of the error encountered in the aforementioned "valley".
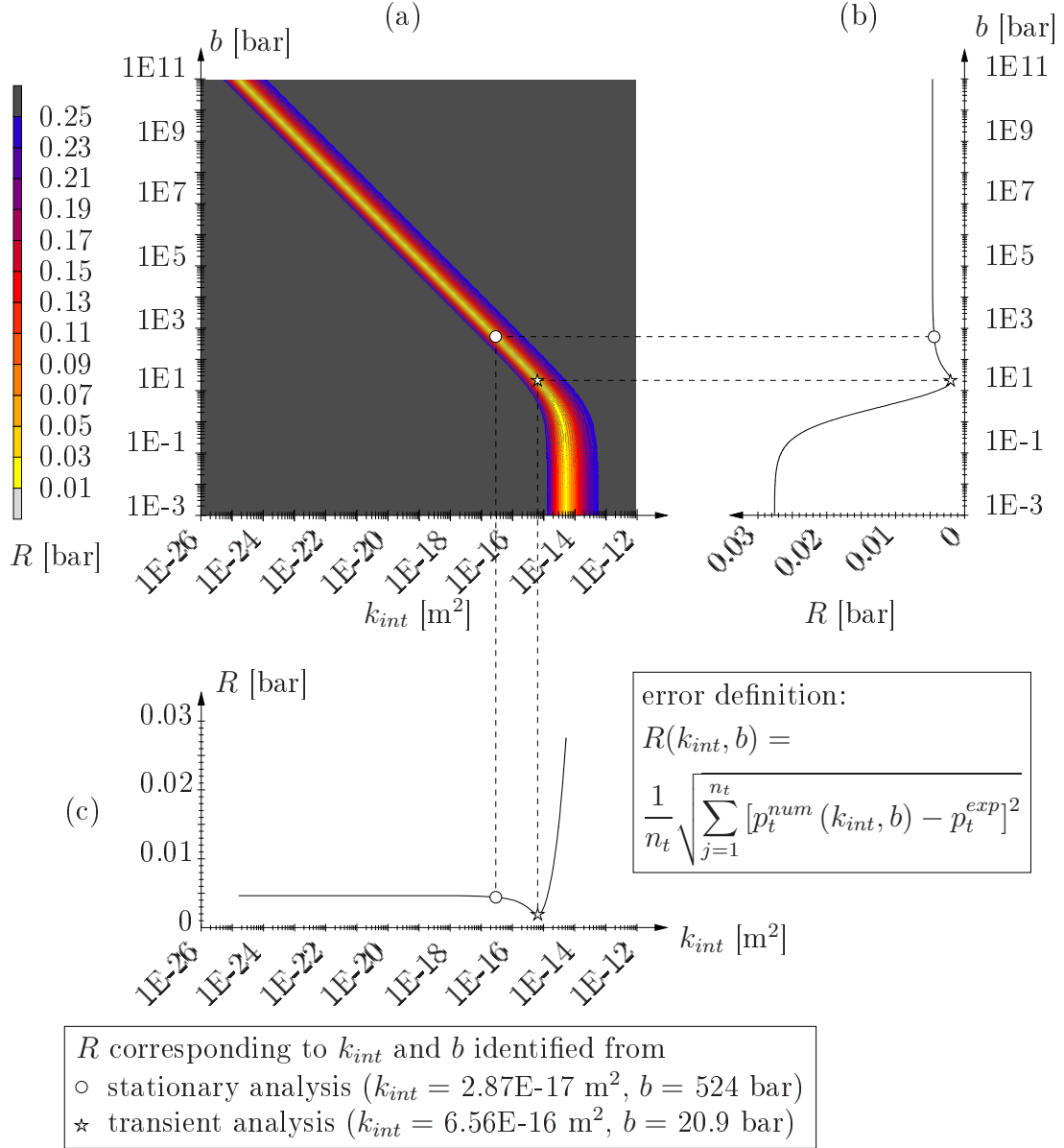
Figure 2.42: Results from transient analysis of selected DPE: (a) distribution of error R as a function of k_{int} and b; plot of error "valley" as a function of (b) b and (c) k_{int} (n_t: number of time instants considered during minimization of R; p_t^{num}: numerical pressure history; p_t^{exp}: measured pressure history)
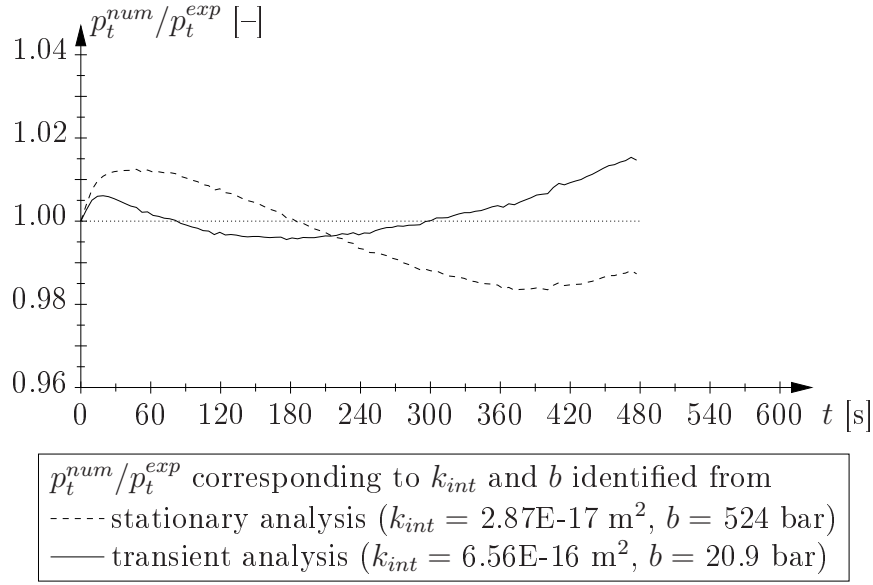
Figure 2.43: Ratio p_t^{num}/p_t^{exp} for two (k_{int}, b)-pairs during transient analysis of selected DPE

2.2.6.3   Influence of PP-fibers and the production process on the permeability

In this subsection, differences (i) between concrete with and without PP-fibers and (ii) between in-situ and laboratory-cast concrete are highlighted. Comparing the results for in-situ concrete with and without PP-fibers (see Figures 2.44 and 2.45), the following differences within certain temperature ranges are observed:

1. At room temperature ($20\,°\mathrm{C}$), a big difference in k_{int} is observed (see Figure 2.44(a)), whereas b is practically the same for concrete with and without PP-fibers (see Figure 2.44(b)). Thus, the permeability k (with $k = k_{int}(1 + b/p)$, see Equation (2.16)) has the same difference as k_{int} (see Figure 2.45).

2. For a pre-heating temperature of $80\,°\mathrm{C}$, the difference of k_{int} between concrete with and without PP-fibers decreases, whereas the opposite is the case for b (b increases considerably for concrete without PP-fibers and it decreases for concrete with fibers, causing an increase of the difference in b). Consequently, the permeability k increases in case of concrete without PP-fibers, whereas a decrease in case of concrete with fibers is observed (see Figure 2.45). The observed behavior of the permeability k illustrates the importance of considering both permeability parameters (k_{int} and b) to represent the gas permeability of concrete.

3. For temperatures between 80 and $140\,°\mathrm{C}$, an oscillating behavior of the permeability parameters is observed with opposite trends for k_{int} and b (see Figure 2.44), giving almost constant values for k within this temperature range.
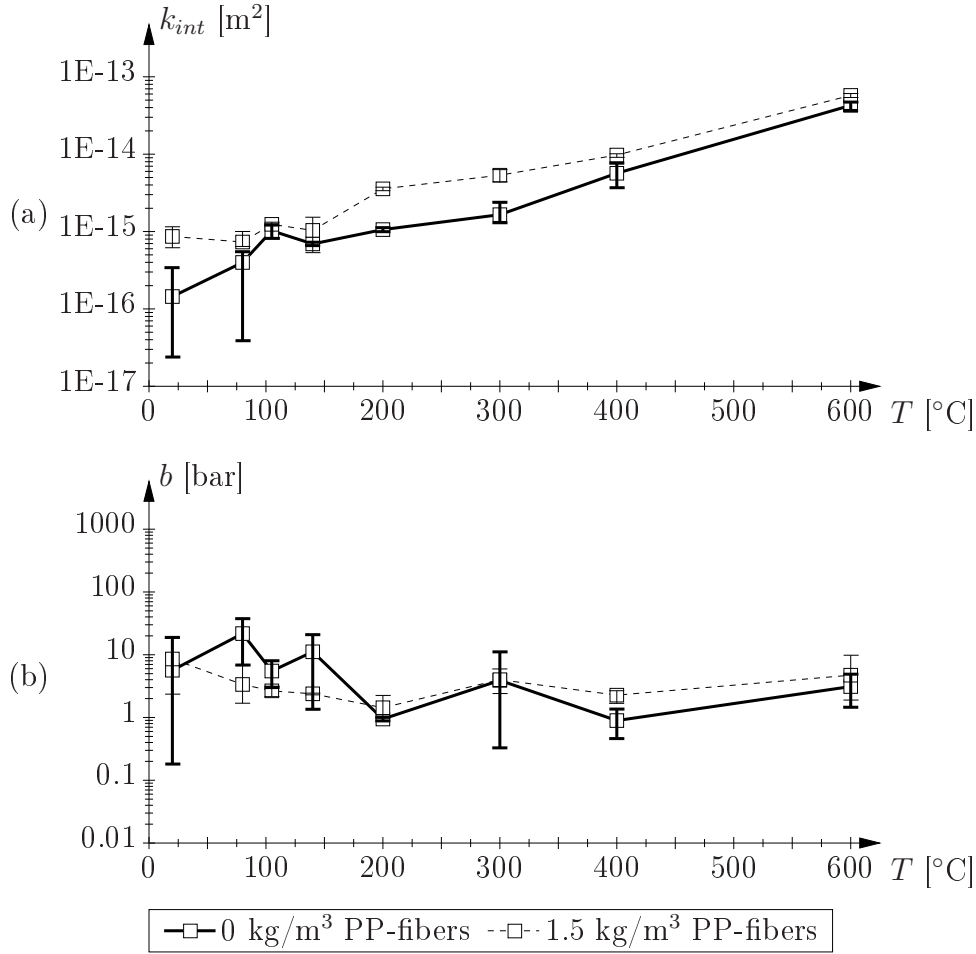
Figure 2.44: Permeability parameters k_{int} and b for in-situ concrete with 0 and 1.5 kg/m^3 PP-fibers (values taken from DPE/transient analysis, see Figures 2.35(b) and 2.36(b); squares represent average values, lines mark minimum and maximum value)

4. For pre-heating temperatures between 140 and 200 °C, the difference in k_{int} between in-situ concrete with and without PP-fibers increases considerably, reaching the same magnitude as observed for the low-temperature permeabilities (for $T = 20$ °C). The difference in b decreases, yielding an increase of the difference in k (see Figure 2.45). This increase is explained by melting of the PP-fibers. In contrast to the results obtained for laboratory-cast concrete [58], showing the maximum difference at a pre-heating temperature of 200 °C, this "fiber effect" was at the most of equal importance as the aforementioned difference in low-temperature permeability, with the latter considered to be mainly affected by the construction process of the concrete members.

5. Above 200 °C, the difference in k_{int} decreases again whereas the difference in b between concrete with and without PP-fibers remains almost constant. This leads
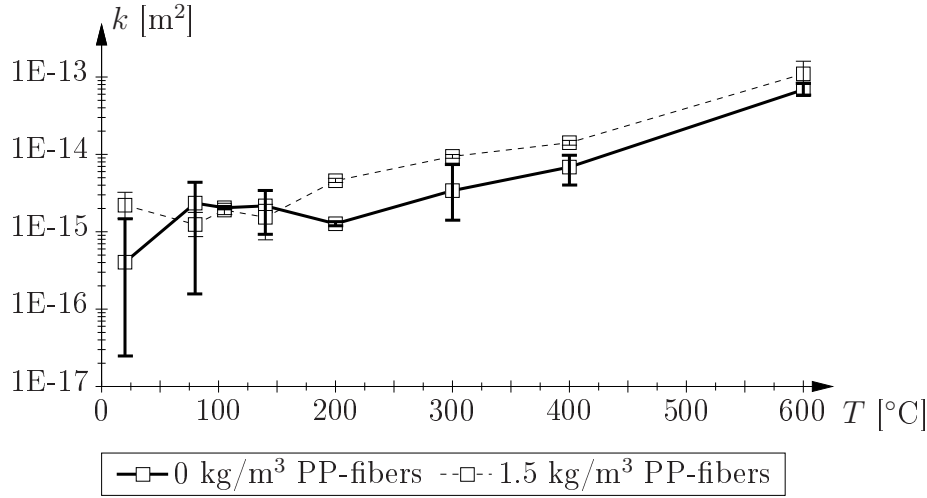
Figure 2.45: Permeability k at $p = 5$ bar (with $k = k_{int}(1 + b/p)$) for in-situ concrete with 0 and 1.5 kg/m^3 PP-fibers (k_{int} and b identified from DPE/transient analysis, see Figures 2.35(b) and 2.36(b); squares represent average values, lines mark minimum and maximum value)

to a decreasing difference of the permeability k (see Figure 2.45), indicating that temperature-induced damage overshadows the effect of melting of the PP-fibers on the permeability.

Comparing laboratory-cast concrete with and without PP-fibers (Figures 2.46 and 2.47), the following observations are made:

1. In contrast to in-situ concrete, laboratory-cast concrete shows no distinct difference in low-temperature permeabilities between concrete with and without fibers. Up to a pre-heating temperature of 105 °C, the intrinsic permeability k_{int} is practically the same (see Figure 2.46(a)). As regards the value of b, only small differences are observed, yielding almost equal values for the permeability k for concrete with and without PP-fibers (see Figure 2.47). This is in agreement with experimental results obtained for laboratory-cast concrete presented in [58].

2. The observed "fiber effect" is also found in laboratory-cast concrete with 1.5 kg/m^3 PP-fibers. Whereas k_{int} increases continuously in case of concrete without PP-fibers between pre-heating temperatures of 105 and 170 °C, a jump of almost one order of magnitude is observed for k_{int} of concrete with fibers. The slip-flow constant b, on the other hand, shows no jump. In case of concrete with PP-fibers, b decreases and becomes lower than the value of b of concrete without fibers. The observed changes in k_{int} and b lead to a sudden increase of the difference of the permeability k (see Figure 2.47) which is considered to be caused by melting of the fibers, as in case of in-situ concrete.
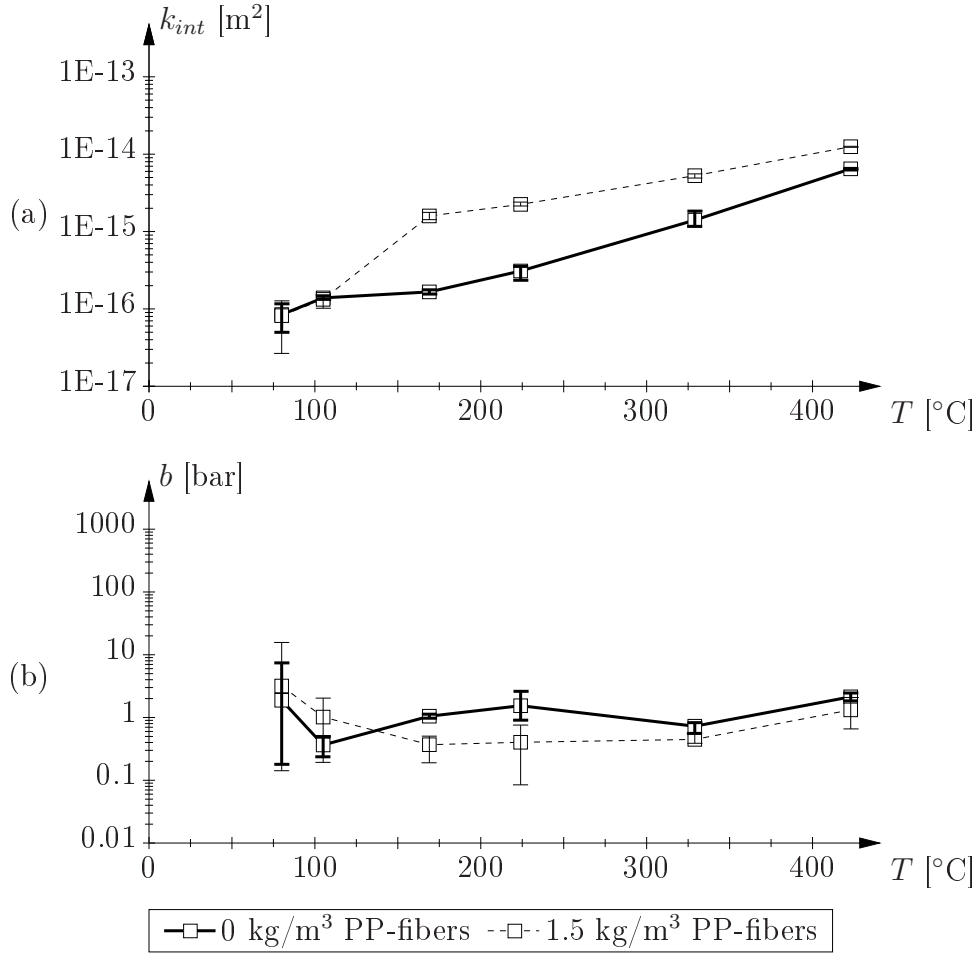
Figure 2.46: Permeability parameters k_{int} and b for laboratory-cast concrete
with 0 and 1.5 kg/m^3 PP-fibers (values taken from CPE/stationary anal-
ysis, see Figures 2.38 and 2.40; squares represent average values, lines
mark minimum and maximum value)

3. For pre-heating temperatures above 170 °C, the difference in k_{int} between concrete
   with and without PP-fibers decreases as observed in case of in-situ concrete. The
   difference in b remains almost constant, yielding a continuous decrease of the differ-
   ence in k. This indicates again that temperature-induced damage reduces the effect
   of melting of the PP-fibers.

The differences between concrete with and without PP-fibers may be explained by:

- For low temperatures, this difference was only observed in case of in-situ concrete,
  whereas similar permeability parameters were observed for laboratory-cast concrete.
  Based on mercury-intrusion-porosimetry (MIP) test results (see Subsection 2.3), the
  observed difference was assigned to the considerably higher pore volume for in-situ
  concrete containing PP-fibers. This higher amount of pore volume was encountered
  in the pore-size range corresponding to the thickness of the interfacial transition
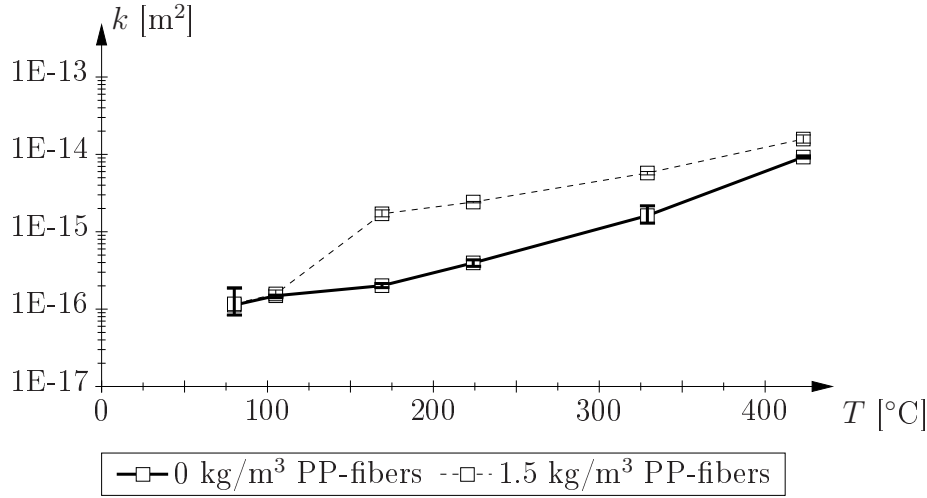
Figure 2.47: Permeability k at $p = 5$ bar (with $k = k_{int}(1+b/p)$) for laboratory-cast concrete with 0 and 1.5 kg/m^3 PP-fibers (k_{int} and b identified from CPE/stationary analysis, see Figures 2.38 and 2.40; squares represent average values, lines mark minimum and maximum value)

zones (ITZ) [132], which is in agreement with theories presented in [16, 67, 110], stating that the PP-fibers introduce additional ITZ at casting. As found by means of numerical simulations of the formation of the concrete microstructure [16], the introduction of additional ITZ by PP-fibers connects locally-percolated ITZ clusters, leading to percolation of the overall pore structure. The effect of PP-fibers on the low-temperature permeability, which was found only for in-situ concrete, is explained by the reduced on-site workability and the lower effect of densification of concrete containing PP-fibers [67], eventually influencing the pore structure of the in-situ concrete and/or the characteristics of the ITZ [132]. Moreover, internal bleeding in consequence of a higher amount of liquefier influences the formation of ITZ [67].

- The sharp increase of the permeability of concrete with PP-fibers at a temperature of $T \approx 170$ °C was observed for in-situ as well as laboratory-cast concrete. According to [58], this permeability jump is caused by melting of the polypropylene fibers followed by the partial or complete absorption of the molten polypropylene by the cement matrix [58], leaving additional pathways for gas to flow through the porous matrix. In fact, an increase in pore volume of in-situ concrete containing PP-fibers was observed in the pore-size range corresponding to the diameter of the employed fibers (see Subsection 2.3). In addition, the different microcracking behavior could have an influence on the considerably different permeability. Experiments [58] revealed a much higher crack density in case fiber-reinforced concrete was heated to temperatures above 170 °C compared to concrete without fibers, whereas larger crack widths were observed for the latter. This difference in cracking behavior might be caused by (i) the fibers acting as discontinuities within the cement

matrix and therefore favoring nucleation of local cracks [58] and (ii) the expansion of polypropylene during melting [58, 108]. As regards the latter, the crystalline part of polypropylene (amounting to 60 vol-% of the employed polypropylene) is transformed into amorphous polypropylene, with the overall density dropping from 910 kg/m^3 to 850 kg/m^3 [89], giving an increase in volume of approximately 7%. In any case, the better-developed network in case of fiber-reinforced concrete increases the permeability via a higher number of pathways for the vapor to move towards the heated surface.

2.3 Pore structure of pre-heated *in-situ* concrete – results from mercury-intrusion porosimetry

In order to explain the observed characteristics of the intrinsic permeability, which strongly depend on the actual pore structure of concrete, results from mercury-intrusion-porosimetry (MIP) experiments performed on small samples of *in-situ* concrete subjected to the same pre-heating temperatures as the permeability specimens (i.e., $T = 20$, 80, 105, 140, 200, 300, 400, and 600 °C) are presented. Since the mercury pressure of the employed MIP device is limited, only a specific range of pore radii (1.9 nm $\leq r \leq 75$ μm) can be detected. Moreover, because of the rather small sample size, only the presence of low-size aggregates is taken into account, disregarding the influence of the ITZ of larger-size aggregates.

Considering the total pore volume obtained from MIP testing, which shows an increasing behavior with increasing temperature (see Figure 2.48), the rather small difference between concrete with and without fibers cannot explain the higher permeability of fiber-reinforced concrete obtained from the permeability tests. As regards the obtained pore-size distributions, an almost similar development for concrete with and without PP-fibers is observed (see Figures 2.49 and 2.50). In both cases, the peak within the pore-size range of $10 \leq r \leq 100$ nm is shifted towards larger radii for increasing pre-heating temperature. In case of concrete with 1.5 kg/m^3 PP-fibers, this peak is less pronounced for $T = 20$ and 80 °C and the largest shift of this peak towards larger pore radii is observed between pre-heating temperatures of 80 and 105 °C. Within the pore-size range of $6 \leq r \leq 10$ μm, the pore volume of concrete with 1.5 kg/m^3 PP-fibers increases (see Figure 2.50), originating from melting and, finally, evaporation of PP-fibers ($\varnothing \approx 18$ μm, see Figures 2.31 and 2.51).
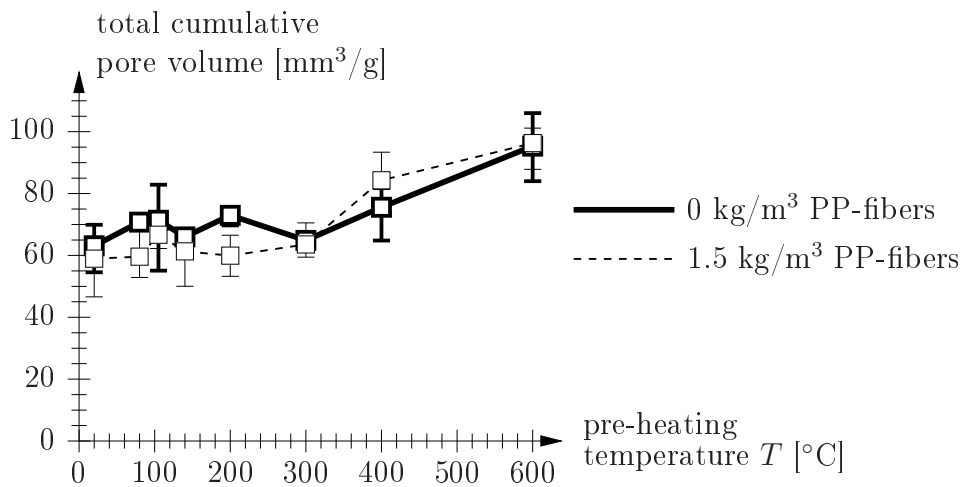
Figure 2.48: Total cumulative pore volume of concrete after exposure to different temperatures [71] (squares represent average values, lines mark minimum and maximum value)
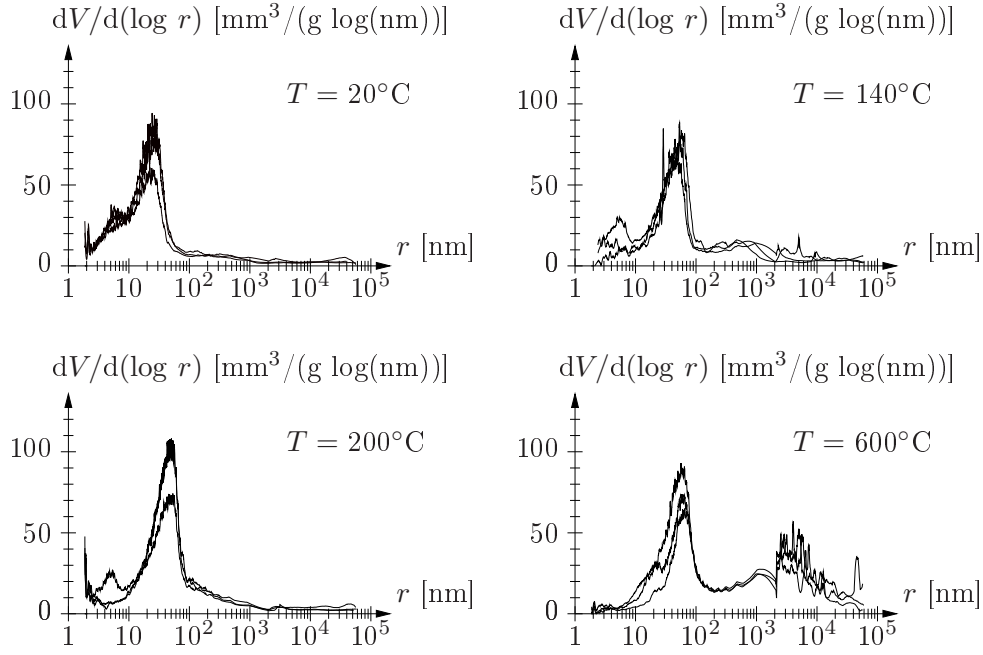
Figure 2.49: $dV/d(\log r)$ of samples of concrete with 0 kg/m^3 PP-fibers after exposure to different temperatures [71]
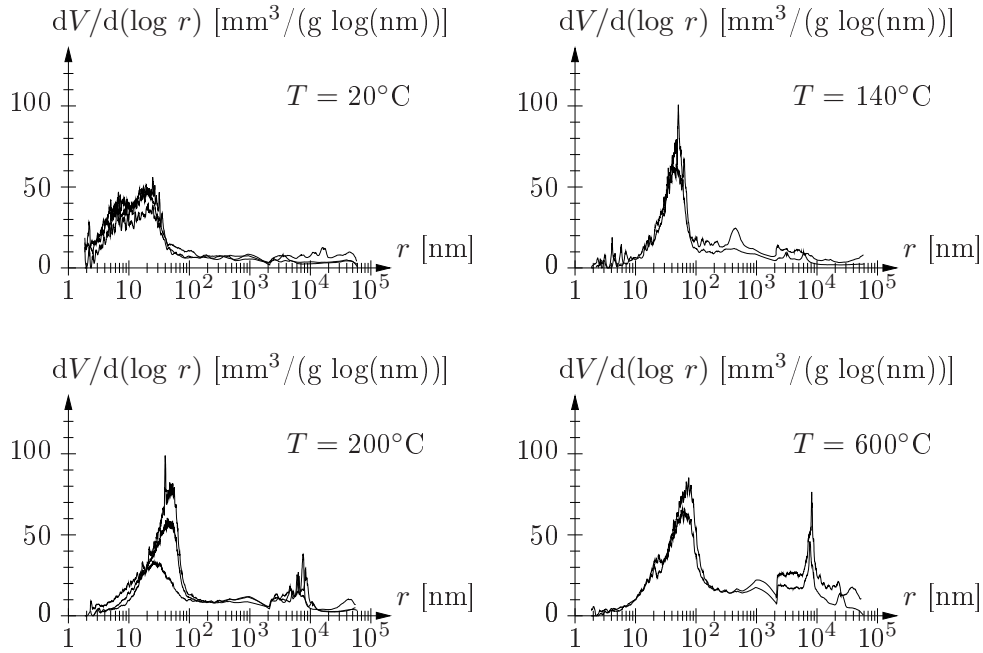
Figure 2.50: $dV/d(\log r)$ of samples of concrete with 1.5 kg/m^3 PP-fibers after exposure to different temperatures [71]

The respective peak in the pore-size distribution starts to develop between pre-heating temperatures of $T = 140$ and $200\ ^\circ$C, which corresponds to the melting temperature of the fibers at $T \approx 170\ ^\circ$C [71].
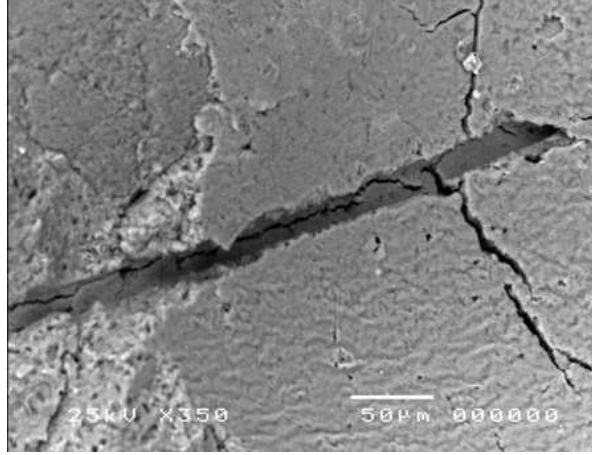
Figure 2.51: Electron-microscope image of concrete pre-heated to a temperature above the vaporization temperature of polypropylene showing an empty fiber channel [67]

The difference between concrete with and without PP-fibers at lower temperatures is highlighted by considering the change of certain pore-size ranges with temperature. As shown in Figures 2.52(a) and (b), the low-temperature values of the pore volume for fiber-reinforced concrete are almost twice as large as the respective values for concrete without fibers for pore radii within[9] 10^3–10^4 and 10^4–10^5 nm (the maximum value for concrete with PP-fibers for pore radii within 10^4–10^5 nm being even three times as large as the average value for concrete without fibers). This pore-size range includes the thickness of the interfacial transition zones (ITZ) which, according to [40], is controlled by the median size of the cement grains (typically $10 - 20$ μm [20]). Because of the rather small sample size, only small aggregates are considered during MIP testing, disregarding the larger porosity of the ITZ of larger-size aggregates.

The effect of melting and evaporation of PP-fibers can be observed in the volume of pores with $10^3 \leq r \leq 10^4$ nm. Whereas the pore volume in this range remains almost constant until 200 °C for concrete without fibers, the pore volume of concrete with 1.5 kg/m^3 PP-fibers is continuously increasing (see Figure 2.52(a)). For $T > 200$ °C, both types of concrete show an increase in the pore volume of this pore-size range with increasing temperature, with no pronounced difference.

---

[9]No distinct differences were observed for smaller-size pores [71].
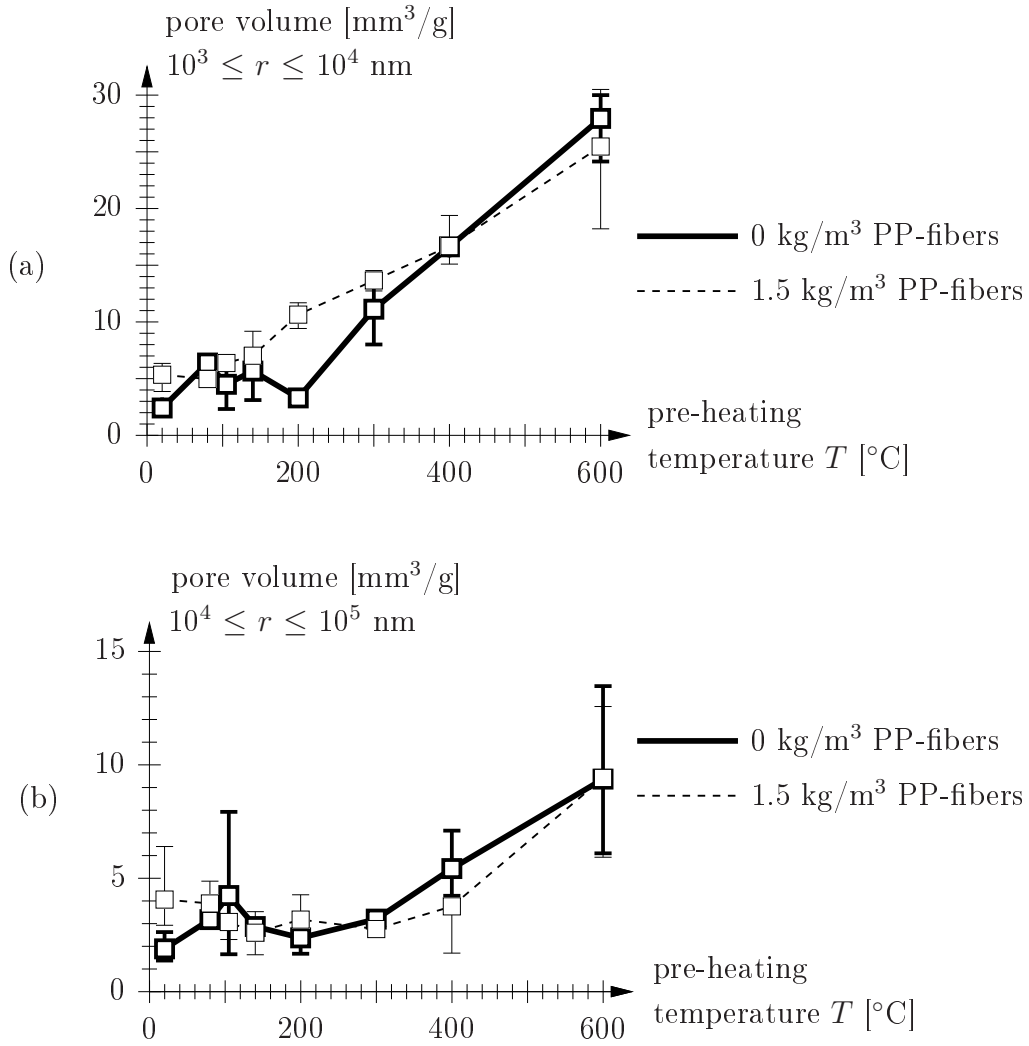
Figure 2.52: Pore volume for certain ranges of pore radii after exposure to different temperatures [71] (squares represent average values, lines mark minimum and maximum value)

Chapter 3

Coupled analysis of governing transport processes in heated concrete

In order to assess the impact of fire loading on concrete structures, the distributions of temperature, saturation, gas pressure etc. are determined by means of coupled analyses simulating heat and mass transport in heated concrete.

3.1 Literature review

In the past, numerous models were developed solving the governing equations of heat and mass transport in a coupled manner [1, 2, 10, 13, 14, 25, 26, 41, 43, 72, 73, 111, 112, 118, 134], giving access to more realistic temperature distributions compared to an uncoupled thermal analysis. Hereby, the governing equations are discretized in space by means of finite elements [1, 2, 10, 13, 14, 41, 43, 72, 111, 112, 118] or finite volumes [25, 26, 73, 134] and are solved with respect to the primary state variables[1], i.e.,

1. the temperature T,

2. the gas pressure p^g, and

3. the capillary pressure[2] p^c [41, 43, 72, 111, 112].

---

[1]The number of primary state variables is equal to the number of governing balance equations.
[2]The capillary pressure may be replaced by the saturation S_w [25, 26, 73], the vapor density ρ^{gw} [118], or the molar mass fraction of water vapor in gas [1, 2].

In [41, 43, 72, 111, 112], the displacement field **u** is added to the list of primary state variables, allowing consideration of thermo-hydro-chemo-mechanical couplings. In contrast to the models formulated in [1, 2, 25, 26, 41, 43, 72, 73, 111, 112, 118], only temperature T and gas pressure p^g are used as primary state variables in [10, 13, 14, 134].

3.2   Finite element (FE) formulation

Within the presented analyses, concrete is treated as a multi-phase medium, consisting of solid, liquid (water), and gaseous (water vapor and dry air) phases. The governing macroscopic balance equations[3] are solved in a fully-coupled manner with respect to the main state variables, i.e., capillary pressure p^c [Pa], gas pressure p^g [Pa], and temperature T [°C] (see Appendix E.1 and, e.g., [41, 43, 72, 111, 112]):

1. Mass balance equation for the water phase (water vapor and liquid water, involving the solid mass balance equation):

$$n(\rho^w - \rho^{gw})\frac{\partial S_w}{\partial t} + n(1 - S_w)\frac{\partial \rho^{gw}}{\partial t} + nS_w\frac{\partial \rho^w}{\partial t}$$

$$-(1-n)\beta_s\left[\rho^{gw} + (\rho^w - \rho^{gw})S_w\right]\frac{\partial T}{\partial t}$$

$$- \operatorname{div}\left(\rho^{gw}\frac{\mathbf{k}k^{rg}}{\eta^g}\operatorname{grad} p^g\right) - \operatorname{div}\left(\rho^w\frac{\mathbf{k}k^{rw}}{\eta^w}\operatorname{grad} p^w\right)$$

$$- \operatorname{div}\left[\rho^g\frac{M_a M_w}{M_g^2}\mathbf{D}_{eff}\operatorname{grad}\left(\frac{p^{gw}}{p^g}\right)\right]$$

$$= -\frac{(1-n)\left[\rho^{gw}(1-S_w) + \rho^w S_w\right]}{\rho^s}\frac{\partial \rho^s}{\partial \xi}\frac{\partial \xi}{\partial t}$$

$$- \left[\rho^{gw}(1-S_w) + \rho^w S_w\right]\frac{\dot{m}_{dehydr}}{\rho^s} + \dot{m}_{dehydr}\,; \tag{3.1}$$

---

[3]In contrast to [41, 43, 72, 111, 112] (i) gravitational effects were not considered, (ii) the sign of the mass source term associated with dehydration of the cement paste, $\dot{m}_{dehydr}$ [kg/(s m³)], was changed, and (iii) the dehydration process was described by the hydration degree ξ [–] instead of the degree of dehydration ξ_{dehydr} [–].

2. Mass balance equation for the dry air phase (involving the solid mass balance equation):

$$-n\rho^{ga}\frac{\partial S_w}{\partial t} + n(1-S_w)\frac{\partial \rho^{ga}}{\partial t} - \rho^{ga}(1-n)(1-S_w)\beta_s\frac{\partial T}{\partial t}$$

$$- \text{div}\left(\rho^{ga}\frac{\mathbf{k}k^{rg}}{\eta^g}\text{grad } p^g\right) - \text{div}\left[\rho^g\frac{M_aM_w}{M_g^2}\mathbf{D}_{eff}\text{ grad }\left(\frac{p^{ga}}{p^g}\right)\right]$$

$$= -\frac{(1-n)\rho^{ga}(1-S_w)}{\rho^s}\frac{\partial \rho^s}{\partial \xi}\frac{\partial \xi}{\partial t} - \rho^{ga}(1-S_w)\frac{\dot{m}_{dehydr}}{\rho^s} ; \tag{3.2}$$

3. Enthalpy balance equation:

$$(\rho c_p)_{eff}\frac{\partial T}{\partial t} - \left(\rho^g c_p^g\frac{\mathbf{k}k^{rg}}{\eta^g}\text{grad } p^g + \rho^w c_p^w\frac{\mathbf{k}k^{rw}}{\eta^w}\text{grad } p^w\right)\text{ grad } T$$

$$- \text{div}\left(\lambda_{eff}\text{ grad } T\right) = -\dot{m}_{vap}h - \dot{m}_{dehydr}l_\xi^w , \tag{3.3}$$

with

$$\dot{m}_{vap} = -n\rho^w\frac{\partial S_w}{\partial t} - nS_w\frac{\partial \rho^w}{\partial t} + \rho^w(1-n)S_w\beta_s\frac{\partial T}{\partial t}$$

$$+ \text{div}\left(\rho^w\frac{\mathbf{k}k^{rw}}{\eta^w}\text{grad } p^w\right) - \frac{(1-n)\rho^w S_w}{\rho^s}\frac{\partial \rho^s}{\partial \xi}\frac{\partial \xi}{\partial t}$$

$$- \rho^w S_w\frac{\dot{m}_{dehydr}}{\rho^s} + \dot{m}_{dehydr} . \tag{3.4}$$

Equations (3.1) to (3.4) were obtained by introducing Darcy's law for pressure-driven flow of water and vapor, Fick's law for diffusional flow, and Fourier's law for heat conduction. Moreover, the following constitutive relations were employed:

- Kelvin-Laplace law (definition of the relative humidity RH [–]),

- Clausius-Clapeyron equation or Hyland-Wexler formula, relating the saturation vapor pressure p^{gws} [Pa] to the temperature T [°C],

- Young-Laplace equation, relating the capillary pressure p^c [Pa] to the pore radius r [m],

- Clapeyron equation (ideal gas law), and

- Dalton's law (definition of partial pressures of water vapor, p^{gw} [Pa], and of dry air, p^{ga} [Pa]).

Additionally, the following relationships were determined from experimental data (for details, see Subsection 3.4):

- Degree of hydration ξ [–] versus temperature T [°C], with $\dot{\xi} < 0$ during heating, extracted from thermogravimetric measurements (see, e.g., [52]).

- Saturation S_w [–] versus capillary pressure p^c [Pa] and temperature T [°C] [9, 46, 79, 90, 124], which can be deduced from MIP or sorption-isotherm experiments.

- Intrinsic permeability k_{int} [m²] versus temperature T [°C], determined from permeability experiments (see Subsection 2.2 and [129, 132]).

- Relative permeabilities to water and gas (k^{rw} [–] and k^{rg} [–]) versus saturation S_w [–] [15, 41, 102, 122], extracted from permeability experiments.

The boundary conditions (BC) within the employed FE formulation are defined by (i) prescribed values for the temperature ($\overline{T}$) and for the pressures ($\overline{p}^g$ and $\overline{p}^c$) (Dirichlet's BC), (ii) prescribed heat fluxes q^T and mass fluxes (q^{ga}, q^{gw}, and q^w) (Neumann's BC), or (iii) heat and mass transfer fluxes (Cauchy's BC) introducing heat and mass-transfer parameters (yielding convective and radiative heat flux, q_c^T and q_r^T, respectively, and convective water-vapor flux q_c^{gw}). The resulting set of governing equations is discretized in space and time and solved by means of a Newton-Raphson iteration scheme (see Appendix E.1).

3.3 Consideration of spalling

In order to simulate heat and mass-transport processes in case of spalling of the tunnel lining, the one-dimensional model[4] of the coupled FE formulation presented in the previous subsection is extended towards a moving boundary, representing the actual location of the spalling front, denoted as $d_s(t)$ [m] (see Figure 3.1). Hereby, the FE nodes characterized by $x_i < d_s(t)$ are deactivated except for the closest node to the spalling front. This node (k-th node in Figure 3.1) is shifted to the actual location of the spalling front, with $x_k = d_s(t)$, allowing consideration of prescribed spalling histories. It is worth mentioning that, since spalling depends on numerous parameters (such as moisture content, heating rate, mechanical loading etc.), the prediction of the risk and the amount of spalling is a very complex task and presently subject of intensive research. Within this work, prescribed spalling histories are considered which were derived on basis of experimental observations/data collected within the fire experiments presented in [67].

3.4 Material properties

Table 3.1 contains the input parameters for the coupled analysis (details on the mix design of the considered concrete can be found in Subsection 2.2 and [129, 132]).

---

[4]Based on the geometrical properties and the loading conditions found during tunnel fires, a one-dimensional FE model is employed.
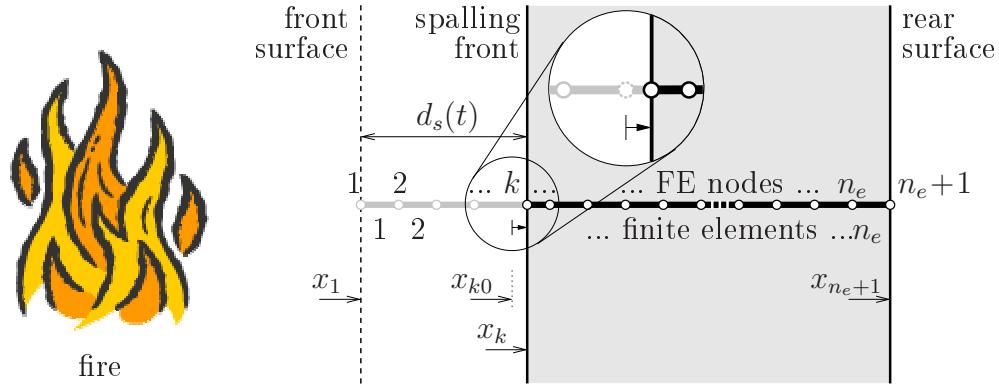
Figure 3.1: One-dimensional FE model taking moving spalling front into account (n_e: number of finite elements, $d_s(t)$ [m]: spalling depth, x_{k0} [m]: original location of k-th node)

Table 3.1: Properties of lining concrete for the coupled analysis

Input parameter	Initial value ($T_0 = 20$ °C)	Temperature dependence	Source
Thermal conductivity λ [kJ/(h m K)]	6.72	$\lambda = \lambda_0 - 0.006(T - T_0)$ for $T < 800$ °C	[90]
Density ρ_c (ρ_s) [kg/m^3]	2362	$\rho = \rho_0 + 0.3(T - T_0)$	[67]
Specific heat capacity c_p [kJ/(kg K)]	0.90	$c_p = c_{p0} + 0.0005(T - T_0)$ for $T < T_{crit} = 374.15$ °C	[90]
Porosity n [–]	0.142	$n = n_0 + 0.0001(T - T_0)$	[59]
Intrinsic permeability k_{int} of concrete with 0 kg/m^3 PP-fibers [m^2]	$1.22 \cdot 10^{-16}$	see Figures 2.44 and 3.4	[132]
Intrinsic permeability k_{int} of concrete with 1.5 kg/m^3 PP-fibers [m^2]	$4.58 \cdot 10^{-16}$	see Figures 2.44 and 3.4	[132]
Specific enthalpy of vaporization h [kJ/kg]	2486	$h = 267.2(T_{crit} - T)^{0.38}$ for $T < T_{crit} = 374.15$ °C	[17]
Specific enthalpy of dehydration l_ξ^w [kJ/kg]	796	–	[128]

3.4.1 Dehydration of heated concrete

The degree of hydration ξ [–], with $\xi = m_h/m_{h0}$ (where m_h [kg/m^3] is the actual amount of chemically-bound water and m_{h0} [kg/m^3] is the initial amount of chemically-bound water due to hydration that is present prior to heating), is defined as a function of temperature (see Figure 3.2). This function, which can be extracted from thermogravimetric measurements (see, e.g., [52]), is used for determination of the rate of weight loss of water

due to dehydration $\dot{m}_{dehydr}$ [kg/(s m^3)] (see Equations (3.1) to (3.4)), defined as

$$\dot{m}_{dehydr} = -m_{h0}\frac{\partial \xi}{\partial t} \, . \tag{3.5}$$

It is worth mentioning that hydration of concrete is temperature-dependent and, in addition, also dependent on the relative humidity (i.e., the vapor pressure). However, the inversion of the hydration process in order to obtain the constitutive relation for dehydration is not straightforward. Because of lack of experimental data concerning the dependence of the dehydration process on the relative humidity, the dehydration process was described as a function of temperature only.
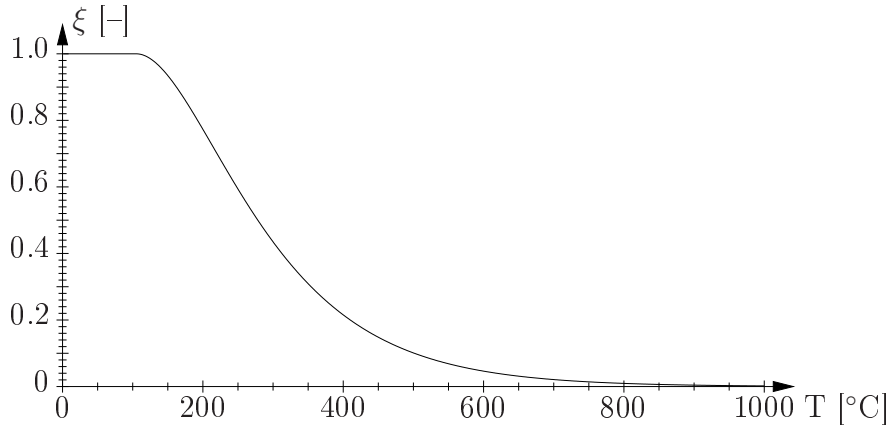
Figure 3.2: Degree of hydration versus temperature [90]

3.4.2 Saturation in heated concrete

According to [124], the saturation S_w [–] is related to the capillary pressure p^c [Pa] by

$$S_w = \left[1 + \left(\frac{p^c}{p_b^c}\right)^{\left(\frac{1}{1-m}\right)}\right]^{-m} , \tag{3.6}$$

the applicability to concrete of which was shown in [9, 79]. In Equation (3.6), p_b^c [Pa] is the so-called bubbling pressure (defined as the minimum value of p^c on a drainage capillary pressure curve, at which a continuous gas phase exists in the void space) and m (with $0 \leq m \leq 1$) is a constant parameter. In order to implement the above described model into the finite element code simulating concrete at elevated temperatures, Relation (3.6) was extended by replacing the (constant) bubbling pressure p_b^c by a temperature-dependent

polynomial function [46, 90], yielding (see Figure 3.3)[5]

$$S_w = \left[1 + \left(\frac{E_s}{A_s} p^c \right)^{\left(\frac{1}{1-m} \right)} \right]^{-m} . \tag{3.7}$$
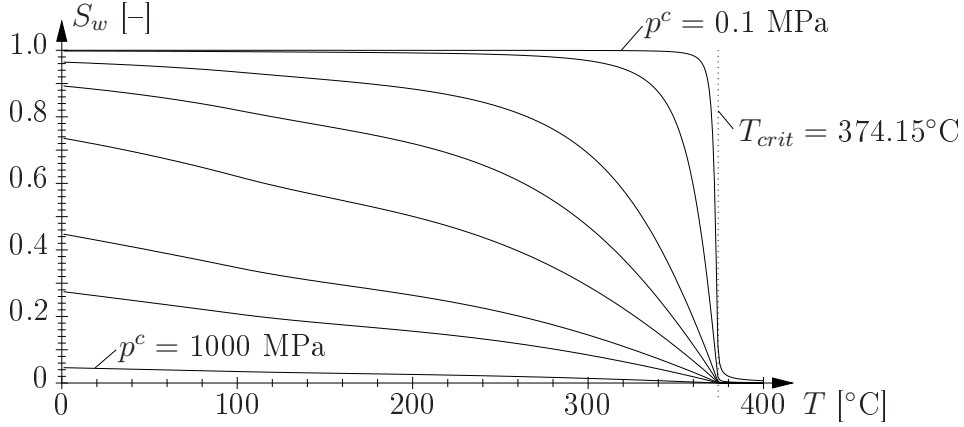
Figure 3.3: Degree of saturation versus temperature for different values for the capillary pressure $p^c = 0.1, 1, 5, 10, 20, 50, 100, 1000$ MPa according to Equation (3.7) [46, 90] (parameters: $p_b^c = 18.624$ MPa, $m = 0.44$, $B_s = 30$ MPa, $N_s = 1.2$, $Z_s = 0.5$ °C)

---

[5]The temperature-dependent parameters in Equation (3.7) are defined as

$$A_s = p_b^c \quad \text{for } T \le 100°C \text{ and}$$

$$A_s = B_s + (p_b^c - B_s) \left[2 \left(\frac{T - 100}{T_{crit} - 100} \right)^3 - 3 \left(\frac{T - 100}{T_{crit} - 100} \right)^2 + 1 \right] \quad \text{for } T > 100°C \text{ ,}$$

and

$$E_s = \left(\frac{T_{crit} - T_0}{T_{crit} - T} \right)^{N_s} \quad \text{for } T \le (T_{crit} - Z_s) \text{ and}$$

$$E_s = E_{s,0} \left[\frac{N_s}{Z_s} T + 1 - \frac{N_s}{Z_s} (T_{crit} - Z_s) \right] \quad \text{for } T > (T_{crit} - Z_s) \text{ ,}$$

with

$$E_{s,0} = \left(\frac{T_{crit} - T_0}{Z_s} \right)^{N_s} .$$

Hereby, B_s [Pa], N_s [–], and Z_s [°C] are constant parameters, with the latter governing the transition over the critical temperature $T_{crit} = 374.15$ °C.

3.4.3   Permeability of heated concrete

The dependence of the intrinsic permeability k_{int} [m^2] on temperature was derived from the experimental results presented in Subsection 2.2 [129, 132] (see Figure 3.4). As already indicated in Subsection 2.2, the absolute permeability k [m^2] (see Equations (3.1) to (3.4)) is – in case of (compressible) gas flow due to the so-called slip-flow phenomenon – dependent on the gas pressure, reading [64]

$$k = k_{int}\left(1 + \frac{b}{p^g}\right) , \qquad (3.8)$$

with b [Pa] as the slip-flow constant. Within the analyses, $b = 1{\cdot}10^5$ Pa is considered. In case of (incompressible) water flow, no slip-flow effect exists. Hence, $k = k_{int}$.

As regards the relative permeability of partially-saturated porous media, various models exist. In [15, 102], the relative permeability to water is given by [15, 41, 102]

$$k^{rw} = \left(\frac{S_w - S_w^r}{1 - S_w^r}\right)^{A_w} , \qquad (3.9)$$

where S_w^r [–] is the residual saturation (the porous medium cannot be dewatered further) and A_w [–] is a constant parameter. The relative permeability to gas is given by [15, 41, 122]

$$k^{rg} = 1 - \left(\frac{S_w}{S_w^{cr}}\right)^{A_g} , \qquad (3.10)$$
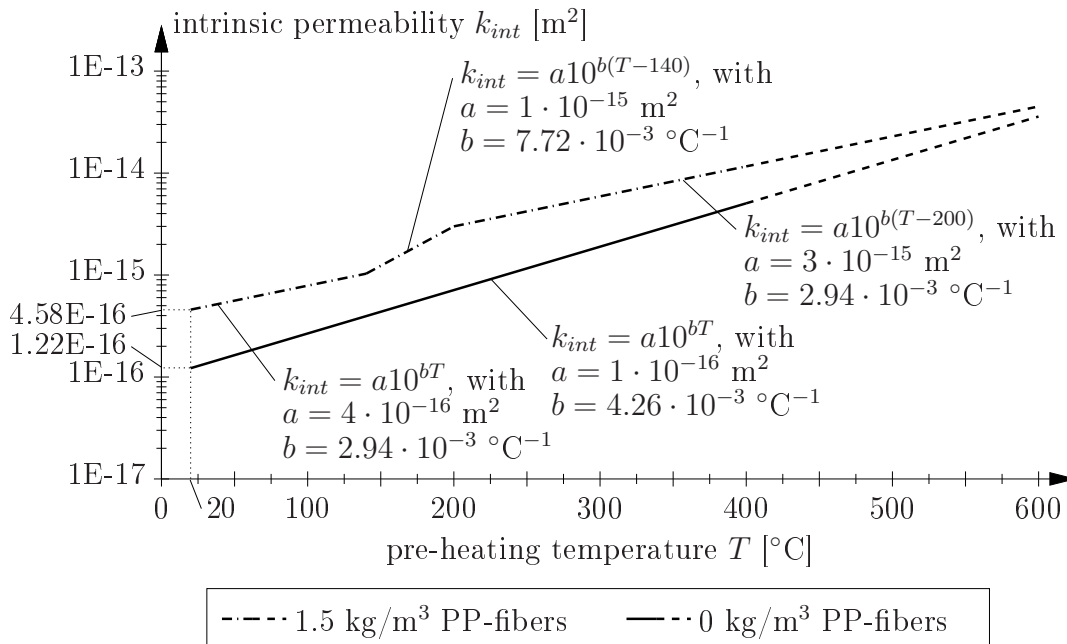
Figure 3.4: Approximation of experimental permeability results for in-situ concrete with 0 and 1.5 kg/m^3 PP-fibers (see Figure 2.44 and [129, 132])
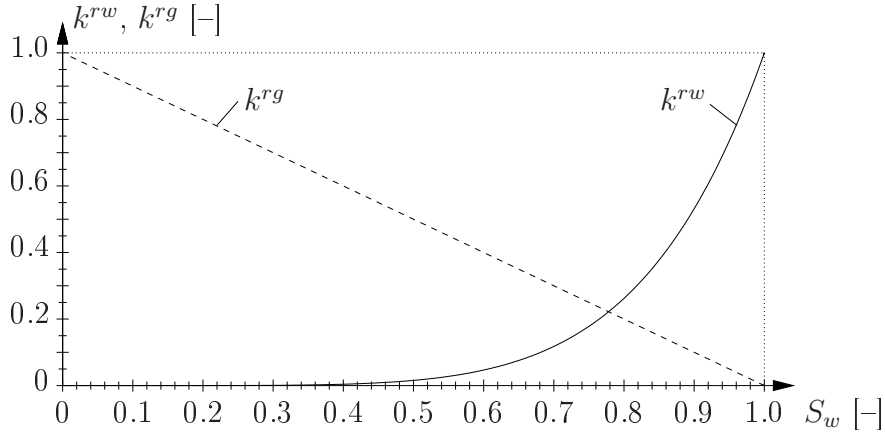
Figure 3.5: Relative permeabilities to water and gas as a function of satura-
tion [41]

where S_w^{cr} [–] is the critical saturation (above which no gas flow exists in the porous
medium) and A_g [–] is a constant parameter. Within the numerical analyses, $S_w^r = 0$,
$A_w = 6.0$, $S_w^{cr} = 1.0$, and $A_g = 1.0$ (see Figure 3.5).

3.5 Application

The presented coupled model is used to (i) re-analyze the fire experiments presented
in [67] (see Subsection 3.5.2) and (ii) investigate the performance of a cross-section of the
Lainzer tunnel (Austria) (see Subsection 3.5.3).

3.5.1 Initial and loading conditions

Within all analyses, the following initial conditions are employed: $T_0 = 20$ °C, $p_0^g =$
101325 Pa, $p_0^c = 55 \cdot 10^6$ Pa (giving, according to Equation (3.7), an initial degree of satu-
ration of $S_{w0} = 0.40$). The boundary conditions (BC) at the heated surface are: (i) direct
prescription of temperature $\overline{T}$ (see Figure 3.6), (ii) direct prescription of the atmospheric
pressure $p^{atm} = 101325$ Pa, and (iii) convective mass transfer (with prescribed vapor
pressure of the surroundings, $p_\infty^{gw} = 1020$ Pa, and a convective mass-transfer parameter
$\beta_c = 0.025$ m/s).

The history of the prescribed surface temperature $\overline{T}$ [°C] was extracted from large-scale fire
experiments [54, 55, 67, 84], characterized by exposure of the specimens to temperature
loading typical for tunnel fires (see Figure 3.6).
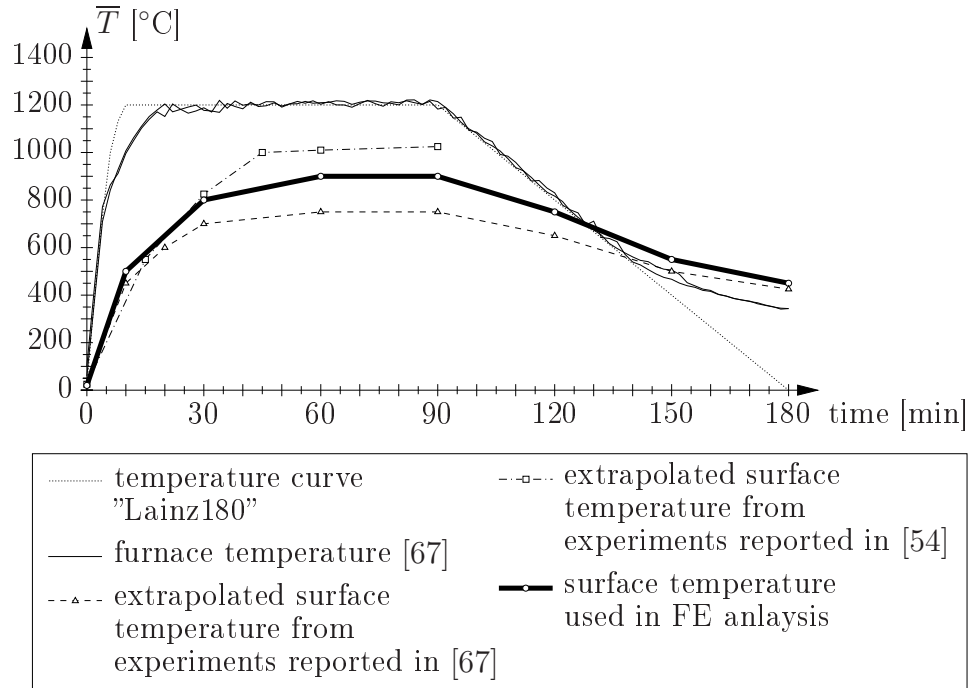
Figure 3.6: History of the surface temperature extracted from large-scale fire experiments [54, 67]

3.5.2 Re-analysis of results from large-scale fire experiments [67]

Figure 3.7 shows comparison of numerical results obtained from the analyses with experimental temperature measurements [67] after 30 minutes of fire loading (only the results for the first 20 cm of the 50 cm thick specimen are shown). Whereas the results from the thermal analysis (dash-dotted line in Figure 3.7, disregarding dehydration, vaporization
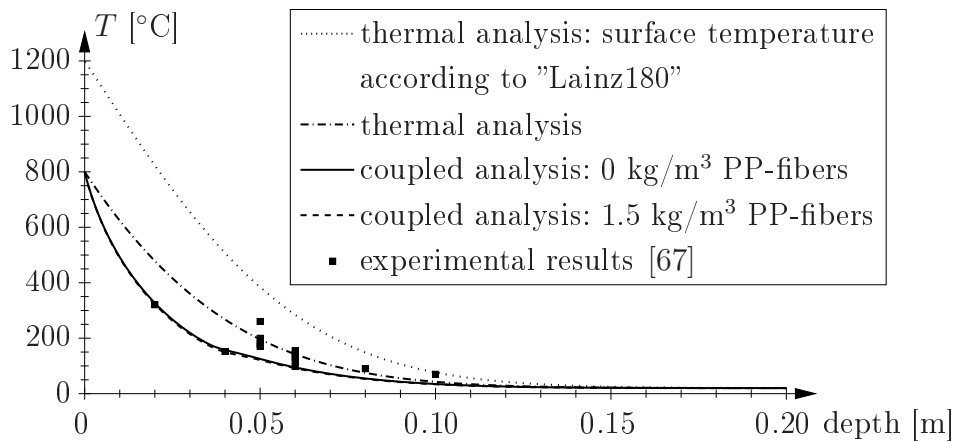
Figure 3.7: Comparison of temperature distributions at $t = 30$ min (PP-fibers are affecting the transport properties only. Hence, the amount of fibers has no effect on the results of the thermal analyses)

of evaporable water, and mass transport, see Appendix E.2) agree well with temperature measurements at depths of 5 and 6 cm, they overestimate the experimental results in 2 and 4 cm depth from the heated surface. The coupled analyses, on the other hand, give the best agreement with the experimental measurements in shallow regions. Moreover, they capture the curvature of the experimentally-observed temperature distributions. According to the numerical results, disregarding dehydration, vaporization of evaporable water, and mass transport results in an overestimation of the temperatures of up to 80% (see Figure 3.8, the differences in temperatures are up to 156 °C). The larger impact, however, had the prescription of the surface temperature: Figure 3.8 shows that prescribing the furnace temperature (referred to as "Lainz180", see Figure 3.6) directly at the heated surface results in an overestimation of the temperatures of up to 240% (dotted line in Figure 3.8, temperature differences are up to 520 °C). Comparison of the results from the coupled analyses reflects the increased mass transport in concrete with 1.5 kg/m^3 PP-fibers, resulting in increased cooling of shallow regions (with, however, rather small deviations of up to 8 °C or, equivalently, up to 5%).

In addition to temperature distributions given in Figure 3.7, the coupled analyses provide also access to gas pressure and saturation distributions within the concrete block. The latter are depicted in Figure 3.9 (again, only the results for the first 20 cm of the 50 cm thick specimen are shown). Whereas the saturation exceeds the initial value of 0.40 in case of concrete without PP-fibers, indicating the formation of a moisture clog, the
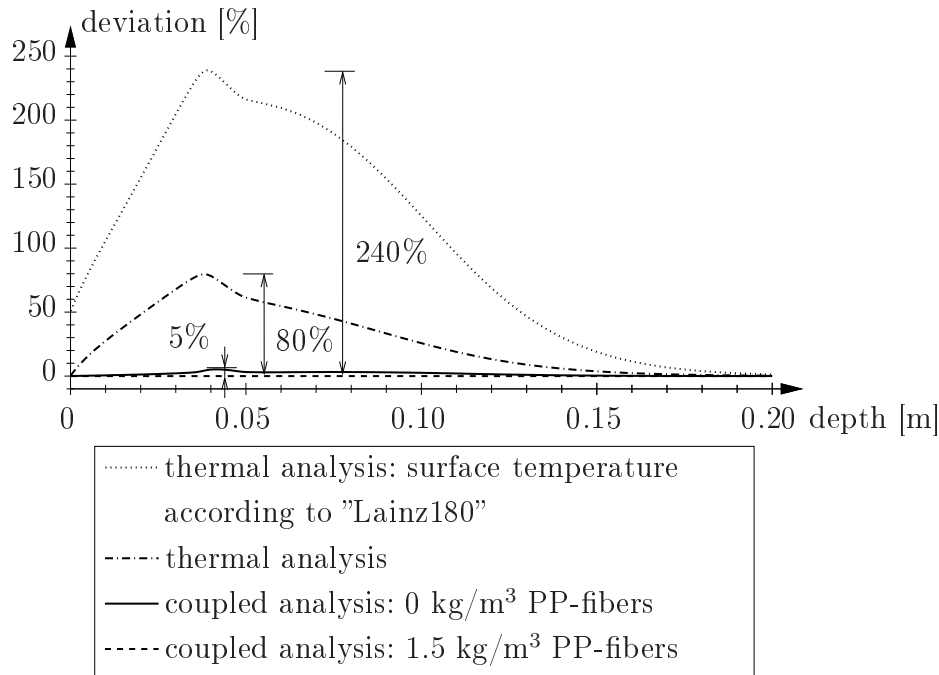
Figure 3.8: Deviation between numerically-obtained temperature distributions at $t = 30$ min (temperature distribution obtained from the coupled analysis of concrete with 1.5 kg/m^3 PP-fibers is used as reference)
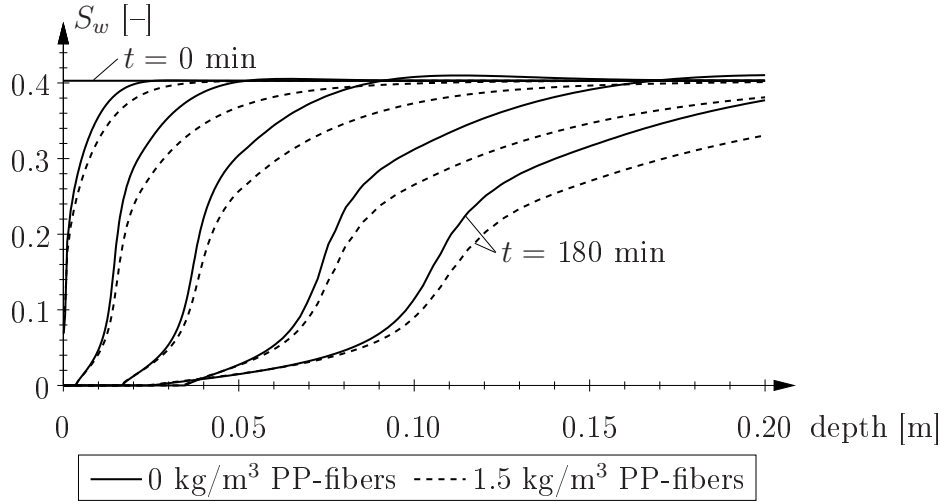
Figure 3.9: Saturation distributions for concrete with 0 and 1.5 kg/m^3 PP-fibers (results for $t = 0$, 2, 10, 30, 90, 180 min)
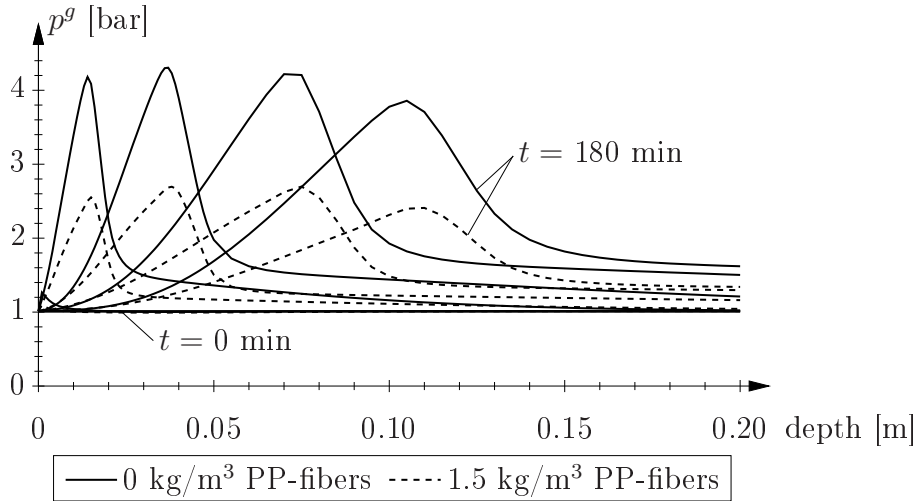
Figure 3.10: Gas-pressure distributions for concrete with 0 and 1.5 kg/m^3 PP-fibers (results for $t = 0$, 2, 10, 30, 90, 180 min)

permeability is sufficient to avoid this phenomenon in case of fiber-reinforced concrete. This different behavior regarding mass transport affects also the pressure distribution within the concrete block (see Figure 3.10). The smaller permeability of concrete with 0 kg/m^3 PP-fibers results in a pressure rise of 3.3 bar above atmospheric pressure, which is almost twice as large as in case of concrete with 1.5 kg/m^3 PP-fibers, where the gas pressure exceeds the atmospheric pressure by about 1.7 bar. This indicates an increased spalling risk of concrete without PP-fibers [132], which is in agreement with observations during fire experiments presented in [54, 67].

3.5.3   Analysis of cross-section of Lainzer tunnel (Austria)

The investigated cross-section is depicted in Figure 3.11. The plastic mat (made of a layer of polyethylene laminated to a polypropylene mat) was installed prior to casting of the tunnel lining in order to ensure unrestrained movement of the tunnel lining along the shotcrete shell. During fire loading, this mat may act as an impermeable layer to water and vapor. On the other hand, gaps between the shotcrete shell and the concrete tunnel lining may allow the water and vapor to expand in the circumferential and/or longitudinal direction. In the numerical analysis, these two limiting cases are considered by prescribing the respective boundary conditions at the outside of the tunnel lining, i.e., (i) sealed and (ii) unsealed conditions.
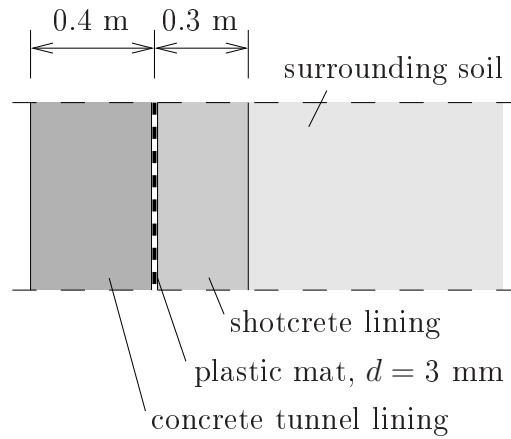
Figure 3.11: Cross-section of the considered tunnel lining of the Lainzer tunnel (Austria)

Within the analyses, the influence of spalling is investigated by prescribing different spalling scenarios (see Figure 3.12) which were derived from the fire experiments presented in [67] (spalling was monitored acoustically as well as by means of dynamic acceleration sensors). Three analyses were performed (see Table 3.2), characterized by temperature distributions obtained from different analysis schemes (uncoupled analysis, see Appendix E.2 and, e.g., [128, 130], or coupled analysis, see Subsection 3.2). The uncoupled as well as the coupled analyses give access to temperature distributions for the

Table 3.2: Analyses performed

Analysis	Temperature distribution obtained from . . .
A	Uncoupled thermal analysis
B	Uncoupled analysis incl. heat sinks
C	Coupled analysis
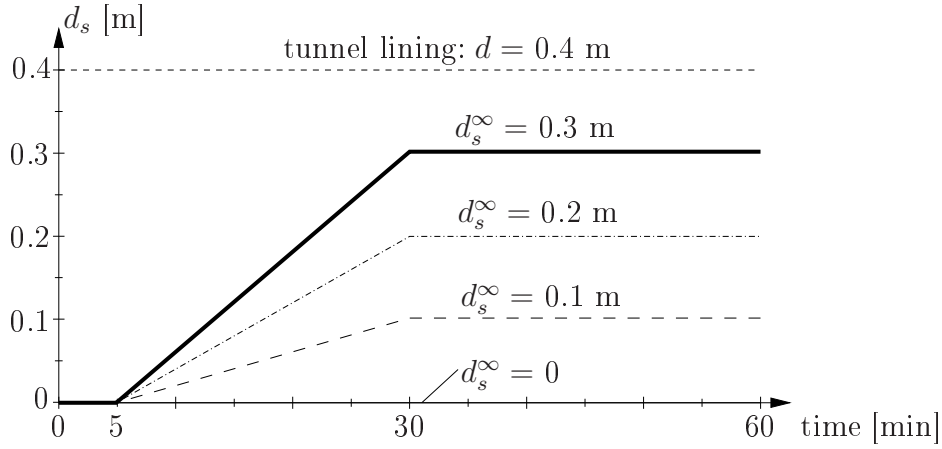
Figure 3.12: Considered spalling scenarios (derived from experimental observations/data [67])

considered spalling scenarios (see Figure 3.13 for $d_s^\infty = 0.2$ m). Spalling results in a faster propagation of the heating front and, therefore, in an increased thermal loading of the remaining tunnel lining, finally giving higher thermal degradation of the cross-section as compared to the analysis with $d_s^\infty = 0$. Comparison of different analyses (Analyses A, B, and C) shows that consideration of heat sinks within the uncoupled analysis (Analysis B) results in lower temperatures compared to the uncoupled thermal analysis (Analysis A). Furthermore, consideration of mass transport within the concrete structure results in cooling of shallow regions, leading to a further decrease of the temperature. In addition, consideration of mass transport results in heating (to a smaller extent) of deeper concrete regions, indicated by a kink in the distribution obtained from Analysis C. Comparison of numerical results with temperature measurements has shown that, even though the prescribed surface temperature follows the experimental temperature history in case of the uncoupled as well as the coupled analysis, the coupled analysis gives more realistic temperature distributions (see Subsection 3.5.2 and [132]).

In contrast to numerical results from the uncoupled analyses (Analyses A and B), the coupled analysis (Analysis C) gives information on quantities related to mass transport. Figure 3.14 shows gas-pressure distributions for a final spalling depth of $d_s^\infty = 0.2$ m. Hereby, the plastic mat located between tunnel lining and shotcrete shell (see Figure 3.11) is considered either as impermeable layer for water and vapor transport or not (sealed and unsealed conditions, respectively), representing the upper and lower limit, respectively, for the gas pressure. The maximum pressure is apparently not (or only little) affected by the plastic mat at the outer surface of the tunnel lining. The pressure distribution between the location of the maximum pressure and the outer surface, however, varies significantly for $t \geq 30$ min, where the gas pressure at the outer surface rises in case the plastic mat is considered as impermeable layer since water and vapor are hindered from escaping at that interface. In case the plastic mat is disregarded, the gas pressure at the interface

between tunnel lining and shotcrete shell remains equal to the atmospheric pressure.
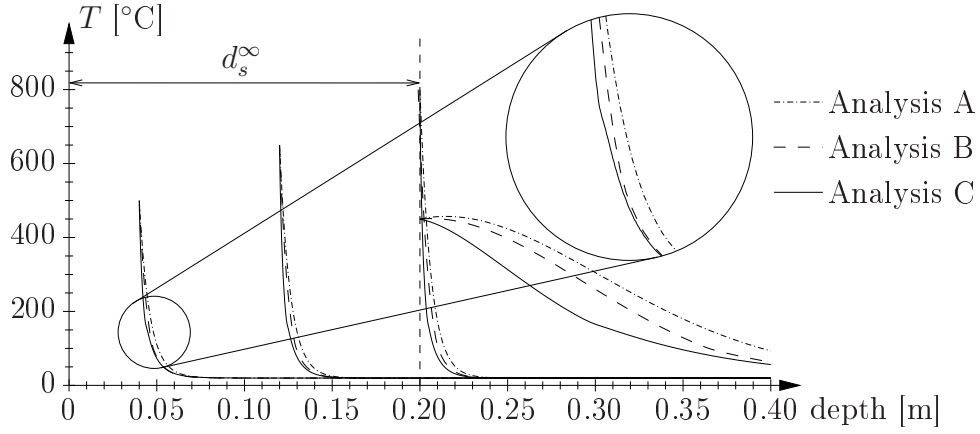
Figure 3.13: Temperature distributions for different analyses ($d_s^\infty = 0.2$ m, $t = 10, 20, 30, 180$ min)
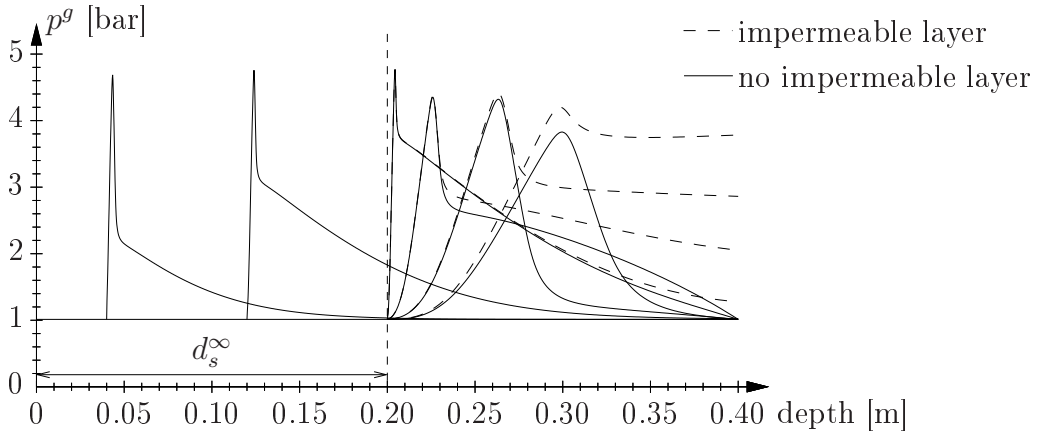
Figure 3.14: Gas-pressure distributions obtained from Analysis C with or without consideration of impermeable layer ($d_s^\infty = 0.2$ m, $t = 0, 10, 20, 30, 40, 90, 180$ min)

Chapter **4**

Structural safety assessment of tunnel linings under fire

4.1 Structural model

The numerical model that is used to analyze tunnel structures mainly depends on the type of the surrounding soil and the depth of the tunnel [31]. E.g., in case of tunnels with high overburden and/or in hard/medium-hard rock or highly cohesive soil, pre-deformations during excavation result in stress release within the surrounding soil, hence, the soil pressure acting on the tunnel structure is reduced. The load-carrying capacity of the surrounding soil is taken into account by plane-strain and 3D-finite element models. In case of tunnels with low overburden and/or in soft soil (which are subject of this work), the load-carrying capacity of the surrounding soil is neglected and the full overburden is considered as load. Hereby, the tunnel lining is discretized either by finite elements or by using a "beam-spring" model [127]. During fire loading, the soil loads the weakening tunnel support structure which can cause its collapse.

Within the structural analysis, temperature loading can be considered by (i) direct implementation of the non-linear temperature distributions as well as consideration of plasticity of the lining material (see, e.g., [3, 33, 93, 101, 113]) or (ii) prescribing a linear temperature distribution (T_m and ΔT, equivalent to the non-linear temperature distribution, see Chapter 1 and, e.g., [98, 126]).

Within the employed "beam-spring" model [101], the tunnel lining is represented by layered finite beam elements (see Figure 4.1(a)). The layer concept enables (i) consideration of spalling of the tunnel lining by deactivation of the respective layers and (ii) assignment of temperature-dependent material parameters of concrete and reinforcement steel to the

remaining layers. The beam elements are supported at the nodes by spring elements (see Figure 4.1(b)). The stiffness $\bar{K}$ [N/m] of these springs is related to the specific subarea of the tunnel wall associated to the node, the Young's modulus E [MPa] of the surrounding soil, and its Poisson's ratio ν [–] (for details, see [101]). In order to account for the zero load-carrying capacity of the soil under tensile loading, the stiffness of the spring elements is only activated when the spring is subjected to compressive loading. In case of tensile loading, $\bar{K}$ is set equal to zero. This enables for a realistic description of the behavior of the surrounding soil in case of low overburden and soft soil. The external load of the surrounding soil is applied at the FE nodes.

<div align="center">(a)   (b)</div>
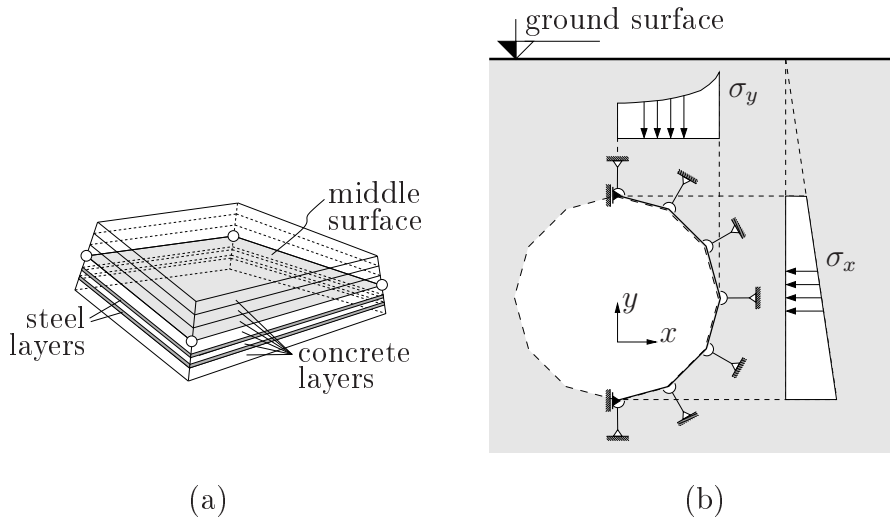
Figure 4.1: Illustration of (a) layered finite beam element (containing concrete and steel layers) and (b) beam-spring model [101]

The mechanical behavior of concrete and steel is modeled by plane-stress elasto-plastic material models[1]. In case of concrete, a multi-surface plasticity model is used, with the Drucker-Prager and the Rankine criterion describing compressive and tensile failure, respectively (for details, see [101]). For description of the mechanical behavior of steel, a 1D model is used, referring to the strain component in the direction of the steel bars. In both cases, associative hardening plasticity is employed. Details on the employed failure criteria, the hardening laws and the temperature dependence of the material parameters can be found in [101]. The temperature dependence of strength and Young's moduli of concrete and steel are described by design curves according to international or national standards [22, 87], giving, e.g., the compressive strength of concrete as

$$f_c(T) = f_c \times \alpha(T), \tag{4.1}$$

where $\alpha(T)$ [–] is a temperature-dependent coefficient, with $0 \leq \alpha(T) \leq 1$. Hereby, the reduction factor $\alpha(T)$ is correlated with the maximum temperature reached in a cer-

---

[1]Because of the rather small thickness of the tunnel lining compared to the radius of the tunnel, the normal stress component perpendicular to the lining surface is set equal to zero.
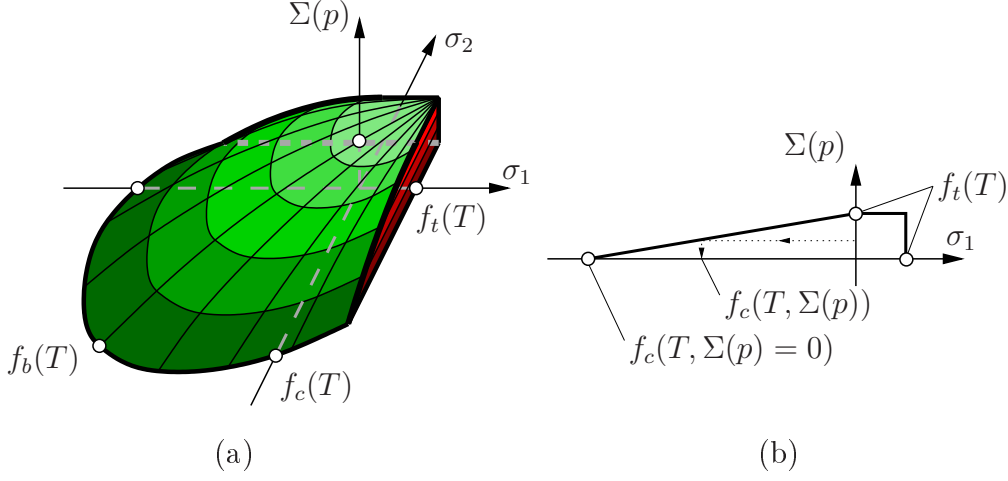
Figure 4.2: (a) Consideration of out-of-plane tensile stress $\Sigma(p)$ within Drucker-Prager failure criterion for concrete, (b) linear decrease of f_c with increasing out-of-plane loading

tain point of the structure during fire loading, hence, $f_c(T) = f_c(T_{max})$. In contrast to the safety-assessment tool presented in [101], tensile loading in the out-of-plane direction resulting from gas pressure within the pore space is considered within the plane-stress elasto-plastic material model for concrete (see Figure 4.2). Taking into account the mainly biaxial compressive state of loading of the tunnel lining close to the heated surface, the effect of the out-of-plane loading by the gas pressure on the strength properties is considered by

$$f_c(T, p) = f_c \times \alpha(T) \times \left(1 - \frac{\Sigma(p)}{f_t(T)} \right) , \tag{4.2}$$

where $\Sigma(p)$ [MPa] is the macroscopic tensile stress perpendicular to the heated surface, representing the overpressure $p = p^g - p^{atm}$ [MPa] acting on the porous network, and $f_t(T)$ [MPa] is the temperature-dependent tensile strength of concrete (see, e.g., [22, 87]). The macroscopic tensile stress $\Sigma(p)$ is related to p by the continuum-micromechanics approach outlined in [23], giving

$$\Sigma(p) = f_g \, p \, \langle A \rangle_p , \tag{4.3}$$

where $f_g = (1 - S_w)n$ [–] is the volume fraction of the gas phase subjected to pressure p [MPa] (with S_w [–] as the liquid saturation and n [–] as the porosity). $\langle A \rangle_p$ [–] represents the so-called localization tensor, reading for the case of spherical inclusions

$$\langle A \rangle_p = \left[(1 - S) \sum_r \frac{f_r}{1 + S \dfrac{k_r - k_m}{k_m}} \right]^{-1} , \tag{4.4}$$

where f_r [–] and k_r [MPa] are the volume fraction and the bulk modulus of the r-th phase, respectively, with $r \in \{m \ldots$ cement matrix, $a \ldots$ aggregates, $l \ldots$ liquid phase, $g \ldots$ gas

phase}. In Equation (4.4), S [–] represents the Eshelby tensor specialized for spherical inclusions, with $S = 1/3\,(1 + \nu_m)/(1 - \nu_m)$, where ν_m [–] denotes Poisson's ratio of the cement matrix.

4.2   Application

The structural safety assessment tool for tunnels subjected to fire loading is used to investigate the performance of a cross-section of the Lainzer tunnel (Austria) (see Figure 4.3 for the geometry). The mechanical parameters of concrete and reinforcing steel used within the structural analysis are listed in Table 4.1. The applied mechanical loading consists of (i) self-weight of the lining, with $\rho = 2500$ kg/m³, and (ii) soil pressure according to the geological situation at the considered cross-section of the tunnel, acting in both vertical and horizontal direction (see [101] for details).

In order to investigate the influence of spalling on the results from the structural analyses, the same spalling scenarios as in Chapter 3 (see Figure 3.12) were considered. Three analyses were performed (see Table 4.2), characterized by temperature distributions obtained from different analysis schemes (uncoupled analysis, see Appendix E.2 and, e.g., [128, 130], or coupled analysis, see Subsection 3.2) and by disregard/consideration of the effect of the gas pressure on the compressive strength of concrete (see Figure 4.2).

Within the structural analysis, the tunnel safety is monitored by the vertical displacement at the top of the tunnel as well as the level of loading of the circumferential reinforce-
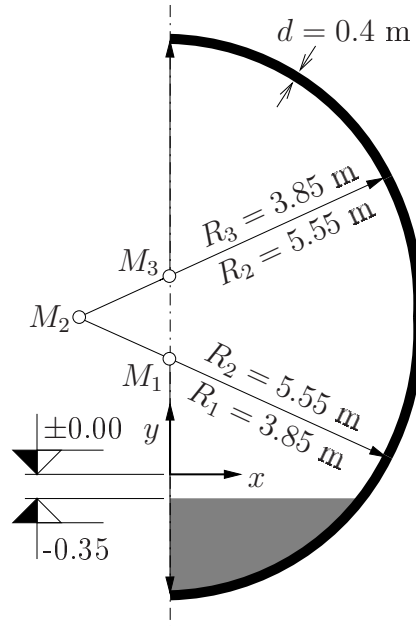
Figure 4.3: Dimensions of the considered cross-section of the Lainzer tunnel (Austria)

Table 4.1: Properties of lining concrete and reinforcement for the structural safety assessment

Input parameter	Value
Concrete:	
Young's modulus E [MPa]	30000
Poisson's ratio ν [$-$]	0.2
Compressive strength f_c [MPa]	30
Tensile strength f_t [MPa]	3
Thermal expansion coefficient α_T [$°C^{-1}$]	$1·10^{-5}$
Reinforcing steel:	
Young's modulus E [MPa]	210000
Yield strength f_y [MPa]	500
Thermal expansion coefficient α_T [$°C^{-1}$]	$1.2·10^{-5}$

Table 4.2: Analyses performed

Analysis	Temperature distribution obtained from ...	Compressive strength of concrete
A	Uncoupled thermal analysis	$f_c = f_c(T)$, see Equation (4.1)
B	Uncoupled analysis incl. heat sinks	$f_c = f_c(T)$, see Equation (4.1)
C	Coupled analysis	$f_c = f_c(T, p)$, see Equation (4.2)

ment. Figure 4.4 shows the vertical displacement v [cm] at the top of the tunnel for different spalling scenarios (see Figure 3.12). Hereby, the vertical displacement due to self weight of the tunnel lining and soil pressure is indicated by v_0. For $d_s^\infty = 0$, v increases gradually until $t = 52$ min resulting from the heat-induced decrease of strength and stiff-
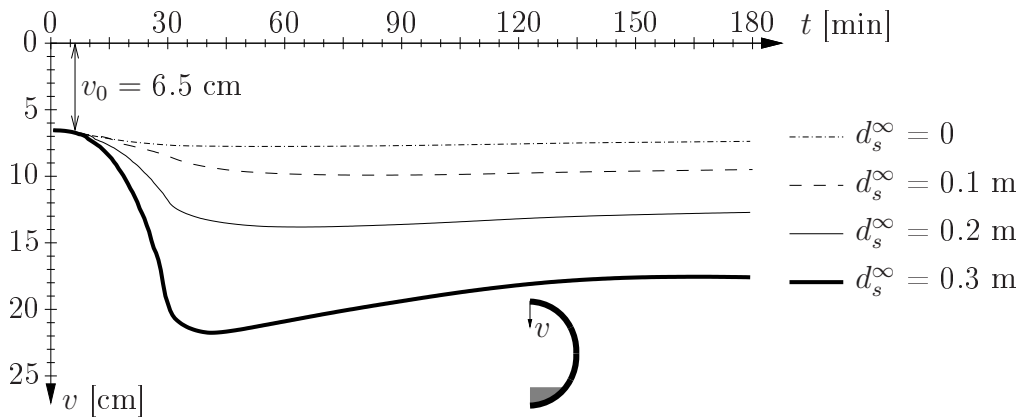
Figure 4.4: History of vertical displacement at top of tunnel obtained from Analysis C considering different spalling scenarios (vertical displacement due to self weight and soil pressure: $v_0 = 6.5$ cm)
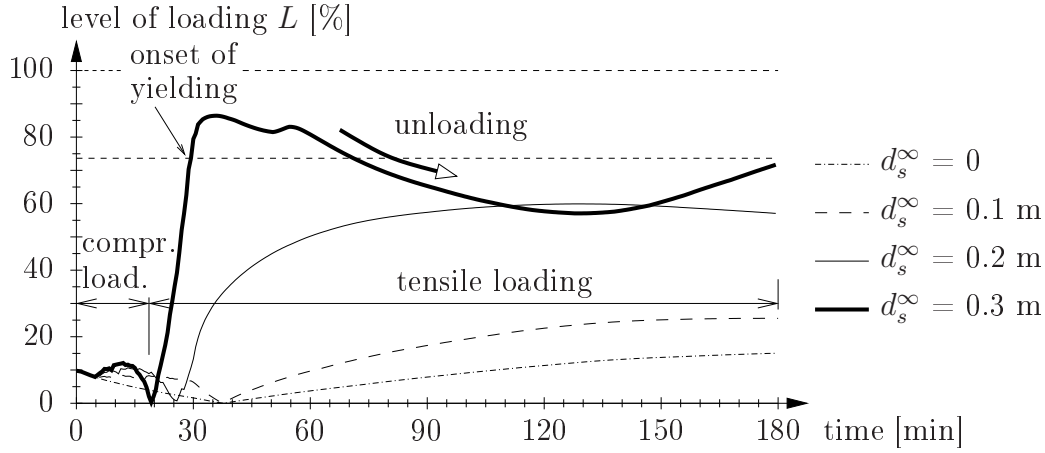
Figure 4.5: History of level of loading of the outer circumferential reinforcement at top of tunnel obtained from Analysis C considering different spalling scenarios

ness of the lining materials, i.e., concrete and steel. With continuation of temperature loading, thermal dilation associated with the continuous heating of the lining results in partial compensation of the temperature-induced displacement. According to Figure 4.4, an increasing spalling depth results in an increased compliance of the tunnel structure. During spalling, v increases rapidly, with the maximum displacement observed after the final spalling depth d_s^∞ is reached. With continuation of temperature loading, again parts of the displacement are compensated by thermal dilation of the remaining lining. In no case, collapse of the tunnel is observed, which would be indicated by a sharp increase of v.

Figure 4.5 shows the level of loading in the outer circumferential reinforcement at the top of the tunnel, defined as [101]

$$L = \frac{|\sigma|}{\max\{\zeta_{RF}(T)\}} = \frac{|\sigma|}{1.1\, f_y(T)} \ , \tag{4.5}$$

where σ [MPa] is the actual stress in the reinforcement and f_y [MPa] is the yield strength of the reinforcing steel. Hereby, concrete cracking is modeled by the smeared-crack approach. L equals zero in case of unloaded reinforcement and amounts to 100% when the stress in the reinforcement reaches the maximum possible loading, given by $1.1 f_y(T)$ [101]. Application of self weight and soil pressure on the tunnel structure results in compressive loading of the outer reinforcement due to bending with $L \approx 10\%$. During temperature loading, thermal dilation results in compressive stresses at the heated surface and, therefore in tensile loading of the outer reinforcement, leading to a reduction of the compressive loading and, thus, of the level of loading. When the loading of the reinforcement changes to tensile loading, L increases again. With increasing spalling depth, this shift from compressive to tensile loading occurs earlier in time. Yielding of the reinforcement (starting at $L = 73.6\%$ [101]) is observed for the analysis with $d_s^\infty = 0.3$ m. As opposed to the other spalling scenarios, unloading of the outer reinforcement is observed after $t = 36$ min in case

of $d_s^\infty = 0.3$ m, which corresponds to the time instant at which the maximum displacement is reached (see Figure 4.4). This unloading is associated with thermal dilation (causing compensation of parts of the vertical displacement), resulting in compressive stresses close to the heated surface and tensile stresses at the outside. In case of $d_s^\infty = 0.3$ m, the outer reinforcement is located closer to the middle surface of the remaining lining after spalling has finished compared to the other considered spalling scenarios, explaining the observed unloading of the reinforcement. As temperature loading continues, L increases in consequence of the continuous reduction of $f_y(T)$ (see Equation (4.5)). Until the end of fire loading, however, no further yielding is observed for $d_s^\infty = 0.3$ m. For all spalling scenarios (see Figure 3.12) and considering the fire loading depicted in Figure 3.6, the level of loading never reached 100%, indicating some remaining load-carrying capacity.
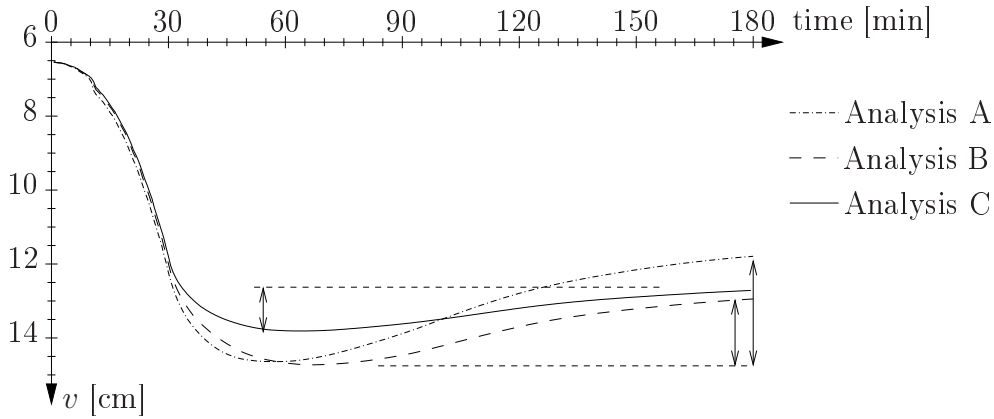
Figure 4.6: History of vertical displacement at top of tunnel for $d_s^\infty = 0.2$ m (Analyses A to C)

The results obtained from Analyses A to C are compared in Figures 4.6 and 4.7, showing little difference until the end of spalling. Thereafter, the higher temperatures within the tunnel lining in case of Analyses A and B result in more thermal degradation of the cross section and, therefore, in larger displacements (see Figure 4.6). The lower (more realistic) temperature loading considered in Analysis C leads to smaller maximum displacements. With continuation of fire loading, the compensation of displacement by the continuous heating of the remaining part of the lining is the highest for Analysis A. As regards the level of loading L (see Figure 4.7), yielding of the outer circumferential reinforcement is observed only for Analyses A and B. As the temperature loading continues, L decreases and plastic loading of the reinforcement, characterized by $L > 73.6\%$, stops. For Analysis C, the lower temperature loading results in $L < 73.6\%$, hence, no yielding of the reinforcement is observed.
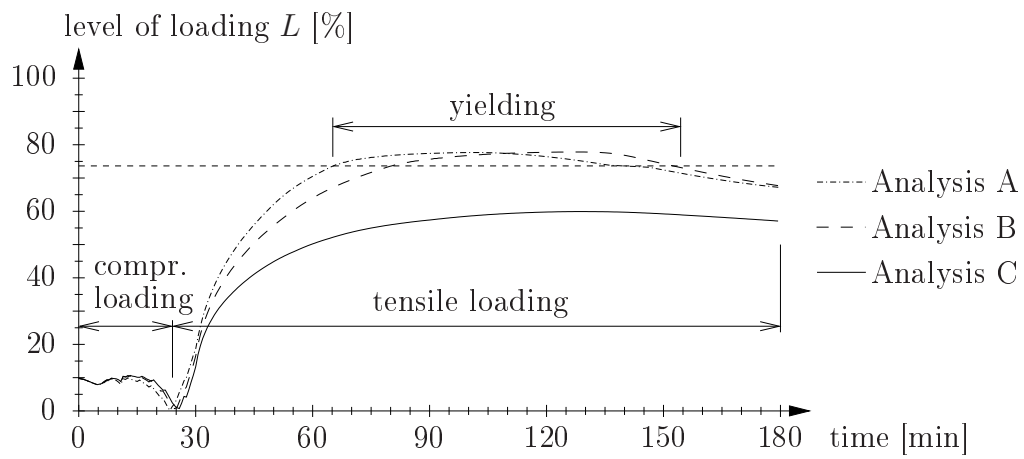
Figure 4.7: History of level of loading of the outer circumferential reinforcement at top of tunnel for $d_s^\infty = 0.2$ m (Analyses A to C)

Chapter **5**

Concluding remarks

5.1 Conclusions

Tunnel fire accidents in the 1990s as well as observations during fire experiments represented the starting point for the research presented in this thesis. The impact of fire loading on concrete used for tunnel linings was investigated by experimental work and numerical simulations. Hereby, the following tasks were tackled:

1. *Experimental investigation of spalling mechanisms and transport parameters of heated concrete:*
   Within the presented spalling experiments, different types of spalling with different piece velocities were observed, ranging from (i) explosive spalling with velocities of up to 14 m/s and (ii) progressive spalling with smaller velocities to (iii) fall-off of concrete pieces with the gravity as the only source of acceleration. In general, volume (mass) and velocity of the spalled-off pieces were inversely-proportional. Based on the experimental observations and considering both thermo-hydral and thermo-mechanical processes to be responsible for spalling, the velocities and kinetic energies associated with these processes were estimated by means of simplified models, giving good agreement between the model-based results and experimental piece velocities for typical values of the vapor pressure right before spalling and concrete temperature. Furthermore, the model-based results gave insight into the influence of various parameters and their individual contribution to the kinetic energy. As the permeability was identified as one of the main parameters responsible for spalling (agreeing with earlier-reported experimental observations), identification of the permeability parameters (intrinsic permeability and slip-flow constant) of pre-heated

in-situ and *laboratory-cast* concrete with and without polypropylene (PP) fibers was performed, employing (i) constant pressure experiments (stationary conditions) and (ii) decreasing pressure experiments (transient conditions). The obtained results were related to temperature-dependent changes of the pore structure of heated concrete, revealing:

- For low temperatures, a difference between concrete with and without PP-fibers was observed in case of in-situ concrete, whereas similar permeability parameters were observed for laboratory-cast concrete. While the values for the total pore volume, which showed no distinct difference between concrete with and without PP-fibers, could not explain the observed difference, the pore volume within pore radii of $1 \leq r \leq 100 \ \mu$m was considerably larger (twice as large) for concrete with PP-fibers compared to concrete without fibers. Since this pore-size range corresponds to the thickness of interfacial transition zones (ITZ), the PP-fibers apparently introduce additional ITZ, resulting in a higher permeability for fiber-reinforced concrete. This effect is amplified for the considered in-situ concrete. On-site conditions, characterized by the reduced workability and the lower effect of densification in case of PP-fiber reinforced concrete, seem to influence the pore structure of in-situ concrete and/or the characteristics of the ITZ.

- The permeability jump in case of concrete including PP-fibers was observed at the melting temperature of polypropylene for in-situ as well as laboratory-cast concrete. In case of the tested in-situ concrete, the effect of melting of PP-fibers had equal impact as the difference in the low-temperature permeability. This permeability increase may be explained by (i) melting of polypropylene followed by its partial absorption by the surrounding cement matrix providing additional pore space and (ii) a different microcracking behavior of concrete with PP-fibers with the fibers acting as discontinuities and/or introducing additional microcracks in consequence of expansion of polypropylene during melting. The investigation of the pore-size distributions of concrete with and without fibers revealed the development of pores with radii within $6 \leq r \leq 10 \ \mu$m, which supported the theory of increased permeability in consequence of melting of the PP-fibers ($\o \approx 18 \ \mu$m) at $T \approx 170$ °C.

2. *Numerical simulation of governing transport processes in heated concrete:*
   Finite-element (FE) analyses with different grade of complexity were performed, leading to the following conclusions:

   - Temperature measurements from large-scale fire experiments [67] were compared to numerical results from different FE analyses. In general, the agreement between numerical and experimental results improved with increasing grade of complexity of the simulation. Disregard of mass transport in the anal-

ysis (uncoupled analysis) resulted in an overestimation of the experimentally-obtained temperatures in regions close to the heated surface. Consideration of mass transport within the coupled analysis led to lower thermal loading of the tunnel lining and, therefore, to less thermal degradation of the cross-section.

- The mode of prescribing the surface temperature had considerable impact on the numerical temperature distributions within the concrete member. Prescribing the furnace temperature applied within the experiments directly at the heated surface resulted in large overestimation of the experimental results, whereas prescription of the experimentally-obtained surface temperature at the heated surface led to numerical results with better agreement with the experimentally-obtained temperatures.

- Comparing the gas-pressure distributions for concrete with and without PP-fibers indicates that the lower (experimentally-observed) permeability in case of concrete without PP-fibers results in sufficiently higher gas pressures and an increase of the saturation (exceeding the initial value), indicating the formation of a moisture clog. Therefore, concrete without PP-fibers exhibits an increased spalling risk which is in agreement with observations during fire experiments presented in [54, 67].

- Investigation of different spalling scenarios within the analyses showed that thermal loading and, therefore, thermal degradation of the remaining lining is higher for increasing spalling depths which further increases the compliance of the tunnel, eventually causing collapse of the structure.

3. *Structural safety assessment of tunnel linings subjected to fire loading:*
   For determination of the structural response of tunnel linings under fire loading, a "beam-spring" model was employed, using the previously-determined temperature and gas pressure as input data. The analysis tool was used to investigate the structural performance of a tunnel cross-section characterized by low overburden (Lainzer tunnel, Austria) subjected to fire loading and different spalling scenarios, showing:

   - With increasing spalling depth, the compliance of the tunnel structure as well as the level of loading in the outer circumferential reinforcement increased. This resulted in increased vertical displacement at the top of the tunnel with increasing spalling depth.

   - The different analyses showed that the lower (and more realistic) temperature distributions obtained from the coupled analyses led to a smaller compliance of the tunnel structure and, therefore, to smaller displacements. With continuation of temperature loading, on the other hand, the lower thermal loading yielded less compensation of vertical displacement due to thermal dilation.

- None of the considered spalling scenarios led to collapse of the tunnel structure for the considered temperature loading, even though a reduction of the lining thickness by 75% due to spalling was considered. In case no collapse of the tunnel is indicated by the numerical analysis, the results allow:

  (a) estimation of the safety level of the tunnel structure during as well as after fire loading, which is important for rescue forces as well as the engineer or the tunnel owner, and

  (b) determination of the necessary amount of repair measures (e.g., lining thickness that has to be replaced), leading to an estimation of the repair time and costs after a tunnel fire.

5.2   Ongoing research and outlook on future work

Based on the observations made during experimental as well as theoretical work, the following items were identified as areas with need for further research work, part of which is currently under way:

- *Multiscale material modeling:*
  The observed differences in permeability are considered to originate from temperature-dependent changes of the material microstructure (e.g., introduction of additional ITZ by PP-fibers and the corresponding percolation threshold, different microcracking behavior of concrete containing fibers). Future work will be devoted to linking macroscopic transport properties to the material microstructure. This link will be established by appropriate upscaling/homogenization techniques within the multiscale framework of material description.

- *Modeling of restrained thermal dilation of concrete:*
  In the past, the behavior of concrete under combined thermal and mechanical loading was modeled by introducing the so-called "load-induced thermal strain (LITS)" (see, e.g., [44, 83, 107, 119, 120]). In Appendix F, a two-phase model is presented, consisting of aggregates embedded in a cement-paste matrix, explaining this behavior by means of micromechanics. This approach is currently extended towards more realistic morphologies (consideration of distributed aggregate diameters) and the influence of interface properties.

- *Extension of structural safety assessment tool:*
  Within the structural model employed in this thesis, a tunnel of 1 m length was considered. The extension of this model towards the longitudinal direction of the tunnel will allow consideration of 3D structural effects and the varying temperature loading. Moreover, the gas pressure determined from the coupled analysis shall be combined with the actual stress state in the lining, enabling determination of the

spalling history as a function of gas-pressure, state of loading, and temperature distribution, finally linking the yet-separated parts of the two-step analysis scheme for the safety assessment of structures subjected to fire load (Chapters 3 and 4).

Bibliography

[1] G. N. Ahmed and J. P. Hurst. An analytical approach for investigating the causes of spalling of high-strength concrete at elevated temperatures. In L. T. Phan, N. J. Carino, D. Duthinh, and E. Garboczi, editors, *Proceedings of the International Workshop on Fire Performance of High-Strength Concrete*, pages 95–108. NIST, Gaithersburg, Maryland, 1997.

[2] G. N. Ahmed and J. P. Hurst. Coupled heat and mass transport phenomena in siliceous aggregate concrete slabs subjected to fire. *Fire and Materials*, 21(4):161–168, 1997.

[3] K. A. M. Ahmed. *Numerical modelling of tunnel lining at high temperature using sandwich element*. PhD thesis, University of Innsbruck, Innsbruck, Austria, 2004.

[4] Y. Anderberg. Spalling phenomena in HPC and OC. In L. T. Phan, N. J. Carino, D. Duthinh, and E. Garboczi, editors, *Proceedings of the International Workshop on Fire Performance of High-Strength Concrete*, pages 69–73. NIST, Gaithersburg, Maryland, 1997.

[5] Y. Anderberg and S. Thelandersson. Stress and deformation characteristics of concrete at high temperatures: 2. experimental investigation and material behaviour model. Technical Report 54, Lund Institute of Technology, Lund, 1976.

[6] C. W. Baierl. Betonplatten für den Gleiskörper von Eisenbahntunnel – Brandversuche [Concrete slabs for the railroad embankment of tunnels – Fire experiments]. Master's thesis, Vienna University of Technology, Vienna, Austria, 2008. In German.

[7] P. B. Bamforth. The relationship between permeability coefficients for concrete obtained using liquid and gas. *Magazine of Concrete Research*, 39(138):3–11, 1987.

[8] P. F. Bamonte and R. Felicetti. On the tensile behavior of thermally-damaged concrete. In A. Carpinteri, P. Gambarova, G. Ferro, and G. Plizzari, editors, *Proceedings of the 6th International Conference on Fracture Mechanics of Concrete and Concrete Structures*, pages 1715–1722. Taylor & Francis, London, UK, 2007.

[9] V. Baroghel-Bouny, M. Mainguy, T. Lassabatere, and O. Coussy. Characterization and identification of equilibrium and transfer moisture properties for ordinary and high-performance cementitious materials. *Cement and Concrete Research*, 29:1225–1238, 1999.

[10] Z. P. Bažant. Analysis of pore pressure, thermal stress and fracture in rapidly heated concrete. In L. T. Phan, N. J. Carino, D. Duthinh, and E. Garboczi, editors, *Proceedings of the International Workshop on Fire Performance of High-Strength Concrete*, pages 155–164. NIST, Gaithersburg, Maryland, 1997.

[11] Z. P. Bažant. Concrete creep at high temperature and its interaction with fracture: recent progress. In G. Pijaudier-Cabot, B. Gérard, and P. Acker, editors, *Proceedings of the 7th International Conference on Creep, Shrinkage and Durability of Concrete and Concrete Structures*, pages 449–460. Hermes Science, London, 2005.

[12] Z. P. Bažant and P. Prat. Effect of temperature and humidity on fracture energy of concrete. *ACI Materials Journal*, 85:262–271, 1988.

[13] Z. P. Bažant and W. Thonguthai. Pore pressure and drying of concrete at high temperature. *Journal of the Engineering Mechanics Division*, 104:1059–1079, 1978.

[14] Z. P. Bažant and G. Zi. Decontamination of radionuclides from concrete by microwave heating. I: theory. *Journal of Engineering Mechanics (ASCE)*, 129(7):777–784, 2003.

[15] J. Bear. *Dynamics of fluids in porous media*. Dover, New York, 1988.

[16] D. P. Bentz. Fibers, percolation, and spalling of high-performance concrete. *ACI Materials Journal*, 97(3):351–359, 2000.

[17] W. Blanke and M. Biermann. *Thermophysikalische Stoffgrößen [Thermophysical material parameters]*, volume 1. Springer, Berlin, 1989. In German.

[18] G. Brux. Brand im Eurotunnel, Ursachen, Schäden und Sanierung [Fire in the channel tunnel, causes, damage, and repair measures]. *Tunnel*, 16(6):31, 1997. In German.

[19] M. D. Burghardt and J. A. Harbach. *Enigneering thermodynamics*. HarperCollins College Publishers, New York, 4th edition, 1993.

[20] G. C. Bye. *Portland Cement*. Thomas Telford Publishing, London, 2nd edition, 1999.

[21] R. Cather, J. W. Figg, A. F. Marsden, and T. P. O'Brien. Improvements to the Figg method for determining the air permeability of concrete. *Magazine of Concrete Research*, 36(129):241–245, 1984.

[22] CEB. *Fire Design of Concrete Structures, Bulletin d'Information 208*. CEB, Lausanne, Switzerland, 1991.

[23] X. Chateau and L. Dormieux. Micromechanics of saturated and unsaturated porous media. *International Journal of Numerical and Analytical Methods in Geomechanics*, 26:831–844, 2002.

[24] P. A. Claisse, H. I. Elsayad, and I. G. Shaaban. Test methods for measuring fluid transport in cover concrete. *Journal of Materials in Civil Engineering*, 11(2):138–143, 1999.

[25] G. R. Consolazio and J. H. Chung. Numeric simulation of near-surface moisture migration and stress development in concrete exposed to fire. *Computers and Concrete*, 1(1):31–46, 2004.

[26] G. R. Consolazio, M. C. McVay, and J. W. Rish III. Measurement and prediction of pore pressure in cement mortar subjected to elevated temperature. In L. T. Phan, N. J. Carino, D. Duthinh, and E. Garboczi, editors, *Proceedings of the International Workshop on Fire Performance of High-Strength Concrete*, pages 125–148. NIST, Gaithersburg, Maryland, 1997.

[27] R. K. Dhir, P. C. Hewlett, E. A. Byars, and I. G. Shaaban. A new technique for measuring the air permeability of near-surface concrete. *Magazine of Concrete Research*, 47(171):167–176, 1995.

[28] R. K. Dhir, P. C. Hewlett, and Y. N. Chan. Near surface characteristics of concrete: assessment and development of in-situ test methods. *Magazine of Concrete Research*, 39(141):183–195, 1987.

[29] S. Diamond. Review mercury porosimetry: an inappropriate method for the measurement of pore size distributions in cement-based materials. *Cement and Concrete Research*, 30:1517–1525, 2000.

[30] S. Diamond and M. E. Leeman. Pore size distribution in hardened cement paste by SEM image analysis. In S. Diamond, S. Mindess, F.P. Glasser, L.R. Roberts, J.P. Skalny, and L.D. Wakely, editors, *Microstructure of Cement-based systems / Bonding and Interfaces in Cementitious Materials*, volume 370, pages 217 – 226. Materials Research Society, Pittsburgh, 1995.

[31] H. (Ed.) Duddeck. Guidelines for the design of tunnels. *Tunneling and Underground Space Technology*, 3(3):237–249, 1988.

[32] C. Ehm. *Versuche zur Festigkeit und Verformung von Beton unter zweiaxialer Beanspruchung und hohen Tempearturen [Experiments on strength and strain of concrete under biaxial loading at high temperatures]*. PhD thesis, University of Braunschweig, Braunschweig, Germany, 1985.

[33] I. A. El-Arabi, H. Duddeck, and H. Ahrens. Structural analysis for tunnels exposed to fire temperatures. *Tunneling and Underground Space Technology*, 7(1):19–24, 1992.

[34] M. Elices, G. V. Guinea, and J. Planas. Measurement of the fracture energy using three-point bend tests: part 3 – influence of cutting the P-δ tail. *Materials and Structures*, 25(6):327–334, 1992.

[35] M. Elices, G. V. Guinea, and J. Planas. On the measurement of concrete fracture energy using three-point bend tests. *Materials and Structures*, 30:375–375, 1997.

[36] R. Felicetti and P. G. Gambarova. On the residual tensile properties of high performance siliceous concrete exposed to high temperature. In *Special Volume in honor of Z. P. Bažant's 60th Anniversary*, pages 167–186. Hermes, Prague, 1998.

[37] J. W. Figg. Methods of measuring the air and water permeability of concrete. *Magazine of Concrete Research*, 25(85):213–219, 1973.

[38] D. J. Furbish. *Fluid physics in geology: an introduction to fluid motions on earth's surface and within its crust.* Oxford University Press, Oxford, 1997.

[39] C. Gallé and J.-F. Daian. Gas permeability of unsaturated cement-based materials: application of a multi-scale network model. *Magazine of Concrete Research*, 52(4):251–263, 2000.

[40] E. J. Garboczi and D. P. Bentz. Multiscale analytical/numerical theory of the diffusivity of concrete. *Advanced Cement Based Materials*, 8:77–88, 1998.

[41] D. Gawin, C. E. Majorana, and B. A. Schrefler. Numerical analysis of hygro-thermal behaviour and damage of concrete at high temperature. *Mechanics of Cohesive-Frictional Materials*, 4:37–74, 1999.

[42] D. Gawin, F. Pesavento, and B. A. Schrefler. Modelling of hygro-thermal behaviour and damage of concrete at temperature above the critical point of water. *International Journal for Numerical and Analytical Methods in Geomechanics*, 26:537–562, 2002.

[43] D. Gawin, F. Pesavento, and B. A. Schrefler. Modelling of hygro-thermal behaviour of concrete at high temperature with thermo-chemical and mechanical material degradation. *Computer Methods in Applied Mechanics and Engineering*, 192:1731–1771, 2003.

[44] D. Gawin, F. Pesavento, and B. A. Schrefler. Modelling of deformations of high strength concrete at elevated temperatures. *Materials and Structures*, 37:218–236, 2004.

[45] D. Gawin, F. Pesavento, and B. A. Schrefler. Towards prediction of the thermal spalling risk through a multi-phase porous media model of concrete. *Computer Methods in Applied Mechanics and Engineering*, 195:5707–5729, 2006.

[46] G. M. Giannuzzi. Centro Ricerche Energia Casaccia – ENEA, Rome, Italy. Private communications, 2000.

[47] G. H. Golub and C. F. Van Loan. *Matrix computations.* The Johns Hopkins University Press, London, 3rd edition, 1996.

[48] Z. C. Grasley, G. W. Scherer, D. A. Lange, and J. J. Valenza. Dynamic pressurization method for measuring permeability and modulus: II. cementitious materials. *Materials and Structures.*, 40:711–721, 2007.

[49] G. V. Guinea, J. Planas, and M. Elices. Measurement of the fracture energy using three-point bend tests: part 1 – influence of experimental procedures. *Materials and Structures*, 25(4):212–218, 1992.

[50] X. H. Guo and R. I. Gilbert. The effect of specimen size on the fracture energy and softening function of concrete. *Materials and Structures*, 33:309–316, 200.

[51] A. Haack. Generelle Überlegungen zur Sicherheit in Verkehrstunneln [General considerations concerning safety in tunnels]. Technical report, Studiengesellschaft für unterirdische Verkehrsanlagen e.V. (STUVA), Köln, Germany, 2002. In German.

[52] T. Z. Harmathy and L. W. Allen. Thermal properties of selected masonry unit concretes. *ACI Journal*, 70(2):132–142, 1973.

[53] K. D. Hertz. Limits of spalling of fire-exposed concrete. *Fire Safety Journal*, 38:103–116, 2003.

[54] J. Horvath. *Beiträge zum Brandverhalten von Hochleistungsbeton [Contributions to the behavior of high-performance concrete under fire].* PhD thesis, Vienna University of Technology, Vienna, Austria, 2003. In German.

[55] J. Horvath, U. Schneider, and U. Diederichs. Brandverhalten von Hochleistungsbetonen [Fire resistance of high performance concrete]. Technical Report 11, Vienna University of Technology, Vienna, Austria, 2004. In German.

[56] R. W. Hyland and A. Wexler. Formulations for the thermodynamic properties of the saturated phases of H2O from 173.15K to 473.15K. *American Society of Heating, Refrigerating and Air-Conditioning Engineers (ASHRAE) Transactions*, 89(2A):500–519, 1983.

[57] F. P. Jacobs. *Permeabilität und Porengefüge zementgebundener Werkstoffe [Permeability and pore structure of cementitious materials]*. PhD thesis, ETH Zürich, Zürich, Switzerland, 1994. In German.

[58] P. Kalifa, G. Chéné, and C. Gallé. High temperature behaviour of HPC with polypropylene fibres: from spalling to microstructure. *Cement and Concrete Research*, 31:1487–1499, 2001.

[59] P. Kalifa, F.-D. Menneteau, and D. Quenard. Spalling and pore pressure in HPC at high temperatures. *Cement and Concrete Research*, 30:1915–1927, 2000.

[60] G. Khoury and C. E. Majorana. Spalling. In G. Khoury and C. E. Majorana, editors, *Effect of Heat on Concrete*. 11 pages. International Centre for Mechanical Science, Udine, 2003.

[61] G. A. Khoury. Tunnel concretes under fire: part 1 – explosive spalling. *Concrete (London)*, 40(10):62–64, 2006.

[62] G. A. Khoury, B. N. Grainger, and P. J. E. Sullivan. Strain of concrete during first heating to 600°C. *Magazine of Concrete Research*, 37(133):195–215, 1985.

[63] G. A. Khoury, B. N. Grainger, and P. J. E. Sullivan. Transient thermal strain of concrete: literature review, conditions within specimen and behaviour of individual constituents. *Magazine of Concrete Research*, 37(132):131–144, 1985.

[64] L. J. Klinkenberg. The permeability of porous media to liquids and gases. *American Petroleum Institute, Drilling Production Practice*, pages 200–213, 1941.

[65] J. J. Kollek. The determination of the permeability of concrete to oxygen by the CEM-Bureau method – a recommendation. *Materials and Structures*, 22:225–230, 1989.

[66] K. Kordina and C. Meyer-Ottens. *Beton Brandschutz Handbuch [Handbook of fire resistance of conrete]*. Verlag Bau + Technik, Düsseldorf, 2nd edition, 1999. In German.

[67] W. Kusterle, W. Lindlbauer, G. Hampejs, A. Heel, P.-F. Donauer, M. Zeiml, W. Brunnsteiner, R. Dietze, W. Hermann, H. Viechtbauer, M. Schreiner, R. Vierthaler, H. Stadlober, H. Winter, J. Lemmerer, and E. Kammeringer. Brandbeständigkeit von Faser-, Stahl- und Spannbeton [Fire resistance of fiber-reinforced, reinforced, and prestressed concrete]. Technical Report 544, Bundesministerium für Verkehr, Innovation und Technologie, Vienna, Austria, 2004. In German.

[68] W. Kusterle and N.-V. Waubke. Die Brandbeständigkeit von Faser-, Stahl- und Spannbeton [Fire resistance of fiber-reinforced, reinforced, and prestressed concrete]. *Schriftenreihe der Österreichischen Vereinigung für Beton- und Bautechnik*, 47:89–96, 2001. In German.

[69] R. Lackner, Ch. Pichler, and A. Kloiber. Artificial ground freezing of fully saturated soil: viscoelastic behavior. *Journal of Engineering Mechanics (ASCE)*, 134(1):1–11, 2008.

[70] A. Lambrechts. NV Bekaert, Zwevegem, Belgium. Private communications, June 2006.

[71] D. Leithner. Experimental investigation of concrete subjected to fire loading: micromechanical approach for determination of the permeability. Master's thesis, Vienna University of Technology, Vienna, Austria, 2004.

[72] R. W. Lewis and B. A. Schrefler. *The finite element method in the static and dynamic deformation and consolidation of porous media*. John Wiley & Sons, Chichester, 2nd edition, 1998.

[73] H.-P. Lien and F. H. Wittmann. Mass transfer in inhomogeneous porous media under thermal gradients. *Nuclear Engineering and Design*, 179:179–189, 1998.

[74] W. Lindlbauer and M. Zeiml. Forschungsvorhaben Brandbeständigkeit von Faser-, Stahl- und Spannbeton – Aufgabenstellung und Versuchsdurchführung [Research project on fire resistance of fiber-reinforced, reinforced, and prestressed concrete – concept, formulation, and conduction of experiments]. *Schriftenreihe der Österreichischen Vereinigung für Beton- und Bautechnik*, 50:67–74, 2002. In German.

[75] J. D. Logan. *Transport modeling in hydrogeomechanical systems*. Springer, New York, 2001.

[76] H. Loosveldt, Z. Lafhaj, and F. Skoczylas. Experimental study of gas and liquid permeability of mortar. *Cement and Concrete Research*, 32:1357–1363, 2002.

[77] F. D. Lydon. Effect of coarse aggregate and water/cement ratio on intrinsic permeability of concrete subject to drying. *Cement and Concrete Research*, 25:1737–1746, 1995.

[78] C. Meyer-Ottens. *Zur Frage der Abplatzungen an Betonbauteilen aus Normalbeton bei Brandbeanspruchung [Spalling of normal–strength concrete structures under fire loading]*. PhD thesis, Braunschweig University of Technology, Braunschweig, Germany, 1972. In German.

[79] J. P. Monlouis-Bonnaire, J. Verdier, and B. Perrin. Prediction of the relative permeability to gas flow of cement-based materials. *Cement and Concrete Research*, 34(5):737–744, 2004.

[80] Y. Mualem. A new model for predicting the hydraulic conductivity of unsaturated porous media. *Water Resources Research*, 12(3):513–522, 1976.

[81] A. M. Neville. *Properties of Concrete*. Pitman Publishing, London, 3rd edition, 1981.

[82] C. V. Nielsen and N. Bićanić. Residual fracture energy of high-performance and normal concrete subject to high temperatures. *Materials and Structures*, 36:515–521, 2003.

[83] C. V. Nielsen, C. J. Pearce, and N. Bićanić. Improved phenomenological modelling of transient thermal strains for concrete at high temperatures. *Computers and Concrete*, 1(2):189–209, 2004.

[84] P. Nischer, J. Steigenberger, and H. Wiklicky. Praxisverhalten von erhöht brandbeständigem (Innenschalen-) Beton (EBB) [Practical use of fire resistant concrete for tunnel linings]. Technical Report , FFF-project no. 806201, Forschungsinstitut der Vereinigung der österreichischen Zementindustrie (VÖZFI), Vienna, Austria, 2004. In German.

[85] ÖNORM B4200-10. *Beton – Herstellung, Verwendung und Gütenachweis [Concrete – Production, use and verification of quality]*. Österreichisches Normungsinstitut, 1996. In German.

[86] ÖNORM B4710-1. *Beton – Teil 1: Festlegung, Herstellung, Verwendung und Konformitätsnachweis [Concrete – Part 1: Specification, production, use and verification of conformity]*. Österreichisches Normungsinstitut, 2004. In German.

[87] ÖNORM EN1992-1-2. *Eurocode 2 – Bemessung und Konstruktion von Stahlbeton- und Spannbetontragwerken – Teil 1-2: Allgemeine Regeln – Tragwerksbemessung für den Brandfall [Eurocode 2 – Design of concrete structures – Part 1-2: General rules – Structural fire design]*. European Committee for Standardization (CEN), 2007. In German.

[88] G. S. Öttl. *A three-phase material model for dewatering of soils by means of compressed air*. PhD thesis, University of Innsbruck, Innsbruck, Austria, 2003.

[89] N. Pasquini. *Polypropylene handbook*. Hanser Publishers, Munich, 2nd edition, 2005.

[90] F. Pesavento. *Non linear modelling of concrete as multiphase porous material in high temperature conditions*. PhD thesis, University of Padua, Padua, Italy, 2000.

[91] P. E. Petersson. Crack growth and development of fracture zones in plain concrete and similar materials. Technical Report TVBM-1006, Division of Building Materials, University of Lund, Lund, Sweden, 1981.

[92] Ch. Pichler. Numerical simulation of tunnels accounting for thermochemomechanical couplings: assessment of the benefits from ground improvement by means of jet grouting and of the loading of tunnel linings under fire exposure. Master's thesis, Vienna University of Technology, Vienna, Austria, 2002.

[93] Ch. Pichler, R. Lackner, and H. A. Mang. Safety assessment of concrete tunnel linings under fire load. *Journal of Structural Engineering (ASCE)*, 132(6):961–969, 2006.

[94] Ch. Pichler, R. Lackner, and H. A. Mang. A multiscale micromechanics model for the autogenous-shrinkage deformation of early-age cement-based materials. *Engineering Fracture Mechanics*, 74:34–58, 2007.

[95] J. Planas, M. Elices, and G. V. Guinea. Measurement of the fracture energy using three-point bend tests: part 2 – influence of bulk energy dissipation. *Materials and Structures*, 25(5):305–312, 1992.

[96] prEN1991-1-2. *Eurocode 1 – Actions on structures – Part 1-2: General actions – Actions on structures exposed to fire.* European Committee for Standardization (CEN), 2002.

[97] W. H. Press, S. A. Teukolsky, W. T. Vetterling, and B. P. Flannery. *Numerical recipes in fortran 77*, volume 1. Cambridge Universtiy Press, Cambridge, 2nd edition, 1996.

[98] E. Richter and D. Hosser. Baulicher Brandschutz bei Verkehrstunneln in offener Bauweise [Fire protection for tunnels]. *Beton- und Stahlbetonbau*, 97(4):178–184, 2002. In German.

[99] RILEM TC 50-FMC. Determination of the fracture energy of mortar and concrete by means of three-point bend tests on notched beams. *Materials and Structures*, 18(4):285–290, 1985.

[100] B. M. Savage and D. J. Janssen. Soil physics principles validated for use in predicting unsaturated moisture movement in portland cement concrete. *ACI Materials Journal*, 94(1):63–70, 1997.

[101] K. Savov, R. Lackner, and H. A. Mang. Stability assessment of shallow tunnels subjected to fire load. *Fire Safety Journal*, 40:745–763, 2005.

[102] A. E. Scheidegger. *The physics of flow through porous media.* University of Toronto Press, Toronto, 3rd edition, 1974.

[103] G. W. Scherer. Measuring permeability of rigid materials by a beam-bending method: I, theory. *Journal of the American Ceramics Association*, 83(9):2231–2239, 2000.

[104] G. W. Scherer. Dynamic pressurization method for measuring permeability and modulus: I. theory. *Materials and Structures*, 39(10):1041–1057, 2006.

[105] U. Schneider. *Zur Kinetik festigkeitsmindernder Reaktionen in Beton bei hohen Temperaturen [On the kinetics of reactions reducing the strength of concrete subjected to elevated temperatures]*. PhD thesis, TU Braunschweig, Braunschweig, Germany, 1973. In German.

[106] U. Schneider. *Ein Beitrag zur Frage des Kriechens und der Relaxation von Beton unter hohen Temperaturen [Contribution to creep and relaxation of concrete under high temperatures]*. Habilitation thesis, TU Braunschweig, Braunschweig, Germany, 1979. In German.

[107] U. Schneider. Concrete at high temperature – a general review. *Fire Safety Journal*, 13:55–68, 1988.

[108] U. Schneider. Center for Material Research, Testing and Fire Safety Science, Vienna University of Technology, Vienna, Austria. Private communications, 2006.

[109] U. Schneider and H. J. Herbst. Permeabilität und Porosität von Beton bei hohen Temperaturen [Permeability and porosity of concrete at high temperatures]. Technical Report 403, Deutscher Ausschuss für Stahlbeton, Berlin, Germany, 1989. In German.

[110] U. Schneider and J. Horvath. Abplatzverhalten an Tunnelinnenschalenbeton [Spalling of concrete for tunnel linings]. *Beton- und Stahlbetonbau*, 97(4):185–190, 2002. In German.

[111] B. A. Schrefler. Mechanics and thermodynamics of saturated/unsaturated porous materials and quantitative solutions. *Applied Mechanics Reviews (ASME)*, 55(4):351–388, 2002.

[112] B. A. Schrefler. Multiphase flow in deforming porous material. *International Journal for Numerical Methods in Engineering*, 60:27–50, 2004.

[113] B. A. Schrefler, P. Brunello, D. Gawin, C. E. Majorana, and F. Pesavento. Concrete at high temperature with application to tunnel fire. *Computational Mechanics*, 29:43–51, 2002.

[114] B. A. Schrefler, D. Gawin, G. Khoury, and C. E. Majorana. Physical, mathematical & numerical modelling. In G. Khoury and C. E. Majorana, editors, *Effect of Heat on Concrete*. 81 pages. International Centre for Mechanical Science, Udine, 2003.

[115] B. A. Schrefler, G. A. Khoury, D. Gawin, and C. E. Majorana. Thermo-hydro-mechanical modelling of high performance concrete at high temperatures. *Engineering Computations*, 19(7):787–819, 2002.

[116] G. Sinkovits. Betonplatten für den Gleiskörper von Eisenbahntunnel – Betontechnologische Untersuchungen [Concrete slabs for the railroad embankment of tunnels – Material tests]. Master's thesis, Vienna University of Technology, Vienna, Austria, 2008. In German.

[117] A. C. Tecchio. Analisi della risposta strutturale a scenari incidentali in contenitori di calcestruzzo di reattori nucleari. Master's thesis, University of Padua, Padua, Italy, 2002. In Italian.

[118] R. T. Tenchev, L. Y. Li, and J. A. Purkiss. Finite element analysis of coupled heat and moisture transfer in concrete subjected to fire. *Numerical Heat Transfer*, 39:685–710, 2001.

[119] M. J. Terro. Numerical modeling of the behavior of concrete structures in fire. *ACI Structural Journal*, 95(2):183–193, 1998.

[120] S. Thelandersson. Modeling of combined thermal and mechanical action in concrete. *Journal of Engineering Mechanics (ASCE)*, 113(6):893–906, 1987.

[121] K.-C. Thienel. Festigkeit und Verformung von Beton bei hoher Temperatur und biaxialer Beanspruchung – Versuche und Modellbildung [Strength and strain of concrete at high temperature – experiments and modeling]. Technical Report 437, Deutscher Ausschuss für Stahlbeton, Berlin, Germany, 1994. In German.

[122] H. R. Thomas and M. R. Sansom. Fully coupled analysis of heat, moisture, and air transfer in unsaturated soil. *Journal of Engineering Mechanics (ASCE)*, 121(3):392–405, 1995.

[123] F.-J. Ulm, O. Coussy, and Z. P. Bažant. The "Chunnel" fire I: chemoplastic softening in rapidly heated concrete. *Journal of Engineering Mechanics (ASCE)*, 125(3):272–282, 1999.

[124] M. T. van Genuchten and D. R. Nielsen. On describing and predicting the hydraulic properties of unsaturated soils. *Annales Geophysicae*, 3(5):615–627, 1985.

[125] W. Vichit-Vadakan and G. W. Scherer. Measuring permeability of rigid materials by a beam-bending method: III, cement paste. *Journal of the American Ceramics Association*, 85(6):1537–1544, 2002.

[126] J. Wageneder. Traglastuntersuchungen unter Brandeinwirkungen [Ultimate-load investigations considering fire load]. *Bauingenieur*, 77:184–192, April 2002. In German.

[127] W. Wissmann. Zur statischen Berechnung beliebig geformter Stollen- und Tunnelauskleidungen mit Hilfe von Stabwerkprogrammen [On static analysis of arbitrarily formed linings of mines and tunnels using computer programs for beam structures]. *Der Bauingenieur*, 43(1):1–8, 1968. In German.

[128] M. Zeiml. Analytical and numerical modeling of heat and water-vapor transport in concrete subjected to fire loading. Master's thesis, Vienna University of Technology, Vienna, Austria, 2004.

[129] M. Zeiml, R. Lackner, D. Leithner, and J. Eberhardsteiner. Identification of residual gas-transport properties of concrete subjected to high temperatures. *Cement and Concrete Research*, 38(5):699–716, 2008.

[130] M. Zeiml, R. Lackner, and H. A. Mang. Coupled analysis of heat and multiphase mass transport in concrete subjected to fire loading. In M. Papadrakakis, E. Oñate, and B. Schrefler, editors, *CD-ROM Proceedings of the International Conference on Computational Methods for Coupled Problems in Science and Engineering (Coupled Problems 2005)*. 23 pages. CIMNE, Barcelona, 2005.

[131] M. Zeiml, R. Lackner, F. Pesavento, and B. A. Schrefler. Thermo-hydro-chemical couplings considered in safety assessment of shallow tunnels subjected to fire load. *Fire Safety Journal*, 43(2):83–95, 2008.

[132] M. Zeiml, D. Leithner, R. Lackner, and H. A. Mang. How do polypropylene fibers improve the spalling behavior of in-situ concrete? *Cement and Concrete Research*, 36(5):929–942, 2006.

[133] B. Zhang and N. Bićanić. Fracture energy of high performance concrete at temperatures up to 450°C. In R. de Borst, J. Mazars, J. Pijaudier-Cabot, and J. G. M. van Mier, editors, *Proceedings of the 4th International Conference on Fracture Mechanics of Concrete and Concrete Structures*, pages 461–468, Cachan, 2001. Balkema.

[134] G. Zi and Z. P. Bažant. Decontamination of radionuclides from concrete by microwave heating. II: computations. *Journal of Engineering Mechanics (ASCE)*, 129(7):785–792, 2003.

<div align="right">

Appendix **A**

</div>

Determination of pressurized pore volume V_0

For determination of the pore volume right before spalling, V_0 [m³] – containing water vapor at pressure p_0 [Pa] – the ratio between pore volume V_p [m³] and total concrete volume (i.e., the porosity n [–]) is assumed to be equal to the area ratio of an arbitrary plane section cut through the porous medium, giving

$$\frac{V_p}{V} = n = \frac{A_p}{A}, \tag{A.1}$$

with A_p [m²] as the cumulative area of the pore sections cut by this plane. In addition, the following is assumed:

1. Pores cut by an arbitrary plane section have different diameters, with the distribution of these diameters following the pore-size distribution obtained from, e.g., mercury-intrusion porosimetry (MIP) and/or image analysis. According to [29, 30, 94], a combination of the two mentioned techniques is appropriate for identification of the pore structure of concrete. For the underlying evaluation, the real pore-size distribution is approximated by a straight line in the $\log(D)$-V_p-diagram (see Figure A.1(a)).

2. Assuming spherical pores, an arbitrary section through concrete does not cut all pores at mid section but rather cuts them in a distributed manner (see Figures 2.6 and A.2). Hence, pores of equal diameter contribute differently to the total area A_p. This is taken into account by evenly distributing the location of the intersecting plane over the sphere diameter (see Figure A.2).

(a)

cumulative pore volume

$\square$ typical data from image analysis

$\circ$ typical data from MIP

limit of image analysis

V_p

1

k

D_{min}

under-estimation by MIP

D_{max} $\log(D)$

(b)

cumulative pore volume/area

V_p, A_p

$A_{p,i}$

D_{min} D_i D_{max} $\log(D)$
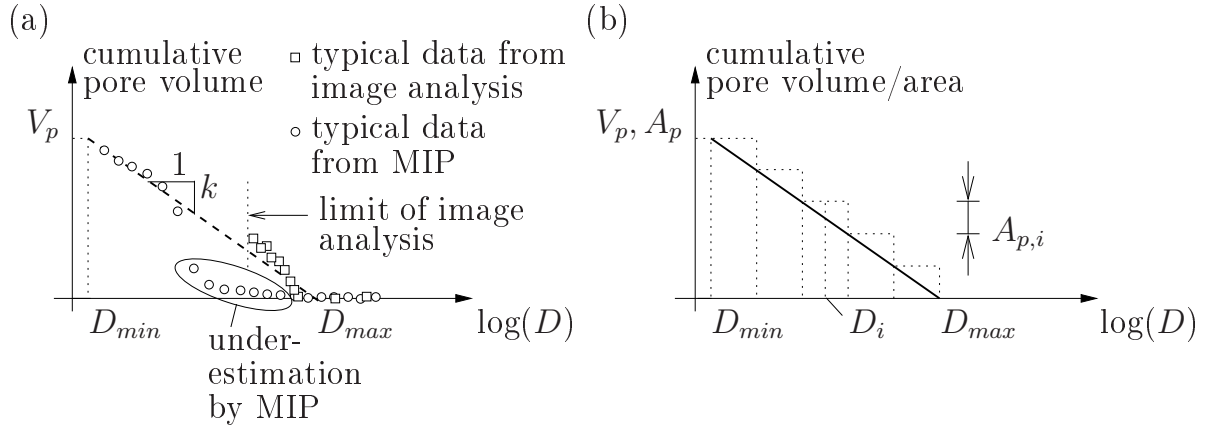
Figure A.1: Illustration of (a) approximation of the pore-size distribution by $[-k \log(D/D_{max})]$ [94] and (b) division of employed pore-size distribution into sub-pore ranges

$t_i/2$ $\quad$ $t_i = D_i/N_i$

(a)

A_j

D_i

$A_{p,i} = \sum_{j=1}^{N_i} A_j$

(b)

x_j $\quad$ x

$D_j/2$ $\quad$ $D_i/2$

D_i

$A_j = \pi \left(\dfrac{D_j}{2} \right)^2 = \pi \left[\left(\dfrac{D_i}{2} \right)^2 - x_j^2 \right]$

with $-\dfrac{D_i}{2} \leq x \leq \dfrac{D_i}{2}$
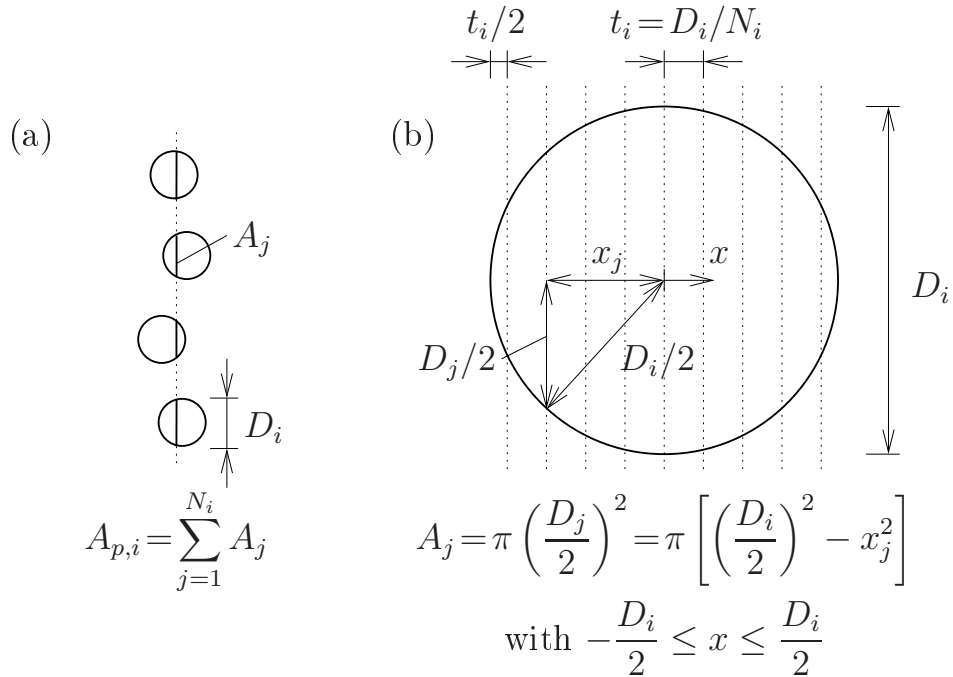
Figure A.2: Illustration of different contribution of spheres with equal diameter to the total area of cut pores

Based on Assumption (1), the employed pore-size distribution is divided into a finite number of sub-pore ranges (see Figure A.1(b)) and the number of pores corresponding to the i-th sub-pore range, N_i [–], is determined from $A_{p,i}$ [m^2] and D_i [m]. Subsequently, the corresponding sub-pore volume, $V_{0,i}$ [m^3], and the total corresponding pore volume right before spalling, V_0 [m^3], are determined as

$$V_{0,i} = N_i V_i = N_i \frac{\pi}{6} D_i^3 \quad \text{giving} \quad V_0 = \sum_i V_{0,i} \,. \tag{A.2}$$

Appendix B

Experimental determination of specific fracture energy of concrete by three-point bending tests

The fracture energy of concrete can be determined by (i) direct tension or (ii) bending tests (see Figure B.1). Regarding the latter, the fracture energy may be determined according to [99]. Hereby, (i) weight-compensated tests (where the self weight of the beam is eliminated by a counter-weight system) and (ii) tests without weight compensation are distinguished. In case of no self-weight compensation, the specific fracture energy G_F [J/m^2] is given by (see Figure B.1(b))

$$G_F = \frac{W_0 + W_1 + W_2 + W_3}{A_{lig}}, \tag{B.1}$$

with A_{lig} [m^2] as the area of the ligament (with $A_{lig} = b(h - a)$, where b [m] is the beam width, h [m] is the beam height, and a [m] is the notch height). In Equation (B.1),

$$W_0 = \int_0^{\delta_0} P_{exp} \, d\delta \tag{B.2}$$

is the external work W_0 [J] (area under the experimentally-obtained load-deflection curve) and

$$W_1 = \left(\frac{m_1}{2} + m_2 \right) g \delta_0 \tag{B.3}$$

is the work performed by the mass of the beam between the supports, m_1 [kg], and the mass of the part of the loading device not attached to the machine, m_2 [kg] (following the beam until failure), $g = 9.81$ m/s is the gravity acceleration, and δ_0 [m] is the mid-span beam deflection at failure. According to [50, 91], W_3 can be neglected.
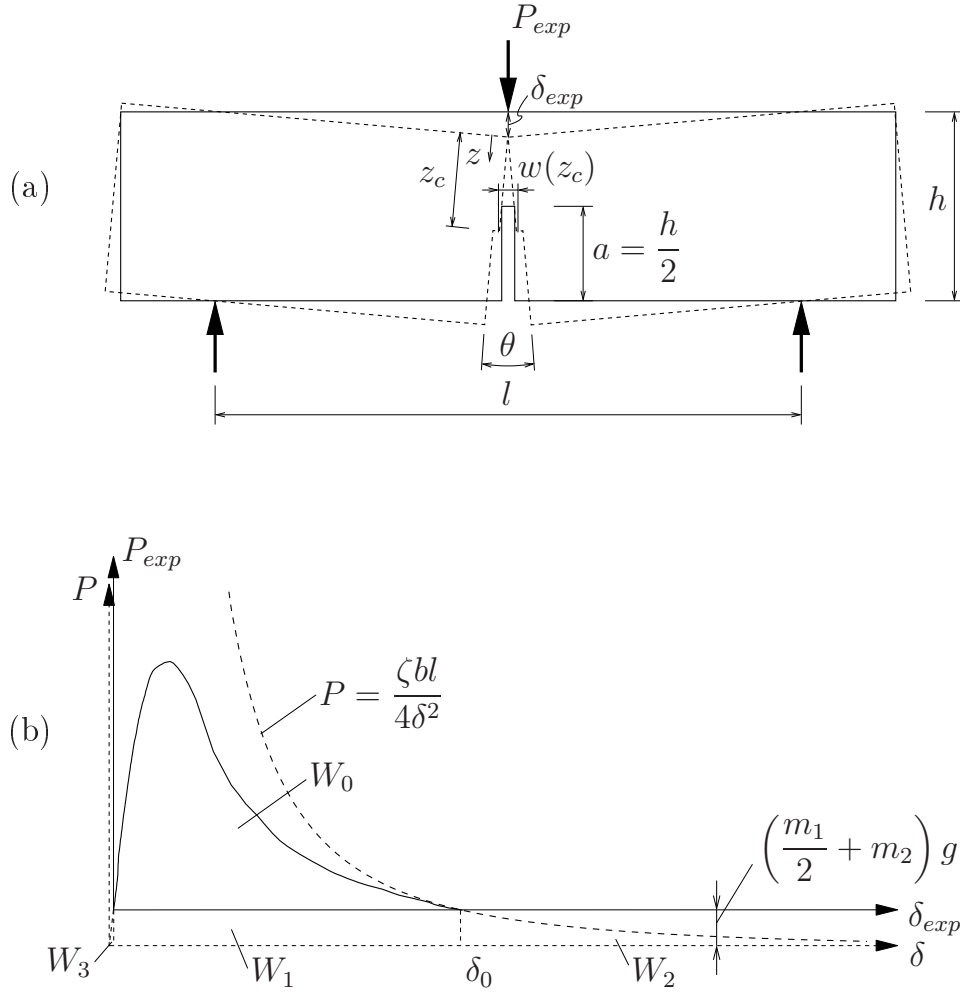
Figure B.1: Three-point bending test: (a) test setup and (b) load-deflection curve in case of no weight compensation [50]

According to [34, 35, 49, 95], the so-obtained fracture energy changes with sample size which is attributed to the following characteristics of the experimental setup:

1. At the supports, friction[1] between support and beam leads to an overestimation of the fracture energy by 2 % to 5 % [49].

2. Dissipation of energy in the bulk material results in an overestimation of the fracture energy by 5 % to 10 % due to damage at central support and 1 % to 2% due to damage in regions of high tensile stresses, respectively [95].

3. W_2 is determined by assuming rigid-body motion of the two parts of the beam [34,

---

[1]In addition to friction, crushing of the beam at the supports is mentioned in [49]. This effect is eliminated by determining the net displacement of the beam (mid-span deflection minus vertical displacement of the beam above the supports).

35], giving

$$M \;=\; b \int_0^{z_c} \sigma\left[w(z)\right] z\,dz = \frac{b}{\theta^2} \int_0^{w(z_c)} \sigma\left(w\right) w\,dw = \frac{\zeta b}{\theta^2}\,, \qquad (B.4)$$

where θ [rad] is the opening angle and z was substituted by w/θ (see Figure B.1(a)). Inserting

$$M = \left[P_{exp} + \left(\frac{m_1}{2} + m_2\right)g\right]\frac{l}{4} = \frac{Pl}{4} \quad \text{and} \quad \theta = \frac{4\delta}{l} \qquad (B.5)$$

into Equation (B.4) leads to [34, 35]

$$\frac{M}{b} = \frac{1}{\theta^2}\zeta \quad \text{and} \quad P = \frac{\zeta bl}{4\delta^2}\,, \qquad (B.6)$$

allowing extrapolation of the experimental P-δ curve as indicated in Figure B.1(b). Hereby, the unknown parameter ζ [N] (introduced in Equation (B.4)) is obtained from linear regression of the experimental results (see Figure B.2).
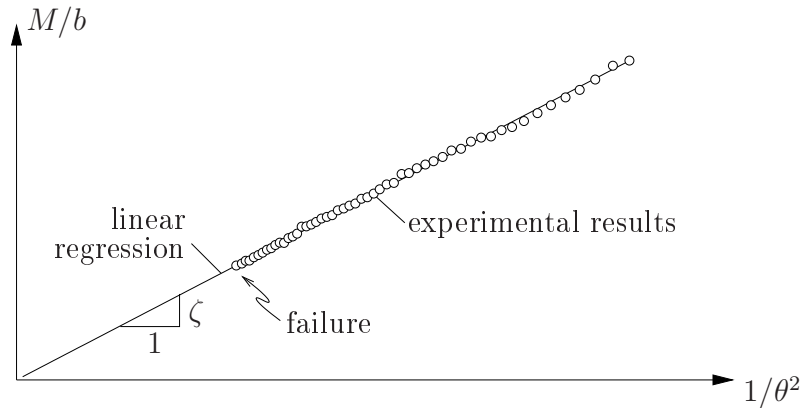
Figure B.2: Determination of parameter ζ from linear regression of the part of the bending experiment close to failure of the beam, i.e., for large values of θ [34]

Accordingly, the specific fracture energy G_F, determined from application of Equations (B.1) and (B.6) to the results of the three-point bending experiments, was reduced by 10 %, accounting for the abovementioned dissipative processes. Moreover, aging of concrete was considered by the empirical relation[2] [12, 81]

$$G_F(28\text{days}) = G_F(t)\frac{1}{1 + 0.277\cdot\log(t/28)}\,. \qquad (B.7)$$

---

[2]The empirical relation is obtained in [81] from compressive-strength data. It is assumed that this relation holds for the increase of G_F in consequence of aging.

Concerning the temperature dependence of the fracture energy, contradictory experimental results are reported in the open literature:

- In [12], the fracture energy of concrete was determined at elevated temperatures up to 200 °C, showing a decrease of G_F with temperature.

- In [82, 133], the residual fracture energy continuously increased up to a temperature of 300 to 400 °C and decreased thereafter. The fracture energy obtained on hot concrete specimens, on the other hand, showed a decreasing behavior up to a temperature of 150 °C followed by a continuous increase. It is, however, stated in [82, 133] that transient effects at temperatures up to 150 °C may have altered the experimental results for G_F at the respective temperatures.

- In [8, 36], no clear trend for the residual fracture energy was obtained and it was therefore concluded that G_F may be assumed to be independent of temperature.

Considering these contradictory conclusions regarding the temperature dependence of the specific fracture energy of concrete, G_F was assumed to be temperature-independent, with a mean value for the fracture energy obtained from 46 experiments given by $G_F = 90$ J/m^2 (see Table B.1).

Table B.1: Adjusting the experimental result for G_F [J/m^2]

Mean value from experimental results		145
Correction, taking into account ...		
dissipative processes	-10%	-15
age of specimens ($\approx$ 580 days)	-27%	-40
Adjusted value of G_F [J/m^2]		90

Appendix C

Klinkenberg's formulation for the slip-flow phenomenon [64]

C.1 Gas flow through a circular tube

The equilibrium condition in the direction of flow formulated for a tube of length dx and inner and outer radius of r and $r + dr$, respectively, reads (see Figure C.1)

$$r \, 2 \, \pi \, dr \left[-\sigma_{xx}(x) + \sigma_{xx}(x + dx) \right]$$

$$-r \, 2 \, \pi \, dx \, \tau_{rx}(r) + (r + dr) \, 2 \, \pi \, dx \, \tau_{rx}(r + dr) = 0, \tag{C.1}$$

where σ_{xx} [Pa] is related to the pressure in the tube, with $\sigma_{xx} = -p$, and τ_{rx} [Pa] is the shear stress. The latter is a function of the dynamic viscosity η [Pa s] and the velocity
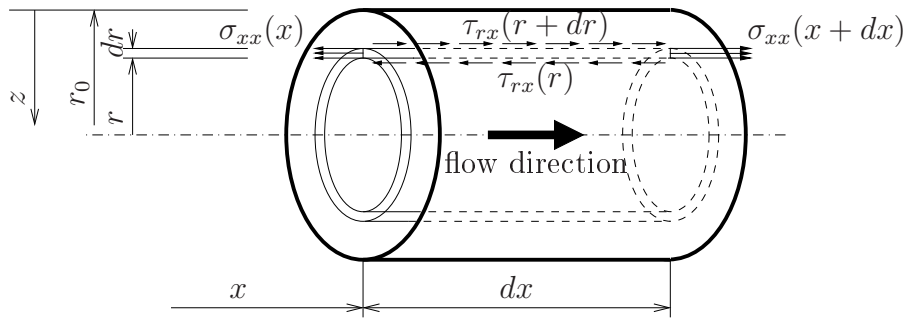
Figure C.1: Stresses acting on an infinitesimal volume element for the gas flow through a circular tube [71]

gradient $\partial v / \partial r$, reading

$$\tau_{rx} = \eta \frac{\partial v}{\partial r}. \tag{C.2}$$

Expressing $\sigma_{xx}(x + dx)$ and $\tau_{rx}(r + dr)$ in Equation (C.1) by means of Taylor series and considering Equation (C.2) gives

$$p\, 2\pi r\, dr - \left[p + \frac{\partial p}{\partial x}dx + \frac{\partial^2 p}{\partial x^2}dx^2 + \ldots \right] 2\pi r\, dr$$

$$-\eta \frac{\partial v}{\partial r}2\pi r\, dx + r \left[\eta \frac{\partial v}{\partial r} + \frac{\partial}{\partial r}\left(\eta \frac{\partial v}{\partial r} \right) dr + \frac{\partial^2}{\partial r^2}\left(\eta \frac{\partial v}{\partial r} \right) dr^2 + \ldots \right] 2\pi\, dx$$

$$+dr \left[\eta \frac{\partial v}{\partial r} + \frac{\partial}{\partial r}\left(\eta \frac{\partial v}{\partial r} \right) dr + \frac{\partial^2}{\partial r^2}\left(\eta \frac{\partial v}{\partial r} \right) dr^2 + \ldots \right] 2\pi\, dx = 0. \tag{C.3}$$

Dividing Equation (C.3) by $2\pi\,\eta\, dx\, dr$, followed by $dr \to 0$ and $dx \to 0$, yields

$$-\frac{r}{\eta}\frac{\partial p}{\partial x} + r\frac{\partial}{\partial r}\left(\frac{\partial v}{\partial r} \right) + \frac{\partial v}{\partial r} = 0 \quad \to \quad \frac{r}{\eta}\frac{\partial p}{\partial x} = \frac{\partial}{\partial r}\left(r\frac{\partial v}{\partial r} \right). \tag{C.4}$$

Integrating Equation (C.4) with respect to the radius r, one gets

$$r\frac{\partial v}{\partial r} = \frac{r^2}{2\eta}\frac{\partial p}{\partial x} + A \quad \text{giving} \quad \frac{\partial v}{\partial r} = \frac{r}{2\,\eta}\frac{\partial p}{\partial x} + A\frac{1}{r}, \tag{C.5}$$

where A is an integration constant. Finally, integration of Equation (C.5) yields the velocity field as

$$v(r) = \frac{r^2}{4\,\eta}\frac{\partial p}{\partial x} + A\ln r + B, \tag{C.6}$$

where the integration constants A and B in Equation (C.6) need to be specified by the boundary conditions at $r = 0$ and $r = r_0$:

- The condition $v < \infty$ at $r = 0$ leads to $A = 0$.

- According to [64], one half of the gas molecules in the layer next to the boundary of the tube, i.e., next to $r = r_0$ is moving towards the wall, whereas the other half moves in the opposite direction. The gas molecules moving towards the wall had their last collision with another molecule somewhere in the flowing mass and, hence, have an average velocity component in the direction of the flow. Based on a finite velocity v_0 near the wall at $r = r_0$ and a constant velocity gradient perpendicular to the wall dv/dz, with $z = r_0 - r$, the velocity next to $r = r_0$ can be approximated as (see Figure C.2)

$$v(z) = v_0 + z\frac{dv}{dz}. \tag{C.7}$$

  Assuming that the average velocity component of the molecules moving towards the wall is equal to the velocity at the location of their last collision, i.e., at λc, where
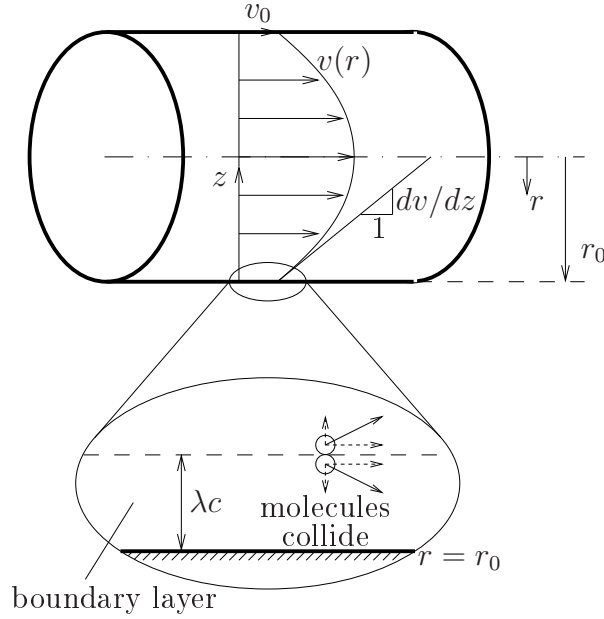
Figure C.2: Distribution of velocity component in the direction of flow and boundary layer λc according to [64]

λ [m] is the mean free path of the gas molecules and c is a proportionality factor, the average velocity of this half of molecules is obtained from Equation (C.7) as

$$\overline{v} = v_0 + c\,\lambda\,\frac{dv}{dz} = v_0 - c\,\lambda\,\frac{dv}{dr}\,. \tag{C.8}$$

Assuming that the molecules moving away from the wall, i.e., after having had contact with the wall, have zero velocity in the direction of the flow, the average velocity component of all molecules in the boundary layer, v_0, equals

$$v_0 = \frac{1}{2}\overline{v} = -c\,\lambda\,\frac{\partial v}{\partial r}\,. \tag{C.9}$$

Expressing Equations (C.9) and (C.6) for $r = r_0$, one gets

$$-c\,\lambda\,\frac{\partial v}{\partial r}\bigg|_{r=r_0} = \frac{r_0^2}{4\,\eta}\,\frac{\partial p}{\partial x} + B, \tag{C.10}$$

finally giving access to the integration constant B in the form

$$B = -c\,\lambda\,\frac{\partial v}{\partial r}\bigg|_{r=r_0} - \frac{r_0^2}{4\,\eta}\,\frac{\partial p}{\partial x}\,. \tag{C.11}$$

Considering Equation (C.5) in Equation (C.11) and inserting the result into the expression for the velocity (Equation (C.6)), the velocity field $v(r)$ is obtained in the form

$$v(r) = -\frac{1}{4\,\eta}\,\frac{\partial p}{\partial x}\left(-r^2 + 2\,c\,\lambda\,r_0 + r_0^2\right). \tag{C.12}$$

The flux through the tube, Q [m³/s], is obtained from integration of the velocity v (Equation (C.12)) over the cross-sectional area, reading

$$Q \;=\; \int_A v\,dA = \int_0^{r_0} 2\pi r\,v\,dr = -\frac{\pi}{2\,\eta}\frac{\partial p}{\partial x}\int_0^{r_0}(-r^3 + 2\,c\,\lambda\,r_0\,r + r_0^2\,r)\,dr$$

$$= \;-\frac{\pi\,r_0^4}{8\,\eta}\frac{\partial p}{\partial x}\left(1 + \frac{4\,c\,\lambda}{r_0}\right). \tag{C.13}$$

Considering that the mean free path λ is inversely proportional to the pressure p, as mentioned in [64], $4c\lambda/r_0$ can be replaced by b/p, giving

$$Q = -\frac{\pi\,r_0^4}{8\,\eta}\frac{\partial p}{\partial x}\left(1 + \frac{b}{p}\right), \tag{C.14}$$

where b [Pa] is a constant.

C.2   Identification of the slip-flow phenomenon

For the Hagen-Poiseuille law for incompressible fluids, $v = 0$ at the boundary of the tube at $r = r_0$, giving B from Equation (C.6) as

$$B = -\frac{r_0^2}{4\eta}\frac{\partial p}{\partial x}. \tag{C.15}$$

Based on the velocity field v, obtained from specification of Equation (C.12) for the case of incompressible flow, reading

$$v(r) = -\frac{1}{4\eta}\frac{\partial p}{\partial x}(-r^2 + r_0^2), \tag{C.16}$$

integration over the cross-sectional area of the tube yields the flux Q in the form

$$Q \;=\; \int_A v\,dA = \int_0^{r_0} 2\pi r\,v\,dr = -\frac{\pi}{2\,\eta}\frac{\partial p}{\partial x}\int_0^{r_0}\left(-r^3 + r_0^2\,r\right)dr$$

$$= \;-\frac{\pi\,r_0^4}{8\,\eta}\frac{\partial p}{\partial x}. \tag{C.17}$$

Comparison of Equation (C.14) with Equation (C.17) shows that the slip-flow phenomenon is represented by the term $(1 + b/p)$. Considering this slip-flow term in Darcy's equation, reading for incompressible flow (where $k = k_{int}$)

$$Q = -k_{int}\frac{A}{\eta}\frac{dp}{dx}, \tag{C.18}$$

the flux of a compressible fluid through porous media is obtained as

$$Q = -k\frac{A}{\eta}\frac{dp}{dx} = -k_{int}\left(1 + \frac{b}{p}\right)\frac{A}{\eta}\frac{dp}{dx}, \tag{C.19}$$

with the permeability k given by

$$k = k_{int} \left(1 + \frac{b}{p} \right) .$$

(C.20)

Appendix D

Back-calculation of material parameters for *in-situ* concrete

Considering the recorded mixing parameters of in-situ concrete without PP-fibers and $f_i = m_i/\rho_i$, with $i \in \{agg \ldots$ aggregates, $cem \ldots$ cement, $fa \ldots$ fly ash, $w \ldots$ water, $a \ldots$ air$\}$, where f_i [–] and m_i [kg/m³] are the specific volume fraction and the mass of the respective constituent per m³ of fresh concrete and ρ_i [kg/m³] is the respective specific density, yields the volume fraction of aggregates as

$$
\begin{aligned}
f_{agg} &= 1 - f_a - f_w - f_{fa} - f_{cem} \\
&= 1 - 0.035 - \frac{157}{1000} - \frac{60}{2300} - \frac{260}{3150} = 0.70\,.
\end{aligned} \tag{D.1}
$$

This leads to the specific aggregate density as

$$
\rho_{agg} = \frac{m_{agg}}{f_{agg}} = \frac{1909}{0.70} = 2730 \text{ kg/m}^3. \tag{D.2}
$$

In case of in-situ concrete with 1.5 kg/m³ PP-fibers, the aggregate mass can be determined from the concrete density as

$$
\begin{aligned}
\rho &= m_{agg} + m_{cem} + m_{fa} + m_w + m_{PP} = 2352 \text{ kg/m}^3 \quad \rightarrow \\
m_{agg} &= \rho - m_{PP} - m_w - m_{fa} - m_{cem} \\
&= 2352 - 1.5 - 157 - 60 - 260 = 1873.5 \text{ kg/m}^3,
\end{aligned} \tag{D.3}
$$

where $m_{PP} = 1.5$ kg/m^3 is the mass of the PP-fibers. With all specific densities at hand, the air content for in-situ concrete with 1.5 kg/m^3 PP-fibers can be determined from

$$
\begin{aligned}
f_a &= 1 - f_{PP} - f_w - f_{fa} - f_{cem} - f_{agg} \\
&= 1 - \frac{1.5}{910} - \frac{157}{1000} - \frac{60}{2300} - \frac{260}{3150} - \frac{1873.5}{2730} = 0.046\,.
\end{aligned}
\tag{D.4}
$$

Finite-element (FE) formulation of governing equations for heat and mass transport in heated concrete

E.1 Coupled FE-formulation of governing equations

E.1.1 Mass and energy balance equations [72, 90]

When the macroscopic mass balance equations for a porous medium (e.g., soil, concrete, etc.) are derived, all considerations are based on a multi-scale approach, starting at the microscopic level. By applying averaging techniques, the macroscopic mass balance equations can be determined from the respective microscopic balance equations [72], yielding[1] [72, 90]:

1. Solid phase (superscript s):

$$\frac{(1-n)}{\rho^s}\frac{D^s\rho^s}{Dt} - \frac{D^s n}{Dt} + (1-n)\ \text{div}\ \mathbf{v}^s = \frac{\dot{m}_{dehydr}}{\rho^s}\ ; \tag{E.1}$$

---

[1]The above depicted equations were derived for soils [72]. In case of concrete, the dehydration of the cement matrix during heating has to be considered additionally [90]. This results in (i) an additional source/sink term on the right-hand side of Equation (E.1) (affecting all other equations since they are obtained by summation with the solid mass balance equation) and Equation (E.2) and (ii) extension of the time derivative of the solid density.

2. Water phase (superscript w, involving the solid mass balance equation):

$$n\rho^w \frac{D^s S_w}{Dt} + nS_w \frac{D^s \rho^w}{Dt} - \rho^w(1-n)S_w \beta_s \frac{D^s T}{Dt} + \rho^w S_w \text{ div } \mathbf{v}^s$$

$$+ \text{ div } \left[\rho^w \frac{\mathbf{k}k^{rw}}{\eta^w} (-\text{grad } p^w + \rho^w \mathbf{g}) \right] - \frac{(1-n)\rho^w S_w}{\rho^s} \frac{\partial \rho^s}{\partial \xi_{dehydr}} \frac{D^s \xi_{dehydr}}{Dt}$$

$$= -\dot{m}_{vap} - \dot{m}_{dehydr} + \rho^w S_w \frac{\dot{m}_{dehydr}}{\rho^s} \; ; \tag{E.2}$$

3. Vapor phase (superscript gw, involving the solid mass balance equation):

$$-n\rho^{gw} \frac{D^s S_w}{Dt} + n(1-S_w) \frac{D^s \rho^{gw}}{Dt} - \rho^{gw}(1-n)(1-S_w) \beta_s \frac{D^s T}{Dt}$$

$$+\rho^{gw}(1-S_w) \text{ div } \mathbf{v}^s + \text{ div } \left[\rho^{gw} \frac{\mathbf{k}k^{rg}}{\eta^g} (-\text{grad } p^g + \rho^g \mathbf{g}) \right]$$

$$- \text{ div } \left[\rho^g \frac{M_a M_w}{M_g^2} \mathbf{D}_{eff} \text{ grad } \left(\frac{p^{gw}}{p^g} \right) \right] - \frac{(1-n)\rho^{gw}(1-S_w)}{\rho^s} \frac{\partial \rho^s}{\partial \xi_{dehydr}} \frac{D^s \xi_{dehydr}}{Dt}$$

$$= \dot{m}_{vap} + \rho^{gw}(1-S_w) \frac{\dot{m}_{dehydr}}{\rho^s} \; ; \tag{E.3}$$

4. Air phase (superscript ga, involving the solid mass balance equation):

$$-n\rho^{ga} \frac{D^s S_w}{Dt} + n(1-S_w) \frac{D^s \rho^{ga}}{Dt} - \rho^{ga}(1-n)(1-S_w) \beta_s \frac{D^s T}{Dt}$$

$$+\rho^{ga}(1-S_w) \text{ div } \mathbf{v}^s + \text{ div } \left[\rho^{ga} \frac{\mathbf{k}k^{rg}}{\eta^g} (-\text{grad } p^g + \rho^g \mathbf{g}) \right]$$

$$- \text{ div } \left[\rho^g \frac{M_a M_w}{M_g^2} \mathbf{D}_{eff} \text{ grad } \left(\frac{p^{ga}}{p^g} \right) \right] - \frac{(1-n)\rho^{ga}(1-S_w)}{\rho^s} \frac{\partial \rho^s}{\partial \xi_{dehydr}} \frac{D^s \xi_{dehydr}}{Dt}$$

$$= \rho^{ga}(1-S_w) \frac{\dot{m}_{dehydr}}{\rho^s} \; . \tag{E.4}$$

Finally, combination of Equations (E.1), (E.2), and (E.3) (in order to eliminate the mass source term associated with vaporization, $\dot{m}_{vap}$) yields the governing mass balance equation for the water phase (comprising both liquid water and water vapor), reading[2] (see

---

[2]For the case of concrete under fire loading (fast heating), several assumptions lead to the following simplifications:

- No movement of the solid phase is considered, therefore the terms including the solid velocity vanish;

- Gravitational effects are considered negligible, therefore the corresponding terms in the advectional flux terms vanish;

Equation (3.1))

$$\underbrace{n(\rho^w - \rho^{gw})\frac{D^s S_w}{Dt}}_{1} + \underbrace{n(1 - S_w)\frac{D^s \rho^{gw}}{Dt}}_{2} + \underbrace{nS_w\frac{D^s \rho^w}{Dt}}_{3}$$

$$\underbrace{-(1 - n)\beta_s \left[\rho^{gw} + (\rho^w - \rho^{gw})S_w\right]\frac{D^s T}{Dt}}_{4}$$

$$-\underbrace{\mathrm{div}\left(\rho^{gw}\frac{\mathbf{k}k^{rg}}{\eta^g}\mathrm{grad}\,p^g\right)}_{5} - \underbrace{\mathrm{div}\left(\rho^w\frac{\mathbf{k}k^{rw}}{\eta^w}\mathrm{grad}\,p^w\right)}_{6}$$

$$-\underbrace{\mathrm{div}\left[\rho^g\frac{M_a M_w}{M_g^2}\mathbf{D}_{eff}\,\mathrm{grad}\left(\frac{p^{gw}}{p^g}\right)\right]}_{7}$$

$$= -\underbrace{\frac{(1 - n)\left[\rho^{gw}(1 - S_w) + \rho^w S_w\right]}{\rho^s}\frac{\partial \rho^s}{\partial \xi}\frac{D^s \xi}{Dt}}_{8}$$

$$-\underbrace{\left[\rho^{gw}(1 - S_w) + \rho^w S_w\right]\frac{\dot{m}_{dehydr}}{\rho^s}}_{9} + \underbrace{\dot{m}_{dehydr}}_{10} . \qquad (E.5)$$

In Equation (E.5), terms 1, 2, 3, and 4 are time derivatives and represent accumulation or capacity terms. Part of term 1 and term 2 are associated with the water-vapor density ρ^{gw}, whereas the other part of term 1 and term 3 are associated with the density of water, ρ^w. Term 4 originates from the time derivative of the solid density ρ^s and is associated with the volume expansion. Terms 5, 6, and 7 are space derivatives and represent flux terms. Whereas terms 5 and 6 account for Darcian (pressure-driven) flow, associated with water vapor and liquid water, respectively, term 7 accounts for Fick's flow (concentration gradient as driving force) of water vapor in the gaseous mixture. On the RHS, source and sink terms are collected, term 8 originates from the time derivative of the solid density ρ^s and is associated with the change in solid density in consequence of dehydration of the cement paste. Terms 9 and 10 are source terms associated with dehydration, whereas term 9 originates from the mass balance equation of the solid phase, which is included in Equation (E.5). Term 10 originates from the mass balance equation of the liquid water

- The term $\dot{m}_{dehydr}$ is considered to be the amount of water that is liberated during dehydration, therefore it needs to be negative in the solid mass balance equation and positive in the water mass balance equation.

- The dehydration process is from now on described by the degree of hydration ξ rather than by the degree of dehydration ξ_{dehydr}, therefore the sign changes in the respective derivatives (because of $\xi_{dehydr} = 1 - \xi$).

phase and corresponds to the water that is liberated during dehydration.

Combination of Equations (E.1) and (E.4) yields the governing mass balance equation for the dry-air phase, reading (see Equation (3.2))

$$
\underbrace{-n\rho^{ga}\frac{D^s S_w}{Dt}}_{1} + \underbrace{n(1-S_w)\frac{D^s \rho^{ga}}{Dt}}_{2} - \underbrace{\rho^{ga}(1-n)(1-S_w)\beta_s\frac{D^s T}{Dt}}_{3}
$$

$$
- \underbrace{\mathrm{div}\left(\rho^{ga}\frac{\mathbf{k}k^{rg}}{\eta^g}\mathrm{grad}\,p^g\right)}_{4} - \underbrace{\mathrm{div}\left[\rho^g\frac{M_a M_w}{M_g^2}\mathbf{D}_{eff}\,\mathrm{grad}\,\left(\frac{p^{ga}}{p^g}\right)\right]}_{5}
$$

$$
= -\underbrace{\frac{(1-n)\rho^{ga}(1-S_w)}{\rho^s}\frac{\partial\rho^s}{\partial\xi}\frac{D^s\xi}{Dt}}_{6} - \underbrace{\rho^{ga}(1-S_w)\frac{\dot{m}_{dehydr}}{\rho^s}}_{7} . \tag{E.6}
$$

In Equation (E.6), terms 1, 2, 3 are time derivatives and represent accumulation or capacity terms. Terms 1 and 2 are associated with the dry-air density ρ^{ga}, whereas term 3 originates from the time derivative of the solid density ρ^s and is associated with the volume expansion. Terms 4 and 5 are space derivatives and represent flux terms. Whereas term 4 accounts for Darcian (pressure-driven) flow of dry air, term 5 accounts for Fick's flow (concentration gradient as driving force) of dry air in the gaseous mixture. On the RHS, source and sink terms are collected, term 6 originates from the time derivative of the solid density ρ^s and is associated with the change in solid density in consequence of dehydration of the cement paste. Term 7 is a source term associated with dehydration and originates from the solid mass balance equation, which is included in Equation (E.6).

In the same manner as for the mass balance equations, the microscopic energy balance equation is derived and transformed (by using the second law of thermodynamics, i.e., entropy inequality) into a macroscopic energy (enthalpy) balance equation (see [72, 90] for details), which is valid for all phases (solid, water, gas). For derivation of the enthalpy balance equation for the multiphase medium, it is assumed that the phases are locally in thermodynamic equilibrium, meaning that the averaged temperatures of the different phases are equal at each point. The macroscopic energy balance equations for the different phases, including dehydration of the cement paste read (under consideration of Fourier's law for heat conduction, giving the heat flux, see [90] for details):

1. Solid phase (superscript s):

$$
\rho_s c_p^s\frac{\partial T}{\partial t} + \rho_s c_p^s\mathbf{v}^s\,\mathrm{grad}\,T - \mathrm{div}\,(\lambda^s\,\mathrm{grad}\,T) = \rho_s h^s + \rho_s R_H^s - \dot{m}_{dehydr}H^{ws}\tag{E.7}
$$

2. Water phase (superscript w):

$$
\rho_w c_p^w\frac{\partial T}{\partial t} + \rho_w c_p^w\mathbf{v}^{ws}\,\mathrm{grad}\,T - \mathrm{div}\,(\lambda^w\,\mathrm{grad}\,T)
$$

$$
= \rho_w h^w + \rho_w R_H^w + \dot{m}_{vap}H^w + \dot{m}_{dehydr}H^w \tag{E.8}
$$

3. Gas phase (water and dry air, superscript g):

$$\rho_g c_p^g \frac{\partial T}{\partial t} + \rho_g c_p^g \mathbf{v}^{gs} \text{ grad } T - \text{ div } (\lambda^g \text{ grad } T) = \rho_g h^g + \rho_g R_H^g - \dot{m}_{vap} H^{gw} \quad \text{(E.9)}$$

Summing up Equations (E.7) to (E.9) results in elimination of the heat exchange terms $(\rho_\pi R_H^\pi)$. Neglecting further the density heat source terms $(\rho_\pi h^\pi)$ and convective heat fluxes within the solid phase yields [41, 42, 43, 90, 112, 115]:

$$(\rho c_p)_{eff} \frac{\partial T}{\partial t} + \rho^g c_p^g \left[\frac{\mathbf{k} k^{rg}}{\eta^g} (-\text{grad } p^g + \rho^g \mathbf{g}) \right] \text{ grad } T$$

$$+ \rho^w c_p^w \left[\frac{\mathbf{k} k^{rw}}{\eta^w} (-\text{grad } p^w + \rho^w \mathbf{g}) \right] \text{ grad } T - \text{ div } (\lambda_{eff} \text{ grad } T)$$

$$= -\dot{m}_{vap} h + \dot{m}_{dehydr} l_\xi^w \,, \quad \text{(E.10)}$$

where the mass flux terms are introduced by using Darcy's law and the mass source term for vaporization, $\dot{m}_{vap}$, is obtained from the mass balance equation for the water phase (Equation (E.2)), yielding

$$\dot{m}_{vap} = -n\rho^w \frac{D^s S_w}{Dt} - n S_w \frac{D^s \rho^w}{Dt} + \rho^w (1-n) S_w \beta_s \frac{D^s T}{Dt} - \rho^w S_w \text{ div } \mathbf{v}^s$$

$$- \text{ div } \left[\rho^w \frac{\mathbf{k} k^{rw}}{\eta^w} (-\text{grad } p^w + \rho^w \mathbf{g}) \right] + \frac{(1-n)\rho^w S_w}{\rho^s} \frac{\partial \rho^s}{\partial \xi_{dehydr}} \frac{D^s \xi_{dehydr}}{Dt}$$

$$+ \rho^w S_w \frac{\dot{m}_{dehydr}}{\rho^s} - \dot{m}_{dehydr} \,. \quad \text{(E.11)}$$

Introduction of the same assumptions as for the mass balance equations ((i) no movement of the solid phase takes place, (ii) gravitational effects are negligible, (iii) opposite sign notation of $\dot{m}_{dehydr}$, (iv) replacing ξ_{dehydr} by ξ), yields the final form of Equation (E.10), reading (see Equation (3.3))

$$\underbrace{(\rho c_p)_{eff} \frac{\partial T}{\partial t}}_{1} - \left(\underbrace{\rho^g c_p^g \frac{\mathbf{k} k^{rg}}{\eta^g} \text{grad } p^g}_{2} + \underbrace{\rho^w c_p^w \frac{\mathbf{k} k^{rw}}{\eta^w} \text{grad } p^w}_{3} \right) \text{ grad } T$$

$$- \underbrace{\text{ div } (\lambda_{eff} \text{ grad } T)}_{4} = - \underbrace{\dot{m}_{vap} h}_{5} - \underbrace{\dot{m}_{dehydr} l_\xi^w}_{6} \,, \quad \text{(E.12)}$$

with (see Equation (3.4))

$$
\dot{m}_{vap} = - \underbrace{n\rho^w \frac{D^s S_w}{Dt}}_{1} - \underbrace{nS_w \frac{D^s \rho^w}{Dt}}_{2} + \underbrace{\rho^w(1-n)S_w \beta_s \frac{D^s T}{Dt}}_{3}
$$

$$
+ \underbrace{\mathrm{div} \left(\rho^w \frac{\mathbf{k}k^{rw}}{\eta^w} \mathrm{grad}\, p^w \right)}_{4} - \underbrace{\frac{(1-n)\rho^w S_w}{\rho^s} \frac{\partial \rho^s}{\partial \xi} \frac{D^s \xi}{Dt}}_{5}
$$

$$
- \underbrace{\rho^w S_w \frac{\dot{m}_{dehydr}}{\rho^s}}_{6} + \underbrace{\dot{m}_{dehydr}}_{7} . \tag{E.13}
$$

In Equation (E.12), term 1 represents the heat capacity of the multi-phase continuum, whereas terms 2, 3, and 4 are space derivatives or flux terms. Terms 2 and 3 account for heat advection caused by mass transport associated with the gas mixture and with the liquid water, respectively. Term 4 represents energy transport in consequence of heat conduction (Fourier's law). On the RHS, source and sink terms are collected. Term 5 accounts for consumption or release of energy due to vaporization or condensation of water, respectively, the corresponding mass source term, $\dot{m}_{vap}$, is given in Equation (E.13). Term 6 represents energy consumption in consequence of dehydration of the cement paste. Equation (E.13) results, as mentioned before, from rearranging the water mass balance equation (Equation (E.2)) and has a similar structure as Equation (E.5).

E.1.2   Primary state variables, constitutive relations

In this analysis, the primary state variables are chosen to be the capillary pressure p^c [Pa], the gas pressure p^g [Pa], and the temperature T [°C].

The capillary pressure p^c [Pa] is defined as the difference between gas pressure p^g and water pressure p^w, reading

$$
p^c = p^g - p^w . \tag{E.14}
$$

For a detailed definition and the derivation of the capillary pressure, see [88].

For definition of the gas pressure p^g [Pa], Dalton's law is employed, defining p^g as the sum of the partial pressures of water vapor and dry air, respectively, hence

$$
p^g = p^{gw} + p^{ga} . \tag{E.15}
$$

In the following, the variables are defined in the order they appear in Equations (E.5), (E.6), and (E.12). For details on selected empirical functions, see [41, 90].

- The porosity of concrete n [–] is considered to be temperature-dependent, thus

$$
n = n(T) = n_0 + A_n(T - T_0) , \tag{E.16}
$$

with A_n [1/°C] as an empirical parameter depending on the concrete mix design and n_0 [–] as reference porosity at reference temperature T_0 [°C].

- The water density ρ^w [(kg water)/(m³ water)] depends on temperature T [°C] and water pressure p^w [Pa]. Since ρ^w increases by 0.4 % for a pressure increase of 10 MPa, the compressibility of liquid water is neglected. For capturing the temperature dependence of ρ^w, an empirical formula (Furbish formula [38]) is introduced, reading (for $T \leq 374.15$ °C)

$$
\begin{aligned}
\rho^w &= \rho^w(T) \\
&= (b_0 + b_1 T + b_2 T^2 + b_3 T^3 + b_4 T^4 + b_5 T^5) \\
&\quad + (p_{w1} - p_{wrif})(a_0 + a_1 T + a_2 T^2 + a_3 T^3 + a_4 T^4 + a_5 T^5), \quad \text{(E.17)}
\end{aligned}
$$

with $b_0 = 1.0213 \cdot 10^3$, $b_1 = -7.7377 \cdot 10^{-1}$, $b_2 = 8.7696 \cdot 10^{-3}$, $b_3 = -9.2118 \cdot 10^{-5}$ $b_4 = 3.3534 \cdot 10^{-7}$ $b_5 = -4.4034 \cdot 10^{-10}$, $p_{w1} = 1.0 \cdot 10^7$ Pa, $p_{wrif} = 2.0 \cdot 10^7$ Pa, $a_0 = 4.8863 \cdot 10^{-7}$, $a_1 = -1.6528 \cdot 10^{-9}$, $a_2 = 1.8621 \cdot 10^{-12}$, $a_3 = 2.4266 \cdot 10^{-13}$, $a_4 = -1.5996 \cdot 10^{-15}$, and $a_5 = 3.3703 \cdot 10^{-18}$.

- The water-vapor density ρ^{gw} [(kg vapor)/(m³ gas)] is expressed by the partial pressure of water vapor via Clapeyron's law for ideal gases, yielding

$$
\rho^{gw} = \rho^{gw}(T, p^{gw}) = \frac{M_w}{R\Theta} p^{gw}, \quad \text{(E.18)}
$$

where M_w [kg/mol] is the molar mass of water, R [J/(mol K)] is the gas constant, and Θ [K] is the absolute temperature. In Equation (E.18), the partial pressure of water vapor, p^{gw} [Pa], is given as the product of saturation vapor pressure p^{gws} [Pa] and relative humidity RH [–], whereas the latter is defined by the Kelvin-Laplace law. p^{gws} can be expressed by the primary state variables as

$$
p^{gw} = p^{gws}(T) \cdot RH(T, p^c, \rho^w(T)) = p^{gws}(T) \exp\left(-\frac{p^c M_w}{\rho^w R\Theta}\right). \quad \text{(E.19)}
$$

The saturation vapor pressure, p^{gws} [Pa], is defined by an empirical relation (Hyland-Wexler formula [56]), reading

$$
p^{gws} = p^{gws}(T) = \exp\left[\frac{c_1}{\Theta} + c_2 + c_3\Theta + c_4\Theta^2 + c_5\Theta^3 + c_6\ln(\Theta)\right], \quad \text{(E.20)}
$$

with $c_1 = -5.8002206 \cdot 10^3$, $c_2 = 1.3914993$, $c_3 = -4.8640239 \cdot 10^{-2}$, $c_4 = 4.1764768 \cdot 10^{-5}$, $c_5 = -1.4452093 \cdot 10^{-8}$, and $c_6 = 6.5459673$.

- The saturation S_w [–] is considered to be a function of temperature T [°C] and capillary pressure p^c [Pa], reading (see Subsection 3.4.2 for details)

$$
S_w = S_w(T, p^c). \quad \text{(E.21)}
$$

- The thermal expansion coefficient for concrete (solid phase), β_s [1/°C], is considered to be constant with an average value for β_s for the temperature range under consideration.

- The intrinsic permeability coefficient $\mathbf{k}$ [m²] is defined by an isotropic temperature-dependent parameter determined from permeability experiments, giving the relationship (see Subsection 3.4.3 for details)

$$\mathbf{k} = k(T)\,\mathbf{1}\,. \tag{E.22}$$

- The relative permeabilities with respect to the gas mixture and the water phase, k^{rg} [–] and k^{rw} [–], respectively, take into account multi-phase flow and, hence, the reduction of the permeability to one phase in case a second phase is present in the pore structure. Therefore,

$$k^{rg} = k^{rg}\left(S_w\left(T,p^c\right)\right) \tag{E.23}$$

and

$$k^{rw} = k^{rw}\left(S_w\left(T,p^c\right)\right) \tag{E.24}$$

need to be taken into account (see Subsection 3.4.3 for details).

The relative permeabilities of soils to water have been under sufficient investigation regarding ground water flow (see, e.g., [80, 88]). More recent research on the permeability of partially-saturated concrete showed that the developed relations are also applicable to concrete [79, 100], reading (see Figure E.1)

$$k^{rw} = S_w^p \left[1 - \left(1 - S_w^{(1/m)}\right)^m\right]^2 \tag{E.25}$$

and

$$k^{rg} = (1 - S_w)^p \left(1 - S_w^{(1/m)}\right)^{2m}\,. \tag{E.26}$$

Another model for the relative permeability to water, k^{rw}, is proposed in [15, 102], where k^{rw} is defined proportionally to the solid-liquid interface, yielding [15, 41, 102]

$$k^{rw} = \left(\frac{S_w - S_w^r}{1 - S_w^r}\right)^{A_w}\,, \tag{E.27}$$

where S_w^r [–] is the residual saturation (the porous medium cannot be dewatered further) and A_w [–] is an empirical parameter. According to [15, 41, 122], the relative permeability to gas can be defined as

$$k^{rg} = 1 - \left(\frac{S_w}{S_w^{cr}}\right)^{A_g}\,, \tag{E.28}$$

where S_w^{cr} [–] is the critical saturation (above which there is no gas flow in the porous medium) and A_g [–] is an empirical parameter. Plots of Equations (E.27) and (E.28) are depicted in Figure E.1.
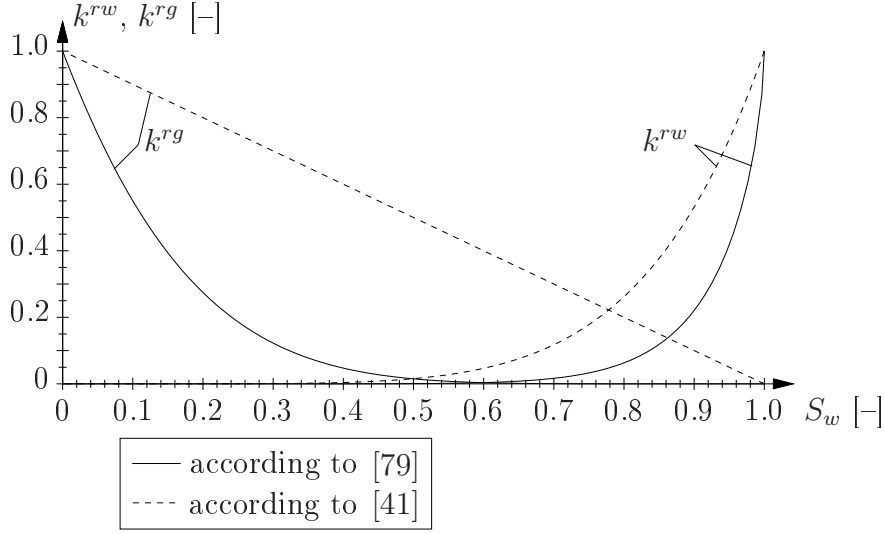
Figure E.1: Relative permeabilities of concrete to water and gas versus degree of saturation (parameters: $p = 5.5$, $m = 0.56$, $S_w^r = 0$, $A_w = 6.0$, $S_w^{cr} = 1.0$, and $A_g = 1.0$)

- The dynamic viscosity for the gas mixture, η^g [Pa s], can be expressed by an empirical relationship, depending on the dynamic viscosities of its constituents, i.e., water vapor and dry air, and the pressures of the gas mixture and the dry air pressure [41, 90]:

$$\eta^g = \eta^g(\eta^{gw}, \eta^{ga}, p^g, p^{ga}). \tag{E.29}$$

The dynamic viscosities of water vapor and dry air, η^{gw} [Pa s] and η^{ga} [Pa s], respectively, are functions of temperature T [°C]:

$$\eta^{gw} = \eta^{gw}(T) \quad \text{and} \quad \eta^{ga} = \eta^{ga}(T). \tag{E.30}$$

Using Equation (E.15), the partial pressure of the dry air phase, p^{ga}[Pa], can be expressed by the pressure of the gas mixture, p^g [Pa], and the partial pressure of the water-vapor phase, p^{gw} [Pa]. This yields

$$
\begin{aligned}
\eta^g &= \eta^g \left(\eta^{gw}(T), \eta^{ga}(T), p^g, p^g - p^{gw}(T, p^c, \rho^w(T)) \right) \\
&= \eta^{gw} + (\eta^{ga} - \eta^{gw}) \left(\frac{p^{ga}}{p^g} \right)^{b_g},
\end{aligned} \tag{E.31}
$$

with

$$\eta^{gw} = \eta^{gw}(T) = \eta^{gw0} + a_{gw}(T - T_0) \tag{E.32}$$

and

$$\eta^{ga} = \eta^{ga}(T) = \eta^{ga0} + a_{ga}(T - T_0) + b_{ga}(T - T_0)^2. \tag{E.33}$$

In Equation (E.31), $b_g = 0.608$. In Equations (E.32) and (E.33), $\eta^{gw0} = 8.85 \cdot 10^{-6}$ Pa s, $a_{gw} = 3.633 \cdot 10^{-8}$ (Pa s)/°C, $\eta^{ga0} = 17.17 \cdot 10^{-6}$ Pa s, $a_{ga} = 4.733 \cdot 10^{-8}$ (Pa s)/°C, and $b_{ga} = -2.222 \cdot 10^{-11}$ (Pa s)/(°C)².

- The dynamic viscosity for the water phase, η^w [Pa s], is expressed by a temperature-dependent empirical function, reading

$$\eta^w = \eta^w(T) = a_w(T + 44.15)^{b_w},$$ (E.34)

with $a_w = 6.612 \cdot 10^{-1}$ and $b_w = -1.562$.

- The gas density ρ^g [(kg gas)/(m³ gas)], which is defined considering Equation (E.15) as the density of the mixture of water vapor and dry air, can be written as

$$\rho^g = \rho^g[\rho^{gw}(T, p^{gw}), \rho^{ga}(T, p^{ga})] = \rho^{gw} + \rho^{ga},$$ (E.35)

where ρ^{gw} [(kg vapor)/(m³ gas)] is the water-vapor density and ρ^{ga} [(kg air)/(m³ gas)] is the dry-air density.

- The molar mass of water and air, M_w and M_a [kg/mol], respectively, are constants, with $M_w = 18.0152 \cdot 10^{-3}$ kg/mol and $M_a = 28.95 \cdot 10^{-3}$ kg/mol (see, e.g., [17]).

- The molar mass of the gas mixture M_g [kg/mol] is determined by application of Clapeyron's law for ideal gases to Equation (E.35), yielding, under consideration of Equation (E.15) for description of the dry-air pressure p^{ga},

$$\rho^g \;=\; \rho^g(T, p^g) = \frac{M_g}{R\Theta} p^g = \frac{M_w}{R\Theta} p^{gw} + \frac{M_a}{R\Theta} p^{ga}$$

$$\rightarrow \quad M_g \;=\; M_g(p^{gw}(p^{gws}(T), RH(T, p^c, \rho^w(T))), p^g)$$

$$\;=\; \frac{1}{p^g}\left(M_w p^{gw} + M_a p^{ga}\right) = M_a + (M_w - M_a)\frac{p^{gw}}{p^g}.$$ (E.36)

- According to [90], the effective diffusivity of concrete, $\mathbf{D}_{eff}$ [m²/s], is isotropic and dependent on the diffusivity of water vapor in dry air of concrete, D_{va} [m²/s], the tortuosity of the pore system, τ [–], and the pore-structure factor f_s [–], thus

$$\mathbf{D}_{eff} = D_{eff}(D_{va}(T, p^g), \tau(n(T), S_w(T, p^c)), f_s(T))\,\mathbf{1}.$$ (E.37)

D_{eff} depends on the diffusivity and the pore structure of the porous medium as well as the degree of saturation, reading

$$D_{eff} = \tau n(1 - S_w) f_s D_{va}.$$ (E.38)

In the presented numerical, model the tortuosity is defined as

$$\tau = n^{1/3}(1 - S_w)^{7/3}.$$ (E.39)

The pore structure factor f_s [–] accounts for the form of the pores within the porous medium and lies within the range $0 \leq f_s \leq 1$. The diffusivity of the porous medium depends on temperature Θ and gas pressure p^g, thus

$$D_{va} = D_{va0} \left(\frac{\Theta}{\Theta_0}\right)^{A_{Dva}} \frac{p_{atm}}{p^g},$$ (E.40)

where D_{va0} [m²/s] is the reference diffusivity at reference temperature Θ_0 [K], $A_{D_{va}}$ is an empirical parameter depending on the mix design under consideration, and p_{atm} [Pa] is the atmospheric pressure.

- The solid skeleton density ρ^s [(kg solid)/(m³ solid)] is temperature dependent, reading

$$\rho^s = \rho^s(T) = \rho^{s0} + A_{\rho^s}(T - T_0)\,, \tag{E.41}$$

with A_{ρ^s} [(kg solid)/(m³ solid °C)] as an empirical parameter depending on the concrete mix design and ρ^{s0} [(kg solid)/(m³ solid)] as reference density at reference temperature T_0 [°C] (see [90] for details).

- The degree of hydration ξ [–] is defined as the ratio between the current and the initial amount of chemically-bound water (water that was consumed during hydration of the cement paste), m_h and m_{h0}, respectively, thus

$$\xi = \frac{m_h}{m_{h0}}\,. \tag{E.42}$$

During dehydration, ξ decreases with increasing temperature (therefore, $\dot{\xi} < 0$) as chemical reactions take place and water is liberated (which is accounted for by the source term $\dot{m}_{dehydr}$ [(kg water)/(s m³)], see Equation (E.47)). Hence, the hydration degree is considered to be a function of the maximum temperature reached in the respective region of the structure (see Subsection 3.4.1 for details):

$$\xi = \xi(T_{max})\,. \tag{E.43}$$

In the numerical model, one of the empirical functions depicted in Figure E.2 can be considered:

1. Relation on basis of thermogravimetric measurements I:
   Hereby, the experimental results presented in [52] are fit by an empirical function, reading [90]

$$\begin{aligned}
\xi &= 1 \quad \text{for } T < 105°\text{C and} \\
\xi &= 1 - \frac{1}{2}\left\{1 + \sin\left[\frac{\pi}{2}\left(1 - 2\exp\left[-0.004(T - 105)\right]\right)\right]\right\} \\
&\quad \text{for } T \geq 105°\text{C}\,. \tag{E.44}
\end{aligned}$$

2. Relation on basis of mechanical properties:
   Hereby, the linear dependence of the Young's modulus on the degree of hydration during cement hydration is extended to dehydration in consequence of temperature loading [123]. On basis of design curves for $E(T)/E_0(T_0)$ (see, e.g., [22]), a curve fit was found for $\xi = \xi(T)$, reading [92]

$$\xi = \sqrt{\exp\left[-(T/345.4285)^2\right]}\,. \tag{E.45}$$

3. Relation on basis of thermogravimetric measurements II:
   On basis of experimental results presented in [117], the empirical function depicted in Figure E.2(c) is introduced within the numerical model, reading

$$
\begin{aligned}
\xi &= 1 \quad \text{for } T < 80°\text{C and} \\
\xi &= \frac{1}{2}\left\{1 + \cos\left[\frac{\pi}{1010}(T-80)\right]\right\} \quad \text{for } 80 \le T \le 1090°\text{C and} \\
\xi &= 0 \quad \text{for } T > 1090°\text{C}.
\end{aligned}
\tag{E.46}
$$

• The liberated mass during dehydration is defined as $\dot{m}_{dehydr}$ [(kg water)/(s m^3 porous material)]. As dehydration of the cement paste results in liberation of water, $\dot{m}_{dehydr}$ is considered to be a function of the degree of hydration ξ [–], yielding

$$
\dot{m}_{dehydr} = \dot{m}_{dehydr}(\xi(T)) = -m_c f_h \frac{m_w}{m_c}\frac{\partial \xi}{\partial t}\,,
\tag{E.47}
$$

where m_w/m_c [(kg water)/(kg binder)] is the water-cement (binder) ratio with m_w [(kg water)/m^3] as the water content and m_c [(kg binder)/m^3] as the cement (binder) content and f_h [(kg hydrated binder)/(kg binder)] is the aging coefficient which describes the degree of hydration that is reached during hardening of the concrete, with $0 \le f_h \le 1$ and $f_h = 1$ only for full hydration.

• The dry-air density ρ^{ga} [(kg air)/(m^3 gas)] can be expressed by the pressure of the dry-air phase, p^{ga} [Pa], under consideration of Clapeyron's law for ideal gases, yielding

$$
\rho^{ga} = \rho^{ga}(T, p^{ga}) = \frac{M_a}{R\Theta}p^{ga}\,.
\tag{E.48}
$$

By application of Equation (E.15), the dry-air pressure can be expressed by the pressure of the gas mixture and the partial pressure of the water-vapor phase (see Equation (E.19)), yielding

$$
\begin{aligned}
p^{ga} &= p^g - p^{gw}(p^{gws}(T), RH(T, p^c, \rho^w(T))) \\
&= p^g - p^{gws}(T)\exp\left(-\frac{p^c M_w}{\rho^w R\Theta}\right)\,.
\end{aligned}
\tag{E.49}
$$

• The effective thermal capacity of concrete as a partially-saturated porous material, $(\rho c_p)_{eff}$ [J/(m^3 K)], is defined as the sum of the thermal capacities of the solid, water, and gas phase, respectively, reading

$$
(\rho c_p)_{eff} = \rho_s c_p^s + \rho_w c_p^w + \rho_g c_p^g\,,
\tag{E.50}
$$

where c_p^s [J/((kg solid) K)], c_p^w [J/((kg water) K)], and c_p^g [J/((kg gas) K)] are the heat capacities of the respective phases.
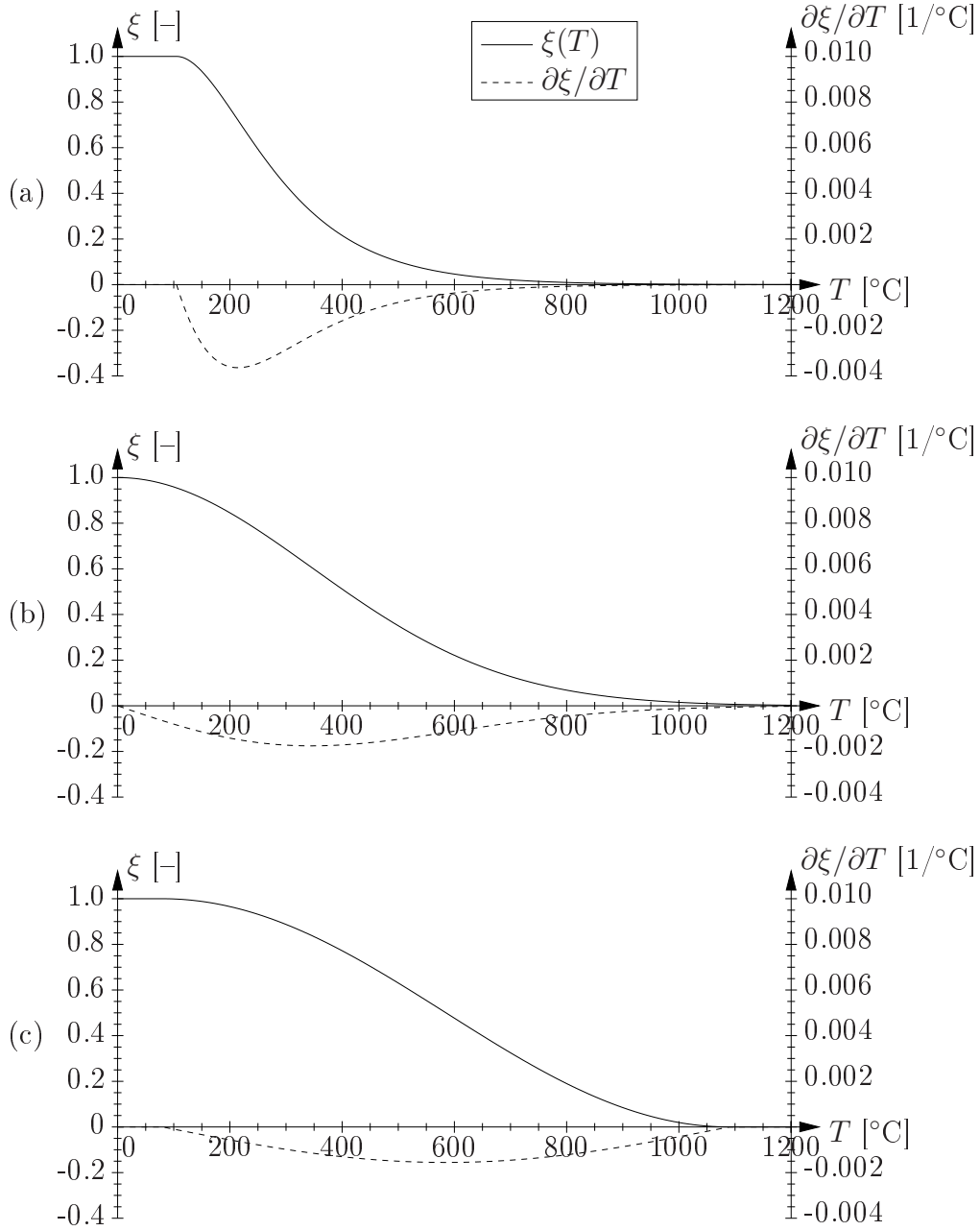
Figure E.2: Empirical functions for describing the degree of hydration with respect to temperature: (a) [90]; (b) [92]; (c) [117]

The temperature-dependent specific heat capacity of the solid phase, c_p^s [J/((kg solid) K)] is given by

$$c_p^s = c_p^s(T) = c_p^{s0} + A_{c_p^s}(T - T_0)\,, \tag{E.51}$$

with $A_{c_p^s}$ [J/((kg solid) K °C] as an empirical parameter depending on the type of concrete and c_p^{s0} [J/((kg solid) K)] as reference specific heat capacity at reference temperature T_0 [°C].

The thermal capacity of the gas phase $(\rho^g c_p^g)$ is a function of the thermal capacities of water vapor and dry air, reading

$$
\begin{aligned}
\rho^g c_p^g &= \rho^g c_p^g \left(\rho^g [\rho^{gw}(T, p^c), \rho^{ga}(T, p^g, p^c)], c_p^{ga}(T), \rho^{gw}(T, p^c), c_p^{gw}(T) \right) \\
&= \rho^g c_p^{ga} + \rho^{gw}(c_p^{gw} - c_p^{ga}).
\end{aligned}
\tag{E.52}
$$

with $c_p^{gw} = 1880.0$ J/(kg K) and $c_p^{ga} = 1007.0$ J/(kg K), which are the respective values for a reference temperature of 20 °C (see, e.g., [17]).

The specific heat capacity of the water phase is set to $c_p^w = 4180.0$ J/(kg K) (see, e.g. [17]).

Introducing the expressions for the densities per unit volume of the porous medium, reading $\rho_s = (1 - n)\rho^s$ [(kg solid)/m³], $\rho_w = nS_w\rho^w$ [(kg water)/m³], and $\rho_g = n(1 - S_w)\rho^g$ [(kg gas)/m³] finally yields [41, 90]

$$
\begin{aligned}
(\rho c_p)_{eff} &= (\rho c_p)_{eff} \left(n(T), \rho^s(T), c_p^s(T), S_w(T, p^c), \rho^w(T), c_p^w(T), \right. \\
&\qquad \left. \rho^g [\rho^{gw}(T, p^c), \rho^{ga}(T, p^g, p^c)], c_p^{ga}(T), \rho^{gw}(T, p^c), c_p^{gw}(T) \right) \\
&= (1 - n)\rho^s c_p^s \\
&\quad + n \left\{ S_w \rho^w c_p^w + (1 - S_w) \left[\rho^g c_p^{ga} + \rho^{gw}(c_p^{gw} - c_p^{ga}) \right] \right\}.
\end{aligned}
\tag{E.53}
$$

- The effective thermal conductivity of concrete, λ_{eff} [W/(m K)], can be defined as the sum of the thermal conductivities of the solid, water, and gas constituent, respectively, reading

$$
\lambda_{eff} = \lambda_s + \lambda_w + \lambda_g = (1 - n)\lambda^s + nS_w\lambda^w + n(1 - S_w)\lambda^g.
\tag{E.54}
$$

Another method to account for the dependence of λ_{eff} upon the three constituents is to introduce porosity n [–] and saturation S_w [–], yielding

$$
\begin{aligned}
\lambda_{eff} &= \lambda_{eff} \left(\lambda^s(T), n(T), \rho^w(T), S_w(T, p^c), \rho^s(T) \right) \\
&= \lambda^s \left[1 + \frac{4n\rho^w S_w}{(1 - n)\rho^s} \right],
\end{aligned}
\tag{E.55}
$$

where λ^s [W/(m K)] is the thermal conductivity of the dry material, which can be expressed by an empirical relationship [52, 90], reading

$$
\lambda^s = \lambda^s(T) = \lambda^{s0} + A_\lambda (T - T_0),
\tag{E.56}
$$

with A_λ [W/(m K °C)] as an empirical parameter depending on the type of concrete and λ^{s0} [W/(m K)] as reference solid thermal conductivity at reference temperature T_0 [°C].

- The specific enthalpy of vaporization, h [J/(kg water)], which describes the phase change of water into vapor, is defined as the difference between the enthalpy of water and the enthalpy of vapor, both being a function of temperature. A temperature-dependent empirical relation for h is introduced, reading

$$h = h(T) = a_h \left(T_{cr} - T\right)^{b_h} , \qquad (E.57)$$

with $a_h = 2.672 \cdot 10^5$ J/kg, $b_h = 0.38$, and $T_{cr} = 374.15\,°C$ as the critical temperature of water.

- The specific enthalpy of dehydration with respect to the water phase, l_ξ^w [J/(kg water)], is deduced from the specific enthalpy of dehydration for the hydration products, l_ξ [J/(kg binder)], reading

$$l_\xi^w \;\; = \;\; l_\xi \frac{m_c}{m_w} , \qquad (E.58)$$

which is constant. In Equation (E.58), the expression m_c/m_w is the inverse of the water-cement (binder) ratio. l_ξ is determined on basis of the chemical composition of the cement under consideration, reading

$$l_\xi = \frac{\displaystyle\sum_i l_{\xi,i} m_i}{\displaystyle\sum_i m_i} , \qquad (E.59)$$

where $l_{\xi,i}$ [J/kg] and m_i [kg] are the specific enthalpy of dehydration and the mass of the i-th cementitious compound, respectively.

E.1.3 Weak formulation and discretization

The complete description of the mass and heat transport problem is achieved by introducing corresponding initial conditions ($p^c(t{=}0) = p_0^c$, $p^g(t{=}0) = p_0^g$, and $T(t{=}0) = T_0$) and boundary conditions at the surface of the concrete structure (FE-nodes "1" and "$n_e{+}1$", see Figure 3.1). The latter are either prescribed pressures and temperatures (Dirichlet's boundary conditions, first kind according to [114]), reading

$$
\begin{array}{llllllll}
p_1^c & = & \overline{p}_1^c & \text{on } S_c^1 & \text{or} & p_1^g = \overline{p}_1^g & \text{on } S_g^1 & \text{or} \quad T_1 = \overline{T}_1 \quad \text{on } S_T^1; \quad \text{(a)} \\
p_{n_e+1}^c & = & \overline{p}_{n_e+1}^c & \text{on } S_c^1 & \text{or} & p_{n_e+1}^g = \overline{p}_{n_e+1}^g & \text{on } S_g^1 & \text{or} \quad T_{n_e+1} = \overline{T}_{n_e+1} \quad \text{on } S_T^1; \quad \text{(b)}
\end{array}
$$

$$(E.60)$$

or prescribed mass and heat fluxes (Neumann's boundary conditions, second kind according to [114]), reading (for the one-dimensional case)

$$
\left(\rho^{gw} \frac{kk^{rg}}{\eta^g} \frac{D^s p^g}{Dx} + \rho^w \frac{kk^{rw}}{\eta^w} \frac{D^s p^w}{Dx} + \rho^g \frac{M_a M_w}{M_g^2} D_{eff} \frac{D^s}{Dx} \left(\frac{p^{gw}}{p^g} \right) \right) \Bigg|_{x_1} = \overline{q}_1^w + \overline{q}_1^{gw}
$$
$$
\text{on } S_c^2
$$

$$
\text{or} \qquad \left(\rho^{ga} \frac{kk^{rg}}{\eta^g} \frac{D^s p^g}{Dx} + \rho^g \frac{M_a M_w}{M_g^2} D_{eff} \frac{D^s}{Dx} \left(\frac{p^{ga}}{p^g} \right) \right) \Bigg|_{x_1} = \overline{q}_1^{ga} \quad \text{on } S_g^2
$$

$$
\text{or} \qquad \left(\lambda_{eff} \frac{D^s T}{Dx} - \rho^w \frac{kk^{rw}}{\eta^w} \frac{D^s p^w}{Dx} h \right) \Bigg|_{x_1} = \overline{q}_1^T \quad \text{on } S_T^2;
$$
$$
\text{(a)}
$$

$$
-\left(\rho^{gw} \frac{kk^{rg}}{\eta^g} \frac{D^s p^g}{Dx} + \rho^w \frac{kk^{rw}}{\eta^w} \frac{D^s p^w}{Dx} + \rho^g \frac{M_a M_w}{M_g^2} D_{eff} \frac{D^s}{Dx} \left(\frac{p^{gw}}{p^g} \right) \right) \Bigg|_{x_{n_e+1}} = \overline{q}_{n_e+1}^w + \overline{q}_{n_e+1}^{gw}
$$
$$
\text{on } S_c^2
$$

$$
\text{or} \qquad -\left(\rho^{ga} \frac{kk^{rg}}{\eta^g} \frac{D^s p^g}{Dx} + \rho^g \frac{M_a M_w}{M_g^2} D_{eff} \frac{D^s}{Dx} \left(\frac{p^{ga}}{p^g} \right) \right) \Bigg|_{x_{n_e+1}} = \overline{q}_{n_e+1}^{ga} \quad \text{on } S_g^2
$$

$$
\text{or} \qquad -\left(\lambda_{eff} \frac{D^s T}{Dx} - \rho^w \frac{kk^{rw}}{\eta^w} \frac{D^s p^w}{Dx} h \right) \Bigg|_{x_{n_e+1}} = \overline{q}_{n_e+1}^T \quad \text{on } S_T^2;
$$
$$
\text{(b)}
$$

$$(E.61)$$

where the unit normal vector at the front and rear surface is $n_1 = -1$ and $n_{n_e+1} = 1$, respectively.

The third kind of boundary conditions (Cauchy's boundary conditions according to [114]), which is of a mixed type, reads

$$
\left(\rho^{gw} \frac{kk^{rg}}{\eta^g} \frac{D^s p^g}{Dx} + \rho^w \frac{kk^{rw}}{\eta^w} \frac{D^s p^w}{Dx} + \rho^g \frac{M_a M_w}{M_g^2} D_{eff} \frac{D^s}{Dx} \left(\frac{p^{gw}}{p^g} \right) \right) \Bigg|_{x_1} =
$$

$$
\beta_1 (\rho_1^{gw} - \rho_{1,\infty}^{gw}) \quad \text{on } S_c^3
$$

or
$$
\left(\rho^{ga} \frac{kk^{rg}}{\eta^g} \frac{D^s p^g}{Dx} + \rho^g \frac{M_a M_w}{M_g^2} D_{eff} \frac{D^s}{Dx} \left(\frac{p^{ga}}{p^g} \right) \right) \Bigg|_{x_1} = 0 \quad \text{on } S_g^3
$$

or
$$
\left(\lambda_{eff} \frac{D^s T}{Dx} - \rho^w \frac{kk^{rw}}{\eta^w} \frac{D^s p^w}{Dx} h \right) \Bigg|_{x_1} =
$$

$$
\alpha_1 (T_1 - T_{1,\infty}) + \varepsilon_1 \sigma \left((T_1)^4 - (T_{1,\infty})^4 \right) \quad \text{on } S_T^3 \,; \qquad \text{(a)}
$$

$$
- \left(\rho^{gw} \frac{kk^{rg}}{\eta^g} \frac{D^s p^g}{Dx} + \rho^w \frac{kk^{rw}}{\eta^w} \frac{D^s p^w}{Dx} + \rho^g \frac{M_a M_w}{M_g^2} D_{eff} \frac{D^s}{Dx} \left(\frac{p^{gw}}{p^g} \right) \right) \Bigg|_{x_{n_e+1}} =
$$

$$
\beta_{n_e+1} (\rho_{n_e+1}^{gw} - \rho_{n_e+1,\infty}^{gw}) \quad \text{on } S_c^3
$$

or
$$
- \left(\rho^{ga} \frac{kk^{rg}}{\eta^g} \frac{D^s p^g}{Dx} + \rho^g \frac{M_a M_w}{M_g^2} D_{eff} \frac{D^s}{Dx} \left(\frac{p^{ga}}{p^g} \right) \right) \Bigg|_{x_{n_e+1}} = 0 \quad \text{on } S_g^3
$$

or
$$
- \left(\lambda_{eff} \frac{D^s T}{Dx} - \rho^w \frac{kk^{rw}}{\eta^w} \frac{D^s p^w}{Dx} h \right) \Bigg|_{x_{n_e+1}} =
$$

$$
\alpha_{n_e+1} (T_{n_e+1} - T_{n_e+1,\infty}) + \varepsilon_{n_e+1} \sigma \left((T_{n_e+1})^4 - (T_{n_e+1,\infty})^4 \right) \quad \text{on } S_T^3 \,; \qquad \text{(b)}
$$
$$
\text{(E.62)}
$$

where the vapor densities of the surroundings ($\rho_{1,\infty}^{gw}$, $\rho_{n_e+1,\infty}^{gw}$) are prescribed and transfer parameters (β_1, β_{n_e+1}) are used. Regarding heat transfer, the temperature of the surroundings ($T_{1,\infty}$, $T_{n_e+1,\infty}$) are prescribed and (α_1, α_{n_e+1}) and (ε_1, ε_{n_e+1}) account for convective and radiative heat transfer fluxes, respectively, where $\sigma = 5.67 \cdot 10^{-8}$ W/(m^2 K^4) is the Stefan-Boltzmann constant.

The mass and energy balance equations (Equations (E.5), (E.6), and (E.12)) are transformed into weak formulations by introducing arbitrary pressure fields δp^c and δp^g and an arbitrary temperature field δT. Combination of Equation (E.5) with Equations (E.60) to (E.62) yields the weak formulation for the one-dimensional mass balance equation for the water species, reading[3]

$$\int_{x_1}^{x_{n_e+1}} \delta p^c \left[n(\rho^w - \rho^{gw})\frac{D^s S_w}{Dt} + n\left(1 - S_w\right)\frac{D^s \rho^{gw}}{Dt} + nS_w \frac{D^s \rho^w}{Dt} - \beta_{swg}\frac{D^s T}{Dt} \right.$$

$$-\frac{D^s}{Dx}\left(\rho^{gw}\frac{kk^{rg}}{\eta^g}\frac{D^s p^g}{Dx}\right) - \frac{D^s}{Dx}\left(\rho^w\frac{kk^{rw}}{\eta^w}\frac{D^s p^w}{Dx}\right) - \frac{D^s}{Dx}\left[\rho^g\frac{M_a M_w}{M_g^2}D_{eff}\frac{D^s}{Dx}\left(\frac{p^{gw}}{p^g}\right)\right]$$

$$+\frac{(1-n)\left[\rho^{gw}(1-S_w) + \rho^w S_w\right]}{\rho^s}\frac{\partial \rho^s}{\partial T}\frac{D^s T}{Dt}$$

$$+ \left[\rho^{gw}(1-S_w) + \rho^w S_w\right]\frac{\dot{m}_{dehydr}}{\rho^s} - \dot{m}_{dehydr} \right] dx$$

$$+\delta p_1^c \left[-\left(\rho^{gw}\frac{kk^{rg}}{\eta^g}\frac{D^s p^g}{Dx} + \rho^w\frac{kk^{rw}}{\eta^w}\frac{D^s p^w}{Dx} + \rho^g\frac{M_a M_w}{M_g^2}D_{eff}\frac{D^s}{Dx}\left(\frac{p^{gw}}{p^g}\right)\right)\bigg|_{x_1} \right.$$

$$\left. +\overline{q}_1^w + \overline{q}_1^{gw} + \beta_1(\rho_1^{gw} - \rho_{1,\infty}^{gw})\right]$$

$$+\delta p_{n_e+1}^c \left[\left(\rho^{gw}\frac{kk^{rg}}{\eta^g}\frac{D^s p^g}{Dx} + \rho^w\frac{kk^{rw}}{\eta^w}\frac{D^s p^w}{Dx} + \rho^g\frac{M_a M_w}{M_g^2}D_{eff}\frac{D^s}{Dx}\left(\frac{p^{gw}}{p^g}\right)\right)\bigg|_{x_{n_e+1}} \right.$$

$$\left. +\overline{q}_{n_e+1}^w + \overline{q}_{n_e+1}^{gw} + \beta_{n_e+1}(\rho_{n_e+1}^{gw} - \rho_{n_e+1,\infty}^{gw})\right] = 0 \,, \tag{E.64}$$

where

$$\beta_{swg} = (1-n)\beta_s\left[\rho^{gw} + (\rho^w - \rho^{gw})S_w\right] \,. \tag{E.65}$$

---

[3]As depicted in Equation (E.41), the solid skeleton density ρ^s [(kg solid)/(m³ solid)] is defined as a function of temperature T. Therefore, the derivative with respect to the hydration degree ξ (occurring in term 8 of Equation (E.5), in term 6 of Equation (E.6), and in term 9 of Equation (E.12)) can be transformed in the following manner:

$$\frac{\partial \rho^s}{\partial \xi}\frac{D^s \xi}{Dt} = \frac{\partial \rho^s}{\partial \xi}\frac{\partial \xi}{\partial T}\frac{D^s T}{Dt} = \frac{\partial \rho^s}{\partial T}\frac{D^s T}{Dt} \,. \tag{E.63}$$

Combination of Equation (E.6) with Equations (E.60) to (E.62) yields the weak formulation for the one-dimensional mass balance equation for the air phase, reading

$$\int_{x_1}^{x_{n_e+1}} \delta p^g \left[-n\rho^{ga}\frac{D^s S_w}{Dt} + n(1-S_w)\frac{D^s\rho^{ga}}{Dt} - \beta_{sa}\rho^{ga}\frac{D^s T}{Dt} \right.$$

$$-\frac{D^s}{Dx}\left(\rho^{ga}\frac{kk^{rg}}{\eta^g}\frac{D^s p^g}{Dx}\right) - \frac{D^s}{Dx}\left[\rho^g\frac{M_a M_w}{M_g^2}D_{eff}\frac{D^s}{Dx}\left(\frac{p^{ga}}{p^g}\right)\right]$$

$$\left. +\frac{(1-n)\rho^{ga}(1-S_w)}{\rho^s}\frac{\partial\rho^s}{\partial T}\frac{D^s T}{Dt} + \rho^{ga}(1-S_w)\frac{\dot{m}_{dehydr}}{\rho^s} \right] dx$$

$$+\delta p_1^g \left[-\left(\rho^{ga}\frac{kk^{rg}}{\eta^g}\frac{D^s p^g}{Dx} + \rho^g\frac{M_a M_w}{M_g^2}D_{eff}\frac{D^s}{Dx}\left(\frac{p^{ga}}{p^g}\right)\right)\bigg|_{x_1} + \overline{q}_1^{ga} \right]$$

$$+\delta p_{n_e+1}^g \left[\left(\rho^{ga}\frac{kk^{rg}}{\eta^g}\frac{D^s p^g}{Dx} + \rho^g\frac{M_a M_w}{M_g^2}D_{eff}\frac{D^s}{Dx}\left(\frac{p^{ga}}{p^g}\right)\right)\bigg|_{x_{n_e+1}} + \overline{q}_{n_e+1}^{ga} \right] = 0 \,, \text{ (E.66)}$$

where

$$\beta_{sa} = (1-n)(1-S_w)\beta_s \,. \tag{E.67}$$

Combination of Equations (E.12) and (E.13) with Equations (E.60) to (E.62) yields the weak formulation for the one-dimensional enthalpy balance equation, reading

$$\int_{x_1}^{x_{n_e+1}} \delta T \left[(\rho c_p)_{eff}\frac{\partial T}{\partial t} - \left(\rho^g c_p^g\frac{kk^{rg}}{\eta^g}\frac{D^s p^g}{Dx} + \rho^w c_p^w\frac{kk^{rw}}{\eta^w}\frac{D^s p^w}{Dx}\right)\frac{D^s T}{Dx} - \frac{D^s}{Dx}\left(\lambda_{eff}\frac{D^s T}{Dx}\right) \right.$$

$$-n\rho^w\frac{D^s S_w}{Dt}h - nS_w\frac{D^s\rho^w}{Dt}h + \beta_{sw}\rho^w\frac{D^s T}{Dt}h + \frac{D^s}{Dx}\left(\rho^w\frac{kk^{rw}}{\eta^w}\frac{D^s p^w}{Dx}\right)h$$

$$\left. -\frac{(1-n)\rho^w S_w}{\rho^s}\frac{\partial\rho^s}{\partial T}\frac{D^s T}{Dt}h - \rho^w S_w\frac{\dot{m}_{dehydr}}{\rho^s}h + \dot{m}_{dehydr}h + \dot{m}_{dehydr}l_\xi^w \right] dx$$

$$+\delta T_1 \left[-\left(\lambda_{eff}\frac{D^s T}{Dx} - \rho^w\frac{kk^{rw}}{\eta^w}\frac{D^s p^w}{Dx}h\right)\bigg|_{x_1} \right.$$

$$+\overline{q}_1^T + \alpha_1\left(T_1 - T_{1,\infty}\right) + \varepsilon_1\sigma\left((T_1)^4 - (T_{1,\infty})^4\right)\Big]$$

$$+\delta T_{n_e+1}\left[\left(\lambda_{eff}\frac{D^s T}{Dx} - \rho^w\frac{kk^{rw}}{\eta^w}\frac{D^s p^w}{Dx}h\right)\bigg|_{x_{n_e+1}} \right.$$

$$+\overline{q}_{n_e+1}^T + \alpha_{n_e+1}\left(T_{n_e+1} - T_{n_e+1,\infty}\right) + \varepsilon_{n_e+1}\sigma\left((T_{n_e+1})^4 - (T_{n_e+1,\infty})^4\right)\Big] = 0 \,, \text{ (E.68)}$$

where

$$\beta_{sw} = (1-n)S_w\beta_s \,. \tag{E.69}$$

In Equations (E.64), (E.66), and (E.68), the dependent functions are introduced in their final form, reading (see Appendix E.1.2)

$$n = n_0 + A_n(T - T_0);\tag{1}$$

$$\rho^w = (b_0 + b_1 T + b_2 T^2 + b_3 T^3 + b_4 T^4 + b_5 T^5)$$
$$+ (p_{w1} - p_{wrif})(a_0 + a_1 T + a_2 T^2 + a_3 T^3 + a_4 T^4 + a_5 T^5)$$
$$(\text{for } T \leq T_{crit});\tag{2}$$

$$\rho^{gw} = \frac{M_w}{R\Theta} p^{gw},\tag{3}$$
$$\text{with } p^{gw} = p^{gws} RH$$
$$\text{and } p^{gws} = \exp\left[\frac{c_1}{\Theta} + c_2 + c_3\Theta + c_4\Theta^2 + c_5\Theta^3 + c_6\ln(\Theta)\right]$$
$$\text{and } RH = \exp\left(-\frac{p^c M_w}{\rho^w R\Theta}\right);$$

$$S_w = \left[1 + \left(\frac{E_s}{A_s}p^c\right)^{\left(\frac{1}{1-m}\right)}\right]^{-m};\tag{4}$$

$$\beta_{swg} = (1-n)\beta_s\left[\rho^{gw} + (\rho^w - \rho^{gw})S_w\right];\tag{5}$$

$$k = k_{int}\left(1 + \frac{b}{p^g}\right) \quad \text{for gas flow and} \quad k = k_{int} \quad \text{for water flow},\tag{6}$$
$$\text{with } k_{int} = k_{int,0} 10^{A_k(T-T_0)}$$

$$k^{rg} = (1 - S_w)^p\left(1 - S_w^{1/m}\right)^{2m} \quad \text{or} \quad k^{rg} = 1 - \left(\frac{S_w}{S_w^{cr}}\right)^{A_g};\tag{7}$$

$$k^{rw} = S_w^p\left[1 - (1 - S_w^{1/m})^m\right]^2 \quad \text{or} \quad k^{rw} = \left(\frac{S_w - S_w^r}{1 - S_w^r}\right)^{A_w};\tag{8}$$

$$\eta^g = \eta^{gw} + (\eta^{ga} - \eta^{gw})\left(\frac{p^{ga}}{p^g}\right)^{b_g} \quad (\text{for } p^{ga} \geq 0),\tag{9}$$
$$\text{with } \eta^{gw} = \eta^{gw0} + a_{gw}(T - T_0)$$
$$\text{and } \eta^{ga} = \eta^{ga0} + a_{ga}(T - T_0) + b_{ga}(T - T_0)^2;$$

$$\eta^w = a_w(T + 44.15)^{b_w};\tag{10}$$

$$\rho^g = \rho^{gw} + \rho^{ga};\tag{11}$$

$$M_g = M_a + (M_w - M_a)\frac{p^{gw}}{p^g};\tag{12}$$

$$D_{eff} = \tau n(1 - S_w)f_s D_{va},\tag{13}$$
$$\text{with } \tau = n^{1/3}(1 - S_w)^{7/3}$$
$$\text{and } D_{va} = D_{va0}\left(\frac{\Theta}{\Theta_0}\right)^{A_{Dva}}\frac{p_{atm}}{p^g} \quad (\text{for } T \leq T_{crit} \text{ and } p^{ga} \geq 0);$$

$$\rho^s = \rho^{s0} + A_{\rho^s}(T - T_0);\tag{14}$$

$$\dot{m}_{dehydr} = -m_c f_h \frac{m_w}{m_c}\frac{\partial \xi}{\partial t},\tag{15}$$
$$\text{with } \xi \text{ according to Figure E.2}$$

$$\tag{E.70}$$

and

$$
\begin{aligned}
\rho^{ga} &= \frac{M_a}{R\Theta} p^{ga} \,, & (1) \\
&\quad \text{with } p^{ga} = p^g - p^{gws} RH \,; \\
\beta_{sa} &= (1-n)(1-S_w)\beta_s \,; & (2) \\
(\rho c_p)_{eff} &= (1-n)\rho^s c_p^s + n \left[S_w \rho^w c_p^w + (1-S_w)\rho^g c_p^g \right] \,, & (3) \\
&\quad \text{with } c_p^s = c_p^{s0} + A_{c_p^s}(T - T_0) \quad (\text{for } T \leq T_{crit}) \,; \\
\rho^g c_p^g &= \rho^g c_p^{ga} + \rho^{gw}(c_p^{gw} - c_p^{ga}) \quad (= \rho^{gw} c_p^{gw} + \rho^{ga} c_p^{ga}) \,; & (4) \\
\rho^w c_p^w &= \rho^w c_p^w \,; & (5) \\
\lambda_{eff} &= \lambda^s \left[1 + \frac{4n\rho^w S_w}{(1-n)\rho^s} \right] \,, & (6) \\
&\quad \text{with } \lambda^s = \lambda^{s0} + A_\lambda(T - T_0) \quad (\text{for } T \leq 800°C) \,; \\
\beta_{sw} &= (1-n)S_w \beta_s \,; & (7) \\
h &= a_h \left(T_{cr} - T \right)^{b_h} \quad (\text{for } T \leq T_{crit}) \,; & (8)
\end{aligned}
\qquad \text{(E.71)}
$$

Integration by parts of the 5th term in Equation (E.64) gives

$$\int_{x_1}^{x_{n_e+1}} \delta p^c \frac{D^s}{Dx} \left(\rho^{gw} \frac{kk^{rg}}{\eta^g} \frac{D^s p^g}{Dx} \right) dx = \delta p^c_{n_e+1} \left(\rho^{gw} \frac{kk^{rg}}{\eta^g} \frac{D^s p^g}{Dx} \right) \bigg|_{x_{n_e+1}}$$

$$- \delta p^c_1 \left(\rho^{gw} \frac{kk^{rg}}{\eta^g} \frac{D^s p^g}{Dx} \right) \bigg|_{x_1} - \int_{x_1}^{x_{n_e+1}} \frac{D^s \delta p^c}{Dx} \rho^{gw} \frac{kk^{rg}}{\eta^g} \frac{D^s p^g}{Dx} dx. \tag{E.72}$$

The same procedure is performed on the 6th and the 7th term in Equation (E.64), the 4th and the 5th term in Equation (E.66), and the 4th and the 8th term in Equation (E.68), yielding

$$\int_{x_1}^{x_{n_e+1}} \delta p^c \frac{D^s}{Dx} \left(\rho^w \frac{kk^{rw}}{\eta^w} \frac{D^s p^w}{Dx} \right) dx = \delta p^c_{n_e+1} \left(\rho^w \frac{kk^{rw}}{\eta^w} \frac{D^s p^w}{Dx} \right) \bigg|_{x_{n_e+1}}$$

$$- \delta p^c_1 \left(\rho^w \frac{kk^{rw}}{\eta^w} \frac{D^s p^w}{Dx} \right) \bigg|_{x_1} - \int_{x_1}^{x_{n_e+1}} \frac{D^s \delta p^c}{Dx} \rho^w \frac{kk^{rw}}{\eta^w} \frac{D^s p^w}{Dx} dx, \tag{E.73}$$

$$\int_{x_1}^{x_{n_e+1}} \delta p^c \frac{D^s}{Dx} \left[\rho^g \frac{M_a M_w}{M_g^2} D_{eff} \frac{D^s}{Dx} \left(\frac{p^{gw}}{p^g} \right) \right] dx = \delta p^c_{n_e+1} \left[\rho^g \frac{M_a M_w}{M_g^2} D_{eff} \frac{D^s}{Dx} \left(\frac{p^{gw}}{p^g} \right) \right] \bigg|_{x_{n_e+1}}$$

$$- \delta p^c_1 \left[\rho^g \frac{M_a M_w}{M_g^2} D_{eff} \frac{D^s}{Dx} \left(\frac{p^{gw}}{p^g} \right) \right] \bigg|_{x_1} - \int_{x_1}^{x_{n_e+1}} \frac{D^s \delta p^c}{Dx} \rho^g \frac{M_a M_w}{M_g^2} D_{eff} \frac{D^s}{Dx} \left(\frac{p^{gw}}{p^g} \right) dx \tag{E.74}$$

$$\int_{x_1}^{x_{n_e+1}} \delta p^g \frac{D^s}{Dx} \left(\rho^{ga} \frac{kk^{rg}}{\eta^g} \frac{D^s p^g}{Dx} \right) dx = \delta p^g_{n_e+1} \left(\rho^{ga} \frac{kk^{rg}}{\eta^g} \frac{D^s p^g}{Dx} \right) \bigg|_{x_{n_e+1}}$$

$$- \delta p^g_1 \left(\rho^{ga} \frac{kk^{rg}}{\eta^g} \frac{D^s p^g}{Dx} \right) \bigg|_{x_1} - \int_{x_1}^{x_{n_e+1}} \frac{D^s \delta p^g}{Dx} \rho^{ga} \frac{kk^{rg}}{\eta^g} \frac{D^s p^g}{Dx} dx, \tag{E.75}$$

$$\int_{x_1}^{x_{n_e+1}} \delta p^c \frac{D^s}{Dx} \left[\rho^g \frac{M_a M_w}{M_g^2} D_{eff} \frac{D^s}{Dx} \left(\frac{p^{ga}}{p^g} \right) \right] dx = \delta p^c_{n_e+1} \left[\rho^g \frac{M_a M_w}{M_g^2} D_{eff} \frac{D^s}{Dx} \left(\frac{p^{ga}}{p^g} \right) \right] \bigg|_{x_{n_e+1}}$$

$$- \delta p^c_1 \left[\rho^g \frac{M_a M_w}{M_g^2} D_{eff} \frac{D^s}{Dx} \left(\frac{p^{ga}}{p^g} \right) \right] \bigg|_{x_1} - \int_{x_1}^{x_{n_e+1}} \frac{D^s \delta p^c}{Dx} \rho^g \frac{M_a M_w}{M_g^2} D_{eff} \frac{D^s}{Dx} \left(\frac{p^{ga}}{p^g} \right) dx \tag{E.76}$$

$$\int_{x_1}^{x_{n_e+1}} \delta T \frac{D^s}{Dx} \left(\lambda_{eff} \frac{D^s T}{Dx} \right) dx = \delta T_{n_e+1} \left(\lambda_{eff} \frac{D^s T}{Dx} \right) \bigg|_{x_{n_e+1}}$$

$$- \delta T_1 \left(\lambda_{eff} \frac{D^s T}{Dx} \right) \bigg|_{x_1} - \int_{x_1}^{x_{n_e+1}} \frac{D^s \delta T}{Dx} \lambda_{eff} \frac{D^s T}{Dx} dx, \tag{E.77}$$

and

$$\int_{x_1}^{x_{n_e+1}} \delta T \frac{D^s}{Dx} \left(\rho^w \frac{kk^{rw}}{\eta^w} \frac{D^s p^w}{Dx} \right) h dx = \delta T_{n_e+1} \left(\rho^w \frac{kk^{rw}}{\eta^w} \frac{D^s p^w}{Dx} \right) h \Big|_{x_{n_e+1}}$$

$$- \delta T_1 \left(\rho^w \frac{kk^{rw}}{\eta^w} \frac{D^s p^w}{Dx} \right) h \Big|_{x_1} - \int_{x_1}^{x_{n_e+1}} \frac{D^s \delta T}{Dx} \rho^w \frac{kk^{rw}}{\eta^w} \frac{D^s p^w}{Dx} h dx, \qquad (E.78)$$

respectively.

Introduction of Equations (E.72), (E.73), and (E.74) into Equation (E.64) yields the final form of the weak formulation of the mass balance equation for the water species, reading

$$\int_{x_1}^{x_{n_e+1}} \left[\delta p^c n (\rho^w - \rho^{gw}) \frac{D^s S_w}{Dt} + \delta p^c n \left(1 - S_w\right) \frac{D^s \rho^{gw}}{Dt} + \delta p^c n S_w \frac{D^s \rho^w}{Dt} - \delta p^c \beta_{swg} \frac{D^s T}{Dt} \right.$$

$$+ \frac{D^s \delta p^c}{Dx} \rho^{gw} \frac{kk^{rg}}{\eta^g} \frac{D^s p^g}{Dx} + \frac{D^s \delta p^c}{Dx} \rho^w \frac{kk^{rw}}{\eta^w} \frac{D^s p^w}{Dx} + \frac{D^s \delta p^c}{Dx} \rho^g \frac{M_a M_w}{M_g^2} D_{eff} \frac{D^s}{Dx} \left(\frac{p^{gw}}{p^g} \right)$$

$$+ \delta p^c \frac{(1-n) \left[\rho^{gw}(1-S_w) + \rho^w S_w \right]}{\rho^s} \frac{\partial \rho^s}{\partial T} \frac{D^s T}{Dt}$$

$$\left. + \delta p^c \left[\rho^{gw}(1-S_w) + \rho^w S_w \right] \frac{\dot{m}_{dehydr}}{\rho^s} - \delta p^c \dot{m}_{dehydr} \right] dx$$

$$+ \delta p_1^c \left[\overline{q}_1^w + \overline{q}_1^{gw} + \beta_1(\rho_1^{gw} - \rho_{1,\infty}^{gw}) \right]$$

$$+ \delta p_{n_e+1}^c \left[\overline{q}_{n_e+1}^w + \overline{q}_{n_e+1}^{gw} + \beta_{n_e+1}(\rho_{n_e+1}^{gw} - \rho_{n_e+1,\infty}^{gw}) \right] = 0. \qquad (E.79)$$

Introduction of Equations (E.75) and (E.76) into Equation (E.66) yields the final form of the weak formulation of the mass balance equation for air, reading

$$\int_{x_1}^{x_{n_e+1}} \left[-\delta p^g n \rho^{ga} \frac{D^s S_w}{Dt} + \delta p^g n (1 - S_w) \frac{D^s \rho^{ga}}{Dt} - \delta p^g \beta_{sa} \rho^{ga} \frac{D^s T}{Dt} \right.$$

$$+ \frac{D^s \delta p^g}{Dx} \rho^{ga} \frac{kk^{rg}}{\eta^g} \frac{D^s p^g}{Dx} + \frac{D^s \delta p^g}{Dx} \rho^g \frac{M_a M_w}{M_g^2} D_{eff} \frac{D^s}{Dx} \left(\frac{p^{ga}}{p^g} \right)$$

$$\left. + \delta p^g \frac{(1-n) \rho^{ga}(1-S_w)}{\rho^s} \frac{\partial \rho^s}{\partial T} \frac{D^s T}{Dt} + \delta p^g \rho^{ga}(1-S_w) \frac{\dot{m}_{dehydr}}{\rho^s} \right] dx$$

$$+ \delta p_1^g \overline{q}_1^{ga} + \delta p_{n_e+1}^g \overline{q}_{n_e+1}^{ga} = 0. \qquad (E.80)$$

Introduction of Equations (E.77) and (E.78) into Equation (E.68) yields the final form of the weak formulation of the enthalpy balance equation, reading

$$\int_{x_1}^{x_{n_e+1}} \left[\delta T \left(\rho c_p\right)_{eff} \frac{\partial T}{\partial t} - \delta T \left(\rho^g c_p^g \frac{kk^{rg}}{\eta^g} \frac{D^s p^g}{Dx} \right) \frac{D^s T}{Dx} - \delta T \left(\rho^w c_p^w \frac{kk^{rw}}{\eta^w} \frac{D^s p^w}{Dx} \right) \frac{D^s T}{Dx} \right.$$

$$+ \frac{D^s \delta T}{Dx} \lambda_{eff} \frac{D^s T}{Dx} - \delta T n \rho^w \frac{D^s S_w}{Dt} h - \delta T n S_w \frac{D^s \rho^w}{Dt} h + \delta T \beta_{sw} \rho^w \frac{D^s T}{Dt} h - \frac{D^s \delta T}{Dx} \rho^w \frac{kk^{rw}}{\eta^w} \frac{D^s p^w}{Dx} h$$

$$\left. - \delta T \frac{(1-n)\rho^w S_w}{\rho^s} \frac{\partial \rho^s}{\partial T} \frac{D^s T}{Dt} h - \delta T \rho^w S_w \frac{\dot{m}_{dehydr}}{\rho^s} h + \delta T \dot{m}_{dehydr} h + \delta T \dot{m}_{dehydr} l_\xi^w \right] dx$$

$$+ \delta T_1 \left[\overline{q}_1^T + \alpha_1 \left(T_1 - T_{1,\infty} \right) + \varepsilon_1 \sigma \left((T_1)^4 - (T_{1,\infty})^4 \right) \right] \tag{E.81}$$

$$+ \delta T_{n_e+1} \left[\overline{q}_{n_e+1}^T + \alpha_{n_e+1} \left(T_{n_e+1} - T_{n_e+1,\infty} \right) + \varepsilon_{n_e+1} \sigma \left((T_{n_e+1})^4 - (T_{n_e+1,\infty})^4 \right) \right] = 0 \,.$$

After obtaining the weak formulations, the capillary pressure, gas pressure, and temperature fields are discretized in space, yielding time-dependent nodal values ($\mathbf{v}_c$, $\mathbf{v}_g$, and $\mathbf{v}_t$, respectively) and space-dependent shape functions ($\mathbf{N}_c$, $\mathbf{N}_g$, and $\mathbf{N}_t$, respectively). This yields

$$\begin{array}{llll} p^c &=& \mathbf{N}_c \mathbf{v}_c \quad \text{and} \quad \delta p^c &= \mathbf{N}_c \delta \mathbf{v}_c = \delta \mathbf{v}_c^T \mathbf{N}_c^T \,; \quad \text{(a)} \\ p^g &=& \mathbf{N}_g \mathbf{v}_g \quad \text{and} \quad \delta p^g &= \mathbf{N}_g \delta \mathbf{v}_g = \delta \mathbf{v}_g^T \mathbf{N}_g^T \,; \quad \text{(b)} \\ T &=& \mathbf{N}_t \mathbf{v}_t \quad \text{and} \quad \delta T &= \mathbf{N}_t \delta \mathbf{v}_t = \delta \mathbf{v}_t^T \mathbf{N}_t^T \,; \quad \text{(c)} \end{array} \tag{E.82}$$

with

$$\mathbf{N}_c = \lfloor N_{c,1}, N_{c,2} \rfloor \quad, \quad \mathbf{N}_g = \lfloor N_{g,1}, N_{g,2} \rfloor \quad \text{and} \quad \mathbf{N}_t = \lfloor N_{t,1}, N_{t,2} \rfloor \tag{E.83}$$

as the linear element shape functions. Discretization in time yields

$$\begin{array}{lll} \dfrac{D^s p^c}{Dt} & \rightarrow & \dfrac{\Delta p^c}{\Delta t} = \mathbf{N}_c \dfrac{\Delta \mathbf{v}_c}{\Delta t} \,; \\[2mm] \dfrac{D^s p^g}{Dt} & \rightarrow & \dfrac{\Delta p^g}{\Delta t} = \mathbf{N}_g \dfrac{\Delta \mathbf{v}_g}{\Delta t} \,; \\[2mm] \dfrac{D^s T}{Dt} & \rightarrow & \dfrac{\Delta T}{\Delta t} = \mathbf{N}_t \dfrac{\Delta \mathbf{v}_t}{\Delta t} \,; \\[2mm] \dfrac{\partial T}{\partial t} & \rightarrow & \dfrac{\Delta T}{\Delta t} = \mathbf{N}_t \dfrac{\Delta \mathbf{v}_t}{\Delta t} \,. \end{array} \tag{E.84}$$

Introduction of Equations (E.82) and (E.84) into Equation (E.79) yields

$$\delta\mathbf{v}_c^T(\mathbf{R}_s^c + \mathbf{R}_{\rho^{gw}}^c + \mathbf{R}_{\rho^w}^c + \mathbf{R}_t^c + \mathbf{R}_{k^g}^c + \mathbf{R}_{k^w}^c + \mathbf{R}_d^c + \mathbf{R}_{\rho^s}^c + \mathbf{R}_\xi^c + \mathbf{R}_b^c) = 0\,, \qquad \text{(E.85)}$$

with

$$\mathbf{R}_s^c = \left[\bigwedge_{e=1}^{n_e} \int_{x_e}^{x_{e+1}} \left(\mathbf{N}_c^T n(\rho^w - \rho^{gw})\frac{\Delta S_w}{\Delta t} \right) dx \right]\,, \qquad \text{(E.86)}$$

$$\mathbf{R}_{\rho^{gw}}^c = \left[\bigwedge_{e=1}^{n_e} \int_{x_e}^{x_{e+1}} \left(\mathbf{N}_c^T n\,(1-S_w)\frac{\Delta\rho^{gw}}{\Delta t} \right) dx \right]\,, \qquad \text{(E.87)}$$

$$\mathbf{R}_{\rho^w}^c = \left[\bigwedge_{e=1}^{n_e} \int_{x_e}^{x_{e+1}} \left(\mathbf{N}_c^T nS_w\frac{\Delta\rho^w}{\Delta t} \right) dx \right]\,, \qquad \text{(E.88)}$$

$$\mathbf{R}_t^c = \left[\bigwedge_{e=1}^{n_e} \int_{x_e}^{x_{e+1}} \left(-\mathbf{N}_c^T \beta_{swg}\frac{\Delta T}{\Delta t} \right) dx \right]\,, \qquad \text{(E.89)}$$

$$\mathbf{R}_{k^g}^c = \left[\bigwedge_{e=1}^{n_e} \int_{x_e}^{x_{e+1}} \left(\frac{D^s\mathbf{N}_c^T}{Dx}\rho^{gw}\frac{kk^{rg}}{\eta^g}\frac{D^sp^g}{Dx} + \frac{D^s\mathbf{N}_c^T}{Dx}\rho^w\frac{kk^{rw}}{\eta^w}\frac{D^sp^g}{Dx} \right) dx \right]\,, \text{(E.90)}$$

$$\mathbf{R}_{k^w}^c = \left[\bigwedge_{e=1}^{n_e} \int_{x_e}^{x_{e+1}} \left(-\frac{D^s\mathbf{N}_c^T}{Dx}\rho^w\frac{kk^{rw}}{\eta^w}\frac{D^sp^c}{Dx} \right) dx \right]\,, \qquad \text{(E.91)}$$

$$\mathbf{R}_d^c = \left[\bigwedge_{e=1}^{n_e} \int_{x_e}^{x_{e+1}} \left(\frac{D^s\mathbf{N}_c^T}{Dx}\rho^g\frac{M_aM_w}{M_g^2}D_{eff}\frac{D^s}{Dx}\left(\frac{p^{gw}}{p^g}\right) \right) dx \right]\,, \qquad \text{(E.92)}$$

$$\mathbf{R}_{\rho^s}^c = \left[\bigwedge_{e=1}^{n_e} \int_{x_e}^{x_{e+1}} \left(\mathbf{N}_c^T \frac{(1-n)\left[\rho^{gw}(1-S_w) + \rho^w S_w\right]}{\rho^s}\frac{\partial\rho^s}{\partial T}\frac{\Delta T}{\Delta t} \right) dx \right]\,, \quad \text{(E.93)}$$

$$\mathbf{R}_\xi^c = \left[\bigwedge_{e=1}^{n_e} \int_{x_e}^{x_{e+1}} \left(-\mathbf{N}_c^T \left[\rho^{gw}(1-S_w) + \rho^w S_w\right]\frac{m_cf_h}{\rho^s}\frac{m_w}{m_c}\frac{\Delta\xi}{\Delta t} \right.\right.$$

$$\left.\left. + \mathbf{N}_c^T m_cf_h\frac{m_w}{m_c}\frac{\Delta\xi}{\Delta t} \right) dx \right]\,, \qquad \text{(E.94)}$$

$$\mathbf{R}_b^c = \mathbf{1}_1\left[\overline{q}_1^w + \overline{q}_1^{gw} + \beta_1(\rho_1^{gw} - \rho_{1,\infty}^{gw})\right]$$

$$+ \mathbf{1}_{n_e+1}\left[\overline{q}_{n_e+1}^w + \overline{q}_{n_e+1}^{gw} + \beta_{n_e+1}(\rho_{n_e+1}^{gw} - \rho_{n_e+1,\infty}^{gw})\right]\,, \qquad \text{(E.95)}$$

where $p^w = p^g - p^c$ and $\dot{m}_{dehydr} = -m_cf_h(m_w/m_c)(\partial\xi/\partial t)$ (including consideration of $\partial\xi/\partial t \to \Delta\xi/\Delta t$) was taken into account. In Equation (E.95), $\mathbf{1}_1$ and $\mathbf{1}_{n_e+1}$ are auxiliary vectors with n_e+1 components, given by $\mathbf{1}_1^T = \lfloor 1,0,0,\dots\rfloor$ and $\mathbf{1}_{n_e+1}^T = \lfloor\dots,0,0,1\rfloor$, respectively.

Introduction of Equations (E.82) and (E.84) into Equation (E.80) yields

$$\delta \mathbf{v}_g^T (\mathbf{R}_s^g + \mathbf{R}_{\rho^{ga}}^g + \mathbf{R}_t^g + \mathbf{R}_{k^g}^g + \mathbf{R}_d^g + \mathbf{R}_{\rho^s}^g + \mathbf{R}_\xi^g + \mathbf{R}_b^g) = 0 \,, \tag{E.96}$$

with

$$\mathbf{R}_s^g = \left[\overset{n_e}{\underset{e=1}{\mathbf{A}}} \int_{x_e}^{x_{e+1}} \left(-\mathbf{N}_g^T n \rho^{ga} \frac{\Delta S_w}{\Delta t} \right) dx \right] \,, \tag{E.97}$$

$$\mathbf{R}_{\rho^{ga}}^g = \left[\overset{n_e}{\underset{e=1}{\mathbf{A}}} \int_{x_e}^{x_{e+1}} \left(\mathbf{N}_g^T n (1 - S_w) \frac{\Delta \rho^{ga}}{\Delta t} \right) dx \right] \,, \tag{E.98}$$

$$\mathbf{R}_t^g = \left[\overset{n_e}{\underset{e=1}{\mathbf{A}}} \int_{x_e}^{x_{e+1}} \left(-\mathbf{N}_g^T \beta_{sa} \rho^{ga} \frac{\Delta T}{\Delta t} \right) dx \right] \,, \tag{E.99}$$

$$\mathbf{R}_{k^g}^g = \left[\overset{n_e}{\underset{e=1}{\mathbf{A}}} \int_{x_e}^{x_{e+1}} \left(\frac{D^s \mathbf{N}_g^T}{Dx} \rho^{ga} \frac{k k^{rg}}{\eta^g} \frac{D^s p^g}{Dx} \right) dx \right] \,, \tag{E.100}$$

$$\mathbf{R}_d^g = \left[\overset{n_e}{\underset{e=1}{\mathbf{A}}} \int_{x_e}^{x_{e+1}} \left(-\frac{D^s \mathbf{N}_g^T}{Dx} \rho^g \frac{M_a M_w}{M_g^2} D_{eff} \frac{D^s}{Dx} \left(\frac{p^{gw}}{p^g} \right) \right) dx \right] \,, \tag{E.101}$$

$$\mathbf{R}_{\rho^s}^g = \left[\overset{n_e}{\underset{e=1}{\mathbf{A}}} \int_{x_e}^{x_{e+1}} \left(\mathbf{N}_g^T \frac{(1 - n) \rho^{ga} (1 - S_w)}{\rho^s} \frac{\partial \rho^s}{\partial T} \frac{\Delta T}{\Delta t} \right) dx \right] \,, \tag{E.102}$$

$$\mathbf{R}_\xi^g = \left[\overset{n_e}{\underset{e=1}{\mathbf{A}}} \int_{x_e}^{x_{e+1}} \left(-\mathbf{N}_g^T \rho^{ga} (1 - S_w) \frac{m_c f_h}{\rho^s} \frac{m_w}{m_c} \frac{\Delta \xi}{\Delta t} \right) dx \right] \,, \tag{E.103}$$

$$\mathbf{R}_b^g = \mathbf{1}_1 \bar{q}_1^{ga} + \mathbf{1}_{n_e+1} \bar{q}_{n_e+1}^{ga} \,, \tag{E.104}$$

where $\dot{m}_{dehydr} = -m_c f_h (m_w/m_c)(\partial \xi/\partial t)$ (including consideration of $\partial \xi/\partial t \to \Delta \xi/\Delta t$) was taken into account. In Equation (E.101),

$$\frac{D^s}{Dx} \left(\frac{p^{ga}}{p^g} \right) = \frac{D^s}{Dx} \left(\frac{p^g - p^{gw}}{p^g} \right) = -\frac{D^s}{Dx} \left(\frac{p^{gw}}{p^g} \right) \tag{E.105}$$

was considered.

Introduction of Equations (E.82) and (E.84) into Equation (E.81) yields

$$\delta\mathbf{v}_t^T(\mathbf{R}_c^t + \mathbf{R}_g^t + \mathbf{R}_w^t + \mathbf{R}_\lambda^t + \mathbf{R}_s^t + \mathbf{R}_t^t + \mathbf{R}_{k^g}^t + \mathbf{R}_{k^w}^t + \mathbf{R}_{\rho^s}^t + \mathbf{R}_\xi^t + \mathbf{R}_{dehydr}^t + \mathbf{R}_b^t) = 0\,, \quad \text{(E.106)}$$

with

$$\mathbf{R}_c^t = \left[\mathop{\mathbf{A}}_{e=1}^{n_e} \int_{x_e}^{x_{e+1}} \left(\mathbf{N}_t^T (\rho c_p)_{eff} \frac{\Delta T}{\Delta t} \right) dx \right], \quad \text{(E.107)}$$

$$\mathbf{R}_g^t = \left[\mathop{\mathbf{A}}_{e=1}^{n_e} \int_{x_e}^{x_{e+1}} \left(-\mathbf{N}_t^T \left(\rho^g c_p^g \frac{kk^{rg}}{\eta^g} \frac{D^s p^g}{Dx} \right) \frac{D^s T}{Dx} \right.\right.$$
$$\left.\left. -\mathbf{N}_t^T \left(\rho^w c_p^w \frac{kk^{rw}}{\eta^w} \frac{D^s p^g}{Dx} \right) \frac{D^s T}{Dx} \right) dx \right], \quad \text{(E.108)}$$

$$\mathbf{R}_w^t = \left[\mathop{\mathbf{A}}_{e=1}^{n_e} \int_{x_e}^{x_{e+1}} \left(\mathbf{N}_t^T \left(\rho^w c_p^w \frac{kk^{rw}}{\eta^w} \frac{D^s p^c}{Dx} \right) \frac{D^s T}{Dx} \right) dx \right], \quad \text{(E.109)}$$

$$\mathbf{R}_\lambda^t = \left[\mathop{\mathbf{A}}_{e=1}^{n_e} \int_{x_e}^{x_{e+1}} \left(\frac{D^s \mathbf{N}_t^T}{Dx} \lambda_{eff} \frac{D^s T}{Dx} \right) dx \right], \quad \text{(E.110)}$$

$$\mathbf{R}_s^t = \left[\mathop{\mathbf{A}}_{e=1}^{n_e} \int_{x_e}^{x_{e+1}} \left(-\mathbf{N}_t^T h n \rho^w \frac{\Delta S_w}{\Delta t} \right) dx \right], \quad \text{(E.111)}$$

$$\mathbf{R}_{\rho^w}^t = \left[\mathop{\mathbf{A}}_{e=1}^{n_e} \int_{x_e}^{x_{e+1}} \left(-\mathbf{N}_t^T h n S_w \frac{\Delta \rho^w}{\Delta t} \right) dx \right], \quad \text{(E.112)}$$

$$\mathbf{R}_t^t = \left[\mathop{\mathbf{A}}_{e=1}^{n_e} \int_{x_e}^{x_{e+1}} \left(\mathbf{N}_t^T h \beta_{sw} \rho^w \frac{\Delta T}{\Delta t} \right) dx \right], \quad \text{(E.113)}$$

$$\mathbf{R}_{k^g}^t = \left[\mathop{\mathbf{A}}_{e=1}^{n_e} \int_{x_e}^{x_{e+1}} \left(-\frac{D^s \mathbf{N}_t^T}{Dx} h \rho^w \frac{kk^{rw}}{\eta^w} \frac{D^s p^g}{Dx} \right) dx \right], \quad \text{(E.114)}$$

$$\mathbf{R}_{k^w}^t = \left[\mathop{\mathbf{A}}_{e=1}^{n_e} \int_{x_e}^{x_{e+1}} \left(\frac{D^s \mathbf{N}_t^T}{Dx} h \rho^w \frac{kk^{rw}}{\eta^w} \frac{D^s p^c}{Dx} \right) dx \right], \quad \text{(E.115)}$$

$$\mathbf{R}_{\rho^s}^t = \left[\mathop{\mathbf{A}}_{e=1}^{n_e} \int_{x_e}^{x_{e+1}} \left(-\mathbf{N}_t^T h \frac{(1-n)\rho^w S_w}{\rho^s} \frac{\partial \rho^s}{\partial T} \frac{\Delta T}{\Delta t} \right) dx \right], \quad \text{(E.116)}$$

$$\mathbf{R}_\xi^t = \left[\mathop{\mathbf{A}}_{e=1}^{n_e} \int_{x_e}^{x_{e+1}} \left(\mathbf{N}_t^T h \rho^w S_w \frac{m_c f_h}{\rho^s} \frac{m_w}{m_c} \frac{\Delta \xi}{\Delta t} \right.\right.$$
$$\left.\left. -\mathbf{N}_t^T h m_c f_h \frac{m_w}{m_c} \frac{\Delta \xi}{\Delta t} \right) dx \right], \quad \text{(E.117)}$$

$$\mathbf{R}_{dehydr}^t = \left[\mathop{\mathbf{A}}_{e=1}^{n_e} \int_{x_e}^{x_{e+1}} \left(-\mathbf{N}_t^T l_\xi m_c f_h \frac{\Delta \xi}{\Delta t} \right) dx \right], \quad \text{(E.118)}$$

$$\mathbf{R}_b^t = \mathbf{1}_1 \left[\overline{q}_1^T + \alpha_1 \left(T_1 - T_{1,\infty} \right) + \varepsilon_1 \sigma \left((T_1)^4 - (T_{1,\infty})^4 \right) \right]$$

$$+ \mathbf{1}_{n_e+1} \left[\overline{q}_{n_e+1}^T + \alpha_{n_e+1} \left(T_{n_e+1} - T_{n_e+1,\infty} \right) \right.$$

$$\left. + \varepsilon_{n_e+1} \sigma \left((T_{n_e+1})^4 - (T_{n_e+1,\infty})^4 \right) \right] , \qquad \text{(E.119)}$$

where $p^w = p^g - p^c$, $\dot{m}_{dehydr} = -m_c f_h (m_w/m_c)(\partial \xi/\partial t)$ (including consideration of $\partial \xi/\partial t \to \Delta \xi/\Delta t$), and $l_\xi^w = l_\xi (m_c/m_w)$ was taken into account.

Since Equations (E.85), (E.96), and (E.106) must hold for arbitrary $\delta \mathbf{v}_c^T$, $\delta \mathbf{v}_g^T$, and $\delta \mathbf{v}_T^T$, respectively, the following equations have to be fulfilled:

$$\mathbf{R}^c = \mathbf{R}_s^c + \mathbf{R}_{\rho^{gw}}^c + \mathbf{R}_{\rho^w}^c + \mathbf{R}_t^c + \mathbf{R}_{k^g}^c + \mathbf{R}_{k^w}^c + \mathbf{R}_d^c + \mathbf{R}_{\rho^s}^c + \mathbf{R}_\xi^c + \mathbf{R}_b^c = \mathbf{0} , \qquad \text{(E.120)}$$

$$\mathbf{R}^g = \mathbf{R}_s^g + \mathbf{R}_{\rho^{ga}}^g + \mathbf{R}_t^g + \mathbf{R}_{k^g}^g + \mathbf{R}_d^g + \mathbf{R}_{\rho^s}^g + \mathbf{R}_\xi^g + \mathbf{R}_b^g = \mathbf{0} , \qquad \text{(E.121)}$$

and

$$\mathbf{R}^t = \mathbf{R}_c^t + \mathbf{R}_g^t + \mathbf{R}_w^t + \mathbf{R}_\lambda^t + \mathbf{R}_s^t + \mathbf{R}_{\rho^w}^t + \mathbf{R}_t^t + \mathbf{R}_{k^g}^t + \mathbf{R}_{k^w}^t + \mathbf{R}_{\rho^s}^t + \mathbf{R}_\xi^t + \mathbf{R}_{dehydr}^t + \mathbf{R}_b^t = \mathbf{0} . \qquad \text{(E.122)}$$

E.1.4 Solution – Newton-Raphson iteration

Determination of the nodal values for $\mathbf{v}_c$, $\mathbf{v}_g$, and $\mathbf{v}_t$, respectively, is achieved by employing the Newton-Raphson iteration scheme (see Figure E.3 for illustration), which leads to a system of linear equations, reading[4]

$$\mathbf{R}_{i+1}^{(k)} + \mathbf{K}_{T,i+1}^{(k)} \Delta(\Delta\mathbf{v}_{i+1})^{(k+1)} = \mathbf{0}\,, \tag{E.123}$$

with

$$\mathbf{K}_{T,i+1}^{(k)} = \frac{d\mathbf{R}_{i+1}}{d(\Delta\mathbf{v}_{i+1})}\bigg|_{\Delta\mathbf{v}_{i+1}^{(k)}}\,, \tag{E.124}$$

where $\mathbf{R}_{i+1}$ is the residuum vector as depicted in Equations (E.120), (E.121), and (E.122). Accordingly, the derivation of the residuum $\mathbf{R}$ (which comprises $\mathbf{R}^c$, $\mathbf{R}^g$, and $\mathbf{R}^t$) has to be performed with respect to every state variable.
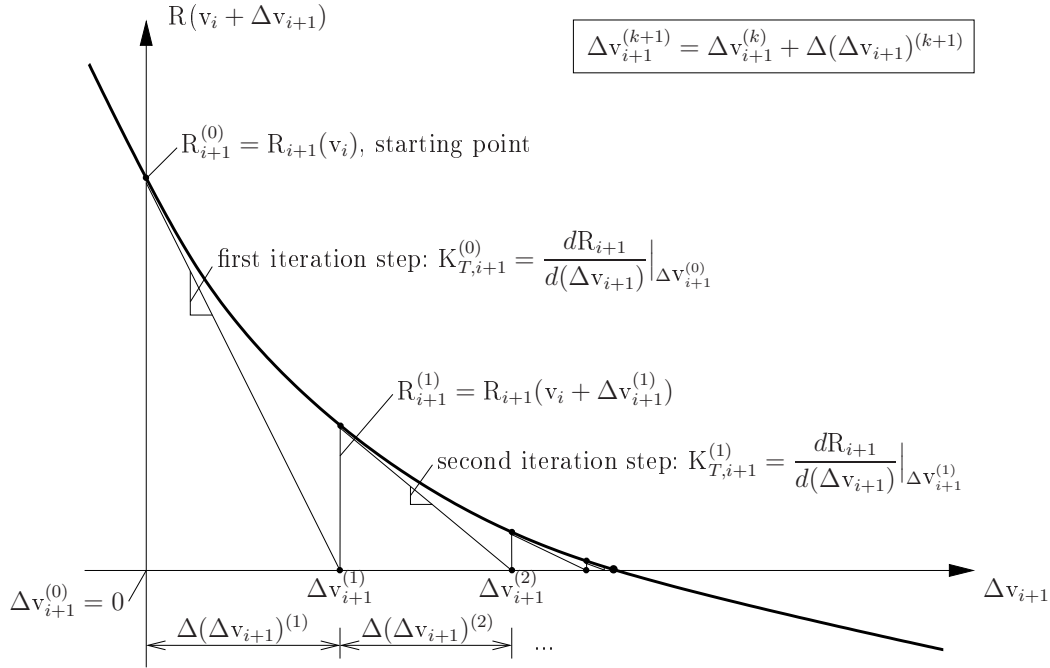
Figure E.3: Illustration of Newton-Raphson iteration for the solution of $R(\Delta\mathrm{v}_{i+1}) = 0$

---

[4]It is worth mentioning that, at a given time step (e.g., "i+1") during the first Newton-Raphson iteration step, the residuum and, hence, the nodal pressures and temperatures are determined with dependent functions which were calculated with pressures and temperatures from time step "i". At the end of the first iteration step, the dependent functions are updated (calculated with the new nodal pressures and temperatures), resulting in a modified residuum. Because of this updating scheme, quadratic convergence is no longer achieved, however the solution for time step "i+1" is determined with linear convergence of the residuum vector.

For illustration purposes, Equation (E.123) is depicted in detail in Appendix E.1.5. In the form of Equation (E.229) in Appendix E.1.5, Equation (E.123) can be solved using a forward-elimination/backward-substitution scheme (see Appendix E.1.6 and, e.g., [47]).

The residuum vector $\mathbf{R}^c$ derived with respect to state variable $\mathbf{v}_c$ reads

$$\frac{\partial \mathbf{R}^c}{\partial \mathbf{v}_c} = \frac{\partial \mathbf{R}^c_s}{\partial \mathbf{v}_c} + \frac{\partial \mathbf{R}^c_{\rho^{gw}}}{\partial \mathbf{v}_c} + \frac{\partial \mathbf{R}^c_{\rho^w}}{\partial \mathbf{v}_c} + \frac{\partial \mathbf{R}^c_t}{\partial \mathbf{v}_c} + \frac{\partial \mathbf{R}^c_{kg}}{\partial \mathbf{v}_c} + \frac{\partial \mathbf{R}^c_{kw}}{\partial \mathbf{v}_c} + \frac{\partial \mathbf{R}^c_d}{\partial \mathbf{v}_c} + \frac{\partial \mathbf{R}^c_{\rho^s}}{\partial \mathbf{v}_c} + \frac{\partial \mathbf{R}^c_\xi}{\partial \mathbf{v}_c} + \frac{\partial \mathbf{R}^c_b}{\partial \mathbf{v}_c} \ , \quad \text{(E.125)}$$

with

$$\frac{\partial \mathbf{R}^c_s}{\partial \mathbf{v}_c} = \left\{ \bigwedge_{e=1}^{n_e} \int_{x_e}^{x_{e+1}} \left[\mathbf{N}_c^T \left(-n \frac{\partial \rho^{gw}}{\partial p^c} \frac{\Delta S_w}{\Delta t} \right.\right.\right.$$
$$\left.\left.\left. + n(\rho^w - \rho^{gw}) \frac{1}{\Delta t} \frac{\partial S_w}{\partial p^c} \right) \mathbf{N}_c \right] dx \right\} \ , \quad \text{(E.126)}$$

$$\frac{\partial \mathbf{R}^c_{\rho^{gw}}}{\partial \mathbf{v}_c} = \left\{ \bigwedge_{e=1}^{n_e} \int_{x_e}^{x_{e+1}} \left[\mathbf{N}_c^T \left(-n \frac{\partial S_w}{\partial p^c} \frac{\Delta \rho^{gw}}{\Delta t} \right.\right.\right.$$
$$\left.\left.\left. + n(1 - S_w) \frac{1}{\Delta t} \frac{\partial \rho^{gw}}{\partial p^c} \right) \mathbf{N}_c \right] dx \right\} \ , \quad \text{(E.127)}$$

$$\frac{\partial \mathbf{R}^c_{\rho^w}}{\partial \mathbf{v}_c} = \left\{ \bigwedge_{e=1}^{n_e} \int_{x_e}^{x_{e+1}} \left[\mathbf{N}_c^T n \frac{\partial S_w}{\partial p^c} \frac{\Delta \rho^w}{\Delta t} \mathbf{N}_c \right] dx \right\} \ , \quad \text{(E.128)}$$

$$\frac{\partial \mathbf{R}^c_t}{\partial \mathbf{v}_c} = \left\{ \bigwedge_{e=1}^{n_e} \int_{x_e}^{x_{e+1}} \left[-\mathbf{N}_c^T \frac{\partial \beta_{swg}}{\partial p^c} \frac{\Delta T}{\Delta t} \mathbf{N}_c \right] dx \right\} \ , \quad \text{(E.129)}$$

$$\frac{\partial \mathbf{R}^c_{kg}}{\partial \mathbf{v}_c} = \left\{ \bigwedge_{e=1}^{n_e} \int_{x_e}^{x_{e+1}} \left[\frac{D^s \mathbf{N}_c^T}{Dx} \left(\frac{\partial \rho^{gw}}{\partial p^c} \frac{k k^{rg}}{\eta^g} \frac{D^s p^g}{Dx} \right.\right.\right.$$
$$\left.\left.\left. + \rho^{gw} k \frac{\partial}{\partial p^c} \left(\frac{k^{rg}}{\eta^g} \right) \frac{D^s p^g}{Dx} + \rho^w k \frac{\partial}{\partial p^c} \left(\frac{k^{rw}}{\eta^w} \right) \frac{D^s p^g}{Dx} \right) \mathbf{N}_c \right] dx \right\} \ , \quad \text{(E.130)}$$

$$\frac{\partial \mathbf{R}^c_{kw}}{\partial \mathbf{v}_c} = \left\{ \bigwedge_{e=1}^{n_e} \int_{x_e}^{x_{e+1}} \left[-\frac{D^s \mathbf{N}_c^T}{Dx} \left(\rho^w k \frac{\partial}{\partial p^c} \left(\frac{k^{rw}}{\eta^w} \right) \frac{D^s p^c}{Dx} \mathbf{N}_c \right.\right.\right.$$
$$\left.\left.\left. + \rho^w \frac{k k^{rw}}{\eta^w} \frac{D^s \mathbf{N}_c}{Dx} \right) \right] dx \right\} \ , \quad \text{(E.131)}$$

$$\frac{\partial \mathbf{R}^c_d}{\partial \mathbf{v}_c} = \left\{ \bigwedge_{e=1}^{n_e} \int_{x_e}^{x_{e+1}} \left[\frac{D^s \mathbf{N}_c^T}{Dx} \left(\frac{\partial \rho^g}{\partial p^c} \frac{M_a M_w}{M_g^2} D_{eff} \frac{D^s}{Dx} \left(\frac{p^{gw}}{p^g} \right) \mathbf{N}_c \right.\right.\right.$$
$$\left. - \rho^g \frac{2 M_a M_w}{M_g^3} \frac{\partial M_g}{\partial p^c} D_{eff} \frac{D^s}{Dx} \left(\frac{p^{gw}}{p^g} \right) \mathbf{N}_c + \rho^g \frac{M_a M_w}{M_g^2} \frac{\partial D_{eff}}{\partial p^c} \frac{D^s}{Dx} \left(\frac{p^{gw}}{p^g} \right) \mathbf{N}_c \right.$$
$$\left.\left.\left. + \rho^g \frac{M_a M_w}{M_g^2} D_{eff} \frac{1}{p^g} \frac{\partial p^{gw}}{\partial p^c} \frac{D^s \mathbf{N}_c}{Dx} \right) \right] dx \right\} \ , \quad \text{(E.132)}$$

$$\frac{\partial \mathbf{R}^c_{\rho^s}}{\partial \mathbf{v}_c} = \left\{ \overset{n_e}{\underset{e=1}{\mathbf{A}}} \int_{x_e}^{x_{e+1}} \left[\mathbf{N}^T_c \left(\frac{(1-n)(1-S_w)}{\rho^s} \frac{\partial \rho^{gw}}{\partial p^c} \frac{\partial \rho^s}{\partial T} \frac{\Delta T}{\Delta t} \right. \right. \right.$$

$$\left. \left. \left. + \frac{(1-n)(\rho^w - \rho^{gw})}{\rho^s} \frac{\partial S_w}{\partial p^c} \frac{\partial \rho^s}{\partial T} \frac{\Delta T}{\Delta t} \right) \mathbf{N}_c \right] dx \right\} , \tag{E.133}$$

$$\frac{\partial \mathbf{R}^c_{\xi}}{\partial \mathbf{v}_c} = \left\{ \overset{n_e}{\underset{e=1}{\mathbf{A}}} \int_{x_e}^{x_{e+1}} \left[-\mathbf{N}^T_c \left(\frac{\partial \rho^{gw}}{\partial p^c}(1-S_w) \right. \right. \right.$$

$$\left. \left. \left. + (\rho^w - \rho^{gw})\frac{\partial S_w}{\partial p^c} \right) \frac{m_c f_h}{\rho^s} \frac{m_w}{m_c} \frac{\Delta \xi}{\Delta t} \mathbf{N}_c \right] dx \right\} , \tag{E.134}$$

$$\frac{\partial \mathbf{R}^c_b}{\partial \mathbf{v}_c} = \mathbf{1}_1 \beta_1 \frac{\partial \rho^{gw}}{\partial p^c} \mathbf{1}^T_1 + \mathbf{1}_{n_e+1} \beta_{n_e+1} \frac{\partial \rho^{gw}}{\partial p^c} \mathbf{1}^T_{n_e+1} , \tag{E.135}$$

and

$$\frac{\partial \beta_{swg}}{\partial p^c} = (1-n)\beta_s \left[(1-S_w)\frac{\partial \rho^{gw}}{\partial p^c} + \frac{\partial S_w}{\partial p^c}(\rho^w - \rho^{gw}) \right] . \tag{E.136}$$

In Equation (E.126),

$$\frac{\partial}{\partial \mathbf{v}_c} \rho^{gw} = \frac{\partial \rho^{gw}}{\partial p^c} \frac{\partial p^c}{\partial \mathbf{v}_c} = \frac{\partial \rho^{gw}}{\partial p^c} \mathbf{N}_c \tag{E.137}$$

and

$$\frac{\partial}{\partial \mathbf{v}_c} \left(\frac{\Delta S_w}{\Delta t} \right) = \frac{1}{\Delta t} \left(\frac{\partial S_w}{\partial p^c} \frac{\partial p^c}{\partial \mathbf{v}_c} \right) = \frac{1}{\Delta t} \frac{\partial S_w}{\partial p^c} \mathbf{N}_c \tag{E.138}$$

were considered, which is generally valid for all dependent functions. In Equation (E.131),

$$\frac{\partial}{\partial \mathbf{v}_c} \left(\frac{D^s p^c}{Dx} \right) = \frac{\partial}{\partial \mathbf{v}_c} \left(\frac{D^s \mathbf{N}_c}{Dx} \mathbf{v}_c \right) = \frac{D^s \mathbf{N}_c}{Dx} \tag{E.139}$$

was taken into account. In Equation (E.132),

$$\frac{\partial}{\partial \mathbf{v}_c} \left(\frac{D^s}{Dx} \left(\frac{p^{gw}}{p^g} \right) \right) = \frac{1}{p^g} \frac{D^s}{Dx} \left(\frac{\partial p^{gw}}{\partial p^c} \frac{\partial p^c}{\partial \mathbf{v}_c} \right) = \frac{1}{p^g} \frac{\partial p^{gw}}{\partial p^c} \frac{D^s \mathbf{N}_c}{Dx} \tag{E.140}$$

was considered.

The residuum vector $\mathbf{R}^c$ derived with respect to state variable $\mathbf{v}_g$ reads

$$\frac{\partial \mathbf{R}^c}{\partial \mathbf{v}_g} = \frac{\partial \mathbf{R}_s^c}{\partial \mathbf{v}_g} + \frac{\partial \mathbf{R}_{\rho^{gw}}^c}{\partial \mathbf{v}_g} + \frac{\partial \mathbf{R}_{\rho^w}^c}{\partial \mathbf{v}_g} + \frac{\partial \mathbf{R}_t^c}{\partial \mathbf{v}_g} + \frac{\partial \mathbf{R}_{kg}^c}{\partial \mathbf{v}_g} + \frac{\partial \mathbf{R}_{kw}^c}{\partial \mathbf{v}_g} + \frac{\partial \mathbf{R}_d^c}{\partial \mathbf{v}_g} + \frac{\partial \mathbf{R}_{\rho^s}^c}{\partial \mathbf{v}_g} + \frac{\partial \mathbf{R}_\xi^c}{\partial \mathbf{v}_g} + \frac{\partial \mathbf{R}_b^c}{\partial \mathbf{v}_g} \,, \quad \text{(E.141)}$$

with

$$\frac{\partial \mathbf{R}_s^c}{\partial \mathbf{v}_g} = \frac{\partial \mathbf{R}_{\rho^{gw}}^c}{\partial \mathbf{v}_g} = \frac{\partial \mathbf{R}_{\rho^w}^c}{\partial \mathbf{v}_g} = \frac{\partial \mathbf{R}_t^c}{\partial \mathbf{v}_g} = 0 \,, \quad \text{(E.142)}$$

$$\frac{\partial \mathbf{R}_{kg}^c}{\partial \mathbf{v}_g} = \left\{ \mathop{\mathbf{A}}_{e\,=\,1}^{n_e} \int_{x_e}^{x_{e+1}} \left[\frac{D^s \mathbf{N}_c^T}{Dx} \left(\rho^{gw} \frac{\partial k}{\partial p^g} \frac{k^{rg}}{\eta^g} \frac{D^s p^g}{Dx} \mathbf{N}_g + \rho^{gw} k \frac{\partial}{\partial p^g} \left(\frac{k^{rg}}{\eta^g} \right) \frac{D^s p^g}{Dx} \mathbf{N}_g \right. \right. $$
$$\left. \left. + \rho^{gw} \frac{k k^{rg}}{\eta^g} \frac{D^s \mathbf{N}_g}{Dx} + \rho^w \frac{k k^{rw}}{\eta^w} \frac{D^s \mathbf{N}_g}{Dx} \right) \right] dx \right\} \,, \quad \text{(E.143)}$$

$$\frac{\partial \mathbf{R}_{kw}^c}{\partial \mathbf{v}_g} = 0 \,, \quad \text{(E.144)}$$

$$\frac{\partial \mathbf{R}_d^c}{\partial \mathbf{v}_g} = \left\{ \mathop{\mathbf{A}}_{e\,=\,1}^{n_e} \int_{x_e}^{x_{e+1}} \left[\frac{D^s \mathbf{N}_c^T}{Dx} \left(\frac{\partial \rho^g}{\partial p^g} \frac{M_a M_w}{M_g^2} D_{eff} \frac{D^s}{Dx} \left(\frac{p^{gw}}{p^g} \right) \mathbf{N}_g \right. \right. $$
$$\left. - \rho^g \frac{2 M_a M_w}{M_g^3} \frac{\partial M_g}{\partial p^g} D_{eff} \frac{D^s}{Dx} \left(\frac{p^{gw}}{p^g} \right) \mathbf{N}_g + \rho^g \frac{M_a M_w}{M_g^2} \frac{\partial D_{eff}}{\partial p^g} \frac{D^s}{Dx} \left(\frac{p^{gw}}{p^g} \right) \mathbf{N}_g \right.$$
$$\left. \left. - \rho^g \frac{M_a M_w}{M_g^2} D_{eff} \frac{p^{gw}}{(p^g)^2} \frac{D^s \mathbf{N}_g}{Dx} \right) \right] dx \right\} \,, \quad \text{(E.145)}$$

$$\frac{\partial \mathbf{R}_{\rho^s}^c}{\partial \mathbf{v}_g} = \frac{\partial \mathbf{R}_\xi^c}{\partial \mathbf{v}_g} = \frac{\partial \mathbf{R}_b^c}{\partial \mathbf{v}_g} = 0 \,. \quad \text{(E.146)}$$

In Equation (E.143),

$$\frac{\partial}{\partial \mathbf{v}_g} \left(\frac{D^s p^g}{Dx} \right) = \frac{\partial}{\partial \mathbf{v}_g} \left(\frac{D^s \mathbf{N}_g}{Dx} \mathbf{v}_g \right) = \frac{D^s \mathbf{N}_g}{Dx} \quad \text{(E.147)}$$

was taken into account, whereas in Equation (E.145),

$$\frac{\partial}{\partial \mathbf{v}_g} \left(\frac{D^s}{Dx} \left(\frac{p^{gw}}{p^g} \right) \right) = p^{gw} \left(-\frac{1}{(p^g)^2} \frac{\partial}{\partial \mathbf{v}_g} \left(\frac{D^s p^g}{Dx} \right) \right) = p^{gw} \left(-\frac{1}{(p^g)^2} \right) \frac{D^s \mathbf{N}_g}{Dx} \quad \text{(E.148)}$$

was considered.

The residuum vector $\mathbf{R}^c$ derived with respect to state variable $\mathbf{v}_t$ reads

$$\frac{\partial \mathbf{R}^c}{\partial \mathbf{v}_t} = \frac{\partial \mathbf{R}^c_s}{\partial \mathbf{v}_t} + \frac{\partial \mathbf{R}^c_{\rho^{gw}}}{\partial \mathbf{v}_t} + \frac{\partial \mathbf{R}^c_{\rho^w}}{\partial \mathbf{v}_t} + \frac{\partial \mathbf{R}^c_t}{\partial \mathbf{v}_t} + \frac{\partial \mathbf{R}^c_{k^g}}{\partial \mathbf{v}_t} + \frac{\partial \mathbf{R}^c_{k^w}}{\partial \mathbf{v}_t} + \frac{\partial \mathbf{R}^c_d}{\partial \mathbf{v}_t} + \frac{\partial \mathbf{R}^c_{\rho^s}}{\partial \mathbf{v}_t} + \frac{\partial \mathbf{R}^c_{\xi}}{\partial \mathbf{v}_t} + \frac{\partial \mathbf{R}^c_b}{\partial \mathbf{v}_t} , \quad \text{(E.149)}$$

with

$$\frac{\partial \mathbf{R}^c_s}{\partial \mathbf{v}_t} = \left\{ \overset{n_e}{\underset{e=1}{\mathbf{A}}} \int_{x_e}^{x_{e+1}} \left[\mathbf{N}_c^T \left(\frac{\partial n}{\partial T}(\rho^w - \rho^{gw})\frac{\Delta S_w}{\Delta t} + n(\frac{\partial \rho^w}{\partial T} - \frac{\partial \rho^{gw}}{\partial T})\frac{\Delta S_w}{\Delta t} \right. \right. \right.$$
$$\left. \left. \left. + n(\rho^w - \rho^{gw})\frac{1}{\Delta t}\frac{\partial S_w}{\partial T} \right) \mathbf{N}_t \right] dx \right\} , \quad \text{(E.150)}$$

$$\frac{\partial \mathbf{R}^c_{\rho^{gw}}}{\partial \mathbf{v}_t} = \left\{ \overset{n_e}{\underset{e=1}{\mathbf{A}}} \int_{x_e}^{x_{e+1}} \left[\mathbf{N}_c^T \left(\frac{\partial n}{\partial T}(1 - S_w)\frac{\Delta \rho^{gw}}{\Delta t} - n\frac{\partial S_w}{\partial T}\frac{\Delta \rho^{gw}}{\Delta t} \right. \right. \right.$$
$$\left. \left. \left. + n(1 - S_w)\frac{1}{\Delta t}\frac{\partial \rho^{gw}}{\partial T} \right) \mathbf{N}_t \right] dx \right\} , \quad \text{(E.151)}$$

$$\frac{\partial \mathbf{R}^c_{\rho^w}}{\partial \mathbf{v}_t} = \left\{ \overset{n_e}{\underset{e=1}{\mathbf{A}}} \int_{x_e}^{x_{e+1}} \left[\mathbf{N}_c^T \left(\frac{\partial n}{\partial T}S_w\frac{\Delta \rho^w}{\Delta t} + n\frac{\partial S_w}{\partial T}\frac{\Delta \rho^w}{\Delta t} \right. \right. \right.$$
$$\left. \left. \left. + nS_w\frac{1}{\Delta t}\frac{\partial \rho^w}{\partial T} \right) \mathbf{N}_c \right] dx \right\} , \quad \text{(E.152)}$$

$$\frac{\partial \mathbf{R}^c_t}{\partial \mathbf{v}_t} = \left\{ \overset{n_e}{\underset{e=1}{\mathbf{A}}} \int_{x_e}^{x_{e+1}} \left[-\mathbf{N}_c^T \left(\frac{\partial \beta_{swg}}{\partial T}\frac{\Delta T}{\Delta t} + \beta_{swg}\frac{1}{\Delta t} \right) \mathbf{N}_t \right] dx \right\} , \quad \text{(E.153)}$$

$$\frac{\partial \mathbf{R}^c_{k^g}}{\partial \mathbf{v}_t} = \left\{ \overset{n_e}{\underset{e=1}{\mathbf{A}}} \int_{x_e}^{x_{e+1}} \left[\frac{D^s\mathbf{N}_c^T}{Dx} \left(\frac{\partial \rho^{gw}}{\partial T}\frac{kk^{rg}}{\eta^g}\frac{D^s p^g}{Dx} + \frac{\partial \rho^w}{\partial T}\frac{kk^{rw}}{\eta^w}\frac{D^s p^g}{Dx} \right. \right. \right.$$
$$\left. + \rho^{gw}\frac{\partial k}{\partial T}\frac{k^{rg}}{\eta^g}\frac{D^s p^g}{Dx} + \rho^w\frac{\partial k}{\partial T}\frac{k^{rw}}{\eta^w}\frac{D^s p^g}{Dx} \right.$$
$$\left. \left. \left. + \rho^{gw}k\frac{\partial}{\partial T}\left(\frac{k^{rg}}{\eta^g}\right)\frac{D^s p^g}{Dx} + \rho^w k\frac{\partial}{\partial T}\left(\frac{k^{rw}}{\eta^w}\right)\frac{D^s p^g}{Dx} \right) \mathbf{N}_t \right] dx \right\} , \quad \text{(E.154)}$$

$$\frac{\partial \mathbf{R}^c_{k^w}}{\partial \mathbf{v}_t} = \left\{ \overset{n_e}{\underset{e=1}{\mathbf{A}}} \int_{x_e}^{x_{e+1}} \left[-\frac{D^s\mathbf{N}_c^T}{Dx} \left(\frac{\partial \rho^w}{\partial T}\frac{kk^{rw}}{\eta^w}\frac{D^s p^c}{Dx} + \rho^w\frac{\partial k}{\partial T}\frac{k^{rw}}{\eta^w}\frac{D^s p^c}{Dx} \right. \right. \right.$$
$$\left. \left. \left. + \rho^w k\frac{\partial}{\partial T}\left(\frac{k^{rw}}{\eta^w}\right)\frac{D^s p^c}{Dx} \right) \mathbf{N}_t \right] dx \right\} , \quad \text{(E.155)}$$

$$\frac{\partial \mathbf{R}_d^c}{\partial \mathbf{v}_t} = \left\{ \mathbf{\overset{n_e}{\underset{e\,=\,1}{A}}} \int_{x_e}^{x_{e+1}} \left[\frac{D^s \mathbf{N}_c^T}{Dx} \left(\frac{\partial \rho^g}{\partial T} \frac{M_a M_w}{M_g^2} D_{eff} \frac{D^s}{Dx} \left(\frac{p^{gw}}{p^g} \right) \mathbf{N}_t \right. \right. \right.$$

$$- \rho^g \frac{2 M_a M_w}{M_g^3} \frac{\partial M_g}{\partial T} D_{eff} \frac{D^s}{Dx} \left(\frac{p^{gw}}{p^g} \right) \mathbf{N}_t + \rho^g \frac{M_a M_w}{M_g^2} \frac{\partial D_{eff}}{\partial T} \frac{D^s}{Dx} \left(\frac{p^{gw}}{p^g} \right) \mathbf{N}_t$$

$$\left. \left. \left. + \rho^g \frac{M_a M_w}{M_g^2} D_{eff} \frac{1}{p^g} \frac{\partial p^{gw}}{\partial T} \frac{D^s \mathbf{N}_t}{Dx} \right) \right] dx \right\}, \tag{E.156}$$

$$\frac{\partial \mathbf{R}_{\rho^s}^c}{\partial \mathbf{v}_t} = \left\{ \mathbf{\overset{n_e}{\underset{e\,=\,1}{A}}} \int_{x_e}^{x_{e+1}} \left[\mathbf{N}_c^T \left(- \frac{\partial n}{\partial T} \frac{\rho^{gw}(1 - S_w) + \rho^w S_w}{\rho^s} \frac{\partial \rho^s}{\partial T} \frac{\Delta T}{\Delta t} \right. \right. \right.$$

$$+ \frac{(1 - n)}{\rho^s} \left[\frac{\partial \rho^{gw}}{\partial T}(1 - S_w) + \frac{\partial \rho^w}{\partial T} S_w \right] \frac{\partial \rho^s}{\partial T} \frac{\Delta T}{\Delta t}$$

$$+ \frac{(1 - n)(\rho^w - \rho^{gw})}{\rho^s} \frac{\partial S_w}{\partial T} \frac{\partial \rho^s}{\partial T} \frac{\Delta T}{\Delta t}$$

$$- (1 - n) \left[\rho^{gw}(1 - S_w) + \rho^w S_w \right] \frac{1}{(\rho^s)^2} \left(\frac{\partial \rho^s}{\partial T} \right)^2 \frac{\Delta T}{\Delta t}$$

$$\left. \left. \left. + \frac{(1 - n) \left[\rho^{gw}(1 - S_w) + \rho^w S_w \right]}{\rho^s} \frac{\partial \rho^s}{\partial T} \frac{1}{\Delta t} \right) \mathbf{N}_t \right] dx \right\}, \tag{E.157}$$

$$\frac{\partial \mathbf{R}_\xi^c}{\partial \mathbf{v}_t} = \left\{ \mathbf{\overset{n_e}{\underset{e\,=\,1}{A}}} \int_{x_e}^{x_{e+1}} \left[-\mathbf{N}_c^T \left(\left[\frac{\partial \rho^{gw}}{\partial T}(1 - S_w) + \frac{\partial \rho^w}{\partial T} S_w \right] \frac{1}{\rho^s} + (\rho^w - \rho^{gw}) \frac{\partial S_w}{\partial T} \frac{1}{\rho^s} \right. \right. \right.$$

$$\left. - \left[\rho^{gw}(1 - S_w) + \rho^w S_w \right] \frac{1}{(\rho^s)^2} \frac{\partial \rho^s}{\partial T} \right) m_c f_h \frac{m_w}{m_c} \frac{\Delta \xi}{\Delta t} \mathbf{N}_t$$

$$+ \mathbf{N}_c^T \left(\left[-\rho^{gw}(1 - S_w) - \rho^w S_w \right] \frac{m_c f_h}{\rho^s} \frac{m_w}{m_c} \right.$$

$$\left. \left. \left. + m_c f_h \frac{m_w}{m_c} \right) \frac{1}{\Delta t} \frac{\partial \xi}{\partial T} \mathbf{N}_t \right] dx \right\}, \tag{E.158}$$

$$\frac{\partial \mathbf{R}_b^c}{\partial \mathbf{v}_t} = \mathbf{1}_1 \beta_1 \frac{\partial \rho^{gw}}{\partial T} \mathbf{1}_1^T + \mathbf{1}_{n_e+1} \beta_{n_e+1} \frac{\partial \rho^{gw}}{\partial T} \mathbf{1}_{n_e+1}^T, \tag{E.159}$$

and

$$\frac{\partial \beta_{swg}}{\partial T} = -\frac{\partial n}{\partial T} \beta_s \left[\rho^{gw} + (\rho^w - \rho^{gw}) S_w \right]$$

$$+ (1 - n) \beta_s \left[(1 - S_w) \frac{\partial \rho^{gw}}{\partial T} + S_w \frac{\partial \rho^w}{\partial T} + \frac{\partial S_w}{\partial T} (\rho^w - \rho^{gw}) \right]. \tag{E.160}$$

In Equation (E.157), the derivation of the solid density ρ^s with respect to temperature was performed following the product rule, yielding (for illustration purposes, constants

are not displayed here)

$$\frac{\partial}{\partial \mathbf{v}_t} \left(\mathbf{N}_c^T \frac{\partial \rho^s}{\partial T} \frac{\Delta T}{\Delta t} \right) = \mathbf{N}_c^T \frac{\partial^2 \rho^s}{\partial T^2} \frac{\Delta T}{\Delta t} \mathbf{N}_t + \mathbf{N}_c^T \frac{\partial \rho^s}{\partial T} \frac{1}{\Delta t} \mathbf{N}_t \,, \tag{E.161}$$

where

$$\frac{\partial}{\partial \mathbf{v}_t} \left(\frac{\partial \rho^s}{\partial T} \right) = \frac{\partial^2 \rho^s}{\partial T^2} \frac{\partial T}{\partial \mathbf{v}_t} = \frac{\partial^2 \rho^s}{\partial T^2} \mathbf{N}_t \tag{E.162}$$

and

$$\frac{\partial}{\partial \mathbf{v}_t} \left(\frac{\Delta T}{\Delta t} \right) = \frac{\partial}{\partial \mathbf{v}_t} \left(\mathbf{N}_t \frac{\Delta \mathbf{v}_t}{\Delta t} \right) = \frac{1}{\Delta t} \mathbf{N}_t \tag{E.163}$$

were taken into account. As depicted in Equation (E.70-(14)), $\rho^s(T)$ is a linear function, resulting in $\partial^2 \rho^s / \partial T^2 = 0$. Therefore, the first term of Equation (E.161) vanishes in Equation (E.157).

The residuum vector $\mathbf{R}^g$ derived with respect to state variable $\mathbf{v}_c$ reads

$$\frac{\partial \mathbf{R}^g}{\partial \mathbf{v}_c} = \frac{\partial \mathbf{R}_s^g}{\partial \mathbf{v}_c} + \frac{\partial \mathbf{R}_{\rho^{ga}}^g}{\partial \mathbf{v}_c} + \frac{\partial \mathbf{R}_t^g}{\partial \mathbf{v}_c} + \frac{\partial \mathbf{R}_{k^g}^g}{\partial \mathbf{v}_c} + \frac{\partial \mathbf{R}_d^g}{\partial \mathbf{v}_c} + \frac{\partial \mathbf{R}_{\rho^s}^g}{\partial \mathbf{v}_c} + \frac{\partial \mathbf{R}_\xi^g}{\partial \mathbf{v}_c} + \frac{\partial \mathbf{R}_b^g}{\partial \mathbf{v}_c} \,, \qquad (\text{E.164})$$

with

$$\frac{\partial \mathbf{R}_s^g}{\partial \mathbf{v}_c} = \left\{ \overset{n_e}{\underset{e=1}{\mathbf{A}}} \int_{x_e}^{x_{e+1}} \left[-\mathbf{N}_g^T \left(n\frac{\partial \rho^{ga}}{\partial p^c}\frac{\Delta S_w}{\Delta t} + n\rho^{ga}\frac{1}{\Delta t}\frac{\partial S_w}{\partial p^c} \right) \mathbf{N}_c \right] dx \right\} \,, \qquad (\text{E.165})$$

$$\frac{\partial \mathbf{R}_{\rho^{ga}}^g}{\partial \mathbf{v}_c} = \left\{ \overset{n_e}{\underset{e=1}{\mathbf{A}}} \int_{x_e}^{x_{e+1}} \left[\mathbf{N}_g^T \left(-n\frac{\partial S_w}{\partial p^c}\frac{\Delta \rho^{ga}}{\Delta t} + n(1-S_w)\frac{1}{\Delta t}\frac{\partial \rho^{ga}}{\partial p^c} \right) \mathbf{N}_c \right] dx \right\} \,, \quad (\text{E.166})$$

$$\frac{\partial \mathbf{R}_t^g}{\partial \mathbf{v}_c} = \left\{ \overset{n_e}{\underset{e=1}{\mathbf{A}}} \int_{x_e}^{x_{e+1}} \left[-\mathbf{N}_g^T \left(\frac{\partial \beta_{sa}}{\partial p^c}\rho^{ga}\frac{\Delta T}{\Delta t} + \beta_{sa}\frac{\partial \rho^{ga}}{\partial p^c}\frac{\Delta T}{\Delta t} \right) \mathbf{N}_c \right] dx \right\} \,, \qquad (\text{E.167})$$

$$\frac{\partial \mathbf{R}_{k^g}^g}{\partial \mathbf{v}_c} = \left\{ \overset{n_e}{\underset{e=1}{\mathbf{A}}} \int_{x_e}^{x_{e+1}} \left[\frac{D^s\mathbf{N}_g^T}{Dx} \left(\frac{\partial \rho^{ga}}{\partial p^c}\frac{kk^{rg}}{\eta^g}\frac{D^s p^g}{Dx} \right. \right.$$

$$\left. \left. +\rho^{ga}k\frac{\partial}{\partial p^c}\left(\frac{k^{rg}}{\eta^g} \right)\frac{D^s p^g}{Dx} \right) \mathbf{N}_c \right] dx \right\} \,, \qquad (\text{E.168})$$

$$\frac{\partial \mathbf{R}_d^g}{\partial \mathbf{v}_c} = \left\{ \overset{n_e}{\underset{e=1}{\mathbf{A}}} \int_{x_e}^{x_{e+1}} \left[-\frac{D^s\mathbf{N}_g^T}{Dx} \left(\frac{\partial \rho^g}{\partial p^c}\frac{M_a M_w}{M_g^2}D_{eff}\frac{D^s}{Dx}\left(\frac{p^{gw}}{p^g} \right)\mathbf{N}_c \right. \right.$$

$$-\rho^g\frac{2M_a M_w}{M_g^3}\frac{\partial M_g}{\partial p^c}D_{eff}\frac{D^s}{Dx}\left(\frac{p^{gw}}{p^g} \right)\mathbf{N}_c + \rho^g\frac{M_a M_w}{M_g^2}\frac{\partial D_{eff}}{\partial p^c}\frac{D^s}{Dx}\left(\frac{p^{gw}}{p^g} \right)\mathbf{N}_c$$

$$\left. \left. +\rho^g\frac{M_a M_w}{M_g^2}D_{eff}\frac{1}{p^g}\frac{\partial p^{gw}}{\partial p^c}\frac{D^s\mathbf{N}_c}{Dx} \right) \right] dx \right\} \,, \qquad (\text{E.169})$$

$$\frac{\partial \mathbf{R}_{\rho^s}^g}{\partial \mathbf{v}_c} = \left\{ \overset{n_e}{\underset{e=1}{\mathbf{A}}} \int_{x_e}^{x_{e+1}} \left[\mathbf{N}_g^T \left(\frac{(1-n)(1-S_w)}{\rho^s}\frac{\partial \rho^{ga}}{\partial p^c}\frac{\partial \rho^s}{\partial T}\frac{\Delta T}{\Delta t} \right. \right.$$

$$\left. \left. -\frac{(1-n)\rho^{ga}}{\rho^s}\frac{\partial S_w}{\partial p^c}\frac{\partial \rho^s}{\partial T}\frac{\Delta T}{\Delta t} \right) \mathbf{N}_c \right] dx \right\} \,, \qquad (\text{E.170})$$

$$\frac{\partial \mathbf{R}_\xi^g}{\partial \mathbf{v}_c} = \left\{ \overset{n_e}{\underset{e=1}{\mathbf{A}}} \int_{x_e}^{x_{e+1}} \left[-\mathbf{N}_g^T \left(\frac{\partial \rho^{ga}}{\partial p^c}(1-S_w) - \rho^{ga}\frac{\partial S_w}{\partial p^c} \right)\frac{m_c f_h}{\rho^s}\frac{m_w}{m_c}\frac{\Delta \xi}{\Delta t}\mathbf{N}_c \right] dx \right\} (\text{E.171})$$

$$\frac{\partial \mathbf{R}_b^g}{\partial \mathbf{v}_c} = 0 \,, \qquad (\text{E.172})$$

and

$$\frac{\partial \beta_{sa}}{\partial p^c} = -(1-n)\frac{\partial S_w}{\partial p^c}\beta_s \,. \qquad (\text{E.173})$$

The residuum vector $\mathbf{R}^g$ derived with respect to state variable $\mathbf{v}_g$ reads

$$\frac{\partial \mathbf{R}^g}{\partial \mathbf{v}_g} = \frac{\partial \mathbf{R}^g_s}{\partial \mathbf{v}_g} + \frac{\partial \mathbf{R}^g_{\rho^{ga}}}{\partial \mathbf{v}_g} + \frac{\partial \mathbf{R}^g_t}{\partial \mathbf{v}_g} + \frac{\partial \mathbf{R}^g_{k^g}}{\partial \mathbf{v}_g} + \frac{\partial \mathbf{R}^g_d}{\partial \mathbf{v}_g} + \frac{\partial \mathbf{R}^g_{\rho^s}}{\partial \mathbf{v}_g} + \frac{\partial \mathbf{R}^g_\xi}{\partial \mathbf{v}_g} + \frac{\partial \mathbf{R}^g_b}{\partial \mathbf{v}_g}, \qquad \text{(E.174)}$$

with

$$\frac{\partial \mathbf{R}^g_s}{\partial \mathbf{v}_g} = \left\{ \mathop{\mathbf{A}}_{e=1}^{n_e} \int_{x_e}^{x_{e+1}} \left[-\mathbf{N}_g^T n \frac{\partial \rho^{ga}}{\partial p^g} \frac{\Delta S_w}{\Delta t} \mathbf{N}_g \right] dx \right\}, \qquad \text{(E.175)}$$

$$\frac{\partial \mathbf{R}^g_{\rho^{ga}}}{\partial \mathbf{v}_g} = \left\{ \mathop{\mathbf{A}}_{e=1}^{n_e} \int_{x_e}^{x_{e+1}} \left[\mathbf{N}_g^T n(1-S_w) \frac{1}{\Delta t} \frac{\partial \rho^{ga}}{\partial p^g} \mathbf{N}_g \right] dx \right\}, \qquad \text{(E.176)}$$

$$\frac{\partial \mathbf{R}^g_t}{\partial \mathbf{v}_g} = \left\{ \mathop{\mathbf{A}}_{e=1}^{n_e} \int_{x_e}^{x_{e+1}} \left[-\mathbf{N}_g^T \beta_{sa} \frac{\partial \rho^{ga}}{\partial p^g} \frac{\Delta T}{\Delta t} \mathbf{N}_g \right] dx \right\}, \qquad \text{(E.177)}$$

$$\frac{\partial \mathbf{R}^g_{k^g}}{\partial \mathbf{v}_g} = \left\{ \mathop{\mathbf{A}}_{e=1}^{n_e} \int_{x_e}^{x_{e+1}} \left[\frac{D^s \mathbf{N}_g^T}{Dx} \left(\frac{\partial \rho^{ga}}{\partial p^g} \frac{k k^{rg}}{\eta^g} \frac{D^s p^g}{Dx} \mathbf{N}_g + \rho^{ga} \frac{\partial k}{\partial p^g} \frac{k^{rg}}{\eta^g} \frac{D^s p^g}{Dx} \mathbf{N}_g \right. \right. $$
$$\left. \left. + \rho^{ga} k \frac{\partial}{\partial p^g} \left(\frac{k^{rg}}{\eta^g} \right) \frac{D^s p^g}{Dx} \mathbf{N}_g + \rho^{ga} \frac{k k^{rg}}{\eta^g} \frac{D^s \mathbf{N}_g}{Dx} \right) \right] dx \right\}, \qquad \text{(E.178)}$$

$$\frac{\partial \mathbf{R}^g_d}{\partial \mathbf{v}_g} = \left\{ \mathop{\mathbf{A}}_{e=1}^{n_e} \int_{x_e}^{x_{e+1}} \left[-\frac{D^s \mathbf{N}_g^T}{Dx} \left(\frac{\partial \rho^g}{\partial p^g} \frac{M_a M_w}{M_g^2} D_{eff} \frac{D^s}{Dx} \left(\frac{p^{gw}}{p^g} \right) \mathbf{N}_g \right. \right. $$
$$\left. - \rho^g \frac{2 M_a M_w}{M_g^3} \frac{\partial M_g}{\partial p^g} D_{eff} \frac{D^s}{Dx} \left(\frac{p^{gw}}{p^g} \right) \mathbf{N}_g + \rho^g \frac{M_a M_w}{M_g^2} \frac{\partial D_{eff}}{\partial p^g} \frac{D^s}{Dx} \left(\frac{p^{gw}}{p^g} \right) \mathbf{N}_g \right. $$
$$\left. \left. - \rho^g \frac{M_a M_w}{M_g^2} D_{eff} \frac{p^{gw}}{(p^g)^2} \frac{D^s \mathbf{N}_g}{Dx} \right) \right] dx \right\}, \qquad \text{(E.179)}$$

$$\frac{\partial \mathbf{R}^g_{\rho^s}}{\partial \mathbf{v}_g} = \left\{ \mathop{\mathbf{A}}_{e=1}^{n_e} \int_{x_e}^{x_{e+1}} \left[\mathbf{N}_g^T \frac{(1-n)(1-S_w)}{\rho^s} \frac{\partial \rho^{ga}}{\partial p^g} \frac{\partial \rho^s}{\partial T} \frac{\Delta T}{\Delta t} \mathbf{N}_g \right] dx \right\}, \qquad \text{(E.180)}$$

$$\frac{\partial \mathbf{R}^g_\xi}{\partial \mathbf{v}_g} = \left\{ \mathop{\mathbf{A}}_{e=1}^{n_e} \int_{x_e}^{x_{e+1}} \left[-\mathbf{N}_g^T \frac{\partial \rho^{ga}}{\partial p^g} (1-S_w) \frac{m_c f_h}{\rho^s} \frac{m_w}{m_c} \frac{\Delta \xi}{\Delta t} \mathbf{N}_g \right] dx \right\}, \qquad \text{(E.181)}$$

$$\frac{\partial \mathbf{R}^g_b}{\partial \mathbf{v}_g} = 0. \qquad \text{(E.182)}$$

The residuum vector $\mathbf{R}^g$ derived with respect to state variable $\mathbf{v}_t$ reads

$$\frac{\partial \mathbf{R}^g}{\partial \mathbf{v}_t} = \frac{\partial \mathbf{R}^g_s}{\partial \mathbf{v}_t} + \frac{\partial \mathbf{R}^g_{\rho^{ga}}}{\partial \mathbf{v}_t} + \frac{\partial \mathbf{R}^g_t}{\partial \mathbf{v}_t} + \frac{\partial \mathbf{R}^g_{k^g}}{\partial \mathbf{v}_t} + \frac{\partial \mathbf{R}^g_d}{\partial \mathbf{v}_t} + \frac{\partial \mathbf{R}^g_{\rho^s}}{\partial \mathbf{v}_t} + \frac{\partial \mathbf{R}^g_\xi}{\partial \mathbf{v}_t} + \frac{\partial \mathbf{R}^g_b}{\partial \mathbf{v}_t} \,, \qquad \text{(E.183)}$$

with

$$\frac{\partial \mathbf{R}^g_s}{\partial \mathbf{v}_t} = \left\{ \bigwedge_{e=1}^{n_e} \int_{x_e}^{x_{e+1}} \left[-\mathbf{N}_g^T \left(\frac{\partial n}{\partial T} \rho^{ga} \frac{\Delta S_w}{\Delta t} + n \frac{\partial \rho^{ga}}{\partial T} \frac{\Delta S_w}{\Delta t} \right. \right. \right.$$
$$\left. \left. \left. + n \rho^{ga} \frac{1}{\Delta t} \frac{\partial S_w}{\partial T} \right) \mathbf{N}_t \right] dx \right\} \,, \qquad \text{(E.184)}$$

$$\frac{\partial \mathbf{R}^g_{\rho^{ga}}}{\partial \mathbf{v}_t} = \left\{ \bigwedge_{e=1}^{n_e} \int_{x_e}^{x_{e+1}} \left[\mathbf{N}_g^T \left(\frac{\partial n}{\partial T} (1 - S_w) \frac{\Delta \rho^{ga}}{\Delta t} - n \frac{\partial S_w}{\partial T} \frac{\Delta \rho^{ga}}{\Delta t} \right. \right. \right.$$
$$\left. \left. \left. + n(1 - S_w) \frac{1}{\Delta t} \frac{\partial \rho^{ga}}{\partial T} \right) \mathbf{N}_t \right] dx \right\} \,, \qquad \text{(E.185)}$$

$$\frac{\partial \mathbf{R}^g_t}{\partial \mathbf{v}_t} = \left\{ \bigwedge_{e=1}^{n_e} \int_{x_e}^{x_{e+1}} \left[-\mathbf{N}_g^T \left(\frac{\partial \beta_{sa}}{\partial T} \rho^{ga} \frac{\Delta T}{\Delta t} + \beta_{sa} \frac{\partial \rho^{ga}}{\partial T} \frac{\Delta T}{\Delta t} \right. \right. \right.$$
$$\left. \left. \left. + \beta_{sa} \rho^{ga} \frac{1}{\Delta t} \right) \mathbf{N}_t \right] dx \right\} \,, \qquad \text{(E.186)}$$

$$\frac{\partial \mathbf{R}^g_{k^g}}{\partial \mathbf{v}_t} = \left\{ \bigwedge_{e=1}^{n_e} \int_{x_e}^{x_{e+1}} \left[\frac{D^s \mathbf{N}_g^T}{Dx} \left(\frac{\partial \rho^{ga}}{\partial T} \frac{k k^{rg}}{\eta^g} \frac{D^s p^g}{Dx} + \rho^{ga} \frac{\partial k}{\partial T} \frac{k^{rg}}{\eta^g} \frac{D^s p^g}{Dx} \right. \right. \right.$$
$$\left. \left. \left. + \rho^{ga} k \frac{\partial}{\partial T} \left(\frac{k^{rg}}{\eta^g} \right) \frac{D^s p^g}{Dx} \right) \mathbf{N}_t \right] dx \right\} \,, \qquad \text{(E.187)}$$

$$\frac{\partial \mathbf{R}^g_d}{\partial \mathbf{v}_t} = \left\{ \bigwedge_{e=1}^{n_e} \int_{x_e}^{x_{e+1}} \left[-\frac{D^s \mathbf{N}_g^T}{Dx} \left(\frac{\partial \rho^g}{\partial T} \frac{M_a M_w}{M_g^2} D_{eff} \frac{D^s}{Dx} \left(\frac{p^{gw}}{p^g} \right) \mathbf{N}_t \right. \right. \right.$$
$$\left. - \rho^g \frac{2 M_a M_w}{M_g^3} \frac{\partial M_g}{\partial T} D_{eff} \frac{D^s}{Dx} \left(\frac{p^{gw}}{p^g} \right) \mathbf{N}_t + \rho^g \frac{M_a M_w}{M_g^2} \frac{\partial D_{eff}}{\partial T} \frac{D^s}{Dx} \left(\frac{p^{gw}}{p^g} \right) \mathbf{N}_t \right.$$
$$\left. \left. \left. + \rho^g \frac{M_a M_w}{M_g^2} D_{eff} \frac{1}{p^g} \frac{\partial p^{gw}}{\partial T} \frac{D^s \mathbf{N}_t}{Dx} \right) \right] dx \right\} \,, \qquad \text{(E.188)}$$

$$\frac{\partial \mathbf{R}_{\rho^s}^g}{\partial \mathbf{v}_t} = \left\{ \mathbf{A}_{e=1}^{n_e} \int_{x_e}^{x_{e+1}} \left[\mathbf{N}_g^T \left(-\frac{\partial n}{\partial T} \frac{\rho^{ga}(1-S_w)}{\rho^s} \frac{\partial \rho^s}{\partial T} \frac{\Delta T}{\Delta t} + \frac{(1-n)(1-S_w)}{\rho^s} \frac{\partial \rho^{ga}}{\partial T} \frac{\partial \rho^s}{\partial T} \frac{\Delta T}{\Delta t} \right. \right. \right.$$

$$- \frac{(1-n)\rho^{ga}}{\rho^s} \frac{\partial S_w}{\partial T} \frac{\partial \rho^s}{\partial T} \frac{\Delta T}{\Delta t} - (1-n)\rho^{ga}(1-S_w)\frac{1}{(\rho^s)^2}\left(\frac{\partial \rho^s}{\partial T}\right)^2 \frac{\Delta T}{\Delta t}$$

$$\left. \left. \left. + \frac{(1-n)\rho^{ga}(1-S_w)}{\rho^s} \frac{\partial \rho^s}{\partial T} \frac{1}{\Delta t} \right) \mathbf{N}_t \right] dx \right\}, \tag{E.189}$$

$$\frac{\partial \mathbf{R}_{\xi}^g}{\partial \mathbf{v}_t} = \left\{ \mathbf{A}_{e=1}^{n_e} \int_{x_e}^{x_{e+1}} \left[-\mathbf{N}_g^T \left(\frac{\partial \rho^{ga}}{\partial T}(1-S_w)\frac{1}{\rho^s} - \rho^{ga}\frac{\partial S_w}{\partial T}\frac{1}{\rho^s} \right. \right. \right.$$

$$\left. -\rho^{ga}(1-S_w)\frac{1}{(\rho^s)^2}\frac{\partial \rho^s}{\partial T} \right) m_c f_h \frac{m_w}{m_c} \frac{\Delta \xi}{\Delta t} \mathbf{N}_t$$

$$\left. \left. -\mathbf{N}_g^T \rho^{ga}(1-S_w)\frac{m_c f_h}{\rho^s} \frac{m_w}{m_c} \frac{1}{\Delta t} \frac{\partial \xi}{\partial T} \mathbf{N}_t \right] dx \right\}, \tag{E.190}$$

$$\frac{\partial \mathbf{R}_b^g}{\partial \mathbf{v}_t} = 0, \tag{E.191}$$

and

$$\frac{\partial \beta_{sa}}{\partial T} = -\frac{\partial n}{\partial T}(1-S_w)\beta_s - (1-n)\frac{\partial S_w}{\partial T}\beta_s. \tag{E.192}$$

In Equation (E.189), the same considerations were applied as for Equation (E.157) (see Equations (E.161) to (E.163)).

The residuum vector $\mathbf{R}^t$ derived with respect to state variable $\mathbf{v}_c$ reads

$$
\begin{aligned}
\frac{\partial \mathbf{R}^t}{\partial \mathbf{v}_c} &= \frac{\partial \mathbf{R}_c^t}{\partial \mathbf{v}_c} + \frac{\partial \mathbf{R}_g^t}{\partial \mathbf{v}_c} + \frac{\partial \mathbf{R}_w^t}{\partial \mathbf{v}_c} + \frac{\partial \mathbf{R}_\lambda^t}{\partial \mathbf{v}_c} + \frac{\partial \mathbf{R}_s^t}{\partial \mathbf{v}_c} + \frac{\partial \mathbf{R}_{\rho^w}^t}{\partial \mathbf{v}_c} + \frac{\partial \mathbf{R}_t^t}{\partial \mathbf{v}_c} \\
&\quad + \frac{\partial \mathbf{R}_{k^g}^t}{\partial \mathbf{v}_c} + \frac{\partial \mathbf{R}_{k^w}^t}{\partial \mathbf{v}_c} + \frac{\partial \mathbf{R}_{\rho^s}^t}{\partial \mathbf{v}_c} + \frac{\partial \mathbf{R}_\xi^t}{\partial \mathbf{v}_c} + \frac{\partial \mathbf{R}_{dehydr}^t}{\partial \mathbf{v}_c} + \frac{\partial \mathbf{R}_b^t}{\partial \mathbf{v}_c},
\end{aligned}
\tag{E.193}
$$

with

$$
\frac{\partial \mathbf{R}_c^t}{\partial \mathbf{v}_c} = \left\{ \mathop{\mathbf{A}}_{e=1}^{n_e} \int_{x_e}^{x_{e+1}} \left[\mathbf{N}_t^T \frac{\partial (\rho c_p)_{eff}}{\partial p^c} \frac{\Delta T}{\Delta t} \mathbf{N}_c \right] dx \right\},
\tag{E.194}
$$

$$
\begin{aligned}
\frac{\partial \mathbf{R}_g^t}{\partial \mathbf{v}_c} = \Bigg\{ \mathop{\mathbf{A}}_{e=1}^{n_e} \int_{x_e}^{x_{e+1}} \Bigg[-\mathbf{N}_t^T \Bigg(& \frac{\partial \left(\rho^g c_p^g \right)}{\partial p^c} \frac{k k^{rg}}{\eta^g} \frac{D^s p^g}{Dx} \frac{D^s T}{Dx} \\
& + \rho^g c_p^g k \frac{\partial}{\partial p^c} \left(\frac{k^{rg}}{\eta^g} \right) \frac{D^s p^g}{Dx} \frac{D^s T}{Dx} \\
& + \rho^w c_p^w k \frac{\partial}{\partial p^c} \left(\frac{k^{rw}}{\eta^w} \right) \frac{D^s p^g}{Dx} \frac{D^s T}{Dx} \Bigg) \mathbf{N}_c \Bigg] dx \Bigg\},
\end{aligned}
\tag{E.195}
$$

$$
\begin{aligned}
\frac{\partial \mathbf{R}_w^t}{\partial \mathbf{v}_c} = \Bigg\{ \mathop{\mathbf{A}}_{e=1}^{n_e} \int_{x_e}^{x_{e+1}} \Bigg[\mathbf{N}_t^T \Bigg(& \rho^w c_p^w k \frac{\partial}{\partial p^c} \left(\frac{k^{rw}}{\eta^w} \right) \frac{D^s p^c}{Dx} \frac{D^s T}{Dx} \mathbf{N}_c \\
& + \rho^w c_p^w \frac{k k^{rw}}{\eta^w} \frac{D^s \mathbf{N}_c}{Dx} \frac{D^s T}{Dx} \Bigg) \Bigg] dx \Bigg\},
\end{aligned}
\tag{E.196}
$$

$$
\frac{\partial \mathbf{R}_\lambda^t}{\partial \mathbf{v}_c} = \left\{ \mathop{\mathbf{A}}_{e=1}^{n_e} \int_{x_e}^{x_{e+1}} \left[\frac{D^s \mathbf{N}_t^T}{Dx} \frac{\partial \lambda_{eff}}{\partial p^c} \frac{D^s \mathbf{N}_t}{Dx} \mathbf{N}_c \right] dx \right\},
\tag{E.197}
$$

$$
\frac{\partial \mathbf{R}_s^t}{\partial \mathbf{v}_c} = \left\{ \mathop{\mathbf{A}}_{e=1}^{n_e} \int_{x_e}^{x_{e+1}} \left[-\mathbf{N}_t^T h n \rho^w \frac{1}{\Delta t} \frac{\partial S_w}{\partial p^c} \mathbf{N}_c \right] dx \right\},
\tag{E.198}
$$

$$
\frac{\partial \mathbf{R}_{\rho^w}^t}{\partial \mathbf{v}_c} = \left\{ \mathop{\mathbf{A}}_{e=1}^{n_e} \int_{x_e}^{x_{e+1}} \left[-\mathbf{N}_t^T h n \frac{\partial S_w}{\partial p^c} \frac{\Delta \rho^w}{\Delta t} \mathbf{N}_c \right] dx \right\},
\tag{E.199}
$$

$$
\frac{\partial \mathbf{R}_t^t}{\partial \mathbf{v}_c} = \left\{ \mathop{\mathbf{A}}_{e=1}^{n_e} \int_{x_e}^{x_{e+1}} \left[\mathbf{N}_t^T h \frac{\partial \beta_{sw}}{\partial p^c} \rho^w \frac{\Delta T}{\Delta t} \mathbf{N}_c \right] dx \right\},
\tag{E.200}
$$

$$
\frac{\partial \mathbf{R}_{k^g}^t}{\partial \mathbf{v}_c} = \left\{ \mathop{\mathbf{A}}_{e=1}^{n_e} \int_{x_e}^{x_{e+1}} \left[-\frac{D^s \mathbf{N}_t^T}{Dx} h \rho^w k \frac{\partial}{\partial p^c} \left(\frac{k^{rw}}{\eta^w} \right) \frac{D^s p^g}{Dx} \mathbf{N}_c \right] dx \right\},
\tag{E.201}
$$

$$
\begin{aligned}
\frac{\partial \mathbf{R}_{k^w}^t}{\partial \mathbf{v}_c} = \Bigg\{ \mathop{\mathbf{A}}_{e=1}^{n_e} \int_{x_e}^{x_{e+1}} \Bigg[\frac{D^s \mathbf{N}_t^T}{Dx} \Bigg(& h \rho^w k \frac{\partial}{\partial p^c} \left(\frac{k^{rw}}{\eta^w} \right) \frac{D^s p^c}{Dx} \mathbf{N}_c \\
& + h \rho^w \frac{k k^{rw}}{\eta^w} \frac{D^s \mathbf{N}_c}{Dx} \Bigg) \Bigg] dx \Bigg\},
\end{aligned}
\tag{E.202}
$$

$$\frac{\partial \mathbf{R}^t_{\rho^s}}{\partial \mathbf{v}_c} = \left\{ \mathop{\mathbf{A}}_{e\,=\,1}^{n_e} \int_{x_e}^{x_{e+1}} \left[-\mathbf{N}_t^T h \frac{(1-n)\rho^w}{\rho^s} \frac{\partial S_w}{\partial p^c} \frac{\partial \rho^s}{\partial T} \frac{\Delta T}{\Delta t} \mathbf{N}_c \right] dx \right\} , \quad \text{(E.203)}$$

$$\frac{\partial \mathbf{R}^t_{\xi}}{\partial \mathbf{v}_c} = \left\{ \mathop{\mathbf{A}}_{e\,=\,1}^{n_e} \int_{x_e}^{x_{e+1}} \left[\mathbf{N}_t^T h \rho^w \frac{\partial S_w}{\partial p^c} \frac{m_c f_h}{\rho^s} \frac{m_w}{m_c} \frac{\Delta \xi}{\Delta t} \mathbf{N}_c \right] dx \right\} , \quad \text{(E.204)}$$

$$\frac{\partial \mathbf{R}^t_{dehydr}}{\partial \mathbf{v}_c} = \frac{\partial \mathbf{R}^t_b}{\partial \mathbf{v}_c} = 0 , \quad \text{(E.205)}$$

and

$$\frac{\partial \beta_{sw}}{\partial p^c} = (1-n)\beta_s \frac{\partial S_w}{\partial p^c} . \quad \text{(E.206)}$$

The residuum vector $\mathbf{R}^t$ derived with respect to state variable $\mathbf{v}_g$ reads

$$
\begin{aligned}
\frac{\partial \mathbf{R}^t}{\partial \mathbf{v}_g} &= \frac{\partial \mathbf{R}_c^t}{\partial \mathbf{v}_g} + \frac{\partial \mathbf{R}_g^t}{\partial \mathbf{v}_g} + \frac{\partial \mathbf{R}_w^t}{\partial \mathbf{v}_g} + \frac{\partial \mathbf{R}_\lambda^t}{\partial \mathbf{v}_g} + \frac{\partial \mathbf{R}_s^t}{\partial \mathbf{v}_g} + \frac{\partial \mathbf{R}_{\rho^w}^t}{\partial \mathbf{v}_g} + \frac{\partial \mathbf{R}_t^t}{\partial \mathbf{v}_g} \\[2mm]
&\quad + \frac{\partial \mathbf{R}_{k^g}^t}{\partial \mathbf{v}_g} + \frac{\partial \mathbf{R}_{k^w}^t}{\partial \mathbf{v}_g} + \frac{\partial \mathbf{R}_{\rho^s}^t}{\partial \mathbf{v}_g} + \frac{\partial \mathbf{R}_\xi^t}{\partial \mathbf{v}_g} + \frac{\partial \mathbf{R}_{dehydr}^t}{\partial \mathbf{v}_g} + \frac{\partial \mathbf{R}_b^t}{\partial \mathbf{v}_g} \,,
\end{aligned}
\tag{E.207}
$$

with

$$
\frac{\partial \mathbf{R}_c^t}{\partial \mathbf{v}_g} = \left\{ \mathop{\mathbf{A}}_{e=1}^{n_e} \int_{x_e}^{x_{e+1}} \left[\mathbf{N}_t^T \frac{\partial \left(\rho c_p \right)_{eff}}{\partial p^g} \frac{\Delta T}{\Delta t} \mathbf{N}_g \right] dx \right\} \,,
\tag{E.208}
$$

$$
\begin{aligned}
\frac{\partial \mathbf{R}_g^t}{\partial \mathbf{v}_g} &= \left\{ \mathop{\mathbf{A}}_{e=1}^{n_e} \int_{x_e}^{x_{e+1}} \left[-\mathbf{N}_t^T \left(\frac{\partial \left(\rho^g c_p^g \right)}{\partial p^g} \frac{k k^{rg}}{\eta^g} \frac{D^s p^g}{Dx} \frac{D^s T}{Dx} \mathbf{N}_g \right. \right. \\[2mm]
&\quad + \rho^g c_p^g \frac{\partial k}{\partial p^g} \frac{k^{rg}}{\eta^g} \frac{D^s p^g}{Dx} \frac{D^s T}{Dx} \mathbf{N}_g + \rho^g c_p^g k \frac{\partial}{\partial p^g} \left(\frac{k^{rg}}{\eta^g} \right) \frac{D^s p^g}{Dx} \frac{D^s T}{Dx} \mathbf{N}_g \\[2mm]
&\quad \left. \left. + \rho^g c_p^g \frac{k k^{rg}}{\eta^g} \frac{D^s \mathbf{N}_g}{Dx} \frac{D^s T}{Dx} + \rho^w c_p^w \frac{k k^{rw}}{\eta^w} \frac{D^s \mathbf{N}_g}{Dx} \frac{D^s T}{Dx} \right) \right] dx \right\} \,,
\end{aligned}
\tag{E.209}
$$

$$
\frac{\partial \mathbf{R}_w^t}{\partial \mathbf{v}_g} = \frac{\partial \mathbf{R}_\lambda^t}{\partial \mathbf{v}_g} = \frac{\partial \mathbf{R}_s^t}{\partial \mathbf{v}_g} = \frac{\partial \mathbf{R}_{\rho^w}^t}{\partial \mathbf{v}_g} = \frac{\partial \mathbf{R}_t^t}{\partial \mathbf{v}_g} = 0 \,,
\tag{E.210}
$$

$$
\frac{\partial \mathbf{R}_{k^g}^t}{\partial \mathbf{v}_g} = \left\{ \mathop{\mathbf{A}}_{e=1}^{n_e} \int_{x_e}^{x_{e+1}} \left[-\frac{D^s \mathbf{N}_t^T}{Dx} h \rho^w \frac{k k^{rw}}{\eta^w} \frac{D^s \mathbf{N}_g}{Dx} \right] dx \right\} \,,
\tag{E.211}
$$

$$
\frac{\partial \mathbf{R}_{k^w}^t}{\partial \mathbf{v}_g} = \frac{\partial \mathbf{R}_{\rho^s}^t}{\partial \mathbf{v}_g} = \frac{\partial \mathbf{R}_\xi^t}{\partial \mathbf{v}_g} = \frac{\partial \mathbf{R}_{dehydr}^t}{\partial \mathbf{v}_g} = \frac{\partial \mathbf{R}_b^t}{\partial \mathbf{v}_g} = 0 \,.
\tag{E.212}
$$

The residuum vector $\mathbf{R}^t$ derived with respect to state variable $\mathbf{v}_t$ reads

$$
\frac{\partial \mathbf{R}^t}{\partial \mathbf{v}_t} = \frac{\partial \mathbf{R}_c^t}{\partial \mathbf{v}_t} + \frac{\partial \mathbf{R}_g^t}{\partial \mathbf{v}_t} + \frac{\partial \mathbf{R}_w^t}{\partial \mathbf{v}_t} + \frac{\partial \mathbf{R}_\lambda^t}{\partial \mathbf{v}_t} + \frac{\partial \mathbf{R}_s^t}{\partial \mathbf{v}_t} + \frac{\partial \mathbf{R}_{\rho^w}^t}{\partial \mathbf{v}_t} + \frac{\partial \mathbf{R}_t^t}{\partial \mathbf{v}_t}
$$
$$
+ \frac{\partial \mathbf{R}_{k^g}^t}{\partial \mathbf{v}_t} + \frac{\partial \mathbf{R}_{k^w}^t}{\partial \mathbf{v}_t} + \frac{\partial \mathbf{R}_{\rho^s}^t}{\partial \mathbf{v}_t} + \frac{\partial \mathbf{R}_\xi^t}{\partial \mathbf{v}_t} + \frac{\partial \mathbf{R}_{dehydr}^t}{\partial \mathbf{v}_t} + \frac{\partial \mathbf{R}_b^t}{\partial \mathbf{v}_t}, \qquad \text{(E.213)}
$$

with

$$
\frac{\partial \mathbf{R}_c^t}{\partial \mathbf{v}_t} = \left\{ \mathop{\mathbf{A}}_{e\,=\,1}^{n_e} \int_{x_e}^{x_{e+1}} \left[\mathbf{N}_t^T \left(\frac{\partial\,(\rho c_p)_{eff}}{\partial T} \frac{\Delta T}{\Delta t} + (\rho c_p)_{eff} \frac{1}{\Delta t} \right) \mathbf{N}_t \right] dx \right\}, \quad \text{(E.214)}
$$

$$
\frac{\partial \mathbf{R}_g^t}{\partial \mathbf{v}_t} = \left\{ \mathop{\mathbf{A}}_{e\,=\,1}^{n_e} \int_{x_e}^{x_{e+1}} \left[-\mathbf{N}_t^T \left(\frac{\partial\,(\rho^g c_p^g)}{\partial T} \frac{kk^{rg}}{\eta^g} \frac{D^s p^g}{Dx} \frac{D^s T}{Dx} \mathbf{N}_t \right.\right.
$$
$$
+ \rho^g c_p^g \frac{\partial k}{\partial T} \frac{k^{rg}}{\eta^g} \frac{D^s p^g}{Dx} \frac{D^s T}{Dx} \mathbf{N}_t + \rho^g c_p^g k \frac{\partial}{\partial T} \left(\frac{k^{rg}}{\eta^g} \right) \frac{D^s p^g}{Dx} \frac{D^s T}{Dx} \mathbf{N}_t
$$
$$
+ \rho^g c_p^g \frac{kk^{rg}}{\eta^g} \frac{D^s p^g}{Dx} \frac{D^s \mathbf{N}_t}{Dx} + \frac{\partial\,(\rho^w c_p^w)}{\partial T} \frac{kk^{rw}}{\eta^w} \frac{D^s p^g}{Dx} \frac{D^s T}{Dx} \mathbf{N}_t
$$
$$
+ \rho^w c_p^w \frac{\partial k}{\partial T} \frac{k^{rw}}{\eta^w} \frac{D^s p^g}{Dx} \frac{D^s T}{Dx} \mathbf{N}_t + \rho^w c_p^w k \frac{\partial}{\partial T} \left(\frac{k^{rw}}{\eta^w} \right) \frac{D^s p^g}{Dx} \frac{D^s T}{Dx} \mathbf{N}_t
$$
$$
\left.\left. + \rho^w c_p^w \frac{kk^{rw}}{\eta^w} \frac{D^s p^g}{Dx} \frac{D^s \mathbf{N}_t}{Dx} \right) \right] dx \right\}, \qquad \text{(E.215)}
$$

$$
\frac{\partial \mathbf{R}_w^t}{\partial \mathbf{v}_t} = \left\{ \mathop{\mathbf{A}}_{e\,=\,1}^{n_e} \int_{x_e}^{x_{e+1}} \left[\mathbf{N}_t^T \left(\frac{\partial\,(\rho^w c_p^w)}{\partial T} \frac{kk^{rw}}{\eta^w} \frac{D^s p^c}{Dx} \frac{D^s T}{Dx} \mathbf{N}_t \right.\right.
$$
$$
+ \rho^w c_p^w \frac{\partial k}{\partial T} \frac{k^{rw}}{\eta^w} \frac{D^s p^c}{Dx} \frac{D^s T}{Dx} \mathbf{N}_t + \rho^w c_p^w k \frac{\partial}{\partial T} \left(\frac{k^{rw}}{\eta^w} \right) \frac{D^s p^c}{Dx} \frac{D^s T}{Dx} \mathbf{N}_t
$$
$$
\left.\left. + \rho^w c_p^w \frac{kk^{rw}}{\eta^w} \frac{D^s p^c}{Dx} \frac{D^s \mathbf{N}_t}{Dx} \right) \right] dx \right\}, \qquad \text{(E.216)}
$$

$$
\frac{\partial \mathbf{R}_\lambda^t}{\partial \mathbf{v}_t} = \left\{ \mathop{\mathbf{A}}_{e\,=\,1}^{n_e} \int_{x_e}^{x_{e+1}} \left[\frac{D^s \mathbf{N}_t^T}{Dx} \left(\frac{\partial \lambda_{eff}}{\partial T} \frac{D^s T}{Dx} \mathbf{N}_t + \lambda_{eff} \frac{D^s \mathbf{N}_t}{Dx} \right) \right] dx \right\}, \qquad \text{(E.217)}
$$

$$
\frac{\partial \mathbf{R}_s^t}{\partial \mathbf{v}_t} = \left\{ \mathop{\mathbf{A}}_{e\,=\,1}^{n_e} \int_{x_e}^{x_{e+1}} \left[-\mathbf{N}_t^T \left(\frac{\partial h}{\partial T} n\rho^w \frac{\Delta S_w}{\Delta t} + h \frac{\partial n}{\partial T} \rho^w \frac{\Delta S_w}{\Delta t} + hn \frac{\partial \rho^w}{\partial T} \frac{\Delta S_w}{\Delta t} \right.\right.
$$
$$
\left.\left. + hn\rho^w \frac{1}{\Delta t} \frac{\partial S_w}{\partial T} \right) \mathbf{N}_t \right] dx \right\}, \qquad \text{(E.218)}
$$

$$\frac{\partial \mathbf{R}_{\rho^w}^t}{\partial \mathbf{v}_t} = \left\{ \mathbf{A}_{e=1}^{n_e} \int_{x_e}^{x_{e+1}} \left[-\mathbf{N}_t^T \left(\frac{\partial h}{\partial T} n S_w \frac{\Delta \rho^w}{\Delta t} + h \frac{\partial n}{\partial T} S_w \frac{\Delta \rho^w}{\Delta t} + h n \frac{\partial S_w}{\partial T} \frac{\Delta \rho^w}{\Delta t} \right. \right. \right.$$
$$\left. \left. \left. + h n S_w \frac{1}{\Delta t} \frac{\partial \rho^w}{\partial T} \right) \mathbf{N}_t \right] dx \right\} , \tag{E.219}$$

$$\frac{\partial \mathbf{R}_t^t}{\partial \mathbf{v}_t} = \left\{ \mathbf{A}_{e=1}^{n_e} \int_{x_e}^{x_{e+1}} \left[\mathbf{N}_t^T \left(\frac{\partial h}{\partial T} \beta_{sw} \rho^w \frac{\Delta T}{\Delta t} + h \frac{\partial \beta_{sw}}{\partial T} \rho^w \frac{\Delta T}{\Delta t} + h \beta_{sw} \frac{\partial \rho^w}{\partial T} \frac{\Delta T}{\Delta t} \right. \right. \right.$$
$$\left. \left. \left. + h \beta_{sw} \rho^w \frac{1}{\Delta t} \right) \mathbf{N}_t \right] dx \right\} , \tag{E.220}$$

$$\frac{\partial \mathbf{R}_{k^g}^t}{\partial \mathbf{v}_t} = \left\{ \mathbf{A}_{e=1}^{n_e} \int_{x_e}^{x_{e+1}} \left[-\frac{D^s \mathbf{N}_t^T}{Dx} \left(\frac{\partial h}{\partial T} \rho^w \frac{k k^{rw}}{\eta^w} \frac{D^s p^g}{Dx} + h \frac{\partial \rho^w}{\partial T} \frac{k k^{rw}}{\eta^w} \frac{D^s p^g}{Dx} \right. \right. \right.$$
$$\left. \left. \left. + h \rho^w \frac{\partial k}{\partial T} \frac{k^{rw}}{\eta^w} \frac{D^s p^g}{Dx} + h \rho^w k \frac{\partial}{\partial T} \left(\frac{k^{rw}}{\eta^w} \right) \frac{D^s p^g}{Dx} \right) \mathbf{N}_t \right] dx \right\} , \tag{E.221}$$

$$\frac{\partial \mathbf{R}_{k^w}^t}{\partial \mathbf{v}_t} = \left\{ \mathbf{A}_{e=1}^{n_e} \int_{x_e}^{x_{e+1}} \left[\frac{D^s \mathbf{N}_t^T}{Dx} \left(\frac{\partial h}{\partial T} \rho^w \frac{k k^{rw}}{\eta^w} \frac{D^s p^c}{Dx} + h \frac{\partial \rho^w}{\partial T} \frac{k k^{rw}}{\eta^w} \frac{D^s p^c}{Dx} \right. \right. \right.$$
$$\left. \left. \left. + h \rho^w \frac{\partial k}{\partial T} \frac{k^{rw}}{\eta^w} \frac{D^s p^c}{Dx} + h \rho^w k \frac{\partial}{\partial T} \left(\frac{k^{rw}}{\eta^w} \right) \frac{D^s p^c}{Dx} \right) \mathbf{N}_t \right] dx \right\} , \tag{E.222}$$

$$\frac{\partial \mathbf{R}_{\rho^s}^t}{\partial \mathbf{v}_t} = \left\{ \mathbf{A}_{e=1}^{n_e} \int_{x_e}^{x_{e+1}} \left[-\mathbf{N}_t^T \left(\frac{\partial h}{\partial T} \frac{(1-n) \rho^w S_w}{\rho^s} \frac{\partial \rho^s}{\partial T} \frac{\Delta T}{\Delta t} - h \frac{\partial n}{\partial T} \frac{\rho^w S_w}{\rho^s} \frac{\partial \rho^s}{\partial T} \frac{\Delta T}{\Delta t} \right. \right. \right.$$
$$+ h \frac{(1-n) S_w}{\rho^s} \frac{\partial \rho^w}{\partial T} \frac{\partial \rho^s}{\partial T} \frac{\Delta T}{\Delta t} + h \frac{(1-n) \rho^w}{\rho^s} \frac{\partial S_w}{\partial T} \frac{\partial \rho^s}{\partial T} \frac{\Delta T}{\Delta t}$$
$$- h (1-n) \rho^w S_w \frac{1}{(\rho^s)^2} \left(\frac{\partial \rho^s}{\partial T} \right)^2 \frac{\Delta T}{\Delta t}$$
$$\left. \left. \left. + h \frac{(1-n) \rho^w S_w}{\rho^s} \frac{\partial \rho^s}{\partial T} \frac{1}{\Delta t} \right) \mathbf{N}_t \right] dx \right\} , \tag{E.223}$$

$$\frac{\partial \mathbf{R}_\xi^t}{\partial \mathbf{v}_t} = \left\{ \mathbf{A}_{e=1}^{n_e} \int_{x_e}^{x_{e+1}} \left[\mathbf{N}_t^T \left(\frac{\partial h}{\partial T} \left(\rho^w S_w \frac{1}{\rho^s} - 1 \right) + h \frac{\partial \rho^w}{\partial T} S_w \frac{1}{\rho^s} + h \rho^w \frac{\partial S_w}{\partial T} \frac{1}{\rho^s} \right. \right. \right.$$
$$\left. - h \rho^w S_w \frac{1}{(\rho^s)^2} \frac{\partial \rho^s}{\partial T} \right) m_c f_h \frac{m_w}{m_c} \frac{\Delta \xi}{\Delta t} \mathbf{N}_t$$
$$\left. \left. + \mathbf{N}_t^T \left(h \rho^w S_w \frac{m_c f_h}{\rho^s} \frac{m_w}{m_c} - h m_c f_h \frac{m_w}{m_c} \right) \frac{1}{\Delta t} \frac{\partial \xi}{\partial T} \mathbf{N}_t \right] dx \right\} , \tag{E.224}$$

$$\frac{\partial \mathbf{R}_{dehydr}^t}{\partial \mathbf{v}_t} = \left\{ \mathbf{A}_{e=1}^{n_e} \int_{x_e}^{x_{e+1}} \left[-\mathbf{N}_t^T l_\xi m_c f_h \frac{1}{\Delta t} \frac{\partial \xi}{\partial T} \mathbf{N}_t \right] dx \right\} , \tag{E.225}$$

$$\frac{\partial \mathbf{R}_b^t}{\partial \mathbf{v}_t} = \mathbf{1}_1 \left[\alpha_1 \mathbf{1}_1^T + \varepsilon_1 \sigma \cdot 4 \left(\mathbf{1}_1^T \mathbf{v}_t \right)^3 \mathbf{1}_1^T \right]$$

$$+ \mathbf{1}_{n_e+1} \left[\alpha_{n_e+1} \mathbf{1}_{n_e+1}^T + \varepsilon_{n_e+1} \sigma \cdot 4 \left(\mathbf{1}_{n_e+1}^T \mathbf{v}_t \right)^3 \mathbf{1}_{n_e+1}^T \right] , \qquad \text{(E.226)}$$

and

$$\frac{\partial \beta_{sw}}{\partial T} = -\frac{\partial n}{\partial T} \beta_s S_w + (1-n)\beta_s \frac{\partial S_w}{\partial T} . \qquad \text{(E.227)}$$

After convergence of the Newton-Raphson iteration scheme, the vector of nodal capillary pressures, gas pressures, and temperatures, respectively, is updated as

$$\mathbf{v}_{i+1}^c = \mathbf{v}_i^c + \Delta \mathbf{v}_{i+1}^c \quad \text{or} \quad \mathbf{v}_{i+1}^g = \mathbf{v}_i^g + \Delta \mathbf{v}_{i+1}^g \quad \text{or} \quad \mathbf{v}_{i+1}^t = \mathbf{v}_i^t + \Delta \mathbf{v}_{i+1}^t . \qquad \text{(E.228)}$$

E.1.5 Solution of governing field equations

Written in block-tridiagonal form (arranged node by node), Equation (E.123) reads

$$
\left[
\begin{array}{cccccccccccccccccc}
\frac{\partial \mathrm{R}_1^c}{\partial \Delta \mathrm{v}_1^c} & \frac{\partial \mathrm{R}_1^c}{\partial \Delta \mathrm{v}_1^g} & \frac{\partial \mathrm{R}_1^c}{\partial \Delta \mathrm{v}_1^t} & \frac{\partial \mathrm{R}_1^c}{\partial \Delta \mathrm{v}_2^c} & \frac{\partial \mathrm{R}_1^c}{\partial \Delta \mathrm{v}_2^g} & \frac{\partial \mathrm{R}_1^c}{\partial \Delta \mathrm{v}_2^t} & 0 & \cdots & \cdots & \cdots & \cdots & \cdots & \cdots & \cdots & \cdots & \cdots & \cdots & 0 \\[8pt]
\frac{\partial \mathrm{R}_1^g}{\partial \Delta \mathrm{v}_1^c} & \frac{\partial \mathrm{R}_1^g}{\partial \Delta \mathrm{v}_1^g} & \frac{\partial \mathrm{R}_1^g}{\partial \Delta \mathrm{v}_1^t} & \frac{\partial \mathrm{R}_1^g}{\partial \Delta \mathrm{v}_2^c} & \frac{\partial \mathrm{R}_1^g}{\partial \Delta \mathrm{v}_2^g} & \frac{\partial \mathrm{R}_1^g}{\partial \Delta \mathrm{v}_2^t} & 0 & \cdots & \cdots & \cdots & \cdots & \cdots & \cdots & \cdots & \cdots & \cdots & \cdots & 0 \\[8pt]
\frac{\partial \mathrm{R}_1^t}{\partial \Delta \mathrm{v}_1^c} & \frac{\partial \mathrm{R}_1^t}{\partial \Delta \mathrm{v}_1^g} & \frac{\partial \mathrm{R}_1^t}{\partial \Delta \mathrm{v}_1^t} & \frac{\partial \mathrm{R}_1^t}{\partial \Delta \mathrm{v}_2^c} & \frac{\partial \mathrm{R}_1^t}{\partial \Delta \mathrm{v}_2^g} & \frac{\partial \mathrm{R}_1^t}{\partial \Delta \mathrm{v}_2^t} & 0 & \cdots & \cdots & \cdots & \cdots & \cdots & \cdots & \cdots & \cdots & \cdots & \cdots & 0 \\[8pt]
\frac{\partial \mathrm{R}_2^c}{\partial \Delta \mathrm{v}_1^c} & \frac{\partial \mathrm{R}_2^c}{\partial \Delta \mathrm{v}_1^g} & \frac{\partial \mathrm{R}_2^c}{\partial \Delta \mathrm{v}_1^t} & \frac{\partial \mathrm{R}_2^c}{\partial \Delta \mathrm{v}_2^c} & \frac{\partial \mathrm{R}_2^c}{\partial \Delta \mathrm{v}_2^g} & \frac{\partial \mathrm{R}_2^c}{\partial \Delta \mathrm{v}_2^t} & \frac{\partial \mathrm{R}_2^c}{\partial \Delta \mathrm{v}_3^c} & \frac{\partial \mathrm{R}_2^c}{\partial \Delta \mathrm{v}_3^g} & \frac{\partial \mathrm{R}_2^c}{\partial \Delta \mathrm{v}_3^t} & 0 & \cdots & \cdots & \cdots & \cdots & \cdots & \cdots & \cdots & 0 \\[8pt]
\frac{\partial \mathrm{R}_2^g}{\partial \Delta \mathrm{v}_1^c} & \frac{\partial \mathrm{R}_2^g}{\partial \Delta \mathrm{v}_1^g} & \frac{\partial \mathrm{R}_2^g}{\partial \Delta \mathrm{v}_1^t} & \frac{\partial \mathrm{R}_2^g}{\partial \Delta \mathrm{v}_2^c} & \frac{\partial \mathrm{R}_2^g}{\partial \Delta \mathrm{v}_2^g} & \frac{\partial \mathrm{R}_2^g}{\partial \Delta \mathrm{v}_2^t} & \frac{\partial \mathrm{R}_2^g}{\partial \Delta \mathrm{v}_3^c} & \frac{\partial \mathrm{R}_2^g}{\partial \Delta \mathrm{v}_3^g} & \frac{\partial \mathrm{R}_2^g}{\partial \Delta \mathrm{v}_3^t} & 0 & \cdots & \cdots & \cdots & \cdots & \cdots & \cdots & \cdots & 0 \\[8pt]
\frac{\partial \mathrm{R}_2^t}{\partial \Delta \mathrm{v}_1^c} & \frac{\partial \mathrm{R}_2^t}{\partial \Delta \mathrm{v}_1^g} & \frac{\partial \mathrm{R}_2^t}{\partial \Delta \mathrm{v}_1^t} & \frac{\partial \mathrm{R}_2^t}{\partial \Delta \mathrm{v}_2^c} & \frac{\partial \mathrm{R}_2^t}{\partial \Delta \mathrm{v}_2^g} & \frac{\partial \mathrm{R}_2^t}{\partial \Delta \mathrm{v}_2^t} & \frac{\partial \mathrm{R}_2^t}{\partial \Delta \mathrm{v}_3^c} & \frac{\partial \mathrm{R}_2^t}{\partial \Delta \mathrm{v}_3^g} & \frac{\partial \mathrm{R}_2^t}{\partial \Delta \mathrm{v}_3^t} & 0 & \cdots & \cdots & \cdots & \cdots & \cdots & \cdots & \cdots & 0 \\[8pt]
0 & 0 & 0 & \ddots & \ddots & \ddots & \ddots & \ddots & \ddots & \ddots & \ddots & \ddots & & & & & & \vdots \\[6pt]
0 & 0 & 0 & \ddots & \ddots & \ddots & \ddots & \ddots & \ddots & \ddots & \ddots & \ddots & & & & & & \vdots \\[6pt]
0 & 0 & 0 & \ddots & \ddots & \ddots & \ddots & \ddots & \ddots & \ddots & \ddots & \ddots & & & & & & \vdots \\[6pt]
\vdots & & & & & \ddots & \ddots & \ddots & \ddots & \ddots & \ddots & \ddots & \ddots & \ddots & 0 & 0 & 0 & \vdots \\[6pt]
\vdots & & & & & \ddots & \ddots & \ddots & \ddots & \ddots & \ddots & \ddots & \ddots & \ddots & 0 & 0 & 0 & \vdots \\[6pt]
\vdots & & & & & \ddots & \ddots & \ddots & \ddots & \ddots & \ddots & \ddots & \ddots & \ddots & 0 & 0 & 0 & \vdots \\[6pt]
0 & \cdots & \cdots & \cdots & \cdots & \cdots & \cdots & \cdots & 0 & \frac{\partial \mathrm{R}_{n_e}^c}{\partial \Delta \mathrm{v}_{n_e-1}^c} & \frac{\partial \mathrm{R}_{n_e}^c}{\partial \Delta \mathrm{v}_{n_e-1}^g} & \frac{\partial \mathrm{R}_{n_e}^c}{\partial \Delta \mathrm{v}_{n_e-1}^t} & \frac{\partial \mathrm{R}_{n_e}^c}{\partial \Delta \mathrm{v}_{n_e}^c} & \frac{\partial \mathrm{R}_{n_e}^c}{\partial \Delta \mathrm{v}_{n_e}^g} & \frac{\partial \mathrm{R}_{n_e}^c}{\partial \Delta \mathrm{v}_{n_e}^t} & \frac{\partial \mathrm{R}_{n_e}^c}{\partial \Delta \mathrm{v}_{n_e+1}^c} & \frac{\partial \mathrm{R}_{n_e}^c}{\partial \Delta \mathrm{v}_{n_e+1}^g} & \frac{\partial \mathrm{R}_{n_e}^c}{\partial \Delta \mathrm{v}_{n_e+1}^t} \\[8pt]
0 & \cdots & \cdots & \cdots & \cdots & \cdots & \cdots & \cdots & 0 & \frac{\partial \mathrm{R}_{n_e}^g}{\partial \Delta \mathrm{v}_{n_e-1}^c} & \frac{\partial \mathrm{R}_{n_e}^g}{\partial \Delta \mathrm{v}_{n_e-1}^g} & \frac{\partial \mathrm{R}_{n_e}^g}{\partial \Delta \mathrm{v}_{n_e-1}^t} & \frac{\partial \mathrm{R}_{n_e}^g}{\partial \Delta \mathrm{v}_{n_e}^c} & \frac{\partial \mathrm{R}_{n_e}^g}{\partial \Delta \mathrm{v}_{n_e}^g} & \frac{\partial \mathrm{R}_{n_e}^g}{\partial \Delta \mathrm{v}_{n_e}^t} & \frac{\partial \mathrm{R}_{n_e}^g}{\partial \Delta \mathrm{v}_{n_e+1}^c} & \frac{\partial \mathrm{R}_{n_e}^g}{\partial \Delta \mathrm{v}_{n_e+1}^g} & \frac{\partial \mathrm{R}_{n_e}^g}{\partial \Delta \mathrm{v}_{n_e+1}^t} \\[8pt]
0 & \cdots & \cdots & \cdots & \cdots & \cdots & \cdots & \cdots & 0 & \frac{\partial \mathrm{R}_{n_e}^t}{\partial \Delta \mathrm{v}_{n_e-1}^c} & \frac{\partial \mathrm{R}_{n_e}^t}{\partial \Delta \mathrm{v}_{n_e-1}^g} & \frac{\partial \mathrm{R}_{n_e}^t}{\partial \Delta \mathrm{v}_{n_e-1}^t} & \frac{\partial \mathrm{R}_{n_e}^t}{\partial \Delta \mathrm{v}_{n_e}^c} & \frac{\partial \mathrm{R}_{n_e}^t}{\partial \Delta \mathrm{v}_{n_e}^g} & \frac{\partial \mathrm{R}_{n_e}^t}{\partial \Delta \mathrm{v}_{n_e}^t} & \frac{\partial \mathrm{R}_{n_e}^t}{\partial \Delta \mathrm{v}_{n_e+1}^c} & \frac{\partial \mathrm{R}_{n_e}^t}{\partial \Delta \mathrm{v}_{n_e+1}^g} & \frac{\partial \mathrm{R}_{n_e}^t}{\partial \Delta \mathrm{v}_{n_e+1}^t} \\[8pt]
0 & \cdots & \cdots & \cdots & \cdots & \cdots & \cdots & \cdots & \cdots & \cdots & \cdots & 0 & \frac{\partial \mathrm{R}_{n_e+1}^c}{\partial \Delta \mathrm{v}_{n_e}^c} & \frac{\partial \mathrm{R}_{n_e+1}^c}{\partial \Delta \mathrm{v}_{n_e}^g} & \frac{\partial \mathrm{R}_{n_e+1}^c}{\partial \Delta \mathrm{v}_{n_e}^t} & \frac{\partial \mathrm{R}_{n_e+1}^c}{\partial \Delta \mathrm{v}_{n_e+1}^c} & \frac{\partial \mathrm{R}_{n_e+1}^c}{\partial \Delta \mathrm{v}_{n_e+1}^g} & \frac{\partial \mathrm{R}_{n_e+1}^c}{\partial \Delta \mathrm{v}_{n_e+1}^t} \\[8pt]
0 & \cdots & \cdots & \cdots & \cdots & \cdots & \cdots & \cdots & \cdots & \cdots & \cdots & 0 & \frac{\partial \mathrm{R}_{n_e+1}^g}{\partial \Delta \mathrm{v}_{n_e}^c} & \frac{\partial \mathrm{R}_{n_e+1}^g}{\partial \Delta \mathrm{v}_{n_e}^g} & \frac{\partial \mathrm{R}_{n_e+1}^g}{\partial \Delta \mathrm{v}_{n_e}^t} & \frac{\partial \mathrm{R}_{n_e+1}^g}{\partial \Delta \mathrm{v}_{n_e+1}^c} & \frac{\partial \mathrm{R}_{n_e+1}^g}{\partial \Delta \mathrm{v}_{n_e+1}^g} & \frac{\partial \mathrm{R}_{n_e+1}^g}{\partial \Delta \mathrm{v}_{n_e+1}^t} \\[8pt]
0 & \cdots & \cdots & \cdots & \cdots & \cdots & \cdots & \cdots & \cdots & \cdots & \cdots & 0 & \frac{\partial \mathrm{R}_{n_e+1}^t}{\partial \Delta \mathrm{v}_{n_e}^c} & \frac{\partial \mathrm{R}_{n_e+1}^t}{\partial \Delta \mathrm{v}_{n_e}^g} & \frac{\partial \mathrm{R}_{n_e+1}^t}{\partial \Delta \mathrm{v}_{n_e}^t} & \frac{\partial \mathrm{R}_{n_e+1}^t}{\partial \Delta \mathrm{v}_{n_e+1}^c} & \frac{\partial \mathrm{R}_{n_e+1}^t}{\partial \Delta \mathrm{v}_{n_e+1}^g} & \frac{\partial \mathrm{R}_{n_e+1}^t}{\partial \Delta \mathrm{v}_{n_e+1}^t}
\end{array}
\right]
\left\{
\begin{array}{c}
\Delta(\Delta \mathrm{v}_1^c) \\[6pt]
\Delta(\Delta \mathrm{v}_1^g) \\[6pt]
\Delta(\Delta \mathrm{v}_1^t) \\[6pt]
\Delta(\Delta \mathrm{v}_2^c) \\[6pt]
\Delta(\Delta \mathrm{v}_2^g) \\[6pt]
\Delta(\Delta \mathrm{v}_2^t) \\[6pt]
\vdots \\[4pt]
\vdots \\[4pt]
\vdots \\[4pt]
\vdots \\[4pt]
\vdots \\[4pt]
\vdots \\[4pt]
\Delta(\Delta \mathrm{v}_{n_e}^c) \\[6pt]
\Delta(\Delta \mathrm{v}_{n_e}^g) \\[6pt]
\Delta(\Delta \mathrm{v}_{n_e}^t) \\[6pt]
\Delta(\Delta \mathrm{v}_{n_e+1}^c) \\[6pt]
\Delta(\Delta \mathrm{v}_{n_e+1}^g) \\[6pt]
\Delta(\Delta \mathrm{v}_{n_e+1}^t)
\end{array}
\right\}
=
\left\{
\begin{array}{c}
-R_1^c \\[6pt]
-R_1^g \\[6pt]
-R_1^t \\[6pt]
-R_2^c \\[6pt]
-R_2^g \\[6pt]
-R_2^t \\[6pt]
\vdots \\[4pt]
\vdots \\[4pt]
\vdots \\[4pt]
\vdots \\[4pt]
\vdots \\[4pt]
\vdots \\[4pt]
-R_{n_e}^c \\[6pt]
-R_{n_e}^g \\[6pt]
-R_{n_e}^t \\[6pt]
-R_{n_e+1}^c \\[6pt]
-R_{n_e+1}^g \\[6pt]
-R_{n_e+1}^t
\end{array}
\right\}.
\tag{E.229}
$$

E.1.6 Solution of a triband matrix with matrix entries

Application of a Newton-Raphson iteration scheme on the one-dimensional coupled finite element formulation of heat and mass transport in concrete subjected to fire loading (see Equation (E.229)) yields a set of equations, reading

$$
\begin{bmatrix}
[\mathbf{B}_1] & [\mathbf{C}_1] & & \cdots & & & \mathbf{0} \\
[\mathbf{A}_2] & [\mathbf{B}_2] & [\mathbf{C}_2] & & & & \\
& [\mathbf{A}_3] & [\mathbf{B}_3] & \ddots & & & \vdots \\
\vdots & & \ddots & \ddots & [\mathbf{C}_{n_e-2}] & & \\
& & & [\mathbf{A}_{n_e-1}] & [\mathbf{B}_{n_e-1}] & [\mathbf{C}_{n_e-1}] \\
\mathbf{0} & & \cdots & & [\mathbf{A}_{n_e}] & [\mathbf{B}_{n_e}]
\end{bmatrix}
\begin{Bmatrix}
\{\mathbf{x}_1\} \\
\{\mathbf{x}_2\} \\
\{\mathbf{x}_3\} \\
\vdots \\
\{\mathbf{x}_{n_e-1}\} \\
\{\mathbf{x}_{n_e}\}
\end{Bmatrix}
=
\begin{Bmatrix}
\{\mathbf{r}_1\} \\
\{\mathbf{r}_2\} \\
\{\mathbf{r}_3\} \\
\vdots \\
\{\mathbf{r}_{n_e-1}\} \\
\{\mathbf{r}_{n_e}\}
\end{Bmatrix},
$$
(E.230)

where $\mathbf{A}_i$, $\mathbf{B}_i$, and $\mathbf{C}_i$ are $k \times k$-matrices with k as the number of primary state variables. In Equation (E.230), $\mathbf{x}_1, \mathbf{x}_2, \ldots \mathbf{x}_{n_e}$ are vectors of the unknown incremental changes of the primary state variables with k components and $\mathbf{r}_1, \mathbf{r}_2, \ldots \mathbf{r}_{n_e}$ are the residuum vectors. In order to solve this set of equations, several solution schemes are applicable. A Gauss-Jordan elimination (see, e.g., [47, 97]) represents a rather time- and storage-consuming method, where the whole matrix on the left-hand side (including all matrices $\mathbf{A}_i$, $\mathbf{B}_i$, and $\mathbf{C}_i$ plus a large amount of 0-submatrices) is inverted, yielding the unknown vectors $\mathbf{x}_i$. A more sufficient way is to employ a scheme where the submatrices are treated separately within a forward-elimination/backward-substitution scheme (see, e.g., [47]). Hereby, the first equation system of Equation (E.230) is solved disregarding $\mathbf{C}_1$. Instead, two additional sets of matrices, namely $\mathbf{H}_i$ and $\mathbf{K}_i$, are calculated including matrices $\mathbf{A}_i$, $\mathbf{B}_i$, and $\mathbf{C}_i$ for $i = 1, \ldots, n_e-1$ (in case of $\mathbf{H}_i$) and for $i = 2, \ldots, n_e$ (in case of $\mathbf{K}_i$), respectively. The solution of the first equation system, vector $\mathbf{g}_1$, is used as input for determination of vector $\mathbf{g}_2$ and so on until $\mathbf{g}_{n_e}$ is calculated. This last vector represents the solution of the unknown incremental changes of the main state variables for node n_e, i.e., $\mathbf{x}_{n_e}$. With that, backward elimination (for $i = n_e-1, n_e-2, \ldots, 1$) under consideration of $\mathbf{K}_i$ and $\mathbf{g}_i$ yields the missing vectors of the unknown changes of the state variables, $\mathbf{x}_i$.

Forward elimination:

$$
\mathbf{H}_1 = -\mathbf{B}_1^{-1}\mathbf{C}_1\,.
$$
(E.231)

For $i = 2, 3, \ldots, n_e-1$ do

$$
\mathbf{H}_i = -\mathbf{K}_i^{-1}\mathbf{C}_i \qquad \text{with} \qquad \mathbf{K}_i = \mathbf{B}_i + \mathbf{A}_i\mathbf{H}_{i-1}\,.
$$
(E.232)

$$
\mathbf{K}_{n_e} = \mathbf{B}_{n_e} + \mathbf{A}_{n_e}\mathbf{H}_{n_e-1}\,.
$$
(E.233)

$$\mathbf{g}_1 = -\mathbf{B}_1^{-1}\mathbf{r}_1 \,. \tag{E.234}$$

For $i = 2, 3, \ldots, n_e$ do

$$\mathbf{g}_i = \mathbf{K}_i^{-1}\mathbf{l}_i \qquad \text{with} \qquad \mathbf{l}_i = \mathbf{r}_i - \mathbf{A}_i\mathbf{g}_{i-1} \,. \tag{E.235}$$

Backward substitution:

$$\mathbf{x}_{n_e} = \mathbf{g}_{n_e} \,. \tag{E.236}$$

For $i = n_e - 1, n_e - 2, \ldots, 1$ do

$$\mathbf{x}_i = \mathbf{g}_i + \mathbf{H}_i\mathbf{x}_{i+1} \,. \tag{E.237}$$

E.2 Numerical analysis of one-dimensional transient heat transport in concrete

For the solution of the thermal problem only (uncoupled analysis), Equation (3.3) is reduced to

$$\rho_c c_p \frac{\partial T}{\partial t} - \text{ div } (\lambda \text{ grad } T) = 0 \,. \tag{E.238}$$

In this case, Equations (3.1) and (3.2) are disregarded.

In case heat sinks associated with (i) vaporization with water and (ii) dehydration of the cement paste are considered, Equation (E.238) is extended, yielding (see [128, 130])

$$\rho_c c_p \frac{\partial T}{\partial t} - \text{ div } (\lambda \text{ grad } T) = E_{\xi_{vap}} \frac{\partial \xi_{vap}}{\partial t} + E_\xi \frac{\partial \xi}{\partial t} \,, \tag{E.239}$$

where $\xi_{vap} = w/m_w$ describes the vaporization process, with w [(kg water)/m³] as the amount of evaporable water at a given time and m_w [(kg water)/m³] as the initial amount of evaporable water (see [128, 130] for details). $\xi = m_h/m_{h0}$ represents the hydration degree (see Equation (E.42)). The corresponding dissipated energies $E_{\xi_{vap}}$ and E_ξ are defined as

$$E_{\xi_{vap}} = m_w h \qquad \text{and} \qquad E_\xi = m_c l_\xi + m_{w,ch} h \,, \tag{E.240}$$

where m_c [(kg binder)/m³] is the cement (binder) content and $m_{w,ch}$ [kg/m³] is the amount of chemically-bound water that is liberated during dehydration of the cement paste (see [128, 130] for details). In Equation (E.240), h [kJ/(kg water)] and l_ξ [kJ/(kg binder)] are the specific enthalpy of vaporization and of hydration/dehydration, respectively.

E.3 Numerical analysis of one-dimensional transient gas flow in concrete

According to [72], the macroscopic mass balance equation of the gas phase in porous media reads for the one-dimensional case[5]

$$-n\rho^g\frac{\partial S_w}{\partial t} + n(1-S_w)\left(\frac{\partial\rho^{ga}}{\partial t} + \frac{\partial\rho^{gw}}{\partial t}\right) - \frac{\partial}{\partial x}\left(\rho^g\frac{kk^{rg}}{\eta}\frac{\partial p^g}{\partial x}\right) = 0\,, \quad \text{(E.241)}$$

where ρ^{ga} and ρ^{gw} [kg/m^3] are the densities of dry air and water vapor, respectively, and ρ^g [kg/m^3] is the gas (mixture of dry air and water vapor) density with $\rho^g = \rho^{ga} + \rho^{gw}$. In Equation (E.241), n [–] is the porosity of concrete, S_w [–] is the water saturation, k^{rg} [–] is the relative permeability of concrete to gas flow, and p^g [Pa] is the gas pressure. Assuming that no water is present within the concrete specimen tested within the permeability experiments presented in Subsection 2.2 gives $S_w = 0$ and $k^{rg} = 1$. Therefore, Equation (E.241) reduces to

$$n\left(\frac{\partial\rho^{ga}}{\partial t} + \frac{\partial\rho^{gw}}{\partial t}\right) - \frac{\partial}{\partial x}\left(\rho^g\frac{k}{\eta}\frac{\partial p^g}{\partial x}\right) = 0\,. \quad \text{(E.242)}$$

Note that the third term in Equation (E.242) contains Darcy's law for pressure-driven flow, reading $v = -k/\eta \cdot \partial p^g/\partial x$, with v [m/s] as the velocity of the advected gas (compare to Equation (2.14) in Subsection 2.2.3, with $Q = A \cdot v$). Since the permeability experiments were performed at room temperature at which vapor transport may be neglected, $\rho^{gw} = 0$ yields $\rho^g = \rho^{ga}$ and $p^g = p^{ga} = p$. Inserting Equation (2.16) into Equation (E.242) and considering Clapeyron's law for ideal gases, giving $\rho^{ga} = M_a/(R\Theta) \cdot p$, with $M_a = 0.029$ kg/mol as the molar mass of air, $R = 8.31$ J/(mol K) as the gas constant, and Θ [K] as the constant temperature, leads to (after division by $M_a/(R\Theta)$)

$$n\frac{\partial p}{\partial t} - \frac{k_{int}}{\eta}\frac{\partial}{\partial x}\left[(p+b)\frac{\partial p}{\partial x}\right] = 0\,. \quad \text{(E.243)}$$

---

[5]In contrast to [72], neither movement of the solid phase nor mass sources/sinks are considered. Moreover, the temperature is assumed to be constant (therefore, the respective time derivative vanishes).

Modeling the strain response of concrete subjected to combined thermal and mechanical loading

So far, the experimentally-observed path dependence of the strain response of concrete subjected to combined thermal and mechanical loading (see Figure F.1 and, e.g., [5, 32, 62, 105, 121]) is captured by introduction of the so-called "load-induced thermal strain (LITS)", leading to decomposition of the strain in the form (see, e.g., [44, 83, 107, 119, 120])

$$E(T, \sigma) = E^\sigma(T, \sigma) + E^{th}(T) + E^{lits}(T, \sigma), \tag{F.1}$$

with $E^\sigma(T, \sigma)$ as the mechanical strain (comprising elastic and plastic components), $E^{th}(T)$ as the free thermal strain (FTS, comprising thermal expansion and shrinkage strains), and $E^{lits}(T, \sigma)$ as the aforementioned load-induced thermal strain (LITS). Departing from Equation (F.1), empirical models for determination of $E^{lits}(T, \sigma)$ were developed in order to reproduce the path dependence shown in Figure F.1 (see, e.g., [44, 83, 119, 120, 107]). When a rate formulation – as opposed to the standard formulation $E^{th} = E^{th}(T)$ used in Equation (F.1) – is introduced, reading

$$\dot{E}^{th} = \dot{E}^{th}(\dot{T}, \sigma), \tag{F.2}$$

the reduced formation of microcracks in the cement paste due to strain incompatibilities (as appearing in case of free thermal dilation) in case mechanical loading is applied can be considered directly in the evolution of the thermal strain. Hence, the introduction of LITS to capture the path dependence shown in Figure F.1 is no longer required.
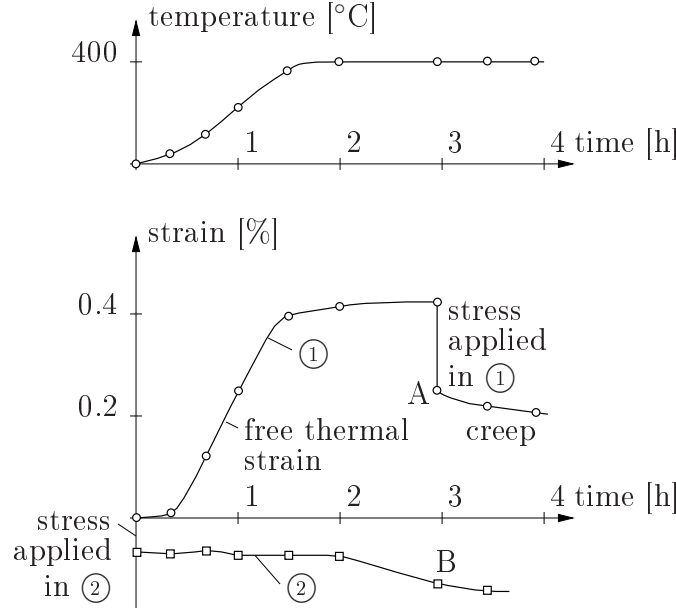
Figure F.1: Illustration of path dependence of combined thermal and mechanical loading of concrete [120]: points A and B exhibit the same temperature and stress level (experimental results obtained with $T_{max} = 400$ °C and $\sigma = 0.45\ f_{c,0}$; $f_{c,0}$: compressive strength of concrete at room temperature)

F.1 Illustrative 1D model for heated concrete

The 1D two-phase model shown in Figure F.2(d) was obtained from combining the two arrangements representing lower (Voigt) and upper (Reuss) bounds of the composite's strain behavior (see Figures F.2(a) and (b)), representing an idealized form of the morphology of concrete divided into N "columns" (see Figure F.2(c)). The material parameters for the two phases are given in Table F.1. The thermal strain of each phase alone is deduced from experimental results (see Figure F.3 and [106]). Hereby, the thermal strain of the cement paste is larger than the respective strain of the aggregate for $T < 212$ °C. For higher temperatures, shrinkage of the cement paste and continuation of thermal expansion of the aggregate results in $\varepsilon_c^{th} < \varepsilon_a^{th}$. The behavior of the cement paste is modeled considering hardening plasticity and temperature-induced softening (in consequence of dehydration), leading to a decrease of the respective material parameters with increasing temperature (see Figure F.4).

Figure F.5 shows the strain response and the corresponding stresses obtained using the different models and, as a first step, disregarding temperature dependence of the material parameters of the cement paste. In case the two material phases are connected in parallel (Voigt), the resulting strain is almost identical to the aggregate strain since the whole cement paste experiences plastic deformations starting at $T \approx 200$ °C (as indicated by the corresponding stresses reaching the tensile strength, see dash-dotted line in Figure F.5(b)). In case the two phases are connected in series (Reuss), the stresses are
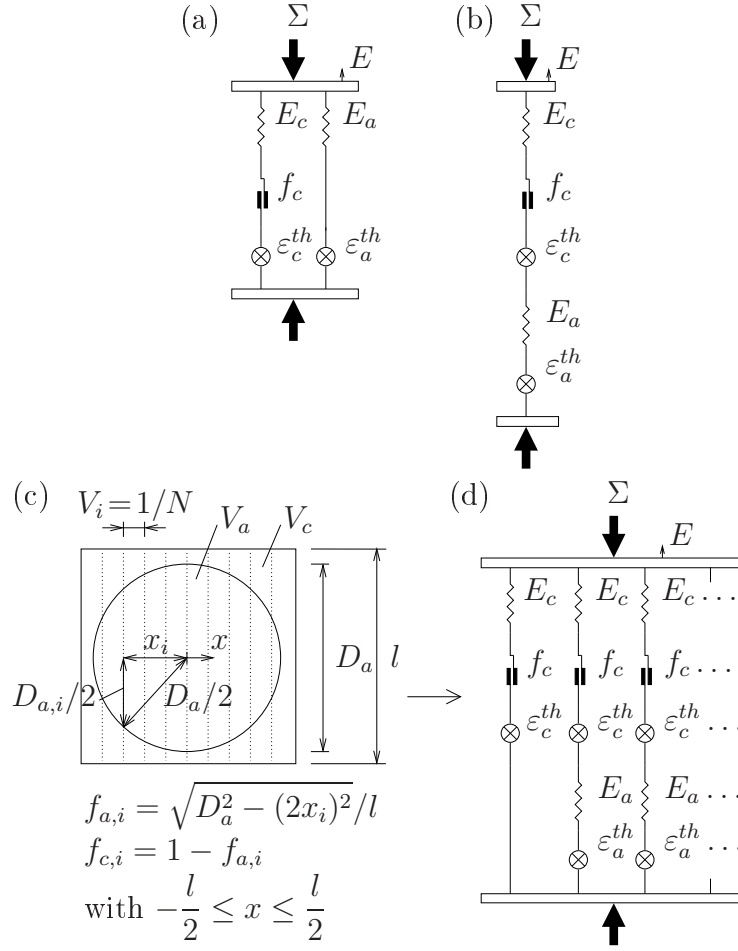
Figure F.2: 1D composite model for heated concrete: (a) Voigt model; (b) Reuss model; (d) employed N-model, taking (c) idealized concrete morphology into account

Table F.1: Input parameters for two-phase composite model

Input parameter	Value
Cement matrix:	
Volume fraction f_c [–]	0.3
Young's modulus $E_{c,0}$ [MPa]	15
Poisson's ratio ν_c [–]	0.2
Compressive strength $f_{c,0}^c$ [MPa]	30
Tensile strength $f_{c,0}^t$ [MPa]	3
Aggregate:	
Volume fraction f_a [–]	0.7
Young's modulus E_a [MPa]	70
Poisson's ratio ν_a [–]	0.2
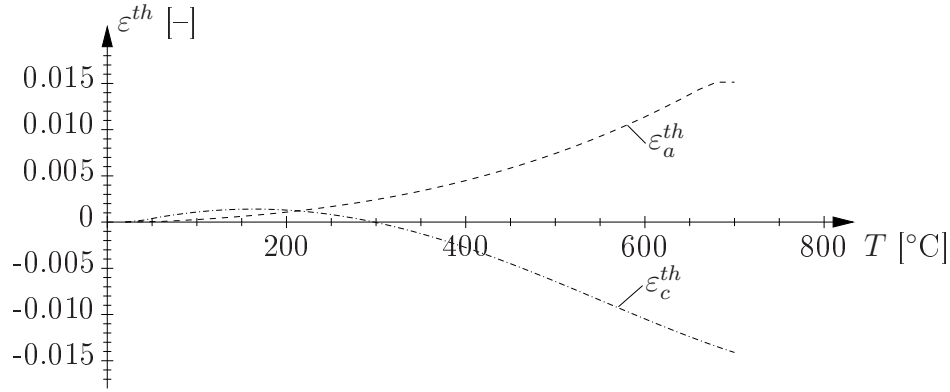
Figure F.3: Free thermal strain (FTS) of cement paste and aggregate, ε_c^{th} and ε_a^{th}, deduced from experiments [106]
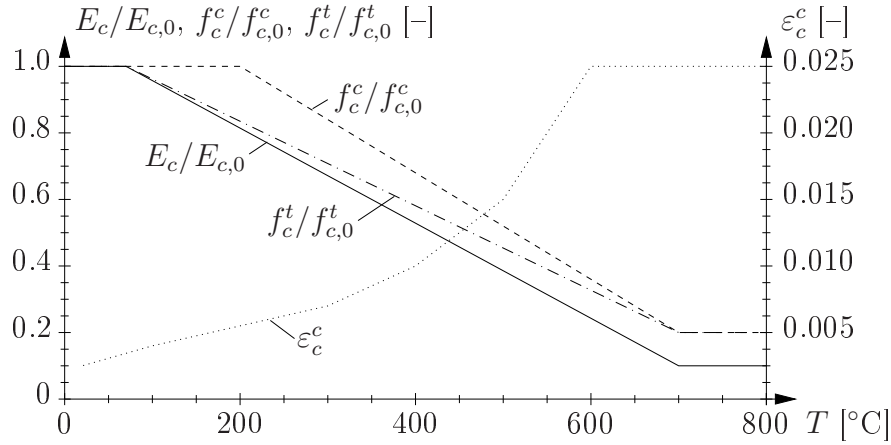
Figure F.4: Temperature dependence of material parameters of cement-matrix phase, derived from design curves given in [22, 87] (ε_c^c: strain at compressive strength f_c^c)

identical in the two phases (Σ in Figure F.5(b)) and no plastic deformations occur. The macroscopic strain response obtained from the N-model lies within these two bounds (see Figure F.5(a)). For temperatures below 212 °C ($\varepsilon_c^{th} > \varepsilon_a^{th}$), tensile plastic deformations within the cement paste are observed in the middle "column". As temperature increases and ε_c^{th} becomes smaller than ε_a^{th}, tensile plastic deformations within the cement paste are observed in the outer "columns" (see Figure F.5(b)).

Considering temperature dependence of the parameters of the cement paste, the following results are obtained (see Figure F.6):

1. Thermal degradation of Young's modulus E_c: The decrease in stiffness of the cement paste results in an overall less stiff composite. Therefore, the mechanical strains in consequence of mechanical loading are slightly higher than in case no temperature dependence of E_c is considered, yielding total strains of slightly smaller magnitude.
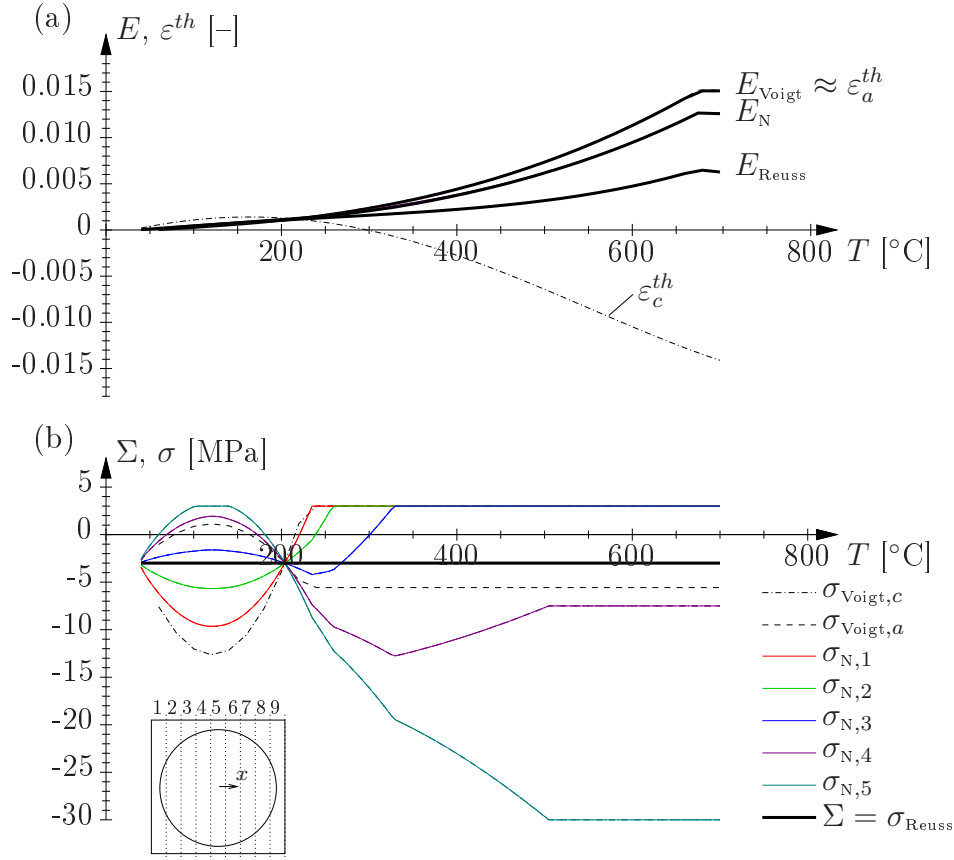
Figure F.5: (a) Strain and (b) stress histories obtained from composite models given in Figure F.2 for $s = \Sigma/f_{c,0} = 0.1$ ($N = 9$; $f_{c,0}$: compressive strength of concrete at room temperature)

2. Thermal degradation of compressive strength f_c^c: The temperature dependence of the compressive strength of the cement paste has the highest influence. At higher temperatures, it leads to compressive plastic deformations within the cement paste in the middle "columns" and, hence, to less macroscopic strain.

3. Thermal degradation of tensile strength f_c^t: The decrease of the tensile strength of the cement paste has a smaller effect on the strain history, shifting the strain response towards ε_a^{th}.

As shown in Figure F.7, the path dependence of the strain response is captured with the N-model given in Figure F.2(d). The difference in strains at $T_{max} = 400$ °C and $s = 0.45$ is explained by different plastic deformations in the cement paste, resulting from predominantly tensile loading of the cement paste in case of heating without mechanical load and predominantly compressive loading in case of heating under mechanical load.

In a next step, the 2D morphology introduced in Figure F.2(c) is replaced by 3D matrix-inclusion morphologies (see Figure F.8 and [69]). The results obtained from an N×N-
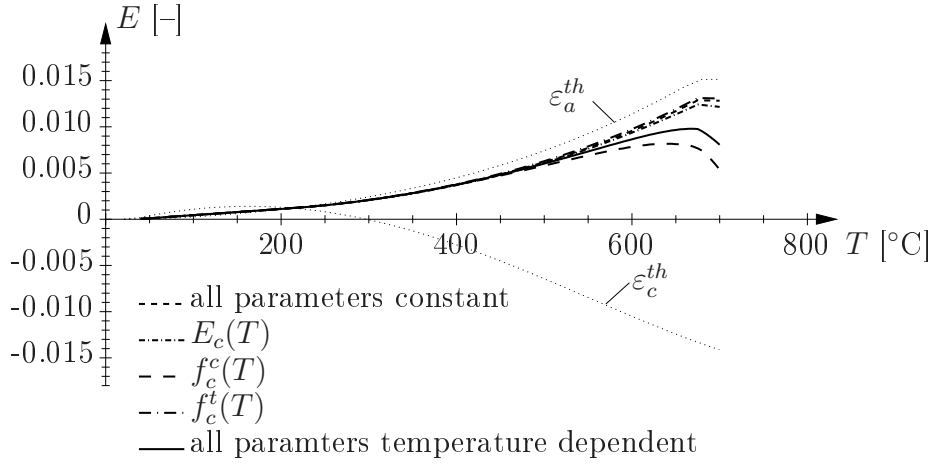
Figure F.6: Influence of temperature dependence of parameters of cement paste on strain history of N-model for $s = \Sigma/f_{c,0} = 0.1$
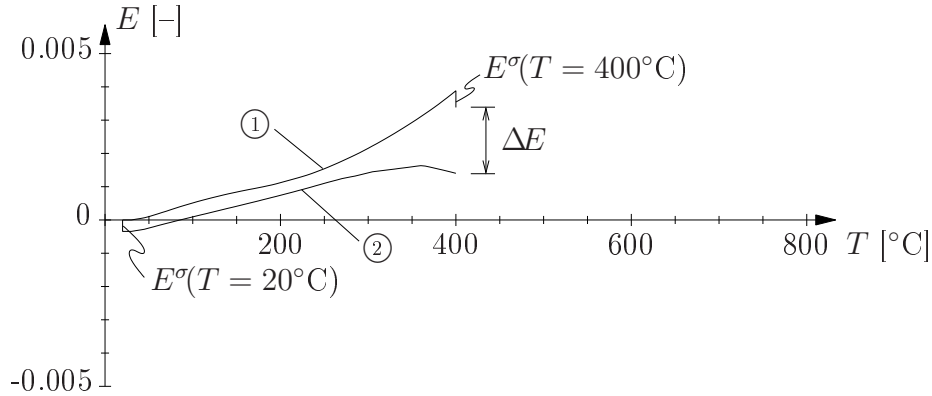

Figure F.7: Model results capturing the path dependence of combined thermal and mechanical loading ($T_{max} = 400$ °C and $s = \Sigma/f_{c,0} = 0.45$)

discretization of the 3D morphology are shown in Figure F.9, comparing also experimental results reported in [32][1]. When no mechanical loading is applied ($s = 0$), the results obtained with the 2D N-model have the highest magnitude, indicating that temperature-induced weakening as well as plastic deformations (in consequence of strain incompatibilities) of the cement paste have the highest influence for this model. This observation is supported by the results considering mechanical loading, where plastic strains in consequence of continuous mechanical loading of the thermally-degrading cement paste are the largest. The 3D model with uniform sphere diameters (see Figure F.8(a)), on the other hand, is apparently influenced least by degradation of the cement paste. The qualitative agreement between experimental and numerical results is satisfactory, considering the grade of simplicity and idealization of the employed models.

---

[1]The experimental results presented in [32] were obtained on concrete specimens with the dimensions $0.20 \times 0.20 \times 0.05$ m heated at a heating rate of 2 K/min under different load levels.
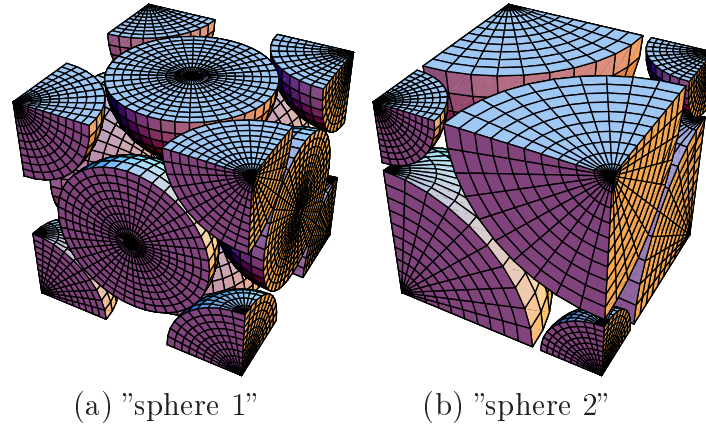
(a) "sphere 1"   (b) "sphere 2"

Figure F.8: 1D composite model considering 3D matrix-inclusion morphology: (a) uniform sphere diameter; (b) two sphere diameters (volume fractions according to Table F.1: $f_c = 0.3$, $f_a = 0.7$)
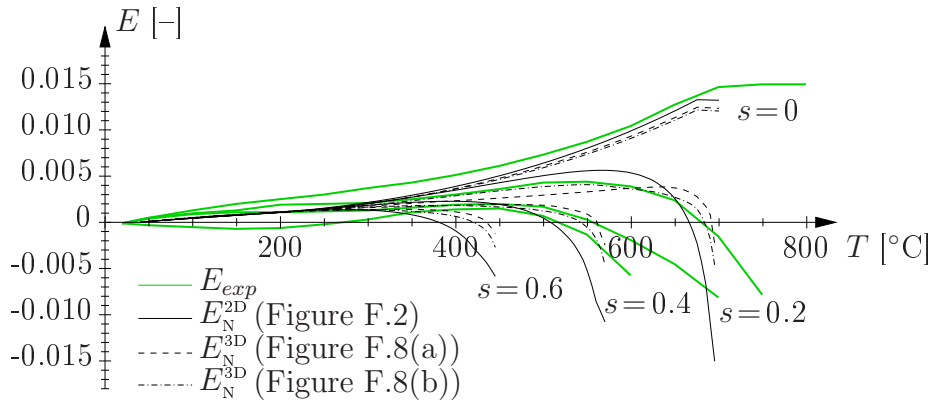

Figure F.9: Comparison of strain measurements [32] with model results considering 2D and 3D morphologies for different levels of loading $s = \Sigma/f_{c,0} = 0, 0.2, 0.4, 0.6$

F.2   Finite-element model for heated concrete

The N-model presented in the previous subsection regards every of the N "columns" separately, only forcing uniform displacements at top and bottom of the composite cell. Hence, relative vertical displacements between the phase interfaces of neighboring "columns" are not hindered. In order to overcome this, finite-element (FE) models representing the investigated morphologies (see Figures F.2(c) and F.8) were analyzed.

Figure F.10 shows comparison of numerical strains obtained by FE analyses of the 2D morphology depicted in Figure F.2(c). Hereby, the volume fractions of the two phases are varied. Compared to the 1D model presented in the previous subsection, the hindered relative vertical displacement results in an overall stiffer structure for the same volume fractions (compare with Figure F.9). In general, the model is able to qualitatively reproduce the experimental observations.
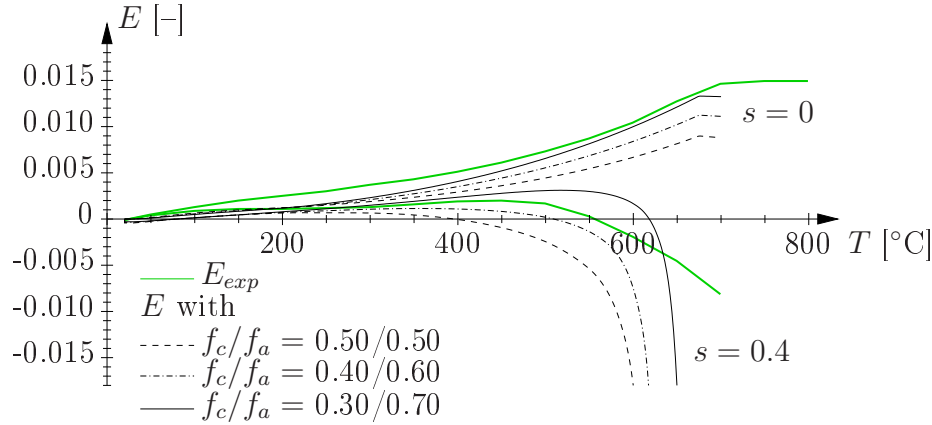
Figure F.10: Comparison of strain measurements [32] with numerical results from FE analysis of 2D model (according to Figure F.2(c)) for different volume fractions of cement paste and aggregate and for $s = \Sigma/f_{c,0} = 0$ and 0.4

The influence of combined mechanical and thermal loading on the numerical results is depicted in Figure F.11, showing the internal variable of the considered Drucker-Prager criterion (α_D [–]) representing plastic deformations under compressive loading. At $T = 20\,°\text{C}$ (see Figure F.11(a)), when only the mechanical loading ($s = 0.4$) is applied, a plastic region develops at the top due to compressive loading. When temperature rises, strain incompatibilities due to different thermal dilation (see Figure F.3) induce compression in circumferential direction in the cement matrix, leading – together with continuous mechanical loading – to development of a second plastic region in the cement matrix (see Figure F.11(b) for $T = 120\,°\text{C}$). With further temperature increase, temperature-induced degradation of the cement paste and the change in thermal-dilation behavior (see Figure F.3) yields further compressive plasticity at the top of the structure (see Figure F.11(c) for $T = 220\,°\text{C}$).

The results obtained by FE analyses of the investigated 3D morphologies are compared to the experimental results in Figure F.12, showing again that hindering the abovementioned relative vertical displacement results in an overall stiffer structure (compare with Figure F.9). The results for thermal strains without mechanical loading show good agreement with the measurements, the strain response of the two morphologies for $s = 0.4$ shows considerable deviation from the corresponding experimental results. The reason for this discrepancy may be explained by (i) restraint introduced by the boundary conditions at the top surface (enforcing uniform displacement of the top surface, see Figure F.8) and (ii) consideration of a limited number of sphere diameters in the model whereas in reality the aggregate diameter is distributed – according to the grading curve – over a certain range of diameters.

Figure F.13 shows numerical results for the 3D morphology with uniform sphere diameter (see Figure F.8(a)). In case no mechanical loading is applied, temperature increase results
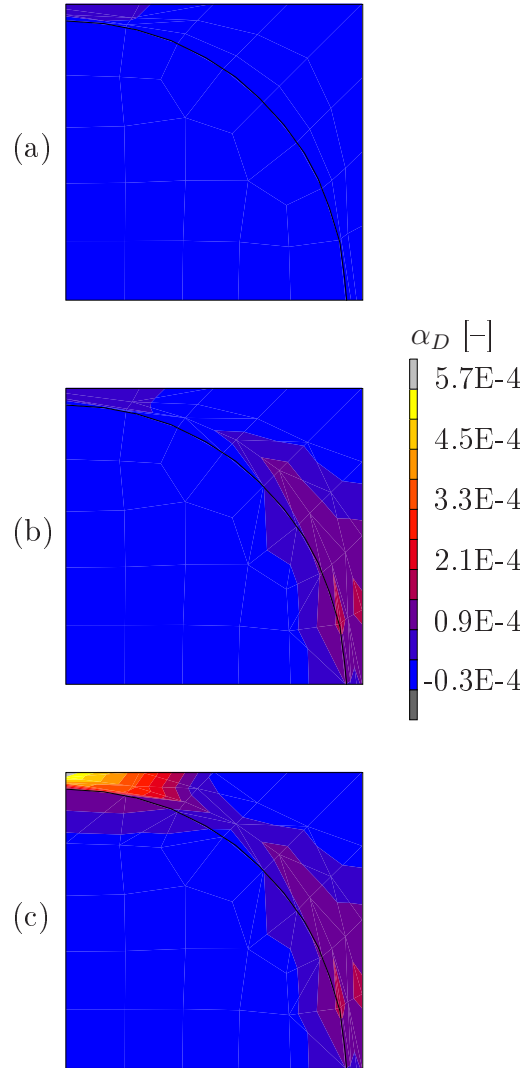
Figure F.11: Internal variable for Drucker-Prager plasticity criterion α_D [–] obtained from FE analysis of 2D model (according to Figure F.2(c)) for $f_c/f_a = 0.30/0.70$ and $s = \Sigma/f_{c,0} = 0.4$, indicating regions of compressive plastic deformations: (a) $T = 20$ °C, (b) $T = 120$ °C, (c) $T = 220$ °C

in symmetric tensile plastic regions in the cement paste (see Figure F.13(a)) and, therefore, a symmetric stress state (see Figure F.13(b)). When mechanical loading is applied prior to temperature increase, the amount of tensile plastic deformations is reduced (see Figure F.13(c)) since part of the tensile stresses are overshadowed by the compressive loading (see Figure F.13(d)). This indicates that damage due to tensile plasticity is reduced in case of mechanical loading prior to temperature loading, which was also observed during experiments (see, e.g., [66]). In addition, the distribution of the vertical stress component shown in Figure F.13(d) illustrates that the stress trajectories follow the stiff aggregate

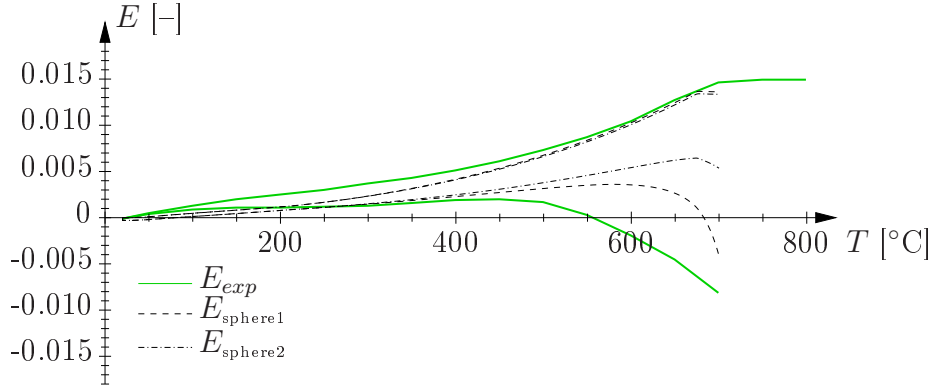phase, leaving smaller compressive stresses in the cement matrix.

Figure F.12: Comparison of strain measurements [32] with numerical results from FE analysis of 3D model (sphere1: see Figure F.8(a); sphere2: see Figure F.8(b)) for $f_c/f_a = 0.30/0.70$ and $s = \Sigma/f_{c,0} = 0, 0.4$
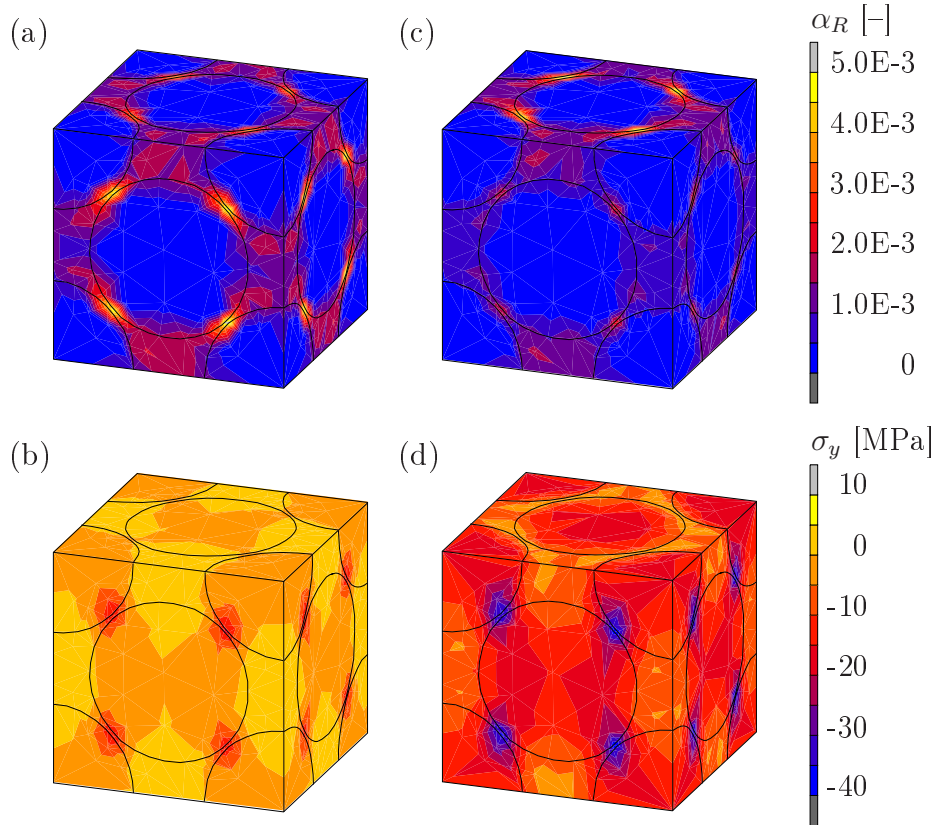

Figure F.13: Results from FE analysis of 3D model (sphere1: see Figure F.8(a)) for $f_c/f_a = 0.30/0.70$ at $T = 250$ °C: (a) α_R and (b) σ_y for $s = 0$; (c) α_R and (d) σ_y for $s = 0.4$ (α_R [–]: internal variable for Rankine plasticity criterion, σ_y [MPa]: vertical stress component)

In case the 3D morphology with two sphere diameters is investigated, similar observations as mentioned before are made. Again, the amount of tensile plastic deformations of the cement paste is reduced in case mechanical compressive loading is applied (compare Figures F.14(a) and (c)). Additionally, the stress trajectories again follow the stiff aggregate phase (see Figures F.14(b) and (d)).
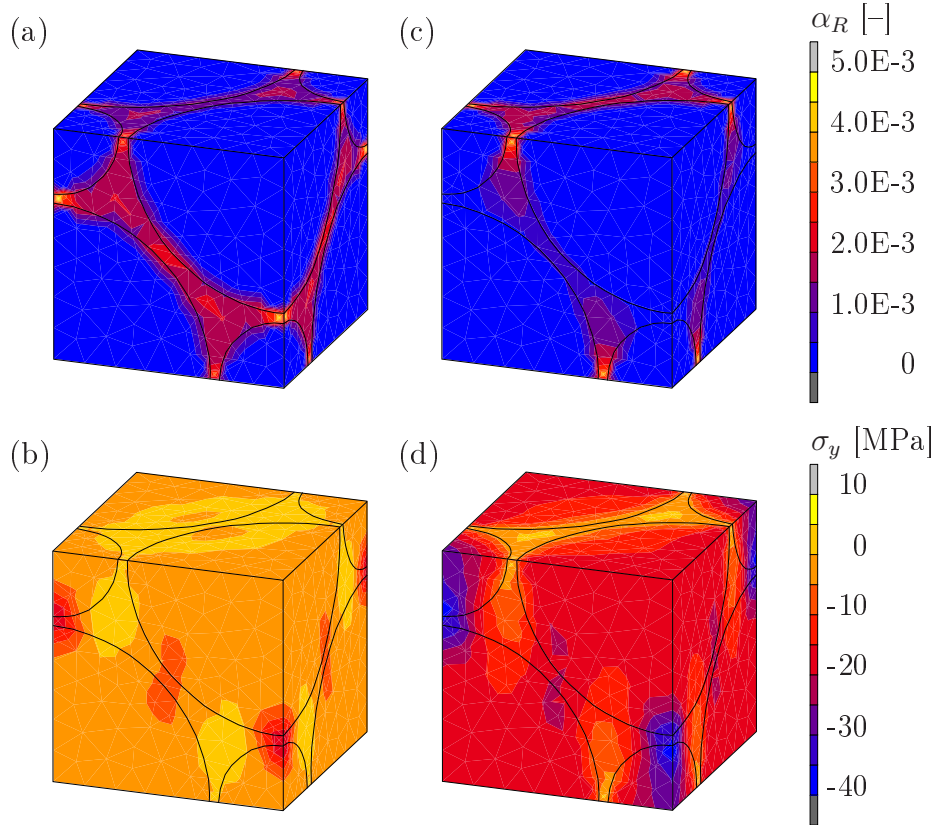

Figure F.14: Results from FE analysis of 3D model (sphere2: see Figure F.8(b)) for $f_c/f_a = 0.30/0.70$ at $T = 250$ °C: (a) α_R and (b) σ_y for $s = 0$; (c) α_R and (d) σ_y for $s = 0.4$ (α_R [–]: internal variable for Rankine plasticity criterion, σ_y [MPa]: vertical stress component)

Matthias ZEIML | Curriculum Vitae

Personal Data

Name:	Matthias ZEIML
Academic Degree:	Dipl.-Ing.
Place/Date of Birth:	Vienna, December 18, 1976
Citizenship:	Austrian

Education

09/1991 - 06/1996	Camillo Sitte High School (Civil Engineering), Vienna, Austria Graduation with distinction
10/1997 - 04/2004	Diploma studies in Civil Engineering, Vienna University of Technology, Vienna, Austria Graduation with distinction
05/2004 - 07/2008	Doctoral studies at Vienna University of Technology, Vienna, Austria Dissertation at the Institute for Mechanics of Materials and Structures

Activities abroad

08/2000 - 05/2001	Colorado School of Mines, Golden CO, USA Department of Civil Engineering (AE3 Joint Study Exchange Program)
11/2004, 01/2005	University of Padua, Padua, Italy Department of Structural and Transportation Engineering (Postgraduate research fellowship, collaboration with Prof. B. A. Schrefler)

Work experience

10/1996 - 09/1997	Civil services, Arbeiter-Samariter-Bund, Vienna, Austria
09/1997 - 09/2001	Baumeister Ing. Paul Chmelar, Mödling, Austria (Part time employee)
05/2001 - 07/2001	Rocky Mountain Prestress, Denver CO, USA
12/2001 - 04/2004	ZT Dr. Wolfgang Lindlbauer, Vienna, Austria (Part time employee)
05/2004 - present	Research/University Assistant Institute for Mechanics of Materials and Structures (IMWS) (former Institute for Strength of Materials) Vienna University of Technology, Vienna, Austria
12/2007 - present	Scientific Head (together with Prof. J. Eberhardsteiner) Laboratory for Macroscopic Material Testing at the IMWS Vienna University of Technology, Vienna, Austria